Stony Brook University

OFFICIAL COPY

The official electronic file of this thesis or dissertation is maintained by the University Libraries on behalf of The Graduate School at Stony Brook University.

© All Rights Reserved by Author.

Nanostructured Iron and Manganese Oxide Electrode Materials for Lithium Batteries: Influence of Chemical and Physical Properties on Electrochemistry

A Dissertation presented

by

Jessica L. Durham

to

The Graduate School

in Partial Fulfillment of the

Requirements

for the Degree of

Doctor of Philosophy

in

Chemistry

Stony Brook University

December 2016

Copyright by
Jessica Durham
2016

Stony Brook University
The Graduate School

Jessica L. Durham

We, the dissertation committe for the above candidate for the
Doctor of Philosophy degree, hereby recommend
acceptance of this dissertation

Dr. Esther S. Takeuchi - Dissertation Advisor
Distinguished Professor, Department of Chemistry

Dr. Kenneth J. Takeuchi - Co-Advior
Distinguished Teaching Professor, Department of Chemistry

Dr. Amy C. Marschilok - Co-Advisor
Research Professor, Department of Chemistry

Dr. Stephen A. Koch - Chairperson of Defense
Professor, Department of Chemistry

Dr. Stanislaus S. Wong - Committee Member
Professor, Department of Chemistry

Dr. Hong Gan - Outside Committee Member
Energy Storage Group Leader, Department of Sustainable Energy Technologies
Brookhaven National Laboratory

This dissertation is accepted by the Graduate School

Nancy Goroff
Interim Dean of the Graduate School

Abstract of the Dissertation

Nanostructured Iron and Manganese Oxide Electrode Materials for Lithium Batteries: Influence of Chemical and Physical Properties on Electrochemistry

by

Jessica L. Durham

Doctor of Philosophy

in

Chemistry

Stony Brook University

2016

The widespread use of portable electronics and growing interest in electric and hybrid vehicles has generated a mass market for batteries with increased energy densities and enhanced electrochemical performance. In order to address a variety of applications, commercially fabricated secondary lithium-ion batteries employ transition metal oxide based electrodes, the most prominent of which include lithium nickel manganese cobalt oxide ($LiNi_xMn_yCo_{1-x-y}O_2$), lithium iron phosphate ($LiFePO_4$), and lithium manganese oxide ($LiMn_2O_4$). Transition metal oxides are of particular interest as cathode materials due to their robust framework for lithium intercalation, potential for high energy density, and utilization of earth-abundant elements (i.e. iron and manganese) leading to decreased toxicity and cost-effective battery production on industrial scales.

Specifically, this research focuses on $MgFe_2O_4$, $Ag_xMn_8O_{16}$, and $AgFeO_2$ transition metal oxides for use as electrode materials in lithium-based batteries. The electrode materials are prepared via co-precipitation, reflux, and hydrothermal methods and characterized by several techniques (XRD, SEM, BET, TGA, DSC, XPS, Raman, etc.). The low-temperature

syntheses allowed for precise manipulation of structural, compositional, and/or functional properties of $MgFe_2O_4$, $Ag_xMn_8O_{16}$, and $AgFeO_2$ which have been shown to influence electrochemical behavior. In addition, advanced *in-situ* and *ex-situ* characterization techniques are employed to study the lithiation/de-lithiation process and establish valid redox mechanisms.

With respect to both chemical and physical properties, the influence of $MgFe_2O_4$ particle size and morphology on electrochemical behavior was established using *ex situ* X-ray absorption spectroscopy (XAS) and transmission electron microscopy (TEM) imaging. Based on composition, tunneled $Ag_xMn_8O_{16}$ nanorods, prepared with distinct Ag^+ contents and crystallite sizes, display dramatic differences in ion-transport kinetics due to structural defects which facilitate Li^+ diffusion through the tunnel walls and intimate electrochemical connection of bundled nanorods. Finally, a one-pot synthesis provided a series of $AgFeO_2/\gamma$-Fe_2O_3 or Ag_xFeO_y composites which, at the lowest silver regime ($Ag_{0.2}FeO_{1.6}$), exhibit 2X higher capacity than stoichiometric $AgFeO_2$ and over 3X greater capacity than nanocrystalline γ-Fe_2O_3 after 50 cycles. Notably, mechanical mixing of $AgFeO_2$ and γ-Fe_2O_3 powders to mimic a one-pot $Ag_{0.2}FeO_{1.6}$ composite yields lower delivered capacity and energy density where the results demonstrate the advantages of the directly prepared composite with more intimate particle connectivity not achievable through mechanical mixing.

Dedication Page

This dissertation is dedicated to my loving parents, Jamie and Rhonda Durham, who have provided me with their unwavering support and endless encouragement over the years. They have instilled in me a strong work ethic and the tenacity and persistence necessary to achieve the goals I set in life. For the unselfish sacrifices they have made throughout my life to allow me to succeed, I am eternally grateful.

Table of Contents

List of Figures

List of Tables

Acknowledgements

The research presented in this dissertation was conducted over four years and required the assistance of several people. I would like to take this opportunity to acknowledge those without whom the data presented in this document would not form a complete and intriguing story.

First and foremost, I would like to thank my advisors, Dr. Esther Takeuchi, Dr. Kenneth Takeuchi, and Dr. Amy Marschilok, for providing me with their guidance and generous support during my time at Stony Brook University. I am truly appreciative of the innovative synthetic challenges they presented to me and for the unique research and collaborative opportunities they provided me with. Their unwavering enthusiasm and encouragement has allowed me to thrive in the laboratory and continually evolve as a scientist. In addition, I would like to gratefully acknowledge Dr. Lisa Szczepura, my undergraduate and graduate advisor at Illinois State University, for introducing me to inorganic synthetic chemistry, offering exceptional guidance during my early career, and motivating me to pursue a doctoral degree in Chemistry.

I have had the opportunity to work alongside and in collaboration with highly successful post docs and graduate students, Dr. Kevin Kirshenbaum, Dr. Christopher Pellicione, Dr. David Bock, Dr. Altug Poyraz, Dr. Wei Zhang, Jianping Huang, and Alexander Brady. I am appreciative of the time each of them took to teach me valuable experimental techniques and for the insightful discussions concerning my research projects. I am fortunate to have collaborated with scientists at Brookhaven National Laboratory, including Dr. Yimei Zhu, Dr. Lijun Wu, Dr. Feng Xu, and Dr. Feng Wang from the Center for Functional Nanomaterials. I would like to acknowledge Dr. Pellicione, Dr. Wu, and Dr. Zhang, in

particular, for analyzing advanced characterization data, the outcome of which significantly established the arguments formed in this dissertation.

I would also like to express my gratitude to my dissertation committee, Dr. Stephen Koch, Dr. Stanislaus Wong, and Dr. Han Gong for the advice, constructive feedback, and thought-provoking discussions they have offered me over the years.

Foreword

A majority of the research presented in this dissertation has been published, therefore, portions of this document have been summarized or paraphrased from the following publications:

CHAPTER III: L. Wu, F. Xu, Y. Zhu, A. B. Brady, J. Huang, J. L. Durham, E. Dooryhee, A. C. Marschilok, E. S. Takeuchi, K. J. Takeuchi. "Structural Defects of Silver Hollandite, $Ag_xMn_8O_y$, Nanorods: Dramatic Impact on Electrochemistry." *ACS Nano* **2015**, *9*, 8430-8439. Adapted with permission. Copyright © 2016 American Chemical Society.

CHAPTERS V and VI: J. L. Durham, K. Kirshenbaum, E. S. Takeuchi, A. C. Marschilok, K. J. Takeuchi. "Synthetic Control of Composition and Crystallite Size of Silver Ferrite Composites: Profound Electrochemistry Impacts." *Chemical Communications* **2015**, *51*, 5120-5123. Reproduced with permission from the Royal Society of Chemistry.

CHAPTER V and VI: J. L. Durham, K. Kirshenbaum, E. S. Takeuchi, A. C. Marschilok, K. J. Takeuchi. "In-Situ Formation of a Series of $AgFeO_2/\gamma$-Fe_2O_3 Composites: Impact on Electrochemical Performance." *MRS Advances* **2016**, *1*, 389-394. Reprinted with permission from Cambridge University Press.

CHAPTER V, VI, and VII: J. L. Durham, C. J. Pelliccione, W. Zhang, A. S. Poyraz, Z. Lin, F. Wang, E. S. Takeuchi, A. C. Marschilok, K. J. Takeuchi. "Silver Ferrite/Maghemite Composites and Mixtures: Impact of One-Pot Composite Preparation on Battery-Relevant Electrochemistry." *Applied Materials Today* **2016**, *accepted*.

J. L. Durham, E. S. Takeuchi, A. C. Marschilok, K. J. Takeuchi. "Nanocrystalline Iron Oxides Prepared via Co-Precipitation for Lithium Battery Cathode Applications." *ECS Transactions* **2015**, *66*, 111-120. Reproduced with permission. Copyright © 2016, The Electrochemical Society.

J. L. Durham, A. S. Poyraz, E. S. Takeuchi, A. C. Marschilok, K. J. Takeuchi. "Impact of Multifunction Bimetallic Materials on Lithium Battery Electrochemistry." *Accounts of Chemical Research* **2016**, *49*, 1864-1872. Adapted with permission. Copyright © 2016 American Chemical Society.

CHAPTER I

INTRODUCTION: TRANSITION METAL OXIDES AS ELECTRODE MATERIALS

1.1 Introduction

The widespread use of portable electronics and growing interest in electric and hybrid vehicles has generated a mass market for batteries with increased energy densities and enhanced electrochemical performance. Notably, rechargeable lithium-ion batteries (LIBs) have dominated the consumer market since they were initially commercialized in the early 1990s.[1] In an effort to address a variety of applications, commercially fabricated secondary LIBs employ several transition metal oxide based electrodes, the most prominent of which include lithium nickel manganese cobalt oxide ($LiNi_xMn_yCo_{1-x-y}O_2$), lithium iron phosphate ($LiFePO_4$), lithium cobalt oxide ($LiCoO_2$), and lithium manganese oxide ($LiMn_2O_4$).[2–11] Transition metal oxides are of particular interest as electrode materials due to their robust framework for lithium intercalation, potential for high energy density, and utilization of earth-abundant elements (e.g. iron and manganese) leading to decreased toxicity and cost-effective battery production on industrial scales.

With respect to the inherent crystal structure, transition metal oxides can be grouped into three main categories: zero-dimensional (0-D), one-dimensional (1-D), and two-dimensional (2-D). In this case, the dimensionality (i.e. 0-D, 1-D, 2-D) of transition metal oxides is defined in terms of ion mobility. Preferred diffusion pathways exist within crystalline materials and it is assumed that ion transport occurs following the path which exhibits the minimum total potential energy. The dimensionality of crystalline material is represented, in this dissertation, as the direction of the path(s) available in the crystalline material through which an ion or electron can be transported.

With regard to electrode materials available on the commercial market, the following statements can be made concerning structural motif and ion transport: 0-D materials ($LiMn_2O_4$[8,9] and $LiMn_{1.5}Ni_{0.5}O_4$[12,13]) are densely packed spinel structures with no direct

paths; 1-D $LiFePO_4$[6] and $LiMn_xFe_{1-x}PO_4$,[14,15] materials allow for the transport of ions or electrons down a tunnel; and $LiCoO_2$,[7] $LiNi_{1/3}Mn_{1/3}Co_{1/3}O_2$ (NMC),[5,16] $LiNi_{0.8}Co_{0.15}Al_{0.05}O_2$ (NCA),[17–20] and $LiNi_{0.5}Mn_{0.5}O_2$[2] are layered 2-D structures where ions can travel in the plane between transition metal oxide layers. **Figure 1.1** illustrates the structural differences between $LiMn_2O_4$[21] (0-D), $LiFePO_4$[22] (1-D), and $LiCoO_2$[23] (2-D) electrode materials and pathways available for Li^+ diffusion.

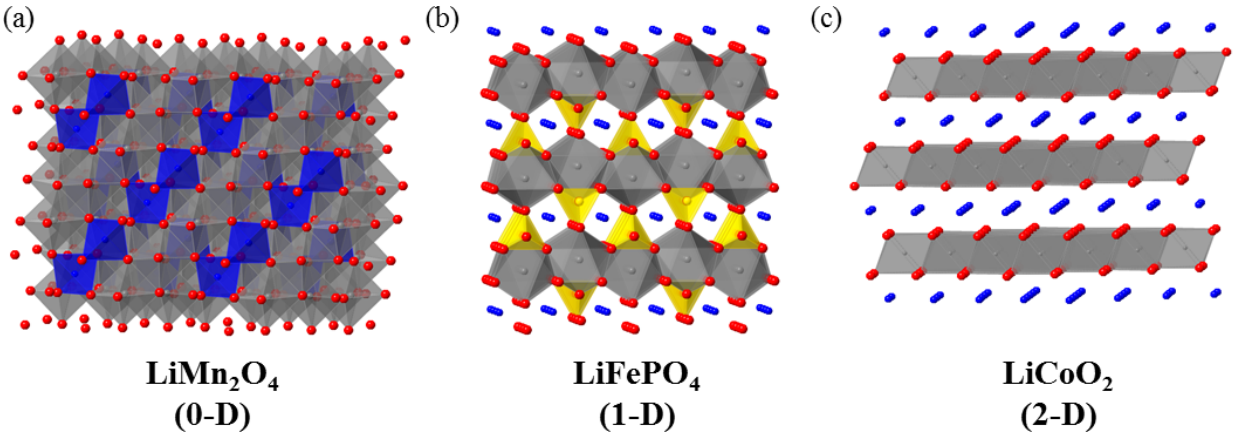

Figure 1.1. Dimensionality of commercially available electrode materials: (a) spinel $LiMn_2O_4$ (ICSD 89985), (b) tunneled $LiFePO_4$ (ICSD 161479), and (c) layered $LiCoO_2$ (ICSD 164802)

The cathode (positive electrode) is combined with an anode (negative electrode), separated by a polymer member, and immersed within an electrically conductive electrolyte to make up an electrochemical cell (**Figure 1.2**). A battery can either consist of a single electrochemical cell or a series of cells which provide power when connected to an external circuit. The battery systems outlined in this dissertation utilize transition metal oxide materials as either the cathode or anode, metallic lithium as the counter electrode, and organic carbonate electrolytes. The movement of ions (Li^+) within the electrochemical cell dictates the ability of the battery to do work.

In an electrical energy storage device, such as a battery, discharge is a spontaneous process in which electrons pass around the external circuit, thus providing useful power, and can be visualized as the migration of electrons and Li^+ ions from the anode to the cathode.

In contrast, charging is a non-spontaneous process which requires a voltage to be applied for the reverse movement of electrons and Li^+ ions (i.e. from the cathode back to the anode). During the discharge process, also referred to as intercalation with respect to Li^+ ions, electrode materials are known to experience alloying, intercalation, or conversion reactions.[24–28] Intercalation and conversion reactions are relevant to the redox mechanisms of the transition metal oxide electrode materials that will be presented in this dissertation. Intercalation includes the insertion of Li^+ ions into the crystalline lattice without compromising the structure while conversion is often a reversible process that occurs when the metal oxide is reduced, thus forming nanosized particles (reduced metal oxide or metallic phases) in a Li_2O matrix.

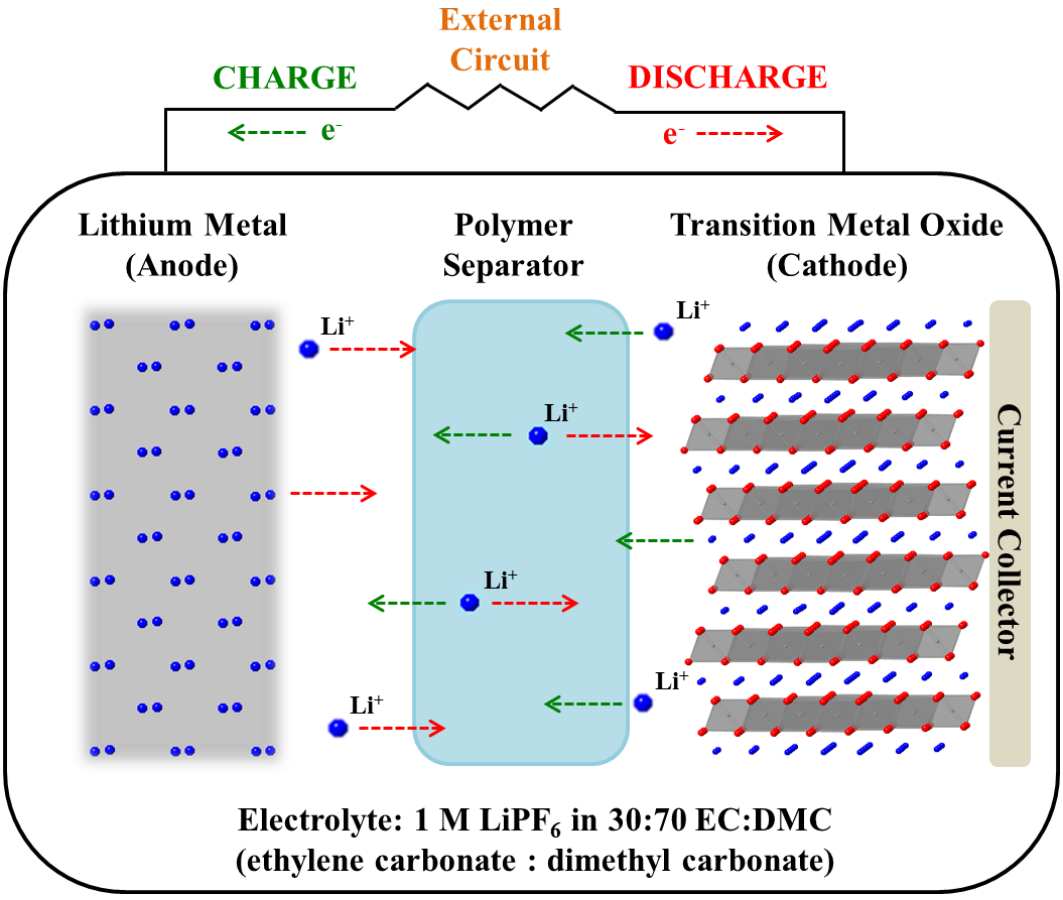

Figure 1.2. Diagram of an electrochemical cell containing a lithium metal anode, transition metal oxide cathode, polymer separator, and organic electrolyte

Table 1.1. Theoretical capacities of common electrode materials for lithium-ion batteries compared to $MgFe_2O_4$, $Ag_xMn_8O_{16}$, and $AgFeO_2$

Electrode Material	**Theoretical Capacity (mAh/g)**	**Electron Count**	**Redox Mechanism**
$LiCoO_2$	272	1	$LiCoO_2 \rightleftharpoons x\ Li^+ + x\ e^- + Li_{1-x}CoO_2$ where $x \leq 0.5$ - 0.6 for practical applications
$LiMn_2O_4$	148	1	$LiMn_2O_4 \rightleftharpoons x\ Li^+ + x\ e^- + Li_{1-x}Mn_2O_4$ where $x \leq 0.8$ for practical applications
Graphite (C_6)	372	1	$Li^+ + e^- + 6C \rightleftharpoons LiC_6$
$LiFePO_4$	170	1	$LiFePO_4 \rightleftharpoons Li^+ + e^- + Li_{1-x}FePO_4$
$MgFe_2O_4$	804	6	$MgFe_2O_4 + 6\ Li^+ + 6\ e^- \longrightarrow MgO + 2\ Fe + 3\ Li_2O$ $Fe + Li_2O \rightleftharpoons FeO + 2\ Li^+ + 2\ e^-$
$Ag_{1.2}Mn_8O_{16}$	260	8	$Ag_{1.2}Mn_8O_{16} + 8\ Li^+ + 8\ e^- \rightleftharpoons LiMnO_2 + 1.2\ Ag^0 + 8\ LiMnO_2$
$AgFeO_2$	274	2	$AgFeO_2 + Li^+ + e^- \rightleftharpoons Li_xFeO_2 + Ag^0$ $Li_xFeO_2 + Ag^0 + Li^+ + e^- \rightleftharpoons Li_2O + FeO + Ag^0$

Particle or crystallite size of the electrode material is an important factor to consider when improving electrochemical performance. Electrode materials in commercial rechargeable batteries are typically on the order of several microns and there has been impelling cause in the battery field, within the past 10 years, to reduced to size of electrode materials to enhance cycle life, power, delivered capacity, and allow for faster reactions kinetics at the surface of the active material. Considerable research demonstrates that high surface area and decreased path-lengths for ion transport inherent of nanostructured metal oxides increases the performance of electrode materials.[29–34] The research presented in this dissertation focuses specifically on nanostructured $MgFe_2O_4$ (0-D), $Ag_xMn_8O_{16}$ (1-D), and $AgFeO_2$ (2-D) as viable electrode materials and the influence that chemical, composition, and physical, size, properties have on electrochemical performance.

1.2 Magnesium Ferrite ($MgFe_2O_4$): A 0-D Electrode Material

Magnesium ferrite is a transition metal oxide that has a densely packed spinel structure which provides no direct pathway for ion and electron transport and is considered 0-D in this dissertation. $MgFe_2O_4$ is of interest owing to its high theoretical capacity, 804 mAh/g, for a complete discharge where all Fe^{3+} is reduced to metallic iron. Compared to classic electrodes for LIBs, such as $LiCoO_2$ (272 mAh/g), $LiMn_2O_4$ (148 mAh/g), graphite (372 mAh/g), and $LiFePO_4$ (170 mAh/g), the capacity of $MgFe_2O_4$ is significantly higher (**Table 1.1**). As an electrode material, $MgFe_2O_4$ is relatively new, being first reported as an anode material in lithium batteries in 2011.[35] Since 2011, a handful of literature articles describe the use of $MgFe_2O_4$ in lithium-based batteries, therefore, the material is not well-established and the redox mechanism is not fully understood.[36–43] To date, the size of the $MgFe_2O_4$ materials studied in lithium-based batteries has been on the nano-scale and was synthesized using a variety of low-temperature, high-temperature, or aqueous techniques.

1.2.1 Magnesium Ferrite Structure

The spinel crystal structure of $MgFe_2O_4$ falls within the cubic $Fd\bar{3}m$ space group (**Figure 1.3 a**).[44] Within an oxide spinel structure, two types of lattice sites exist, one type of site is octahedrally coordinated by oxygen while the remaining sites are tetrahedrally coordinated by oxygen. The lattice structure contains oxygen (O^{2-}) anions arranged in a cubic close-packed fashion, **Figure 1.3 b**.

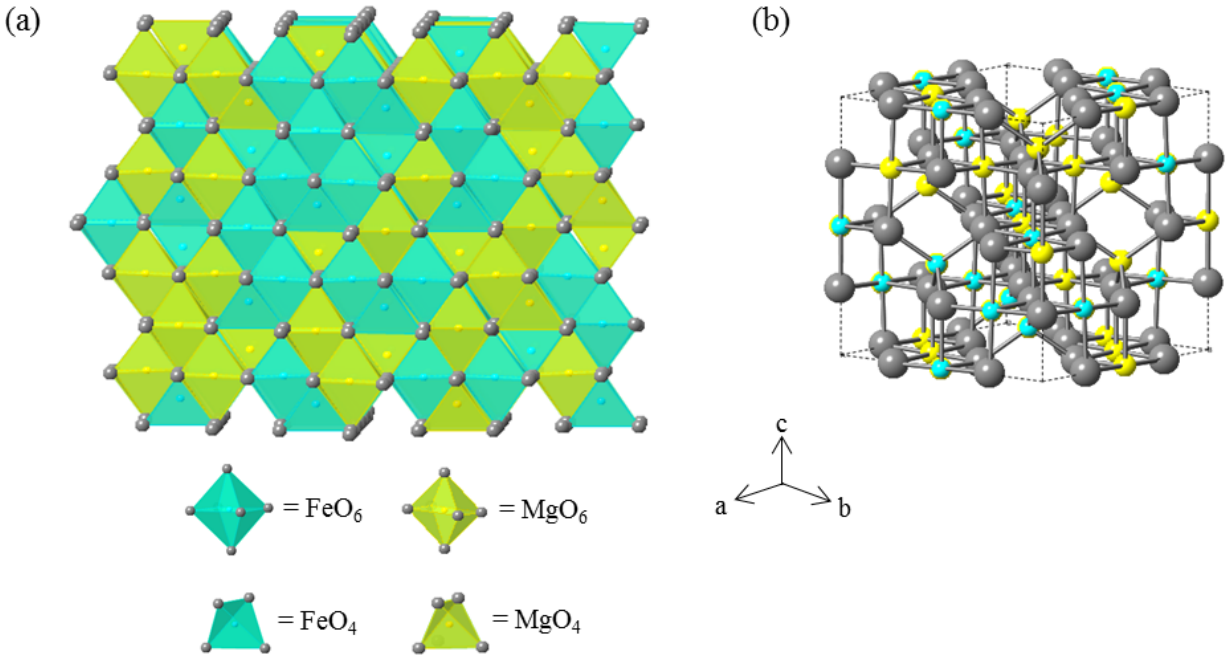

Figure 1.3. $MgFe_2O_4$ structure (ICSD 240799): (a) Polyhedral model and (b) unit cell

In a "normal" spinel, the A cation (e.g. Mg^{2+}) occupies the tetrahedral sites and the B cation (e.g. Fe^{3+}) occupies the octahedral site. In a fully inverse spinel, the tetrahedral sites contain only B cations and the octahedral site contains equal numbers of A and B cations. The structure of $MgFe_2O_4$ is unique in the fact that is fall between the normal and inverse definitions of a spinel.[45] In $MgFe_2O_4$, a fraction of the tetrahedral and octahedral sites are occupied by both Mg^{2+} and Fe^{3+}.

1.2.2 Synthesis of Magnesium Ferrite

The preparation of nanostructured magnesium ferrite can be achieved using microwave,[46] milling,[35,41] reverse micelle,[47,48] hydrothermal,[43,49–51] sol-gel,[37,38,48] co-precipitation,[36,48,50] combustion,[38–40] ceramic,[35,52] and electrospinning techniques.[42,48] Common issues concerning the synthesis of $MgFe_2O_4$ are the simultaneous formation of iron oxide phases, like hematite (α-Fe_2O_3), the lack of uniform morphology and size, and limited ability to control size with a single synthetic technique.[36,39,41,48–51] Ilhan et al. reported a synthesis to prepare $MgFe_2O_4$ that included co-precipitation followed by a hydrothermal step at 300, 350, 400, and 450°C with various Mg^{2+}:Fe^{3+} molar reagent ratios, however, pure $MgFe_2O_4$ was not obtained.[50] In an effort to control size, Sivakumar et al. synthesized $MgFe_2O_4$ (72 nm) via the calcination of α-Fe_2O_3 and MgO, the 72 nm magnesium ferrite sample was then milled to afford 19 nm particles.[35] The influence of synthetic technique (i.e. co-precipitation, sol-gel, and reverse micelle) on the morphology of $MgFe_2O_4$ was studied by Chandradass et al. and showed a significant dependence on processing methods.[48] For example, reverse micelle yielded pure $MgFe_2O_4$ samples that were uniform in size ($\sim$19 nm) while co-precipitation products were impure and gel-combustion led to non-uniform size distribution of porous nanoparticles and aggregate formation. Based on the literature, it can be seen that a synthetic technique which effectively controls size and morphology of pure-phase $MgFe_2O_4$ is needed.

1.3 Silver Hollandite ($Ag_xMn_8O_{16}$): A 1-D Electrode Material

Hollandites—namely octahedral molecular sieves or OMS-2—are a class of transition metal oxide materials in which manganese oxide tunnels, characterized by a 2 x 2 motif of MnO_6 octahedra, are substituted by various cations, including K^+, Na^+, Rb^+, Ag^+, Pb^{2+}, Ba^{2+}, Ca^{2+}, and Cr^{3+} occupying the tunnel.[53–58] The 1-D tunneled structure of hollandite provides a robust framework for the intercalation and de-intercalation of lithium ions during electrochemical processes, thus hollandites are promising candidates for electrode ma-

terials in rechargeable batteries. Conventional syntheses employed to prepare $Ag_xMn_8O_{16}$ include solid state,[53,59] ion-exchange,[60] reflux coupled with a high-temperature calcination step,[61] co-precipitation,[62–64] and hydrothermal reactions.[65,66] The cation located within typical hollandite structures is often electrochemically inert; however, Ag^+ has the potential to contribute to the electrochemical behavior of silver hollandite. Specifically, silver hollandite ($Ag_xMn_8O_{16}$) is of interest owing to the silver component of the materials which has been reported to significantly enhance the conductivity and associated electrochemistry of vanadium oxide cathode materials upon discharge.[67] Few reports of silver hollandite electrochemistry exist, outside of the Takeuchi group, which describe the utilization of silver hollandite as a cathode in lithium based batteries.[66,68]

1.3.1 Silver Hollandite Structure

The crystal structure of silver hollandite, obtained via a high temperature and pressure solid state synthesis, was first reported by Chang and Jansen in 1984.[53] Conceptually, a formula of $Ag_2Mn_8O_{16}$ is expected since the unit cell of silver hollandite has the ability to accommodate two silver atoms per formula unit. Chang and Jansen's single crystal diffraction data, however, illustrated a formula of $Ag_{1.8}Mn_8O_{16}$ for silver hollandite, indicating tunnel occupancy of 89.7% and a tetragonal space group, $I4/m$.[53] Tunneled hollandite materials consist of octahedral units of edge and corner-sharing manganese oxide octahedra (MnO_6) which interlink to form 2 x 2 tunnels with dimensions of 0.46 nm x 0.46 nm (**Figure 1.4**). The Mn cations in hollandite possess a mixture of 3+ and 4+ oxidation states while cations (1+ or 2+) generally occupy the tunnel as a means of charge stabilization.

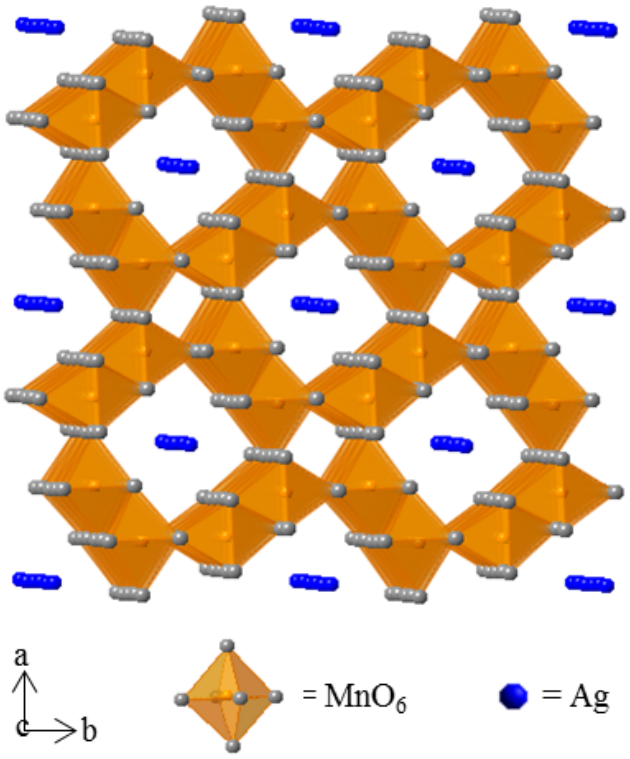

Figure 1.4. $Ag_{1.8}Mn_8O_{16}$ structure (ICSD 60155) as viewed down *c*-axis

As mentioned previously, a variety of hollandite materials are attainable and central tunnel cations can include K^+, Na^+, Rb^+, Ag^+, Pb^{2+}, Ba^{2+}, Ca^{2+}, or Cr^{3+}. It is suggested that the nature of the central tunnel ion can impact the overall dimensions of the MnO_6 tunneled framework in hollandite-type materials. For example, the small Ag^+ cation in silver hollandite acts as a covalent ion and attracts the walls of the 2 x 2 MnO_6 tunnels, pulling them inward, while the larger K^+ cation in cryptomelane (i.e. the potassium analog of silver hollandite, $K_xMn_8O_{16}$) is ionic in nature and repels the walls of the tunnel, pushing them further way (**Figure 1.5**). Unit cell dimensions are reported in **Table 1.2**, illustrating that K^+ cations within the tunnels increase the lattice parameters in the *a* and *b* directions, whereas, a decrease in the same parameters is observed with Ag^+ occupancy when compared to the vacant Mn_8O_{16} structure.

Table 1.2. Unit cell dimensions of various hollandite-type materials with respect to the *a*, *b*, *c* axes

Material	*a* (Å)	*b* (Å)	*c* (Å)
Mn_8O_{16}	9.815	9.815	2.847
$K_{0.66}Mn_8O_{16}$	9.866	9.866	2.872
$Ag_{1.8}Mn_8O_{16}$	9.725	9.725	2.885

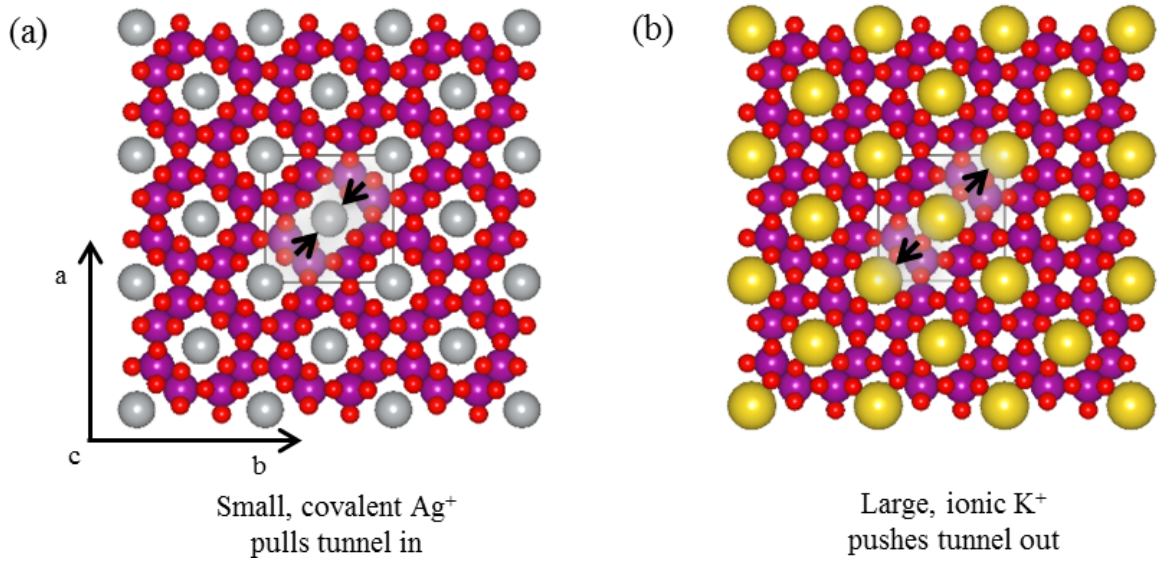

Figure 1.5. Hollandite structures consisting of an MnO_6 octahedral framework with: (a) Ag^+ (b) K^+ cations residing in the tunnel

1.3.2 Synthesis of Silver Hollandite

Silver hollandite was synthesized, for the first time, in 1984 by Chang and Jansen via a high temperature, high pressure solid-state technique.[53] The product prepared using this method was $Ag_{1.8}Mn_8O_{16}$ which contained impurity oxide phases of Mn_2O_3 and Ag_2O, therefore, it was necessary to leach to material with acid to yield pure product. A new technique did not appear in the literature for the next 20 years when an ion-exchange procedure was attempted by combining cryptomelane (KMn_8O_{16}) with an excess of silver nitrate ($AgNO_3$) in an effort to synthesize $Ag_xMn_8O_{16}$.[60] This approach allowed for the utilization of lower temperatures to generate silver hollandite, however, potassium (K^+) was detected in the final

product and constituted approximately 6.7 % of the total tunnel ion (Ag^+ and K^+) content. Additionally, X-ray diffraction (XRD) and transmission electron microscopy (TEM) detected trace quantities of metallic silver (Ag^0) which was attributed to the decomposition of excess $AgNO_3$ after calcination at high temperature. In 2007 and 2011, hydrothermal syntheses of $Ag_xMn_8O_{16}$ were reported in which silver permanganate ($AgMnO_4$) and manganese nitrate ($Mn(NO_3)_2$) were used as starting reagents.[65,66] Contrary to the ion-exchange technique discussed above, no metallic Ag^0 was detected in the XRD pattern of hydrothermally prepared silver hollandite. The disadvantage of the hydrothermal technique is a limited temperature range with temperatures above 200°C affording an impurity phase of pyrolusite (β-MnO_2).

A low-temperature, reflux-based synthesis was initially proposed in 2007 and incorporated a subsequent high temperature calcination step.[61] While the major phase collected after reflux was silver hollandite, evidence of a fairly significant β-MnO_2 phase was observed. A separate low-temperature synthesis of $Ag_xMn_8O_{16}$ was suggested in 2008 in which $AgMnO_4$ and manganese acetate tetrahydrate ($Mn(Ac)_2{\cdot}4H_2O$) were reacted at 100°C, in the solid state, and subsequently annealed at high temperature.[59] The few discernible diffraction peaks of silver hollandite produced at low temperatures (100°C and 300°C) were broad, indicating an extremely nanocrystalline material, while material calcined at 800°C was composed of a mixture of crystalline Mn_2O_3 and Ag metal. The Takeuchi group has more recently demonstrated that pure silver hollandite ($Ag_xMn_8O_{16}$, $1.0 \leq x \leq 1.8$) with silver content (x) of varying degrees can be prepared by systematically manipulating starting reagent quantities during a low-temperature, aqueous co-precipitation reaction where the crystallite size of $Ag_xMn_8O_{16}$ increases with larger values of x.[62–64] This co-precipitation reaction allows for the reproducible synthesis of nanostructured $Ag_xMn_8O_{16}$ with control over both the chemical and physical properties of the material.

1.4 Silver Ferrite ($AgFeO_2$): A 2-D Electrode Material

Silver ferrite belongs to the delafossite mineral family which consists of ternary transition metal oxides with the chemical formula ABO_2. Such ternary metal oxides are applicable as

electrodes for lithium-based secondary batteries as a result of their layered crystalline motif which facilitates 2-D transport of ions within the structure. Typical techniques to produce ABO_2 delafossites include cation exchange,[69–72] microwave or ultrasonic irradiation,[73,74] co-precipitation,[75–78] and high-temperature hydrothermal or solid state reactions.[77,79–84] A finite number of reports in the literature describe the presence of ABO_2 ternary delafossite oxides in batteries, especially those based on lithium. Thus far, information is limited to $AgNiO_2$ in alkaline and zinc batteries, $CuFeO_2$ as an anode in lithium-ion batteries, or $AgCuO_2$, $AgCu_{0.5}Mn_{0.5}O_2$, and $CuFeO_2$ as cathodes in lithium batteries.[85–89]

1.4.1 Silver Ferrite Structure

Silver ferrite, $AgFeO_2$, is a bimetallic transition metal oxide that exemplifies a layered delafossite-type structure. Bimetallic delafossites, ABO_2, consist of A cations that are normally a monovalent species (Cu, Ag, Pt, Pd) while the B cation site can incorporate a variety of trivalent transition metal cations including, but not limited to, Co, Sc, Ti, Ru, Y, Mn, V, Cr, Fe, Rh, and Ni.[82,90,91] In an effort to tune various properties of delafossites, however, it is becoming increasingly common to replace B^{3+} with a mixture of aliovalent metal cations (e.g. Ru,[92] Li,[92,93] Sn,[93] Mn,[85] Tl,[94] Ni,[94–96] V,[94,97], Ti[93,95], etc.) as opposed to a single metal cation.[91]

The $AgFeO_2$ structure contains alternating layers of edge-shared FeO_6 octahedra with layers of close-packed Ag^+ metal cations between (**Figure 1.6**). The Ag^+ transition metal cations are linearly coordinated between two oxygen molecules in the parallel layers. Two major polytypes of delafossite compounds exist upon crystallization. Either a rhombohedral (3R, $R\bar{3}m$) or hexagonal (2H, $P6_3/mmc$) geometry is possible based on the manner in which alternating layers of edge-shared BO_6 octahedra and linearly coordinated noble metal A-site cations stack. The layers of the 3R polytype stack in an AaBbCcAaBbCc sequence while the 2H polytype layers stack as AaBbAaBb.[90,91,98]

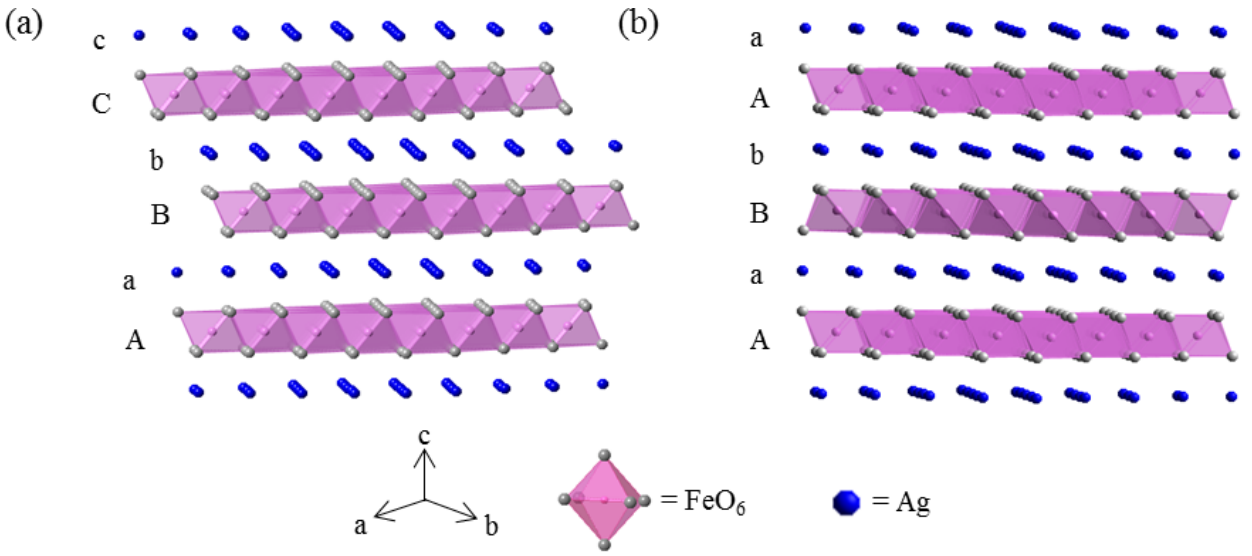

Figure 1.6. (a) 3R-$AgFeO_2$ (ICSD 31919) (b) 2H-$AgFeO_2$ (ICSD 2786)

1.4.2 Synthesis of Silver Delafossites

A number of synthetic strategies have been employed in the literature to produce ternary delafossite-type oxides. The most common reaction pathways to synthesize delafossites include high-temperature hydrothermal, solid state (oxidizing flux), cation exchange (metathesis), and microwave or ultrasonic irradiation. The earliest syntheses of delafossite oxides, starting in the 1930s, focused on combining the corresponding A^+ and B^{3+} metal oxides or hydroxides, commonly A_2O and BOOH or B_2O_3, using hydrothermal or solid state techniques.[79–83,83,84,99–102] Although hydrothermal/solid state techniques are ideal for producing copper-containing delafossites, the high temperatures necessary to create a flux of reagents prove to be problematic for silver, palladium, and platinum delafossites. Specifically, silver oxide (Ag_2O) has a low free energy of formation and decomposes or dissociates at a temperature (i.e. 300°C) that is too low to create a flux of material especially in open systems.[82] Literature reports frequently identify the presence of metallic silver in the final delafossite product following high-temperature, high-pressure syntheses.[77,90,103]

Consequently, ABO_2 delafossite oxides (A = Ag^+, Pt^+, Pd^+) are prepared by low-temperature, direct reactions in closed solid-state systems or by cation exchange reac-

tions. Several silver delafossites have been prepared using low-temperature methods, such as $AgCoO_2$,[69,71,82] $AgGaO_2$,[72] $AgScO_2$,[90] $AgInO_2$,[104,105] $AgCrO_2$,[82] $AgFeO_2$,[82] $AgRhO_2$,[82] and $AgNiO_2$[103]. To date, cation exchange synthesis is widely accepted as the leading technique since it requires the lowest temperatures, however, precursors (e.g. $NaCoO_2$, $NaGaO_2$, etc.) made via solid state reactions are necessary. In comparison to cation exchange, microwave and ultrasonic irradiation syntheses are rapid and employ mild reaction conditions.[73,74] On the other hand, it was illustrated that the irradiation power utilized affects the metal oxide phases present and overall homogeneity of the delafossite sample.

In 2003, Shariari and coworkers reported the first single-step, low-temperature, low-pressure hydrothermal synthesis of a silver-containing delafossite.[77] The reaction was conducted inside of a Telfon pouch under a temperature of 175°C and a pressure less than 10 atm. A yield in excess of 90% was obtained for the delafossite ($AgInO_2$), however, traces of Ag^0 were detected in the powder X-Ray diffraction (XRD) pattern. Shariara et al.'s results demonstrated that even milder reaction conditions are essential for the preparation of silver delafossite oxides. Seven years later, Murthy et al. reported the first co-precipitation synthesis, characterization, and magnetization studies of nanocrystalline silver ferrite in which $AgFeO_2$ was reported as a single phase subsequent to calcination at 400°C, 700°C, and 900°C.[78] The reaction conditions (70°C, aqueous solution with sodium hydroxide, atmospheric pressure) verified that delafossites could be developed at lower temperatures and pressures than previously assumed. Attempts to control the properties of $AgFeO_2$ during synthesis, Krehula and Musič employed a similar co-precipitation synthetic technique. Unfortunately, the combination of non-stoichiometric ratios of Ag^+ and Fe^{3+} nitrate reagents produced nanocrystalline oxide impurity phases of Ag_2O and α-FeOOH.[76]

1.5 Advantages of Co-Precipitation Synthesis

Each of the 0-D ($MgFe_2O_4$), 1-D ($Ag_xMn_8O_{16}$), and 2-D ($AgFeO_2$) electrode materials presented in this dissertation have one thing in common, they can be prepared using co-precipitation techniques. The synthetic schemes used to prepare the nanostructured tran-

sition metal oxides are low-temperature and utilize commercially available, water-soluble metal-based salts as starting reagents in an aqueous medium. Co-precipitation syntheses are considerably safer than hydrothermal or solid state reactions because they do not necessitate high temperatures, excessive pressures, or harsh chemical solvents. Since the synthesis of magnesium ferrite, silver hollandite, and silver ferrite can be carried out in water, the chemistry is classified as sustainable or green and the methods show promise for scale-up to industry. The overall simplicity, provided by this method, results from one's ability to reliably produce different crystallite sizes or compositions of $MgFe_2O_4$, $Ag_xMn_8O_{16}$, and $AgFeO_2$ solely by altering the initial reagent concentrations or reaction temperatures. The ability to synthetically tune the chemical and physical properties of a material allows for specific products to be targeted and for investigation into the influence of material properties on electrochemical behavior.

1.6 Potential as Electrode Materials

The transition metal oxide electrode materials proposed in this dissertation–$MgFe_2O_4$ (**Figure 1.3**), $Ag_xMn_8O_{16}$ (**Figure 1.4**), and $AgFeO_2$ (**Figure 1.6**)–demonstrate structures conducive for ion and electron mobility. Moreoever, the theoretical capacities of the oxide materials are comparable to or exceed those of conventional LIB electrodes, $MgFe_2O_4$ (804 mAh/g), $Ag_{1.2}Mn_8O_{16}$ (260 mAh/g), and $AgFeO_2$ (274 mAh/g), see **Table 1.1**. As mentioned earlier, capacities include 272, 148, 372, and 170 mAh/g for $LiCoO_2$, $LiMn_2O_4$, graphite, and $LiFePO_4$ LIB electrode materials, respectively.

Another reason for choosing both $Ag_xMn_8O_{16}$ and $AgFeO_2$ stems from the silver component of the materials. Evidence of silver ions (Ag^+) reducing to silver metal (Ag^0) nanoparticles upon discharge has been observed in silver vanadium oxide cathode materials where Ag^0 particles are suggested to initiate the *in-situ* formation of a conductive percolation network of metallic nanoparticles during lithiation. This paradigm was first established with silver vanadium oxide ($Ag_2V_4O_{11}$), then later extended to silver vanadium phosphorous oxide ($Ag_2VO_2PO_4$) where the electrical conductivity of $Ag_2VO_2PO_4$ was increased 15,000-fold

upon lithiation of $Ag_2VO_2PO_4$ due to the formation of an electrically conducting percolation network of Ag^0 nanoparticles.[67,106,107] The presence of Ag^+ ions in $Ag_xMn_8O_{16}$ and $AgFeO_2$ may lend to interesting electrochemical behavior.

The $MgFe_2O_4$, $Ag_xMn_8O_{16}$, and $AgFeO_2$ materials chosen as viable candidates for electrodes in lithium-based batteries in this dissertation are all relatively understudied in the battery field. Mechanistically speaking, the lithiation and delthiation processes reported in the literature are either incomplete ($MgFe_2O_4$) or relatively non-existent ($Ag_xMn_8O_{16}$ and $AgFeO_2$). There is considerable work to be done to adequately characterize the electrochemically active materials and establish valid redox mechanisms.

1.6.1 Magnesium Ferrite

Magnesium ferrite initially entered the battery field in 2011 when it was introduced as a nanostructured anode for LIBs.[35] Over the past 5 years, nanosized $MgFe_2O_4$ has been investigated in LIBs and demonstrates significant capacity fade upon electrochemical cycling.[36–43] It is not uncommon for pure $MgFe_2O_4$ electrodes to exhibit first cycle capacities in excess of 1000 mAh/g which fade to $\leq$ 400 mAh/g after 10-50 cycles.[35,37?] A few researchers have successfully coated or incorporated $MgFe_2O_4$ with carbon and improved the electrochemical performance due to the poor cycle life.[36,40,42] The effect of $MgFe_2O_4$ size on cycle life has been studied by Sivakumar et al. where they synthesized $MgFe_2O_4$ (72 nm) via calcination of α-Fe_2O_3 and MgO, then milled the as-synthesized sample afford 19 nm particles.[35] The capacity was observed over 10 cycles where the 19 nm sample was higher than the 72 nm sample over the first 6 and both stabilized to approximately $\sim$300 mAh/g in the next 4 cycles. This data shows a great deal of promise and is the basis for the magnesium ferrite study in this dissertation where different crystallite sizes of $MgFe_2O_4$ are prepared using the same synthetic method.

1.6.2 Silver Hollandite

Very few studies of silver hollandite as an electrode in lithium-based batteries have been reported outside of the Takeuchi group.[66,68] The first electrochemical data of nanocrystalline silver hollandite showed reliable cycling performance, delivering 180 mAh/g initial discharge capacity and >95% capacity retention from cycles 3–30 in a 2-electrode cell containing a lithium metal anode. Within the next few years, the Takeuchi group demonstrated compositional control of silver hollandite ($Ag_xMn_8O_{16}$, $1.0 \leq x \leq 1.8$, 12-26 nm) using the same low-temperature, aqueous co-precipitation reaction.[63,64,108] Across the $Ag_xMn_8O_{16}$ series ($1.0 \leq x \leq 1.8$, 12-26 nm) significant differences in electrochemistry (e.g. cyclic voltammetry (CV), galvanostatic intermittent titration technique (GITT), pulsed discharge, DC resistance) were observed.[63,64,108–110] Manipulation of the silver content (x) or Ag/Mn ratio of $Ag_xMn_8O_{16}$ via precise manipulation of $AgMnO_4$ and $MnSO_4$ starting reagents influenced the crystallite size of the nanorods and positively affects the electrochemical performance of the manganese oxide material, however, the mechanism by how this occurs is unknown.

1.6.3 Silver Ferrite

Silver ferrite was first reported as a cathode material by the Takeuchi group in 2012.[75] However, there are few reports of other silver delafossites as electrode materials, including $AgNiO_2$ in alkaline and zinc batteries[86,87] and $AgCuO_2$ and $AgCu_{0.5}Mn_{0.5}O_2$ in lithium-type batteries.[85] Due to lack of electrochemical information available for silver delafossites, the Takeuchi group chose to examine an $AgFeO_2$ cathode which displayed consistent discharge capacities above 50 mAh/g for 50 cycles (voltage >1.5 V) in a lithium-based battery.[75] Interestingly, Ag^0 was found on the surface of a discharged silver ferrite cathode using XRD and scanning electron microscopy (SEM). The stable cycle life and presence of Ag^0 show silver ferrite's potential as an electrode material.

1.7 Summary

The objective of the research portrayed in this document is to study the effects that manipulating various reaction parameters (i.e. temperature and reagent concentration) has on the chemical and physical properties of spinel-type $MgFe_2O_4$, tunneled $Ag_xMn_8O_{16}$ nanorods, and layered $AgFeO_2$. To that end, the chemical and physical properties of these materials are important factors to consider with respect to electrochemical performance.

The goal of Chapter II is to control the size of $MgFe_2O_4$ particles to influence electrochemistry and utilize advanced *in-situ* and *ex-situ* techniques to better understand the redox mechanism of the material.

Chapters III and IV will focus on silver hollandite, $Ag_xMn_8O_{16}$. The presence of structural defects, in the form of oxygen vacancies, will be probed in Chapter III using both local and bulk measurements. Silver hollandite with the same silver content and different crystallite sizes is synthesized in Chapter IV in an effort to deconvolute the effects of crystallite size and silver content, for the first time.

Chapters V, VI, VII, VIII, and IX focus on $AgFeO_2$. The premise of Chapters V, VI, VII, and VIII is to demonstrate the *in-situ* preparation of $AgFeO_2$ and $AgFeO_2/\gamma$-Fe_2O_3 composites with distinct compositions and crystallites sizes and observe the effects that altering the chemical and physical properties has on the electrochemical performance of the materials. Chapter V and VI will discuss the characterization and electrochemical performance of a series of $AgFeO_2/\gamma$-Fe_2O_3 composites while Chapter VIII aims to establish the redox mechanism of $AgFeO_2$ and a low silver content composite. Chapter VII examines the electrochemical performance of $AgFeO_2/\gamma$-Fe_2O_3 composites in terms of direct (one-pot) preparation *versus* mechanical mixing. Finally, Chapter XI, demonstrates the preparation of stoichiometric $AgFeO_2$ with different crystallite sizes via a co-precipitation reaction with varying quantities of NaOH as a secondary alternative to influence the electrochemistry of the layered transition metal oxide material.

CHAPTER II

IMPLICATIONS OF $MgFe_2O_4$ CRYSTALLITE SIZE ON CYCLING EFFICIENCY AND REDOX MECHANISM

2.1 Introduction

Magnesium ferrite has been selected as a representative 0-D, spinel structured electrode material (**Figure 1.3**) because of its high theoretical capacity (804 mAh/g), low cost, and promising data which illustrates enhanced electrochemical performance of 19 nm compared to 72 nm $MgFe_2O_4$.[35] Magnesium ferrite first appeared in the literature as an electrode material in 2011,[35] with limited reports since that time.[36–43] The disadvantage of $MgFe_2O_4$ electrode materials, without carbonaceous coating[36,40] or specialized structures (hollow spheres[43] or electrospun nanowires[42]), is that they exhibit rapid capacity fade (>1000 mAh/g first cycle capacity to $\leq$ 400 mAh/g after 10-50 cycles)[35,37–39] and the failure mechanism is not well understood. Size and morphology are important factors to take into consideration when designing electrode materials. Chandradass et al. found that both the size and morphology of $MgFe_2O_4$ were dependent on processing methods (co-precipitation, sol-gel, and reverse micelle).[48] For example, co-precipitation products were impure and gel-combustion led to non-uniform size distribution of porous nanoparticles and aggregate formation, whereas reverse micelle yielded pure $MgFe_2O_4$ samples that were uniform in size ($\sim$19 nm). This chapter is aimed at developing a new synthetic process to control $MgFe_2O_4$ size on the nanoscale, determining the effects of size on electrochemical performance, and establishing a valid redox mechanism using advanced *in-situ* and *ex-situ* techniques.

2.2 Experimental

2.2.1 General Methods and Materials

Magnesium ferrite was synthesized via a combination of co-precipitation and hydrothermal reactions with a subsequent calcination step modified from previously reported schemes.[50–52] Magnesium(II) nitrate, iron(III) nitrate, and sodium hydroxide reagents were used as re-

ceived from vendor. Water utilized during synthesis was deionized water filtered through a Thermo Scientific Barnstead Nanopure ultrapure water purification system. Aqueous solutions of magnesium(II) nitrate, iron(III) nitrate, and sodium hydroxide dissolved in deionized water were combined, affording rapid formation of a red-brown precipitate in solution. The reaction mixture was stirred at room temperature, collected by centrifugation, and washed with H_2O. The wet material was placed in a hydrothermal bomb with H_2O and heated at 160°C for 10 hours in a muffle furnace. The solid was collected by centrifugation and reduced to dryness *in vacuo*. The dry material was annealed in a tube furnace at 400°C and 500°C for small and large crystallite sizes, respectively.

2.2.2 Characterization

X-Ray powder diffraction (XRD) spectra of magnesium ferrite was collected with Cu Kα radiation and Bragg-Brentano focusing geometry using a Rigaku SmartLab X-Ray diffractometer and a Scintillation detector. The XRD spectra were measured in a 2θ range from 5° to 90°. Rigaku PDXL2 software with an ICDD PDF-2 database was used for search-match analysis. Magnesium ferrite crystallite sizes were approximated by applying the Scherrer equation to the (3 3 1) reflection at a 2θ value of approximately 35° in the XRD pattern. Quantitative elemental analysis of magnesium and iron, determined by inductively coupled plasma-optical emission spectroscopy (ICP-OES), was performed on a ThermoScientific iCap 6000 ICP spectrometer. Simultaneous thermogravimetric analysis/differential scanning calorimetry (TGA/DSC) was run on a TA Instruments SDT Q600 and used to investigate the thermal stability of magnesium ferrite. Samples weighing approximately 15 mg were placed in alumina thermogravimetric analysis pans and heated from room temperature to 1000°C under an atmosphere of nitrogen gas at a rate of 1°C/min.

In-situ XRD measurements were conducted using a novel vacuum-sealed plastic pouch electrochemical cell in a Rigaku Miniflex diffractometer utilizing a D/tex 1D Si strip detector to facilitate fast and high quality spectra acquisition. A specially designed sample holder was used to ensure proper mounting of pouch cells and maximize data quality in the

Bragg-Brentano XRD geometry. $MgFe_2O_4$ electrodes were discharged at C/15 rate using a Bio-Logic multichannel potentiostat/galvanostat. XRD spectra were continuously collected during discharge in a 2θ region of 25–85° with a step size of 0.03° and a scan rate of 3°/min after an initial XRD spectra was collected at open circuit voltage (OCV). All measurements were conducted in a low humidity dry room. After data acquisition, the XRD scans were correlated to the electrochemistry of the cell by comparing time-stamps of the electrochemical data and XRD scans respectively.

X-ray absorption spectroscopy (XAS) measurements of 10 nm $MgFe_2O_4$ were collected at end station F3 of the Cornell High Energy Synchrotron Source (CHESS) at Cornell University and the 19 nm $MgFe_2O_4$ were acquired at the Materials Research Collaborative Access Team (MRCAT, sector 10-BM) of the Advanced Photon Source at Argonne National Laboratory. All samples were measured at the Fe K-edge (7.112 keV) with a double crystal Si (111) monochromator. Samples at CHESS were measured in transmission geometry utilizing ionization chambers filled with 100% N_2 and the measurements at MRCAT were conducted with 50%/50% N_2/He and 85%/15% N_2/Ar in the incident and transmission ion chambers respectively. A reference Fe foil was used for initial beam energy calibration, and was also measured simultaneously with all samples to ensure proper energy alignment of multiple scans. 10 nm $MgFe_2O_4$ electrodes that were electrochemically discharged to 0.5, 2, 4, and 6 e^- along with fully discharged and charged samples that were removed from coin-type cells at the appropriate lithiation state and sealed between Kapton tape in an inert Ar atmosphere. 19 nm $MgFe_2O_4$ was discharged to $2e^-$, fully discharged, and fully charged following the same preparation procedures as the 10 nm $MgFe_2O_4$ sample. Samples were stored in a sealed pouch and were removed immediately before XAS measurements to limit possible contamination from air exposure. All XAS spectra were aligned, merged, deglitched and normalized using Athena.[111] The AUTOBK algorithm was used to limit background contributions below Rbkg = 1.0 Å. Each spectrum was fit using Artemis with theoretical structural models generated via FEFF6.[111–113] All samples were fit using a k-range of 2.0–9.5 Å in k,

k^2 and k^3 k-weightings simultaneously using a Hanning window (dk = 3). An R-range of 1.0–3.8 Å or 1.0–3.0 Å was utilized to fully encompass the second shell peak. A $MgFe_2O_4$ structural model was created utilizing the nominal inverse-spinel $Fd\bar{3}m$ Fe_3O_4 crystal structure and replacing 50% of Fe atoms located at the 16d site, and 10% of Fe atoms located at the 8a site with Mg in the FEFF calculation. In addition to the initial $MgFe_2O_4$ structure, rock salt $Fm\bar{3}m$ FeO[114] and $Im\bar{3}m$ body centered cubic (bcc) Fe metal[115] structural models were also utilized. Intrinsic losses in the electron propagation and scattering process that govern XAS measurements were accounted for by experimentally determining the amplitude reduction factor, S_0^2, via fitting the Fe metal standard and applying this S_0^2 (0.85) to all experimental fits. This facilitates more accurate relative amplitudes, and correspondingly, number of neighboring atoms for experimental samples.

TEM images, electron diffraction patterns, and EELS mapping were recorded at 200 kV in the JEM-ARM200F microscope equipped with a Gatan image filter spectrometer, cold-field emission gun and double aberration correctors. Element sensitive EELS mapping was carried out for Fe L-edge and Mg K-edge across single particles. The discharged Li/$MgFe_2O_4$ cells were disassembled in an Ar-filled glove box and a sample of the powder electrode ($MgFe_2O_4$/Super P carbon black) was washed with dimethyl carbonate. The $MgFe_2O_4$ electrode powders were loaded onto a TEM grid and transferred to a vacuum transfer holder, which was sealed in a bag, before transferring the sample into the TEM column to avoid exposure of the sample to air.

2.2.3 Electrochemistry

Coin-cell type batteries with lithium anodes were used to probe the electrochemical performance of magnesium ferrite. Composite electrodes were prepared by mixing magnesium ferrite with conductive carbon and PVDF binder for a composition of 70% active material, 20% ketjenblack carbon, and 10% binder (CV) and 85% active material, 10% Super P carbon black, and 5% binder (cycling) and coated onto a copper foil substrate. An electrolyte solution of 1 M $LiPF_6$ in 30/70 (*v/v*) ethylene carbonate/dimethyl carbonate was used for

galvanostatic cycling and cyclic voltammetry tests. A rate of 0.05 mV/s was applied to the two-electrode cells for three consecutive cycles between voltage limits of 3.0 and 0.1 V. Galvanostatic cycling, over 40 cycles, was performed on a Maccor Series 4000 Battery Test System in a chamber maintained at 30°C. Galvanostatic cycling tests were conducted using a two electrode assembly with lithium metal anode and an applied current density of 25 mA/g between 0.2–3.0 V. GITT tests were performed on coin cells with a 30 minute discharge pulse (100 mA/g current density) followed by a 12 hour rest period from 3.0–0.2 V.

Coin cells with powder $MgFe_2O_4$ electrodes and lithium anodes were prepared for TEM imaging studies. Powder electrodes contained a 50/50 mixture of $MgFe_2O_4$/Super P carbon black which was milled for 15 minutes. Coin cells were assembled with an electrolyte solution of 1 M $LiPF_6$ in 30/70 (*v/v*) ethylene carbonate/dimethyl carbonate and a Whatman glass fiber separator. The cells were discharge to 0.1 V at a rate of 1 electron per 3 hours and the cells were held at 0.1 V for 10 hours prior to disassembling.

2.2.4 Acknowledgment of Collaboration

The research in Chapter II was conducted in collaboration with Dr. Christopher J. Pelliccione, Dr. Wei Zhang, and Dr. Feng Wang (Brookhaven National Laboratory). The XAS data was collected and analyzed by Dr. Pelliccione while TEM imaging studies were performed by Dr. Zhang.

2.3 Results and Discussion

2.3.1 Structural and Elemental Composition

Magnesium ferrite ($MgFe_2O_4$) in Chapter II has been prepared by a combination of co-precipitation and hydrothermal reactions with a subsequent calcination step modified from previously reported syntheses.[50–52] It was necessary to use each of the three techniques to obtain pure, nanocrystalline $MgFe_2O_4$. **Figure A1** shows the material obtained after co-precipitation and hydrothermal reactions. This material is extremely nanocrystalline and there is no evidence of $MgFe_2O_4$, thus the annealing step is required to obtain crystalline mag-

nesium ferrite. Interestingly, the co-precipitation material cannot be converted to $MgFe_2O_4$ directly via calcination at low temperatures ($\leq$ 500°C), the material remains amorphous. The semi-crystalline material collected after the hydrothermal reaction provides nucleation sites to initiate crystal growth during heat treatment and the temperature used (400 or 500°C) determines the crystallite size of the resulting magnesium ferrite product. The X-ray diffraction patterns of $MgFe_2O_4$ annealed at 400°C and 500°C is show in **Figure 2.1** with a $MgFe_2O_4$ spinel ($Fd\bar{3}m$) reference pattern indicating that no impurity phases are present in the as-synthesized materials.[44]

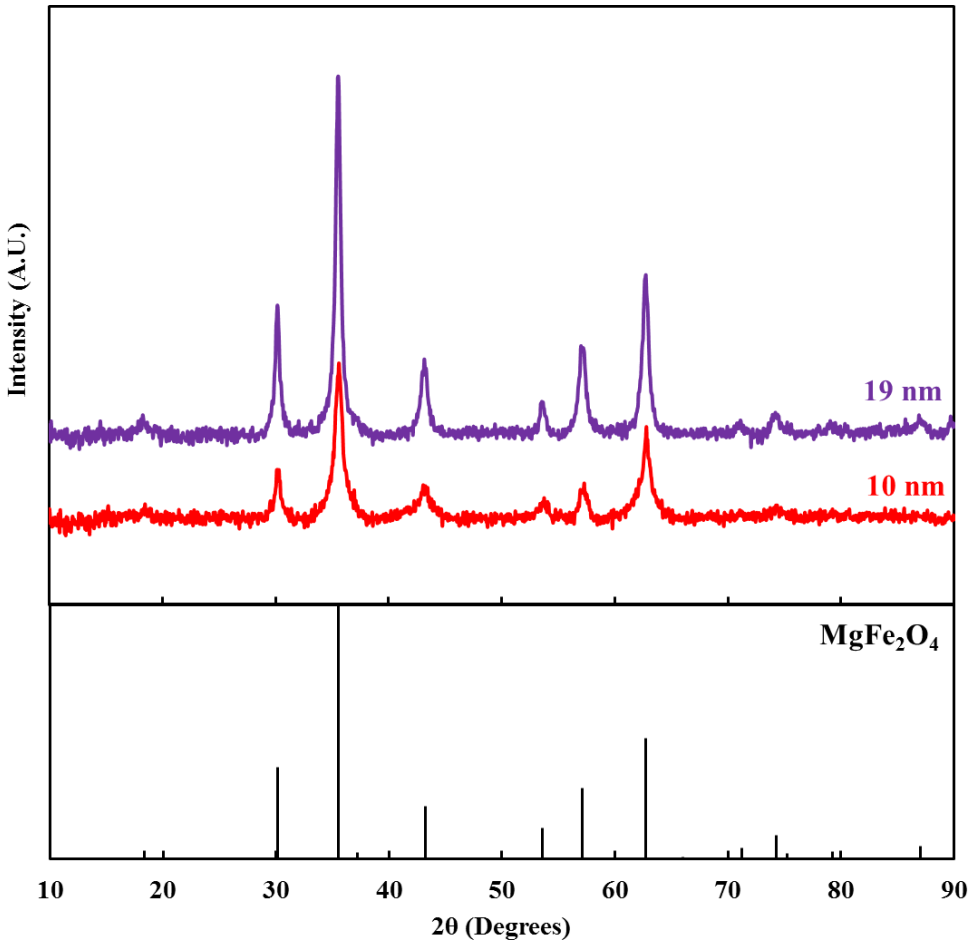

Figure 2.1. X-ray diffraction (XRD) of 10 and 19 nm $MgFe_2O_4$ samples with an $MgFe_2O_4$ reference pattern (ICSD 240799)

The increased nanocrystallinity of the 10 nm $MgFe_2O_4$ sample, approximated by applying the Scherrer equation to the (3 3 1) reflection at a 2θ value of approximately 35°. The

Scherrer equation is typically used to approximate crystallite sizes of nanosized particles, <0.1-0.2 μm, and is shown in **Equation 2.1** where τ is the size of the crystalline domain in nanometers, K is a shape factor (typically ~0.9), λ is the X-ray wavelength (1.542 Å for Cu Kα), β is the line broadening at full width half maximum (FWHM) after subtracting the instrumental line broadening, and θ is the Bragg angle in degrees of the reflection of interest.[116,117] It is important to note that the Scherrer equation provides a lower bound estimate of size.

$$\tau = \frac{K\lambda}{\beta \cos\theta} \tag{2.1}$$

The decreased crystallinity of 10 nm $MgFe_2O_4$ is apparent in the broad diffraction peaks and decreased intensity of the reflections compared to the higher crystallite size, 19 nm $MgFe_2O_4$. Rietveld refinement of 10 and 19 nm $MgFe_2O_4$ is shown in **Figure A2** and **Figure A3**, respectively, and results are summarized in **Table 2.1**. Refinement of 10 and 19 nm $MgFe_2O_4$ shows good agreement of lattice parameters compared to crystalline $MgFe_2O_4$ with an $Fd\bar{3}m$ space group (8.3674 Å)[44] and decreased crystallite of 10 nm $MgFe_2O_4$.

Table 2.1. Structural parameters from Rietveld refinement of 10 and 19 nm $MgFe_2O_4$

$MgFe_2O_4$		**10 nm**	**19 nm**
Unit Cell	*a*	8.3745(9) Å	8.3793(4) Å
	b	8.3745(9) Å	8.3793(4) Å
	c	8.3745(9) Å	8.3793(4) Å
Space Group		$Fd\bar{3}m$	$Fd\bar{3}m$
Size		10.1 nm	32.7 nm
R_{wp}		0.76%	0.90%

2.3.2 Thermogravimetric Analysis (TGA)

The thermogravimetric analysis (TGA) of 10 and 19 nm $MgFe_2O_4$ samples is shown in **Figure 2.2**. The loss of physisorbed is observed before ~600°C and corresponds to mass losses of approximately 5% and 11% for 19 and 10 nm $MgFe_2O_4$, respectively. The 10 nm sample displays a greater loss of water, likely a result of the larger surface area of 10 nm $MgFe_2O_4$ crystallites available to accommodate water molecules. No significant weight loss events which would be characterized by sharp endothermic peaks in the differential scanning calorimetry (DSC) plot (**Figure A4**) are observed in 10 or 19 nm $MgFe_2O_4$, therefore, it can be assumed that the nanocrystalline $MgFe_2O_4$ prepared in Chapter II is stable within this temperature window.

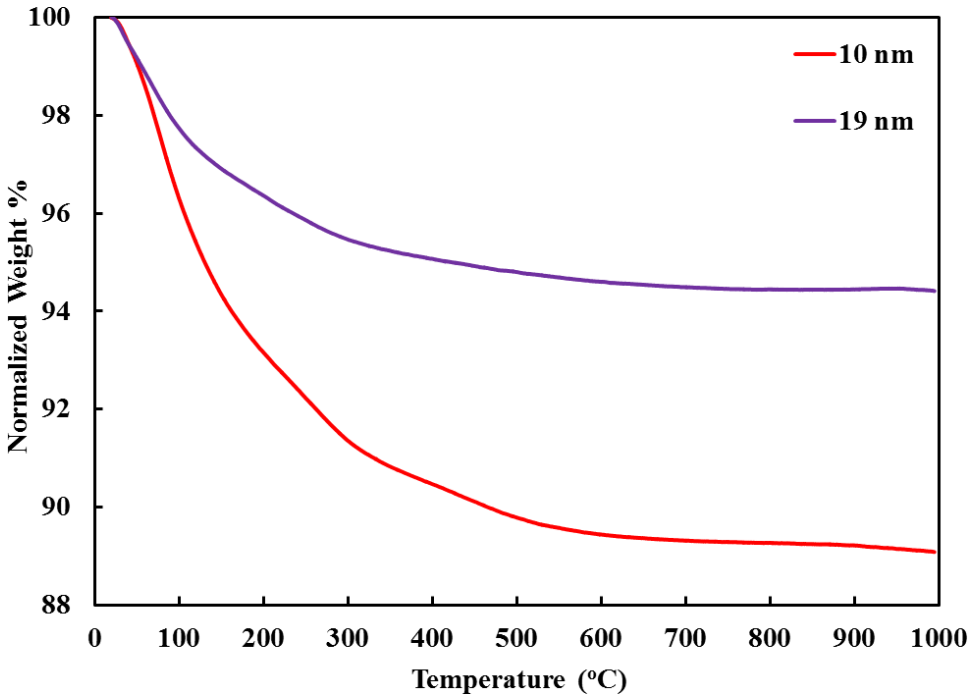

Figure 2.2. Thermogravimetric analysis (TGA) of 10 and 19 nm $MgFe_2O_4$

2.3.3 Electrochemical Evaluation

Few lithiation/delithiation mechanisms have been proposed for $MgFe_2O_4$ based on similar MFe_2O_4 (M = Cu, Co, Zn, Ni, Ca, etc.) materials and the most generally accepted mechanism is shown in **Equations 2.2** and **2.3** concerning charge and discharge processes,

respectively.[35,37,41] Upon discharge, it is believed that Mg^{2+} does not reduce, thus leaving Fe^{3+} as the electrochemically active cation. To that end, a full discharge would include the full reduction of Fe^{3+} to metallic Fe^0 involving the transfer of 6 electrons. The fully discharged state of an $MgFe_2O_4$ electrode would contain MgO, metallic Fe, and Li_2O (**Equation 2.2**).

$$MgFe_2O_4 + 6Li^+ + 6e^- \longrightarrow MgO + 2Fe + 3Li_2O \tag{2.2}$$

Since Mg^{2+} is not electrochemically active, the efficiency of $MgFe_2O_4$ during cycling is solely dependent on the reversible conversion between Fe^0 and FeO. Further, Fe^0 does not oxidize back to the Fe^{3+} state, therefore, some irreversible capacity loss is observed. In this case, charge requires the transfer of 2 electrons to afford FeO (**Equations 2.3**).

$$Fe + Li_2O \rightleftharpoons FeO + 2Li^+ + 2e^- \tag{2.3}$$

Cyclic voltammetry was collected for 10 and 19 nm $MgFe_2O_4$ samples in a voltage window of 0.1–3.0 V with a scan rate of 0.1 mV/sec for 11 cycles. The $MgFe_2O_4$ CV data presented in **Figure 2.3** agrees closely with CV data presented in the literature.[35,37–40,42] During cycle 1, a small cathodic peak is observed at ∼1.6 V while a more intense cathodic peak is observed at 0.58 and 0.34 V for 10 and 19 nm, respectively. The small cathodic peak is likely a result of Li^+ insertion into the $MgFe_2O_4$ crystal structure and minor reduction of Fe^{3+} to Fe^{2+}. Further, the intense cathodic peaks below 0.6 V must be due to more complete reduction of Fe^{3+} in $MgFe_2O_4$ to Fe^0 along with the formation of MgO and Li_2O. During oxidation, a broad anodic peak near 1.6 V is observed for 10 and 19 nm $MgFe_2O_4$ and can be attributed to the oxidation of Fe^0. The 5th cycle illustrates a shift of the cathodic peak to higher voltages, 0.70 and 0.76 V for 10 and 19 nm $MgFe_2O_4$, respectively, as a result of electrode polarization due to SEI (solid electrolyte interface) formation and irreversible capacity loss. The anodic peak does not shift after the first cycle and the quasi-reversible nature of the voltammograms in cycles 1-11 indicate reversibility of redox processes.

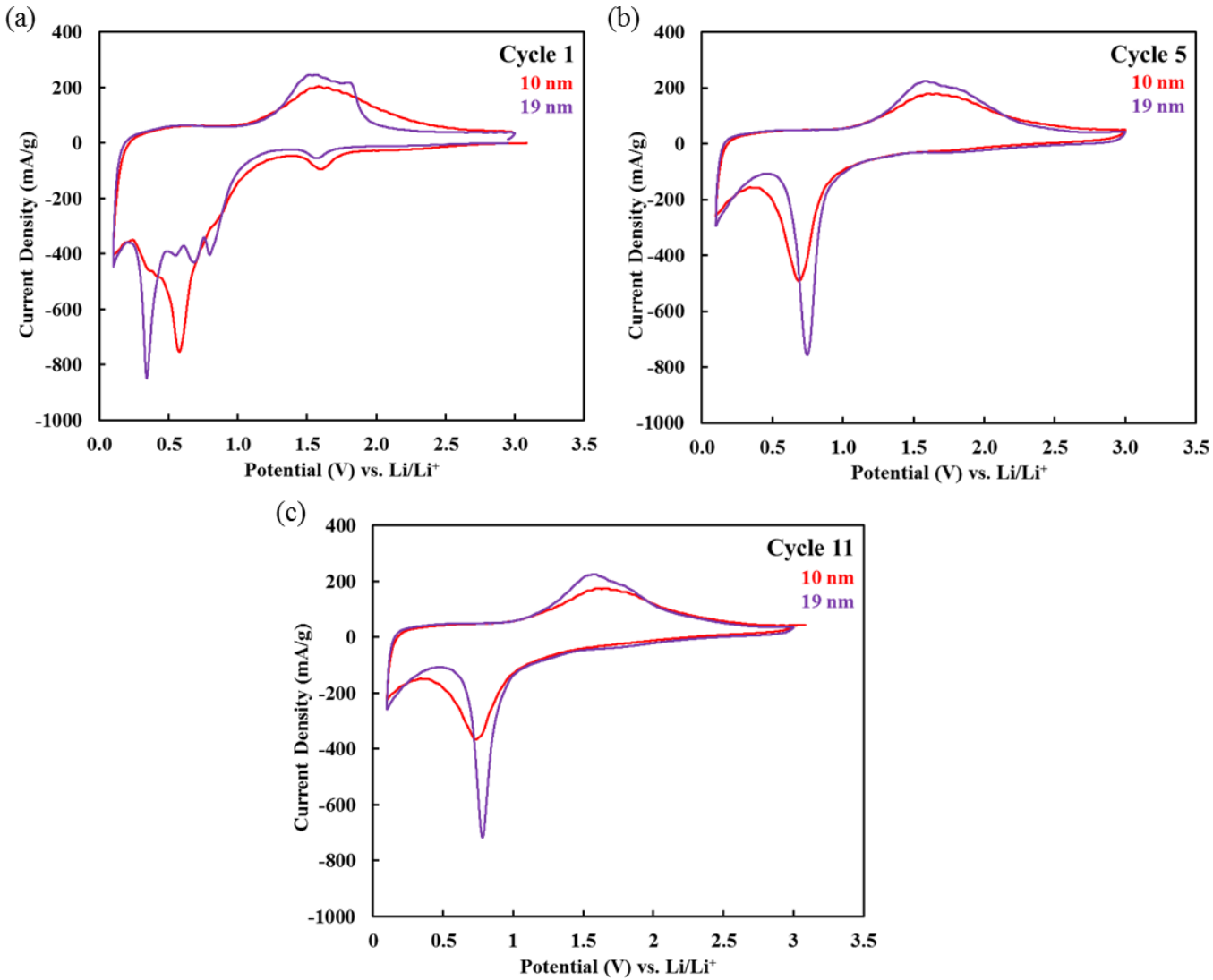

Figure 2.3. CV of 10 and 19 nm Li/$MgFe_2O_4$ cells at a rate of 0.1 mV/sec: (a) cycle 1, (b) cycle 5, and (c) cycle 11

Figure 2.4 shows the evolution of the discharge capacity of $MgFe_2O_4$ electrodes over 40 cycles at fast (100 mA/g) and slow (25 mA/g) discharge rates while the voltage profiles of 10 and 19 nm $MgFe_2O_4$ are shown in **Figure 2.5**. Discharge capacity curves in **Figure 2.4** illustrate high delivered capacities, clear discrepancies between the two crystallite sizes of $MgFe_2O_4$, and a significant dependence on discharge rate. First cycle discharge capacities exceed the theoretical capacity of $MgFe_2O_4$, 804 mAh/g, with values ranging between 968–1282 mAh/g for 10 and 19 nm cells discharged at fast (100 mA/g) and slow (25 mA/g) rates. The excess capacity delivered by 10 and 19 nm $MgFe_2O_4$ electrochemical cells is related to the decomposition of the electrolyte and the formation of the SEI and Li_2O on the surface of the pristine electrode at the electrolyte interface, a process that coincides with the irreversible capacity loss between cycles 1 and 2.[36,37,42,118–120]

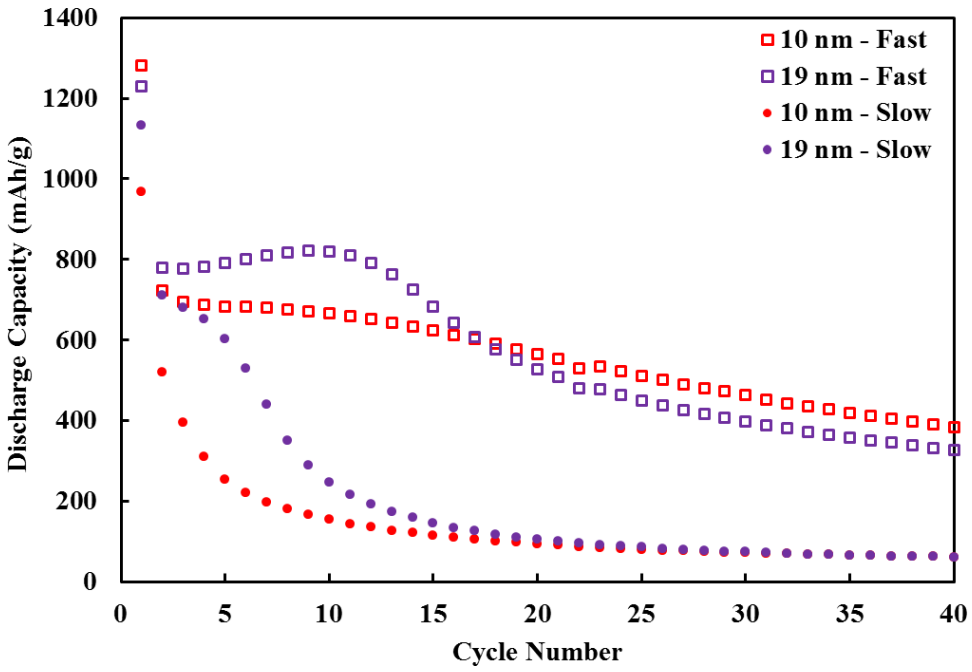

Figure 2.4. Galvanostatic cycling of 10 and 19 nm $MgFe_2O_4$/Li cells between 0.1–3.0 V at fast (100 mA/g, squares) and slow (25 mA/g, circles) rates of discharge

A discernible dependence of cycling efficiency on discharge rate is observed in **Figure 2.4** where the fast rate (100 mA/g) of discharge generates higher capacities for 10 and 19 nm $MgFe_2O_4$ in comparison with a slower rate (25 mA/g) that promotes substantially greater

capacity fade. Following 40 cycles, 10 and 19 nm $MgFe_2O_4$ cells discharged using a 100 mA/g current density deliver capacities of 384 and 326 mAh/g, respectively, while those discharge with a 25 mA/g density stabilize near 70 mAh/g (i.e. $\leq$ 21% of capacity delivered by the faster rate). At a slow discharge rate (25 mA/g), the 19 nm $MgFe_2O_4$ material exhibits 15% capacity loss in cycles 2-5 cycles, whereas, the 10 nm $MgFe_2O_4$ cell experiences substantial fade with a 40% loss in capacity. In total, the capacity loss is 56% (10 nm) and 65% (19 nm) at 100 mA/g and 86% (10 nm) and 90% (19 nm) at 25 mA/g (**Table 2.2**). The trend of higher capacity with larger nanosized spinel material has been observed for $Li_{4+x}Ti_5O_{12}$ where 31 nm material consistently delivered higher capacity over 50 cycles.[121] The loss in capacity of the small, 12 nm material was rationalized as mechanical failure due to changes in solubility limits from strain and interface energy which is suggested to initiate restructuring of the electrode surface.[122,123] This argument may be valid for 10 nm $MgFe_2O_4$ which has a larger amount of active material surface area exposed to the electrolyte, therefore, making the material vulnerable to parasitic reactions.

Table 2.2. Capacity loss of 10 and 19 nm $MgFe_2O_4$ electrodes between cycles 2 and 5 at fast (100 mA/g) and slow (25 mA/g) discharge rates

Crystallite Size	**Discharge Current Density (mA/g)**	**Capacity Loss (%)**
10 nm	100	56
	25	86
19 nm	100	65
	25	90

Examination of the voltage profiles of 10 and 19 nm $MgFe_2O_4$ from 0.01–3.0 V in **Figure 2.5** provides insight in to the discharge mechanism. A small plateau between 1.6–1.7 V is observed in both 10 an 19 nm $MgFe_2O_4$ electrochemical cells on cycle 1, agreeing with the CV data in **Figure 2.3**. This voltage plateau is representative of Li^+ insertion into the densely packed spinel structure of $MgFe_2O_4$ and the short length ($\leq$ 0.2 electrons) suggests

that a small amount of Li^+ is intercalated within the structure during this lithiation event **Figure 2.5 a**. Below 1.5 V in the first cycle, the discharge curves of 10 and 19 nm $MgFe_2O_4$ diverge from each other, thus implying slightly different reaction kinetics (e.g. polarization) within the crystalline material.

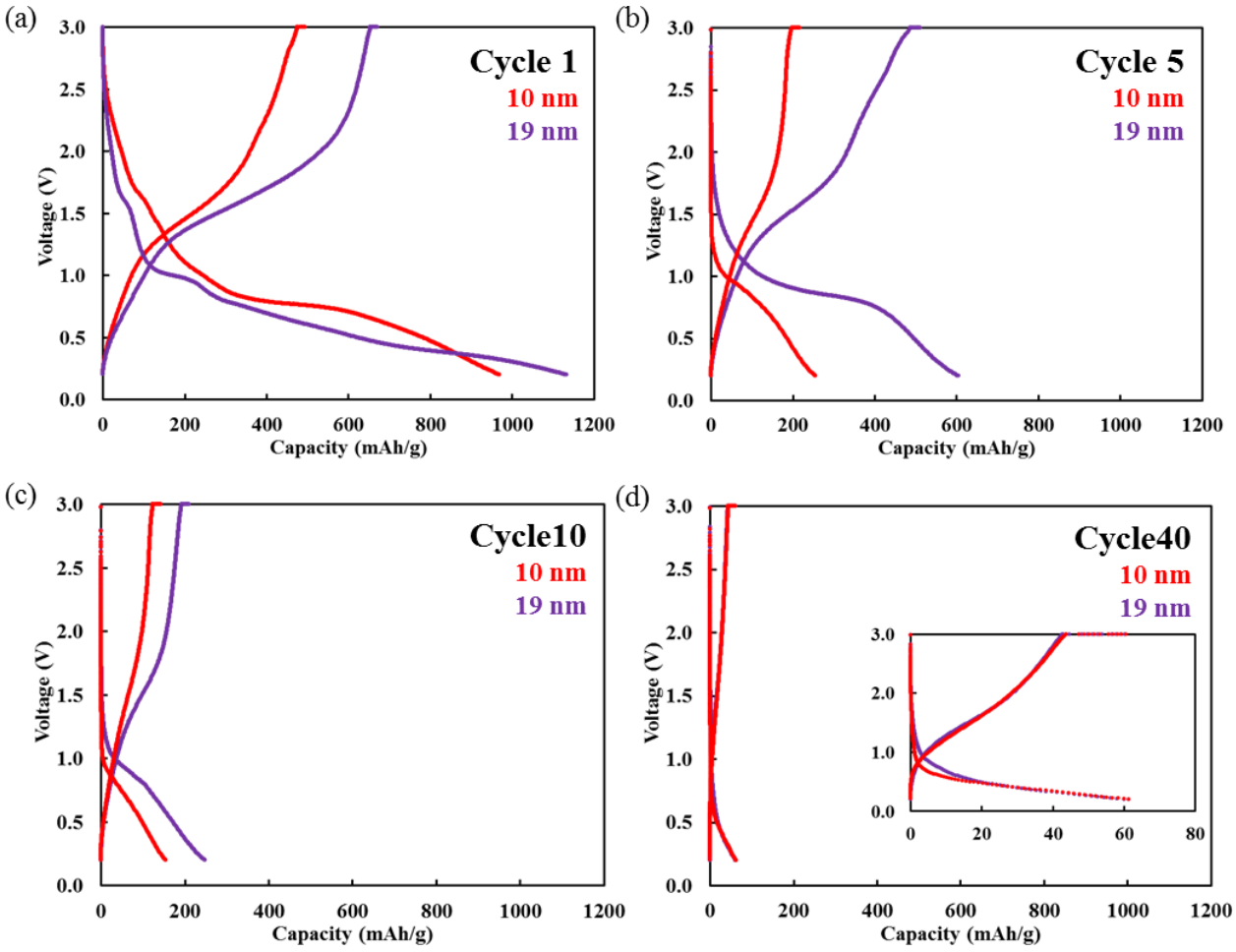

Figure 2.5. Voltage profiles, as a function of capacity, for 10 and 19 nm $MgFe_2O_4$/Li cells discharged at 25 mA/g: (a) cycle 1, (b) cycle 5, (c) cycle 10, and (d) cycle 40

The 19 nm material display a voltage plateau at 1.0 V ($\sim$ 1 electron in length) and is likely a result of the reduction of Fe^{3+} to Fe^{2+} and the corresponding phase conversion of $MgFe_2O_4$ to of FeO, MgO, and Li_2O. A particularly gradual slope is observed below 1.0 V in 19 nm $MgFe_2O_4$ with no further voltage plateaus, indicating that either the crystallite size or large spinel framework may be contributing to sufficient polarization in the electrode. In comparison, the 10 nm material indicates a voltage plateau at a lower voltage of approxi-

mately 0.77 V (∼2.5 electrons in length) followed by a steady slope to 0.1 V. The discharge regions below 1.0 V, for both 10 and 19 nm materials, must consist a multi-phase mixture involving the complete conversion of $MgFe_2O_4$ to FeO and FeO to metallic Fe^0 when taking **Equation 2.2** into consideration. Cycles 5 and 10 (**Figure 2.5 b** and **c**), display voltage plateaus between 0.9–1.0V which is likely the repeating conversion of FeO to metallic Fe^0 (**Equation 2.2**), as previously reported.[35,37,41] Notably, by cycle 40, there are no distinct plateaus present in the $MgFe_2O_4$ electrodes which may be a result of the highly amorphous nature of the nanostructured active material after cycling.

To determine the extent of voltage polarization present in 10 and 19 nm $MgFe_2O_4$, GITT (galvanostatic intermittent titration technique) tests were conducted from 3.0–0.2 V and the electrochemical results are shown in **Figure 2.6**. GITT allows for the open-circuit voltage (OCV) profile to be measured which reflects the equilibrium redox potentials at different capacities or states of charge ($Li_xMgFe_2O_4$). To my knowledge, this is the first report of GITT for an $MgFe_2O_4$ electrode.

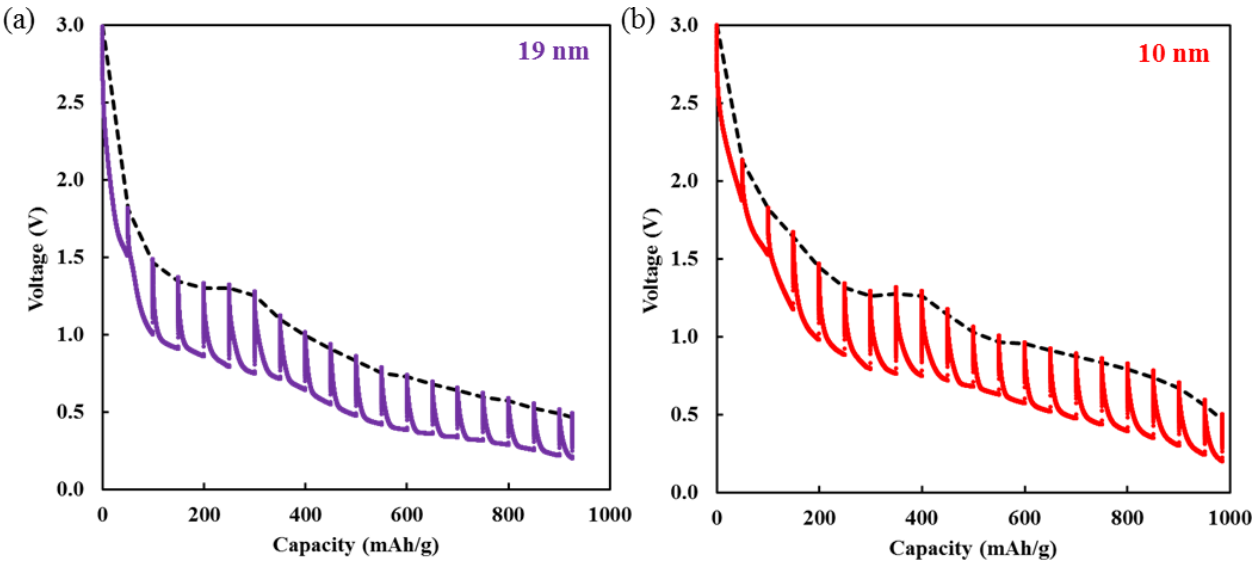

Figure 2.6. Pulsed-discharge profiles from GITT (galvanostatic intermittent titration technique) electrochemical testing for $MgFe_2O_4$/Li cells: (a) 19 nm and (b) 10 nm

On the initial discharge pulse (30 minute pulse with a 100 mA/g current density), significant voltage polarization is observed for 19 nm material which discharges to 1.53 V while

10 nm only reaches 1.91 V. This trend occurs for approximately the next 3 discharge pulses when the voltage polarization of the 19 nm material begins to stabilize. The GITT data confirms a voltage plateau in the OCV profile before a capacity of 400 mAh/g which was not distinguishable in the discharge curve in **Figure 2.5 a**.

2.4 Investigation of $MgFe_2O_4$ Redox Mechanism via Advanced *In-Situ* and *Ex-Situ* Techniques

The most complete investigation of the redox mechanism of $MgFe_2O_4$ was conducted by Permien et al. in 2015 using *ex-situ* X-ray diffraction, *ex-situ* ^{7}Li NMR spectroscopy, and ^{57}M*ö*ssbauer spectroscopy on 8 and 100 nm $MgFe_2O_4$.[41] The *ex-situ* X-ray diffraction and ^{7}Li NMR spectroscopy indicates that 8 nm $MgFe_2O_4$ under Li^+ intercalation at approximately 1.6 V while data for the 100 nm material suggests that Li_2O is deposited on the surface of the $MgFe_2O_4$ crystals as a result of slow diffusion. Upon the insertion of 2 electron equivalents, both 8 and 100 nm $MgFe_2O_4$ electrodes experienced a phase transition from spinel $MgFe_2O_4$ to the rock salt FeO structure which was also detected by ^{57}M*ö*ssbauer spectroscopy. Fe^{2+} in FeO was shown to be fully reduced to metallic Fe^0 after the insertion of 4 electrons. However, XRD was not able to distinguish reflections from the MgO phase during discharge. The absence of MgO in the diffraction pattern was attributed to the destruction of the $MgFe_2O_4$ spinel framework during Li^+ intercalation and resulting phase separation which eliminates long-range ordering. Advanced *in-situ* and *ex-situ* techniques are discussed below in an effort to fill the gaps in the $MgFe_2O_4$ redox mechanism proposed by Permien et. al.

2.4.1 *In-Situ* X-Ray Diffraction (XRD)

In-situ XRD results of 10 and 19 nm $MgFe_2O_4$ are shown in **Figures 2.7 and 2.8**, respectively. Intense reflections located at $\sim 36^o$, 43^o, 52^o, and 65^o correlate to the (1 1 0), (2 0 0) and (2 1 1) Li metal Bragg reflections respectively.[124] Peaks at $\sim 35^o$, 57^o and 63^o are from the (3 1 1), (5 1 1) or (3 3 3), and (4 4 0) lattice planes of the nominal $MgFe_2O_4$ crystal structure.[44] All other small, unchanging diffraction peaks are from components of

the *in-situ* pouch cell.

The 10 nm $MgFe_2O_4$ electrode undergoes subtle crystalline changes during initial Li^+ intercalation (**Figure 2.7** where the pristine $MgFe_2O_4$ electrode is indicated by the red XRD scan at the bottom of the figure). During discharge, the voltage plateau at 1.6 V (i.e. third and fourth XRD scans) initiates shifting of the $MgFe_2O_4$ reflection at 63° to lower values of 2θ. The crystal structure of $MgFe_2O_4$ partially remains intact during Li^+ intercalation at 1.6 V while Fe^{3+} is reduced and the rock salt FeO phase begins to appear. The shifting of this reflection to 61° is complete by 0.8 V, the second red XRD scan from the bottom in **Figure 2.7**, indicating that all Fe^{3+} has been reduced to Fe^{2+}. By the end of discharge to 0.2 V (third red XRD from bottom), amorphization of the nanocrystalline active material is observed by broadening and eventual disappearance of the peaks. These reflections do no reappear upon charge indicating that the reversibility of 10 nm $MgFe_2O_4$ is due to an amorphous material that cannot be detected by diffraction.

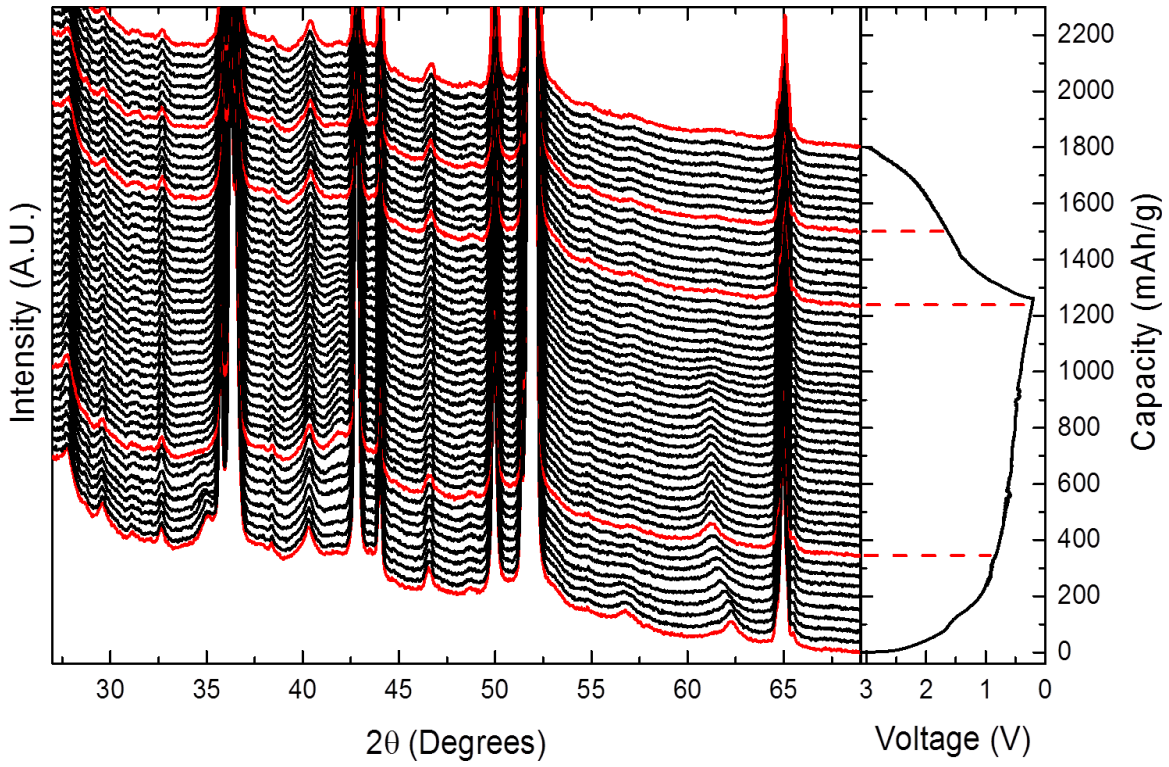

Figure 2.7. *In-situ* XRD of 10 nm $MgFe_2O_4$ electrodes

The structural evolution of the 19 nm $MgFe_2O_4$ electrode via *in-situ* XRD is more straightforward due to the increased size of the material which provides more intense reflections in the diffraction pattern (**Figure 2.8**) where the pristine $MgFe_2O_4$ electrode is indicated by the red XRD scan at the bottom of the figure). Specifically, as lithium is inserted into the structure at 1.6 V (second XRD scan), the FeO reflection emerges as a shoulder on the lower 2θ side of the $MgFe_2O_4$ peak at 63°. The phase evolution of $MgFe_2O_4$ to FeO seems to be stabilize by 0.6 V in 19 nm $MgFe_2O_4$ with the rock salt FeO reflection at 61.4° remaining rather crystalline. Notably, the $MgFe_2O_4$ peak at 57° does not disappear suggesting that some of the spinel material remains intact. Further discharge of 19 nm $MgFe_2O_4$ to 0.2 V illustrates reduction of the intensity and overall crystallinity of the $MgFe_2O_4$ and FeO reflections. After charge to 3.0 V, the FeO/$MgFe_2O_4$ peak shifts to 61.7°. The shift to higher values of 2θ may indicate that some of the some of the Fe^{2+} is oxidized to Fe^{3+}, however, full conversion to $MgFe_2O_4$ is not possible.

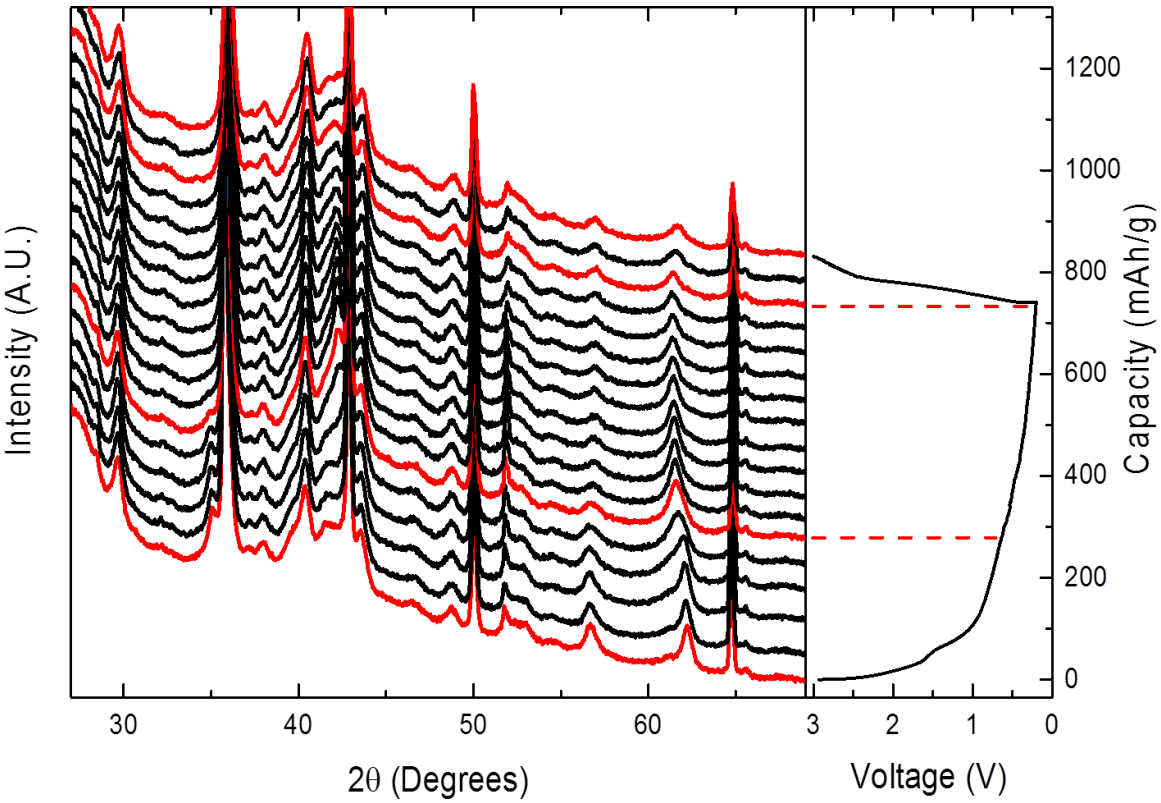

Figure 2.8. *In-situ* XRD of 19 nm $MgFe_2O_4$ electrodes

2.4.2 *Ex-Situ* X-Ray Absorption Spectroscopy (XAS)

In an effort to further probe the redox mechanism of $MgFe_2O_4$, *ex-situ* X-ray absorption spectroscopy (XAS) was conducted on electrodes recovered from electrochemical cells at various states of discharge and charge. XAS is a useful method to study the electrochemical processes displayed by $MgFe_2O_4$ composites since the materials are nanocrystalline in nature, especially after electrochemical testing. The sensitivity of XAS, particularly in the X-ray absorption near-edge structure (XANES) region, to localized structure allows for valuable insight into the oxidation state and coordination number of the nanocrystalline material participating in the electrochemical reactions. **Figure 2.9** shows both the XANES along with k^2-weighted $|\chi(R)|$ (Fourier transform of $\chi(k)$) spectra of 10 and 19 nm $MgFe_2O_4$ electrodes at various depths of discharge during the 1^{st} cycle. In the undischarged state, the initial XANES edge position (defined as the maximum of the 1^{st} derivative of $x\mu(E)$) is 7127 eV for both crystallite sizes. Once discharged to 2 e^-, the edge position has shifted to 7125 eV, suggesting the reduction of Fe^{3+} has begun. This trend continues until reaching the fully discharged state, where the edge position dramatically shifts to ~7113 eV for the 10 nm $MgFe_2O_4$, which is similar to the metallic Fe edge position of 7112 eV, suggesting a primarily metallic Fe environment. The 19 nm $MgFe_2O_4$, however, has a larger edge position of 7122 eV, suggesting a significantly more oxidized local environment in the 19 nm $MgFe_2O_4$ when fully discharged. When fully charged to 3.0 V, the edge positions of both 10 and 19 nm $MgFe_2O_4$ shift back to an oxidized state at ~7125 eV. This edge energy is slightly lower than the undischarged state (7127 eV), suggesting that Fe does not completely re-oxidize to the undischarged oxidation state/local atomic environment.

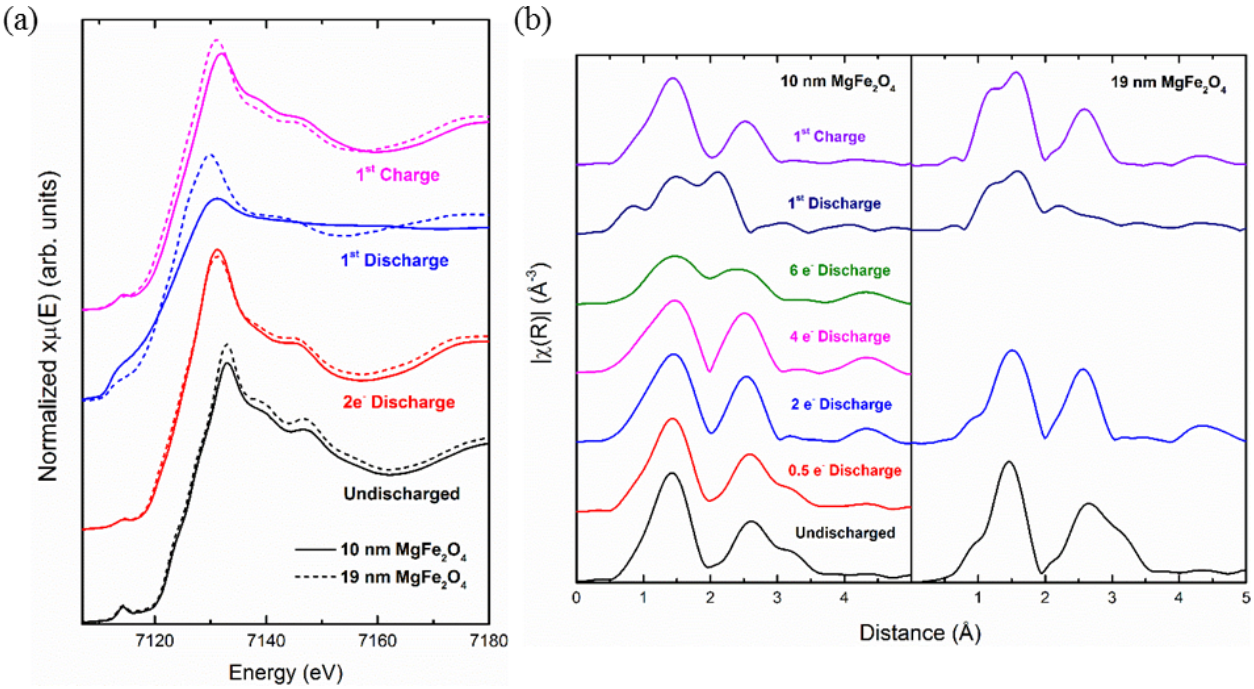

Figure 2.9. (a) XANES of undischarged, 2 e^-, 1st discharge, and 1st charge states of 10 and 19 nm $MgFe_2O_4$ (b) k^2-weighted $|\chi(R)|$ of the complete electrochemical states of the 10 and 19 nm $MgFe_2O_4$

The local atomic structural evolution can be observed in the $|\chi(R)|$ spectra in **Figure 2.9 b**. In the undischarged state, the local environment is similar to magnetite, Fe_3O_4.[125,126] Once discharged to 2 e^-, there is a considerable change in the local environment for both 10 and 19 nm $MgFe_2O_4$, in particular the shoulder at $\sim$ 3.2 Å observed in the undischarged and 0.5 e^- states is no longer observed (peak positions in **Figure 2.9 b** are $\sim$ 0.3 Å shorter than the actual interatomic distances due to uncorrected phase shifts due to the scattering process). Instead only two peaks at $\sim$ 1.5 Å and 2.6 Å remain suggesting a significant shift in the local atomic arrangement around Fe atoms at this depth of discharge. Once the 10 nm $MgFe_2O_4$ was discharged to 6 e^-, there is again a shift in the local structure, as the peak at $\sim$ 2.6 Å becomes broad, and the peak at $\sim$ 1.5 Å reduces in intensity. Once fully discharged, a metallic-like peak emerges at $\sim$ 2.2 Å, aligning well with the XANES edge position suggesting a primarily metallic-like local Fe atomic arrangement. The 19 nm $MgFe_2O_4$, however, is considerably different than the 10 nm when fully discharged. Instead of

a metallic-like peak evolving at ∼2.2 Å, a larger oxygen peak still remains, with very small contributions in the 2nd shell region between 2.0–3.0 Å. In accordance with the XANES, this suggests a highly oxidized iron environment in the fully discharged state for the 19 nm $MgFe_2O_4$. When recharged, the $|\chi(R)|$ is similar to what was observed at 2 e^- and 4 e^-, with the exception of the intensity of the 2nd shell peak at ∼ 2.6 Å. This heavily suggests that the local atomic structure does not revert to the original structure, as was also suggested by the XANES edge shifts.

Each XAS spectrum was fit with theoretical models to quantitatively track the atomic structural changes induced with lithium insertion. The 10 nm $MgFe_2O_4$ undischarged state was modeled with Fe and Mg atoms sharing the 16d and 8a sites in the nominal inverse-spinel $MgFe_2O_4$ structure, with the Fe-Fe/$Mg_{octahedral}$ interatomic distance of 2.95 ± 0.02 Å while the Fe-Fe/$Mg_{tetrahedral}$ interatomic distance was determined to be 3.46 ± 0.05 Å. When discharged to 0.5 e^-, there are no statistically significant changes in the interatomic distance or number of neighboring atoms in the local structure. However, when discharged to 2 e^-, a large structural change is observed. There is no longer observation of Fe atoms in the 8a tetrahedral sites, along with no direct evidence of neighboring Mg atoms in either 16d or 8a sites. Instead, the spectrum was modeled using a rock salt FeO-like structure, with the interatomic distance of iron and neighboring oxygen atoms of 2.03 ± 0.02 Å and other iron atoms at 3.06 ± 0.02 Å. As the discharge continues, the first observation of Fe metal is at 6 e^-, with the emergence of a Fe-Fe interatomic distance of 2.56 ± 0.01 Å. At this depth of discharge, there is observation of both FeO-like and Fe metal phases as shown in **Figure 2.10**. Once fully discharged however, only Fe metal is observed with a relative phase amplitude of 0.58 ± 0.23 (or 4.6 ± 1.8 Fe metal neighboring atoms). This reduced phase amplitude from the nominal bulk value (i.e. 1) is likely due to the sufficiently small particle sizes creating a large enough surface to bulk ratio, allowing the incomplete coordination spheres of the surface Fe atoms to significantly contribute to the observed number of neighboring atoms. The magnitude of reduction in neighboring atoms can provide a rough estimate of

particle size using geometric based arguments. The observed reduction in neighboring Fe metal atoms suggests the Fe metal nanoparticles that form when fully discharged are on the order of several nanometers.[127–129]

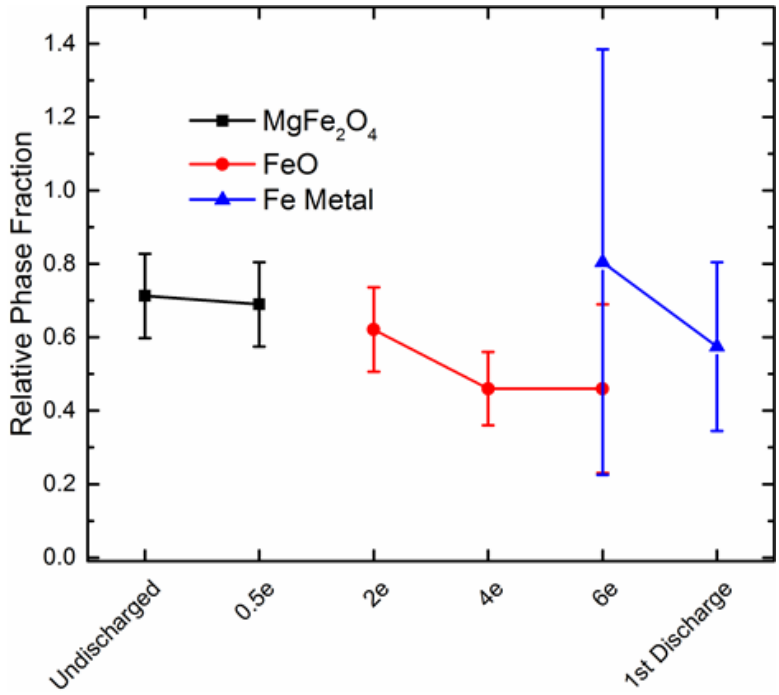

Figure 2.10. Relative phase fractions determined from EXAFS modeling of various depths of discharge during the initial discharge of $MgFe_2O_4$

The 19 nm $MgFe_2O_4$ electrode undergoes similar structural changes in the initial lithiation as the 10 nm $MgFe_2O_4$ electrode, with a clear transition from the inverse-spinel structure to the rock salt-like FeO phase when discharged to 2 e^- with both relative amplitudes and inter-atomic distances with standard deviations of the 10 nm EXAFS modeling results. However, when fully discharged, there is no clear metallic Fe contribution to the EXAFS spectrum. This electrochemical state was modeled with a combination of rock salt FeO and metallic Fe. The modeling results indicate there is not a statistically significant amount of Fe metal in the spectrum, rather a highly disordered iron oxide phase is present.

When fully recharged, it is clear that the local structure of both the 10 and 19 nm $MgFe_2O_4$ has re-oxidized to a structure similar to that observed between 2 to 6 e^- in the initial discharge (**Figure 2.9 b**). EXAFS modeling determined that Fe atoms are in a highly

disordered FeO-like structure. In the 10 nm $MgFe_2O_4$, there is a significant reduction in the relative amplitude of the 2nd shell Fe-Fe contribution, reduced from 0.52 ± 0.09 (determined from the 1st shell Fe-O contribution) to 0.23 ± 0.18. In addition, the Debye-Waller factor which accounts for static and thermal disorder was determined to be 0.013 ± 0.008 $Å^{-2}$ for the 2nd shell contributions. The 19 nm $MgFe_2O_4$ also indicates a similar disordered FeO-like phase when fully charged. This disordered structure is consistent with previous XAS studies on Fe_3O_4.[125] The interatomic distances for Fe-O (1.98 ± 0.02 Å) and Fe-Fe (3.04 ± 0.03 Å) are consistent with the FeO-like structures determined during the discharge (2.03 ± 0.02 Å and 3.06 ± 0.02 Å respectively).

2.4.3 *Ex-Situ* Transmission Electron Microscopy (TEM)

As a complement to *in-situ* XRD and *ex-situ* XAS, *ex-situ* transmission electron microscopy (TEM) imaging was conducted on 10 and 19 nm $MgFe_2O_4$ nanopowders obtained from electrochemically discharged coin cells (**Figures 2.11** and **2.12**). Images **a** from **Figures 2.11** and **2.12** illustrate significantly different sizes and morphologies of 10 and 19 nm $MgFe_2O_4$. The 10 nm $MgFe_2O_4$ sample is comprised of spherically shaped particles while the 19 nm sample is a mixture of smaller spherical particles and large rectangular particles on the order of a few hundred nanometers.

The discrepancy in size and morphology is likely the cause of the voltage polarization during GITT (**Figures 2.6**) where the 19 nm sample demonstrated significant polarization from the slow diffusion of Li^+ ions through the large particles. Electron diffraction of the discharged materials (**Figures 2.11 b** and **2.12 b**)) demonstrates the presence of the MgO phase in addition to Li_2O, metallic Fe^0, and remaining $MgFe_2O_4$ spinel. This data is the first evidence of crystalline MgO detected after the discharge of $MgFe_2O_4$. As mentioned previously, Permien et al. reported that the absence of MgO in their *ex-situ* XRD pattern was due to phase separation from the decomposition of the spinel $MgFe_2O_4$ framework which eliminates long-range ordering.[41] In our case, electron diffraction via TEM provides adequate spatial resolution to detect MgO in the bulk electrode.

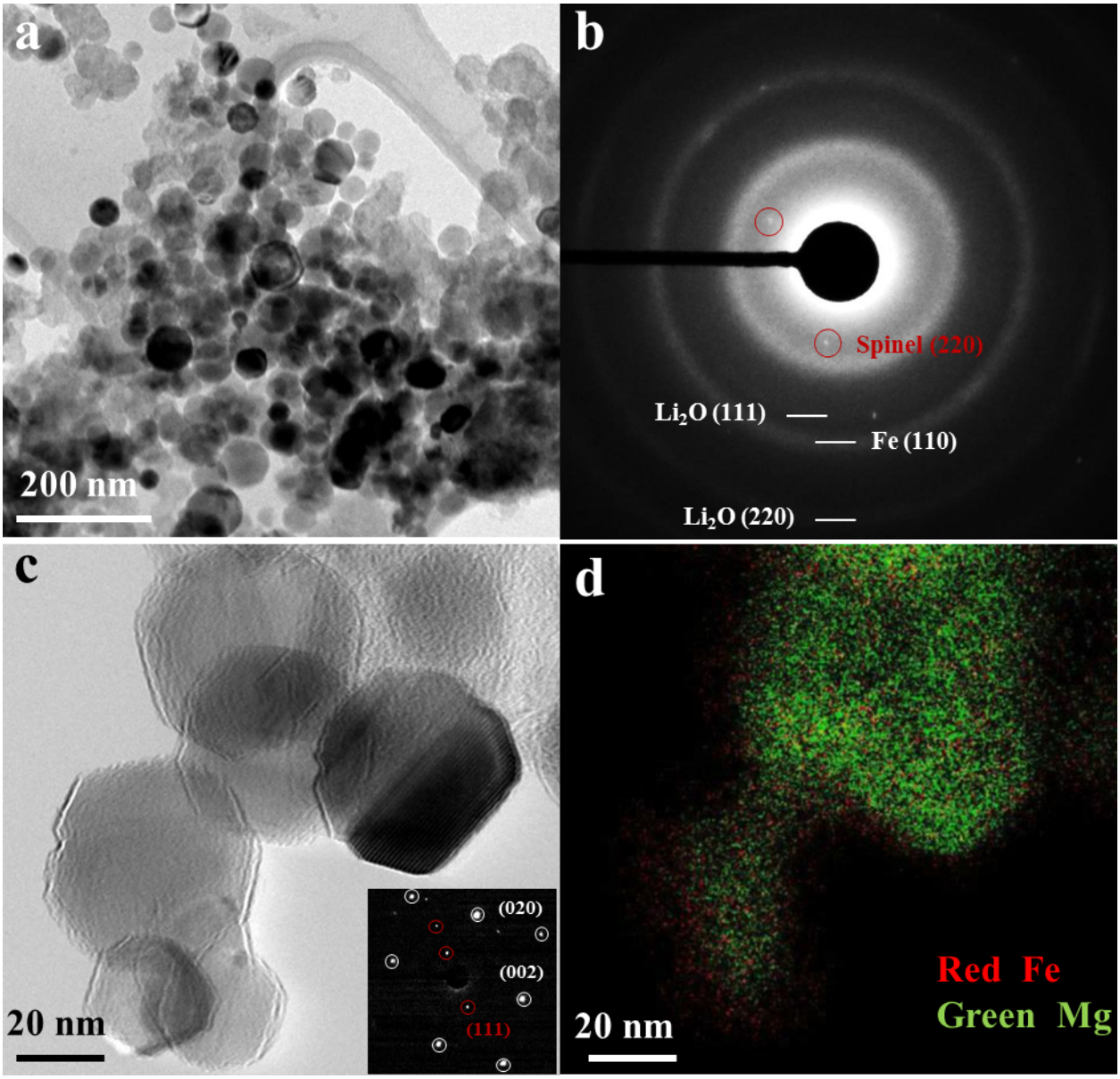

Figure 2.11. Morphology and composition distribution of 10-nm size $MgFe_2O_4$ samples after discharge. (a) TEM image shows the spherical morphology of discharge $MgFe_2O_4$ nanoparticles. (b) A typical electron diffraction pattern obtained from the sample in (a), indicating the existence of Li_2O and Fe phases. The diffraction spots marked by red circles correspond to the (2 2 0) lattice planes of the spinel structure. (c) A magnified TEM image showing a uniform morphology of single nanoparticles. The corresponding electron diffraction pattern in the inset shows the existence of rock-salt structured MgO (white circles) and spinel-structured $MgFe_2O_4$ (red circles). (d) EELS mapping showing Fe and Mg distribution in the nanoparticles in (c).

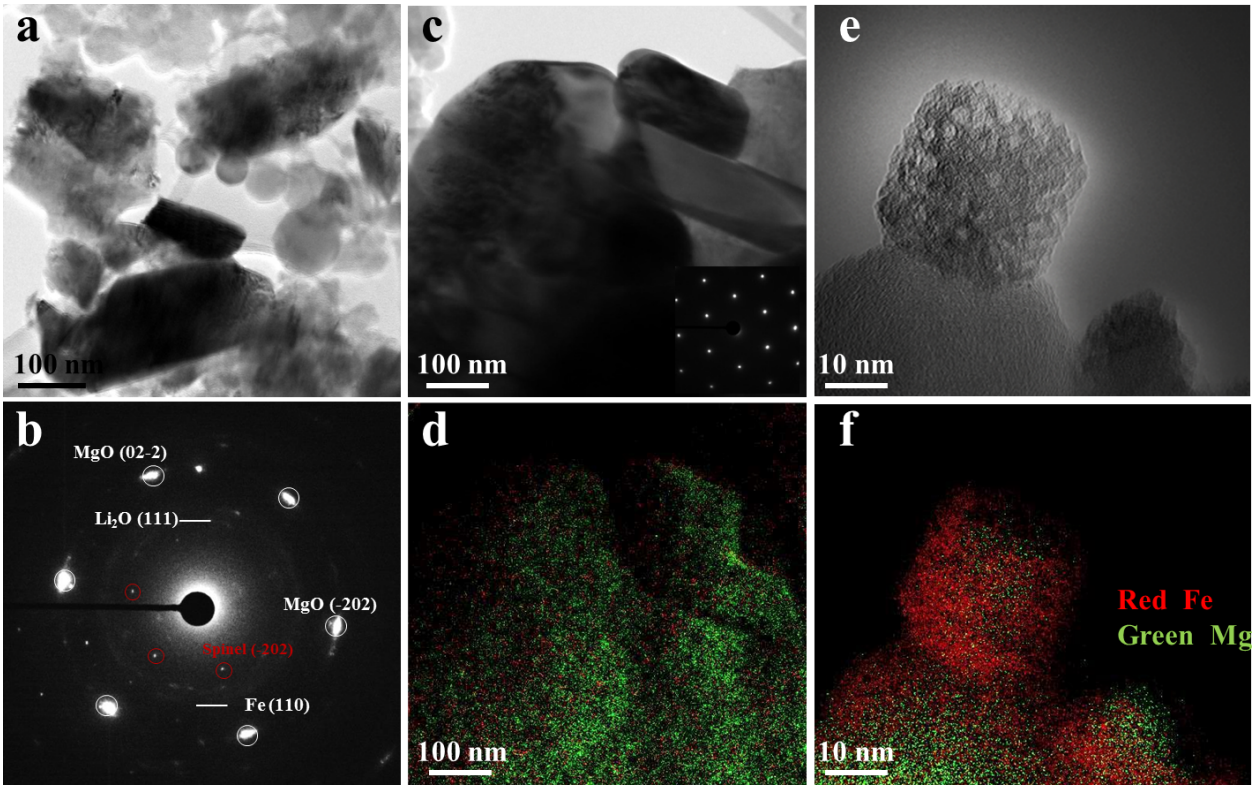

Figure 2.12. Morphology and composition distribution of 19-nm size $MgFe_2O_4$ samples after discharge. (a) TEM image of discharged $MgFe_2O_4$ samples with spherical and irregular-shaped morphology. (b) A typical electron diffraction pattern obtained from the sample in (a), indicating the existence of Li_2O, metallic Fe, MgO (white circles), and $MgFe_2O_4$ (red circles). The diffraction spots marked by red circles correspond to the (2 2 0) lattice planes of the spinel structure. (c) A magnified TEM image of a single-crystalline particle with spinel structure, as indicated by the corresponding electron diffraction pattern in the inset. (d) EELS mapping showing the uniform distribution of Fe (red) and Mg (green) in the particles in (c). (e) A magnified TEM image of discharge nanoparticles. (f) A EELS mapping showing the core-shell distribution of Fe (red) and Mg (green) in the nanoparticles in (c)

Although similar reduced phases are present in the 10 and 19 nm $MgFe_2O_4$ electrodes, EELS (electron energy loss spectroscopy) mapping of the discharge materials illustrate subtle differences between the reduction processes. In **Figure 2.11 d**, $MgFe_2O_4$ particles with small size and spherical shape were mainly transformed to the MgO and metallic Fe^0 phases with some $MgFe_2O_4$ spinel surviving. The discharge particles in the 10 nm $MgFe_2O_4$ electrode demonstrate a core-shell structure with Fe (green) segregated near the outer-edges of the shell and Mg (red) concentrated in the core. In contrast, large particles from the 19 nm $MgFe_2O_4$ electrode in **Figure 2.12 d** with an irregular, rectangular shape mainly possess

the $MgFe_2O_4$ spinel structure with uniform distribution of Fe and Mg. The mapping in image **d** agrees with the *in-situ* XRD data (**Figure 2.8**) where reflections from the spinel material were still present after discharge.

2.5 Conclusion

In Chapter II, $MgFe_2O_4$ was prepared using a combination of co-precipitation and hydrothermal reactions with a subsequent, relatively low-temperature calcination step. Calcination temperatures of 400°C to 500°C were used to control the crystallite size of $MgFe_2O_4$, yielding 10 and 19 nm materials, respectively. The electrochemistry of 10 and 19 nm $MgFe_2O_4$ electrode materials was investigated using cyclic voltammetry (CV), galvanostatic cycling, and galvanostatic intermittent titration technique (GITT) tests. Subtle differences in electrochemical performance were observed between 10 and 19 nm $MgFe_2O_4$, such as polarization and the presence/absence of voltage plateaus, and strong dependence on discharge rate was discovered for $MgFe_2O_4$. The redox mechanism of $MgFe_2O_4$ was then established via *in situ* XRD, *ex situ* X-ray absorption spectroscopy (XAS), and *ex situ* transmission electron microscopy (TEM) imaging. 10 and 19 nm $MgFe_2O_4$ follow the typical redox mechanism for spinel materials where Li^+ is observed followed by the phase conversion of $MgFe_2O_4$ to a rock salt FeO structure and finally reduction of FeO to metallic Fe^0 upon discharge to 0.1 V. Notably, TEM imaging of discharged $MgFe_2O_4$ powder electrodes provide the first evidence of MgO after the reduction of magnesium ferrite and illustrates large particles, on the order of a few hundred nanometers, for 19 nm $MgFe_2O_4$ while 10 nm $MgFe_2O_4$ is composed of small, spherically-shaped particles Although similar reduced phases are present in the discharged 10 and 19 nm $MgFe_2O_4$ electrodes, EELS (electron energy loss spectroscopy) mapping of the discharge materials illustrate subtle differences between the reduction processes where small particles are transformed to MgO and metallic Fe^0 while large 200-300 nm particles are mainly composed of $MgFe_2O_4$ which was also confirmed by EXAFS modeling. The data in Chapter II shows that particle size and morphology of $MgFe_2O_4$ significantly influences electrochemical behavior.

CHAPTER III

SYNTHETIC MANIPULATION OF $Ag_xMn_6O_{18}$ NANOROD COMPOSITION AND CRYSTALLITE SIZE: IMPACT ON ELECTROCHEMICAL PERFORMANCE

3.1 Introduction

Hollandites (often denoted OMS-2, OMS = octahedral molecular sieve) are transition metal oxide based materials which exhibit a tunneled motif and permit one-dimensional insertion and de-insertion of ions along the *c*-direction. Silver hollandite ($Ag_xMn_6O_{18}$) is of particular interest owing to the potential for electrochemical activity of the Ag^+ cation residing in the center of a 2 x 2 tunnel composed of edge and corner-sharing MnO_6 octahedra (**Figure 1.4**).[53,130] As described in Chapter I, silver hollandite syntheses are widespread in the literature, however, the preparation of pure silver hollandite remained elusive for decades.[53,59–61,65,66] The synthesis of silver hollandite via a low-temperature, aqueous co-precipitation reaction, proposed by the Takeuchi group, allows for the variation of Ag:Mn reagent ratios which enables for the manipulation of silver content, crystallite size, and bulk surface area of $Ag_xMn_6O_{18}$ ($1.0 \leq x \leq 1.8$).[62–64,108]

The first electrochemical assessment of silver hollandite was made possible by this co-precipitation synthesis as it allowed for the preparation of pure material in sufficient quantities.[62] Moreover, enabling systematic variation of physical properties of silver hollandite via synthetic manipulation facilitated a more comprehensive investigation of the electrochemical behavior of $Ag_xMn_6O_{18}$.[63,64] A variety of electrochemical tests were conducted for a series of silver hollandite samples, $Ag_xMn_6O_{18}{\cdot}nH_2O$ ($1.0 \leq x \leq 1.8$, $n \sim 2$). Constant current discharge, cycle testing, galvanostatic intermittent titration type (GITT) testing, and pulse testing demonstrated enhanced performance (i.e. increase in delivered capacity and improved reversibility) of the smaller crystallite size materials as a result of crystallite size/silver content reduction. In this chapter, Ag hollandite nanorods are studied through the combined use of local (atomic imaging, electron diffraction, electron energy-loss spectroscopy) and bulk

(thermogravimetric analysis) techniques to elucidate the effect of composition and crystallite size on electrochemical behavior.[110]

3.2 Experimental

3.2.1 General Methods and Materials

Silver hollandite was synthesized via a co-precipitation reaction modified from previously reported schemes.[62,63] Manganese(II) sulfate and nitric acid reagents were used as received from the vendors. Silver permanganate was prepared using a precipitation technique which involved the addition of an aqueous solution of silver nitrate to an aqueous potassium permanganate solution. Water utilized during synthesis was deionized water filtered through a Thermo Scientific Barnstead Nanopure ultrapure water purification system. Aqueous solutions of silver permanganate ($AgMnO_4$), manganese (II) sulfate monohydrate ($MnSO_4 \cdot H_2O$), and nitric acid (HNO_3) were combined and heated under reflux for 12 h. Solid silver hollandite was obtained by centrifugation, washed with H_2O, and reduced to dryness on a Labconco FreeZone freeze dry system. To obtain silver hollandite samples with varying Ag content and unique crystallite sizes, the ratios of Ag:Mn starting materials were altered accordingly. After synthesis, silver hollandite samples were annealed at 300°C for 6h to removed absorbed surface water.

3.2.2 Characterization

Powder X-ray diffraction (XRD) of silver hollandite was collected on a Rigaku SmartLab X-Ray diffractometer using a D/tex detector with Cu Kα radiation and Bragg-Brentano focusing geometry. Search-match analysis was performed on Rigaku PDXL2 software containing an ICDD PDF-2 database. Crystallite sizes of silver hollandite were determined by applying the Scherrer equation to the (2 1 1) peak at a 2θ near 37.5° in the powder diffraction pattern. Inductively coupled plasma-optical emission spectroscopy (ICP-OES) was employed on a ThermoScientific iCap 6000 ICP spectrometer for the quantitative elemental analysis of silver and manganese. Synchrotron X-ray powder diffraction (XPD) was

performed on L-Ag-OMS-2 and H-Ag-OMS-2 samples where $x = 1.22$ and 1.66, respectively. Ceria powder was used as a standard. The samples were sealed in capillaries and positioned in the synchrotron X-ray beam at the XPD 1 beamline in NSLS-II. The beam was calibrated to a wavelength of 0.2478 Å. Detection was performed using an amorphous silicon digital flat panel fitted with a CsI scintillator. During measurements, the sample was rotated to reduce preferred orientation effects. The two-dimensional data was integrated to simulate a one-dimensional pattern using the Fit2D software.[131] Rietveld refinement was carried out using GSAS II software.[132] High-resolution TEM/STEM imaging was performed using the double aberration-corrected JEOL-ARM200CF microscope with a cold-field emission gun, operating at 200 kV. TA Instruments SDT Q600 was used to collect simultaneous thermogravimetric analysis/differential scanning calorimetry (TGA/DSC) for investigation of the thermal stability and oxygen content of silver hollandite samples ($x = 1.16$, 1.60). TGA was conducted in alumina thermogravimetric analysis pans and heated from room temperature to 950°C under an atmosphere of nitrogen gas at a rate of 1°C/min.

3.2.3 Electrochemistry

CR 2320 coin cell type were used to probe the electrochemical performance of silver hollandite samples. Composite electrodes were prepared by mixing silver hollandite with conductive carbon and PVDF binder for a composition of 85% active material, 5% Super P conductive carbon black, 5% graphite, and 5% binder and coating onto an aluminum foil substrate. The coatings were dried under vacuum for 12 hours and, to ensure intimate contact of the electrode material with the aluminum current collector, pressed using a hydraulic press to afford a thin film with a thickness $\sim$2 μm. Electrodes were cut into circular discs, 0.5 inches or 1.27 cm in diameter, with a single electrode containing an average of 2.7 mg active material. Cells were fabricated with lithium metal anodes and 1 M $LiPF_6$ in 30/70 (v/v) ethylene carbonate/dimethyl carbonate as the electrolyte. Galvanostatic cycling, over a 50 cycle range, was performed on a Maccor Series 4000 Battery Test System in a chamber maintained at 30°C. Galvanostatic cycling tests were conducted using a constant applied

current of 35 mA/g over 50 cycles between 2.0–3.8 V.

3.2.4 Acknowledgment of Collaboration

The research in Chapter III was conducted in collaboration with Alexander Brady (Stony Brook University) and Dr. Yimei Zhu, Dr. Feng Xu, and Dr. Lijun Wu (Brookhaven National Laboratory). Alexander collected synchrotron diffraction data and performed Rietveld analysis while Dr. Zhu's group performed the TEM imaging studies.

3.3 Results and Discussion

3.3.1 Structural and Elemental Composition

Powder X-ray diffraction (XRD) was collected for silver hollandite and indicates that $Ag_xMn_6O_{18}$, with distinct silver contents (x), are pure and maintain a similar crystalline structure which is consistent with the $Ag_{1.8}Mn_8O_{16}$ reference pattern[53] (**Figure 3.1**). Peak intensities of $Ag_{1.16}Mn_8O_{16}$, in the diffraction pattern, decrease compared to $Ag_{1.6}Mn_8O_{16}$, resulting in a broadening of peaks. Average crystallite sizes were calculated by applying the Scherrer equation (**Equation 2.1**) to the (2 1 1) peak at near 37.5° 2θ in the powder diffraction pattern. The sizes were determined to be 10 and 15 nm for low and high x content $Ag_xMn_6O_{18}$, respectively. For simplicity, the low silver content sample will be denoted as L-Ag-OMS-2 while the high silver content samples will appear as H-Ag-OMS-2 herein.

The silver and manganese content of 10 and 15 nm $Ag_xMn_6O_{18}$ was determined though inductively coupled plasma-optical emission spectroscopy (ICP-OES). The silver content (x) of $Ag_xMn_6O_{18}$ samples as a function of crystallite size is illustrated in **Figure 3.2**. A trend is observed where crystallite size decreases as a function of x. Of particular interest, for electrochemical investigation of silver hollandite, are the low (L-Ag-OMS-2, 10 nm) and high (H-Ag-OMS-2, 15 nm) silver regimes which are indicated by black and red data points in **Figure 3.2**, respectively. The silver content (x) of H-Ag-OMS-2 and L-Ag-OMS-2, as a function of crystallite size, is confirmed by ICP-OES and indicates average silver contents for H-Ag-OMS-2 ($x = 1.60$) and L-Ag-OMS-2 ($x = 1.16$).

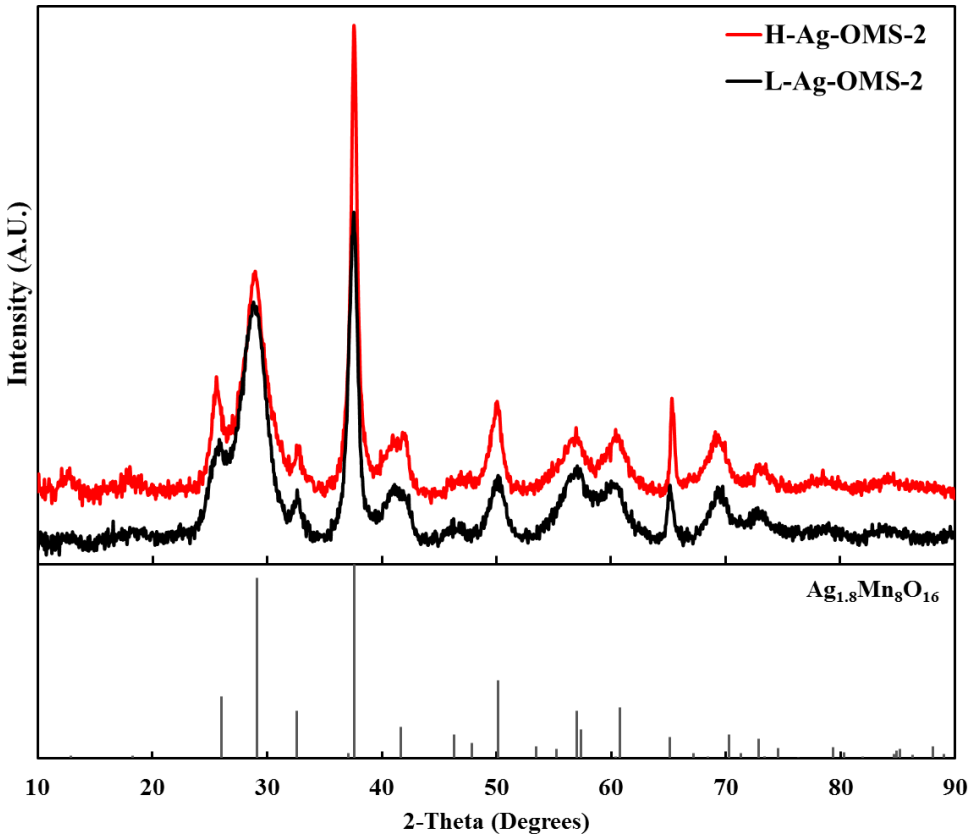

Figure 3.1. XRD of H-Ag-OMS-2 (16 nm, red) and L-Ag-OMS-2 (10 nm, black) hollandite samples, dried in a furnace at 300°C, with $Ag_{1.8}Mn_8O_{16}$ reference (ICSD 60155)

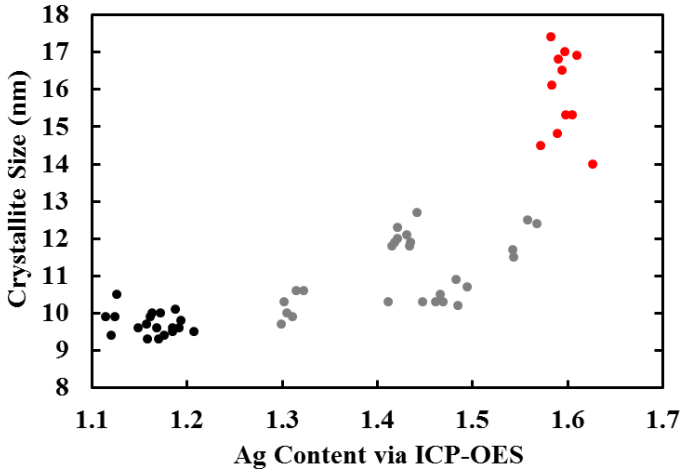

Figure 3.2. Silver content (x) as a function of crystallite size for $Ag_xMn_6O_{18}$ samples prepared via a low-temperature, aqueous co-precipitation reaction with L-Ag-OMS (low silver, black) and H-Ag-OMS-2 (high silver, red) regions of interest

X-ray powder diffraction data of L-Ag-OMS-2 and H-Ag-OMS-2 was also collected using a synchrotron (**Figure A5**) and provided high-quality data for the first Rietveld refinement of silver hollandite nanowires (**Table 3.1**). The high signal-to-noise ratio of the synchrotron diffraction data provides the necessary sensitivity to determine lattice parameters and atomic factors with a high degree of accuracy for a nanocrystalline material. The $I4/m$ structure[53] was used for fitting, however, the Rietveld refinement of the silver hollandite nanorod powders proved difficult due to significant crystal shape anisotropy of the samples. In this case, goodness of fit values (R_{wp}) range from 2.5 to 5.0%, as detailed in **Table 3.1**.

Table 3.1. Structural parameters from Rietveld refinement of L-Ag-OMS-2 and H-Ag-OMS-2

Chemical Composition		**L-Ag-OMS-2**	**H-Ag-OMS-2**
Unit Cell	a	9.770(2) Å	9.783(2) Å
	b	9.770(2) Å	9.783(2) Å
	c	2.8536(3) Å	2.8620(2) Å
Space Group		$I4/m$	$I4/m$
R_{wp}		3.23%	5.03%

The L-Ag-OMS-2 sample shows a larger value of 9.770 Å for the a and b dimensions compared to 9.738 Å for the high silver sample, H-Ag-OMS-2, **Table 3.1**. As discussed in Chapter I, Group I metal cations (including K^+ and Na^+) increase the dimensions of the 2 x 2 tunnels where higher occupancies of the tunnel ions increase the lattice parameters (**Table 1.2**).[133] The refined structures of each silver hollandite sample was used to calculate the tunnel dimensions in the ab plane bisecting the silver sites. In contrast to the results reported for the Group I metal cations, our results for Ag^+ show that higher occupancy of silver decreases the a and b lattice parameters. The silver hollandite structure prepared at high temperature with a silver content of $x = 1.8$ has a tunnel dimension of 4.873 Å in the ab plane bisecting the silver from the analysis of a single crystal.[53] As the silver content

decreases to $x = 1.66$ (H-Ag-OMS-2) and 1.22 (L-Ag-OMS-2), the tunnel dimensions increase to 5.072 and 5.176 Å, respectively. Thus, the trend observed at all three silver levels indicates decreased lattice parameters with increasing silver content is likely related to more covalent bonding character of Ag^+ compared to Group I metal ions.

3.3.2 Electrochemical Evaluation

After the preparation of silver hollandite samples with low and high silver contents and distinct crystallite sizes ($Ag_xMn_6O_{18}$, $x = 1.16$ and 10 nm or $x = 1.60$ and 15 nm), galvanostatic cycling was performed to determine the effects of silver content (x) and crystallite size on electrochemical performance. A constant current of 35 mA/g was applied to electrochemical cells containing lithium anodes and capacity was monitored as a function of voltage over 50 cycles. Preliminary calculations of theoretical capacity, which take into account the difference in the composition/molecular weight and number of electrons expected for discharge, demonstrated approximately a 5% difference in capacity. The theoretical capacity of L-Ag-OMS-2 is 260 mAh/g *versus* H-Ag-OMS-2 which is expected to deliver 247 mAh/g during an 8 electron discharge process. Experimental data, however, demonstrates a 7-fold increase in capacity of L-Ag-OMS-2 (160 mAh/g) compared to H-Ag-OMS-2 (23 mAh/g), see **Figure 3.3**.

The significant difference in delivered capacity cannot be rationalized by composition alone, as shown by the theoretical calculations. Galvanostatic cycling of $Li/Ag_xMn_6O_{18}$ (x = 1.16 and 1.60) electrochemical cells, over 50 cycles, continues to illustrate enhanced performance of the low silver, small crystallite size material over the high silver, large crystallite size material (**Figure 3.4**). By the end of 50 cycles, L-Ag-OMS retains a capacity over 400% greater than H-Ag-OMS-2. Such large differences in capacity motivated a more detailed study of silver hollandite nanorods, specifically related to the structural aspects of the material.

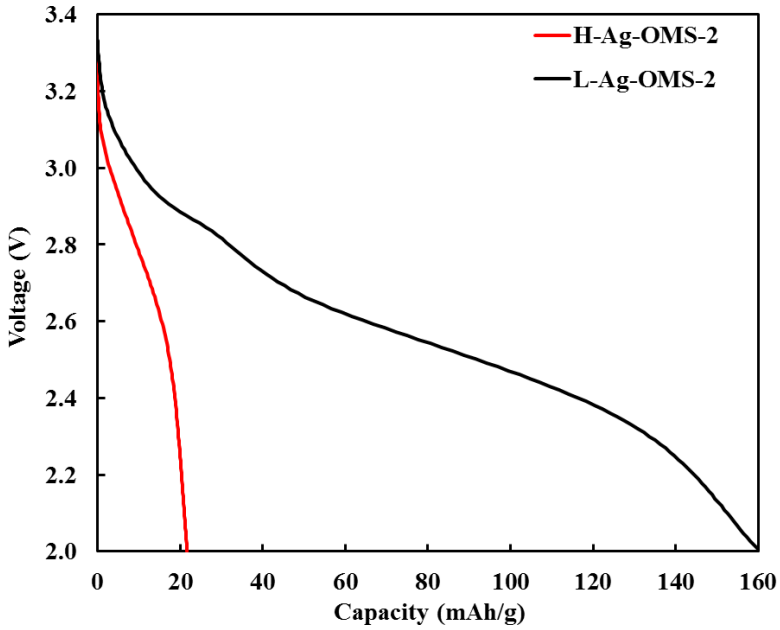

Figure 3.3. First cycle discharge of $Li/Ag_{1.20}Mn_8O_{16}$ (L-Ag-OMS-2) and $Li/Ag_{1.60}Mn_8O_{16}$ (H Ag-OMS-2) cells under a constant current of 35 mA/g

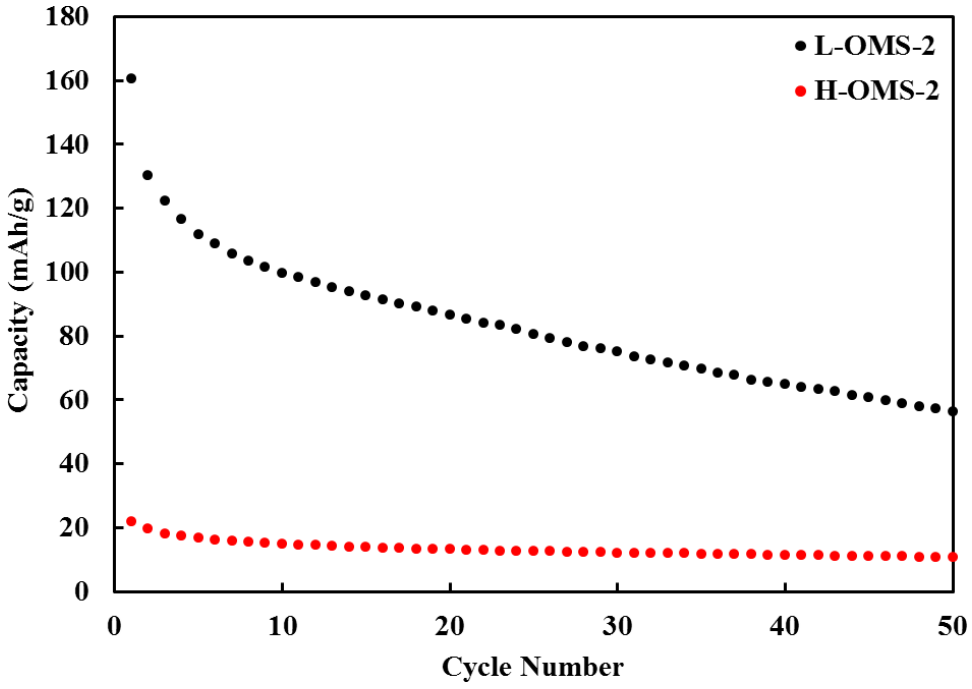

Figure 3.4. Galvanostatic cycling of $Li/Ag_{1.20}Mn_8O_{16}$ (L-Ag-OMS-2) and $Li/Ag_{1.60}Mn_8O_{16}$ (H Ag-OMS-2) cells under a constant current of 35 mA/g

3.3.3 Electron Imaging to Determine Oxygen Vacancies

A 7-fold increase in delivered capacity for Li/$Ag_xMn_6O_{18}$ electrochemical cells (160 vs. 23 mAh/g) was observed upon a seemingly small change in silver content of 1.16 for L-Ag-OMS-2 and 1.60 for H-Ag-OMS-2 and led to characterization of the structure and defects of silver hollandite nanorods. Transmission electron microscopy (TEM) imaging revealed a difference in the diameters of high and low silver, silver hollandite nanorods (**Figure 3.5**). Diameters of a few nm to 20 nm are observed for L-Ag-OMS-2 nanorods while diameters of 40-50 nm were measured for H-Ag-OMS-2 nanorods and the size directly correlates with differences in crystallite size calculated from diffraction data. Selected area diffraction of the high and low silver, silver hollandite nanorods in **Figure 3.5** shows a tetragonal crystal structure, also consistent with the XRD data which indicates an $I4/m$ space group.[53]

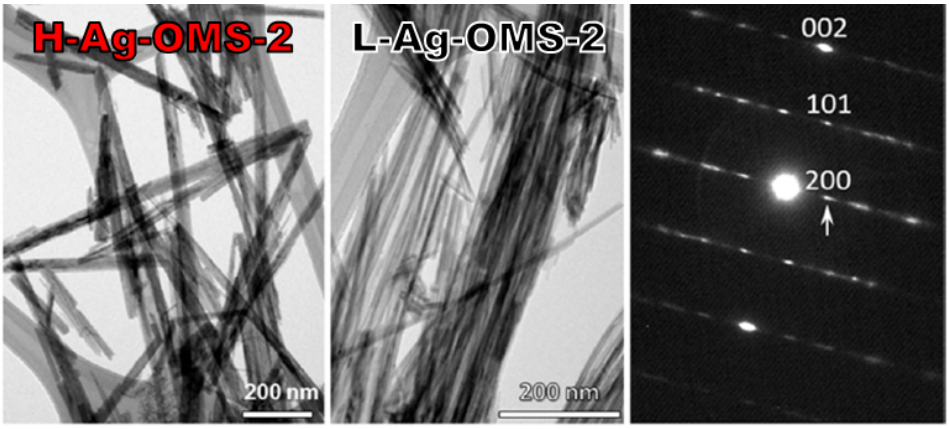

Figure 3.5. TEM bright field images of H-Ag-OMS-2 and L-Ag-OMS-2 nanorods with an electron diffraction pattern (EDP) illustrating the tetragonal structure of the nanorods

In addition to the TEM images shown in **Figure 3.5**, high resolution transmission electron microscopy (HRTEM) images were collected to probe the structural differences between L-Ag-OMS-2 and H-Ag-OMS-2 nanorods, scanning transmission electron microscopy (STEM) with a high angle annular dark field (HAADF) detector was used to study the structural defects and quantify the occupancy of silver and manganese in the nanorods, and electron energy loss spectroscopy (EELS) in the STEM mode was employed to precisely

measure oxygen vacancies and determine manganese valence. HRTEM images indicate the presence of point defects in the nanorods and stacking faults which suggest MnO_6 octahedral distortion and vacancies in the Ag^+ site. In an effort to quantify Ag^+ vacancies, STEM-HAADF was employed and indicates significant variation in Ag^+ occupancy of the tunnels in silver hollandite nanorods and specific instances where $Mn^{3+/4+}$ deviates from expected positions, indicative of MnO_6 distortion. Specifically, Ag^+ content in H-Ag-OMS-2 nanorods was observed in the range of $x = 0.4$–1.8. In addition to determining Ag^+ occupancy, EELS was used to quantify oxygen vacancies and manganese oxidation state in the structure. The intensity of the oxygen K-edge is less intense in the L-Ag-OMS-2 EELS spectrum and directly correlates with increase quantities of oxygen vacancies compared to larger H-Ag-OMS-2 nanorods. When scanning across $Ag_xMn_8O_{16}$ nanorods, EELS shows decreased amounts of both oxygen and manganese on the surface *versus* inside of the nanorods. A decrease in the L_3/L_2 edge intensity of manganese in the EELS spectra suggest a lower Mn oxidation state on the surface relative to the interior of the nanorods, where the average Mn valence is calculated to be approximately $Mn^{3.7+}$ for H-Ag-OMS-2 and $Mn^{3.5+}$ for L-Ag-OMS-2 nanorods. Although vacancies and defects exist within the silver hollandite materials the nanorods are consistent with the silver hollandite structure, overall.

Local TEM measurements indicate a greater quantity of oxygen vacancies in L-Ag-OMS-2 resulting in lower average manganese valence relative to H-Ag-OMS-2. The higher delivered capacity of L-Ag-OMS-2, as observed in **Figure 3.4**, may be related to presence of increased oxygen vacancies compared to H-Ag-OMS-2. It is proposed that the oxygen vacancies and MnO_6 octahedral distortion open the wall at the intersection of corner-sharing MnO_6 octahedra, thus facilitating Li^+ diffusion in the *ab* plane (**Figure 3.6**). The TEM results indicate that crystallite size and surface defects are significant factors that may effect cathode behavior and battery performance.

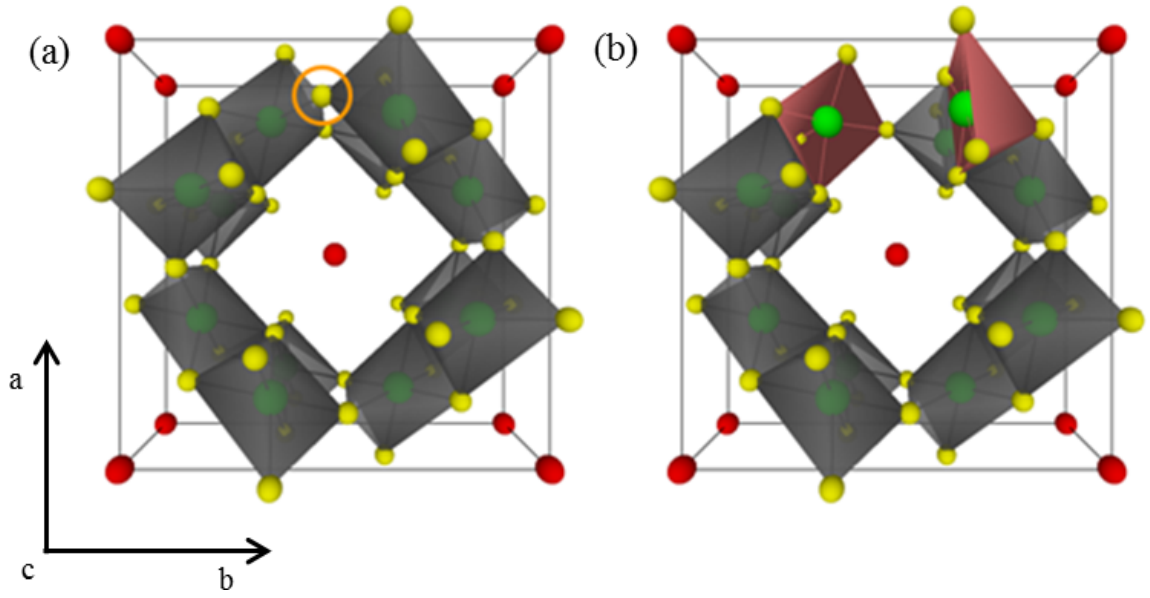

Figure 3.6. View of silver hollandite ($Ag_2Mn_8O_{16}$) along the *c*-direction where Ag^+ occupies the tunnel and is surrounded by eight MnO_6 octahedra: (a) intact silver hollandite structure and (b) removal of corner-sharing oxygen in the yellow circle proposed to facilitate Li^+ diffusion in the *ab* direction

3.3.4 Thermal Stability and Oxygen Content

To complement local measurements by TEM, thermogravimetric analysis (TGA) was used as a bulk characterization technique. TGA was employed to monitor thermal decomposition and assess the oxygen content of heat-treated silver hollandite samples with silver contents (x) of 1.16 and 1.60. The TGA experimental details were adapted from previous thermal investigation of hollandite-type structures.[55,134–136] First and foremost, it is imperative that silver hollandite samples are dried in a tube furnace prior to characterization or running electrochemical measurements. Hollandite, as an octahedral molecular sieve (OMS), is prone to absorbing and retaining surface water. The presence of surface water could potentially affect electrochemical performance by inhibiting the transport of ions at the surface of $Ag_xMn_6O_{18}$. L-Ag-OMS-2 and H-Ag-OMS-2 samples, as-prepared and dried at 300°C for 6 h in a tube furnace, are compared in **Figure 3.7**.

Once dry, the samples are handled in a humidity-controlled dry room. Dehydration of water adsorbed on the surface of hollandite is observed below 360°C (**Figure 3.7**). Signif-

icant differences are observed in water content between as-prepared and dry L-Ag-OMS-2 and H-Ag-OMS-2 samples, **Table 3.2** summarizes the results. Almost 2X as much water is lost after drying L-Ag-OMS-2 while H-Ag-OMS-2 shows over 3X difference in water content. The TGA results indicate the importance of materials handling.

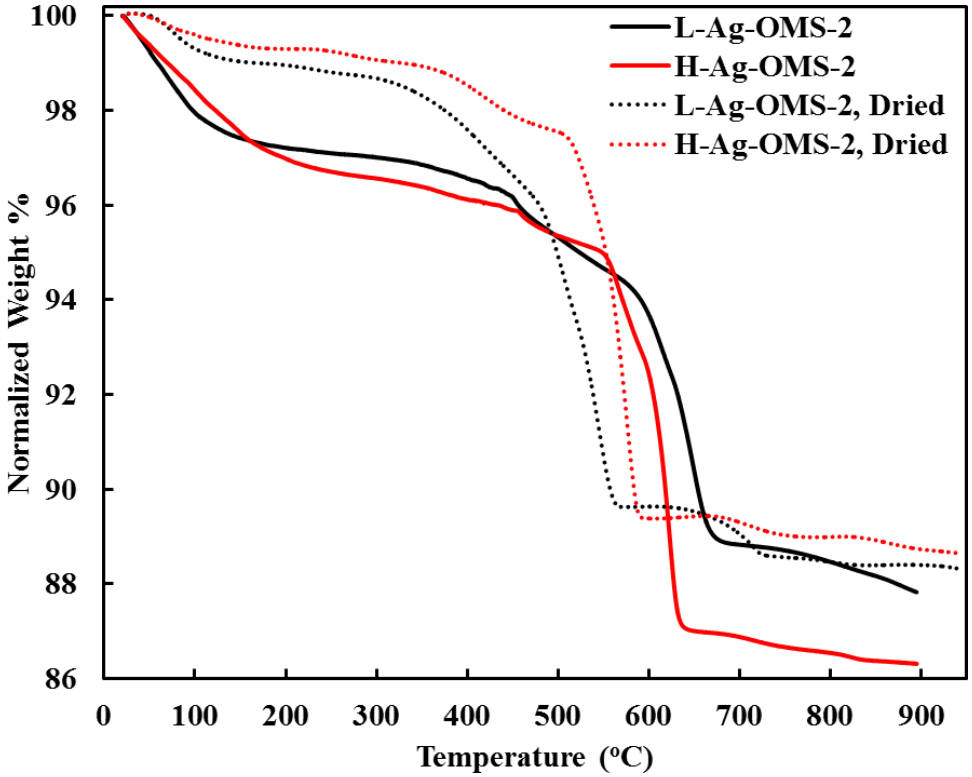

Figure 3.7. TGA of H-Ag-OMS-2 and L-Ag-OMS-2, as-prepared and after annealing at 300°C in a tube furnace

Table 3.2. Water content of L-Ag-OMS-2 and H-Ag-OMS-2 samples, as-prepared and after annealing, via TGA

Sample	Formula	H_2O per Formula Unit*
L-Ag-OMS-2	$Ag_{1.20}Mn_8O_{16}$	1.51
H-Ag-OMS-2	$Ag_{1.60}Mn_8O_{16}$	1.83
L-Ag-OMS-2, Annealed	$Ag_{1.20}Mn_8O_{16}$	0.82
H-Ag-OMS-2, Annealed	$Ag_{1.60}Mn_8O_{16}$	0.54

*Weight loss from room temperature to 360°C

Dried L-Ag-OMS-2 and H-Ag-OMS-2 sample were used to determine thermal stability and oxygen content of silver hollandite. As mentioned before, dehydration of water adsorbed on the surface of hollandite and water within the tunneled MnO_6 motif, $Ag_xMn_6O_{18}{\cdot}nH_2O$ where $n = 0.7$–0.9, is initially observed below 360°C (**Figure 3.8**).

The low silver content hollandite nanorods (L-Ag-OMS-2) exhibit increased surface-adsorbed water below 100°C, indicative of surface defects, often owing to oxygen, within a hollandite-type structure.[137–139] Decomposition of silver hollandite between 360-750°C occurs via a succession of weight-loss events that include a breakdown of the MnO_6 tunneled structure, formation of silver metal and Mn_2O_3, and decomposition of Mn_2O_3 into Mn_3O_4 (**Equation 3.4**).[134,135]

$$\begin{aligned} Ag_xMn_8O_{16} \cdot nH_2O &\longrightarrow Ag_xMn_8O_{16} \\ \longrightarrow xAg + 4Mn_2O_3 + 2O_2 &\longrightarrow xAg + \frac{8}{3}Mn_3O_4 + \frac{4}{6}O_2 \end{aligned} \tag{3.4}$$

The decomposition L-Ag-OMS-2 occurs at lower temperatures than H-Ag-OMS-2, thus illustrating a decrease in the intrinsic thermal stability of the low silver, nanocrystalline material. Analysis of the post-decomposition TGA samples via XRD confirms the exclusive presence of silver metal and Mn_3O_4 (**Figure 3.9**). During decomposition, the weight loss corresponds to the evolution of O_2 which can be used to systematically assess the oxygen content of silver hollandite samples with distinct compositions. The weight-loss profile and the first derivative as a function of temperature were used to determine the precise region of oxygen loss for the calculation (**Figure 3.8**). The calculated oxygen contents of 14.8 (L-Ag-OMS-2) and 15.7 (H Ag-OMS-2) are analogous with the results of EELS analysis during TEM which provided local compositions of $Ag_{1.22}Mn_8O_{14.8}$ and $Ag_{1.63}Mn_8O_{15.6}$ for the L-Ag-OMS and H-Ag-OMS-2 materials, respectively. Using a combination of local and bulk measurements, the extent of surface defects (i.e. oxygen vacancies) was effectively quantified.

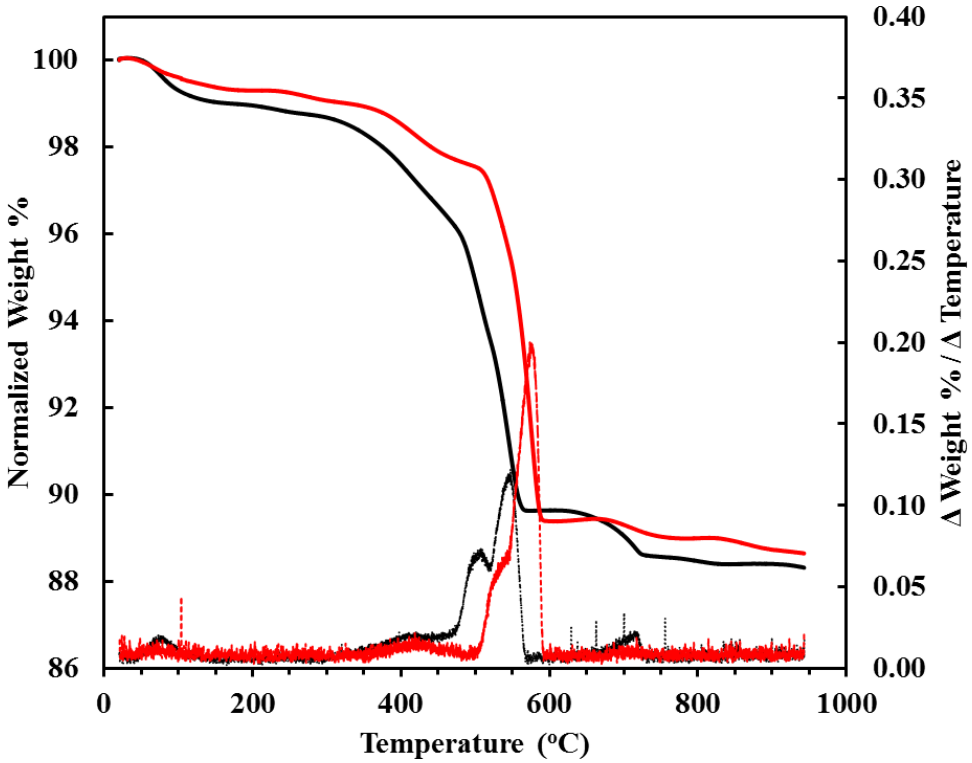

Figure 3.8. TGA and first derivative of weight as a function of temperature for $Ag_{1.16}Mn_8O_{16}$ (L Ag-OMS-2, red) and $Ag_{1.60}Mn_8O_{16}$ (H-Ag-OMS-2, black)

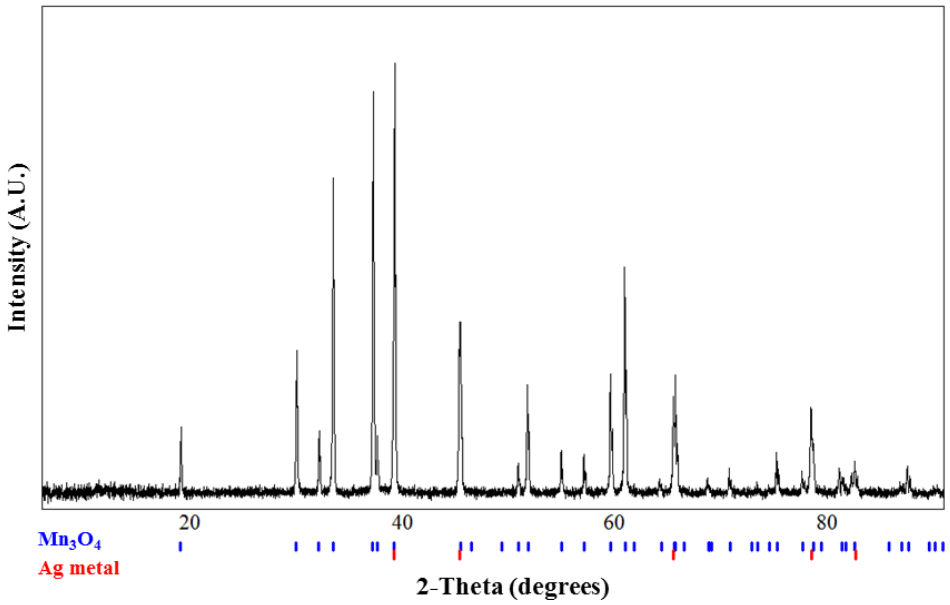

Figure 3.9. Post-TGA XRD of $Ag_xMn_6O_{18}$ with Mn_3O_4 (ICSD 31094) and Ag metal (ICSD 64706) reference patterns

3.4 Conclusion

In this chapter, a 7-fold increase in capacity for low silver, small crystallite size material ($Ag_{1.2}Mn_8O_{16}$, L-Ag-OMS-2) compared to high silver, large crystallite size ($Ag_{1.6}Mn_8O_{16}$, H-Ag-OMS-2) was observed with delivered first cycle capacities of 160 and 23 mAh/g, respectively. Based on the chemical composition silver hollandite, only a 5% difference in delivered capacity was anticipated corresponding to theoretical capacities of 260 mAh/g (L-Ag-OMS-2) and 247 mAh/g (H-Ag-OMS-2). Local (transmission electron microscopy (TEM), electron-energy loss spectroscopy (EELS), and electron diffraction) and bulk (thermogravimetric analysis (TGA)) measurements were employed to characterize the materials. The results indicated greater quantities of oxygen vacancies in L-Ag-OMS-2, resulting in lower average manganese valence relative to H-Ag-OMS-2. Oxygen vacancies (i.e. MnO_6 octahedral distortion) may rationalize the dramatic change in electrochemistry by facilitating Li^+ diffusion in the *ab* plane of silver hollandite nanorods demonstrating that surface defects, through such vacancies, play a significant role in electrochemical performance. The electrochemical results described in this Chapter III highlight the opportunity to improve electrochemical behavior of active electrode materials by tuning the properties of the material via appropriate design of the synthetic method.

CHAPTER IV

DECONVOLUTION OF COMPOSITION AND CRYSTALLITE SIZE OF $Ag_xMn_6O_{18}$ NANORODS: INFLUENCING ELECTROCHEMICAL BEHAVIOR

4.1 Introduction

In prior reports, it has been demonstrated that pure silver hollandite ($Ag_xMn_6O_{18}$, $1.0 \leq x \leq 1.8$) with silver content (x) of varying degrees can be prepared by systematically manipulating starting reagent quantities during a low-temperature, aqueous co-precipitation reaction where the crystallite size of the $Ag_xMn_6O_{18}$ product increases with increasing values of x.[62,63] Significant differences in electrochemistry were observed across the series ($Ag_xMn_6O_{18}$, $1.0 \leq x \leq 1.8$, 12-26 nm), however, it was difficult to determine whether the effects were resultant of a change in silver content, crystallite size, or a combination of the two. For the first time, Chapter IV describes $Ag_xMn_6O_{18}$ ($x = 1.4$) synthesized by an analogous technique to afford silver hollandite with distinct crystallite sizes (10 and 15 nm) and equivalent silver content (x) by increasing the concentration of the manganese starting material. Keeping the silver content (x) in $Ag_xMn_6O_{18}$ uniform allows for the deconvolution of electrochemical effects related to crystallite size versus those related to silver content, which was not possible previously. As-prepared $Ag_{1.4}Mn_6O_{18}$ nanorods (10 and 15 nm) are confirmed to be structurally analogous by XRD, HRTEM, XPS, and TGA. The electrochemical behavior and lithium diffusion properties of small (10 nm, 10-Ag-OMS-2) and large (15 nm, 15-Ag-OMS-2) crystallite size $Ag_{1.4}Mn_8O_{16}$ are investigated by galvanostatic cycling, CV, AC impedance, pulsed-discharge experiments, and *ex-situ* XAS analysis of cycled cathodes.

4.2 Experimental

4.2.1 General Methods and Materials

Silver hollandite was synthesized via an aqueous co-precipitation reaction adapted from previously reported schemes.[62,63] Water used during synthesis was deionized water filtered through a Thermo Scientific Barnstead Nanopure system. Aqueous solutions of silver per-

manganate ($AgMnO_4$), manganese (II) sulfate monohydrate ($MnSO_4 \cdot H_2O$), and nitric acid (HNO_3) were combined and heated at reflux for 12 h. Solid silver hollandite was obtained by centrifugation, washed with H_2O, and reduced to dryness on a Labconco FreeZone freeze dry system. To obtain silver hollandite samples with similar Ag content and unique crystallite sizes, the concentrations of each reagent were altered accordingly. Milling of high crystallite size silver hollandite was performed in a McCrone Micronising Mill using cylindrical agate grinding elements and water.

4.2.2 Characterization

Powder X-Ray diffraction (XRD) of silver hollandite and corresponding thermal decomposition products were collected using a Rigaku SmartLab X-Ray diffractometer equipped with a D/tex detector in Bragg-Brentano focusing geometry and Cu Kα radiation. Rigaku PDXL2 software with an ICDD PDF-2 database was used for search-match analysis. Crystallite size of silver hollandite samples was approximated by applying the Scherrer equation to the (2 1 1) reflection at a 2θ value of approximately 37.5^o in the XRD pattern. Quantitative elemental analysis of silver and manganese was determined by inductively coupled plasma-optical emission spectroscopy (ICP-OES) on a ThermoScientific iCap 6000 ICP spectrometer. Brunauer-Emmett-Teller (BET) surface area measurements were collected on a Quantachrome Nova 4200e using an 11-point BET method, nitrogen gas adsorbate, and 100 mg silver hollandite. High-resolution TEM/STEM imaging, electron diffraction, elemental and Mn valence mapping were performed using a double aberration corrected JEOL-ARM200CF microscope with a cold-field emission gun and operated at 200 kV. The microscope was equipped with JEOL and Gatan HAADF detectors for incoherent HAADF (Z-contrast) imaging and a Gatan GIF Quantum ER Energy Filter with dualEELS for EELS. The energy positions of Mn L_3 and L_2 were obtained by fitting the EELS spectrum with a combined Gaussian and Lorentz function. The L_3/L_2 intensity ratio was calculated from the EELS spectrum based on the Pearson method with double step functions. To assist interpretation of the HRTEM and HRSTEM images, image simulations were carried out using

computer codes based on the multislice method with frozen phonon approximation. Thermal stability and oxygen content of silver hollandite was investigated using simultaneous thermogravimetric analysis/differential scanning calorimetry (TGA/DSC) with a TA Instruments SDT Q600. Alumina thermogravimetric analysis pans were filled with approximately 10 mg silver hollandite and heated from room temperature to 950°C at a rate of 1°C/min under an atmosphere of nitrogen gas. X-ray photoelectron spectroscopy (XPS) measurements were collected on a RHK Technology UHV 7500 variable temperature atomic force and scanning tunneling microscope. The UHV chamber was held at a base pressure of 2 x 10^{-10} Torr and was equipped with a SPECS Phoibos 100 MCD analyzer. A non-monochromatized Al-Kα X-ray source (hν = 1486.6 eV) was utilized which operated with a 30 mA current and an accelerating voltage of 10 kV. Powder samples of silver hollandite were adhered to conductive copper tape and mounted onto a sample holder. Charging effects in XPS spectra were corrected by calibrating the binding energy of the adventitious C1s peak to 284.8 eV.

X-ray absorption spectroscopy (XAS) measurements of 10-Ag-OMS-2 and 15-Ag-OMS-2 electrodes (undischarged, discharged to 3 e^-, and recharged) were acquired at the Materials Research Collaborative Access Team (MRCAT) beamline, sector 10-BM, at the Advanced Photon Source at Argonne National Laboratory, IL. Each sample was removed from coin-type electrochemical cells, washed with dimethyl carbonate (DMC), dried, and sealed between Kapton tape in an inert Ar atmosphere. The samples were then sealed within air-tight pouches to ensure the samples were stored under inert atmosphere until XAS measurements were collected. Each sample was measured in transmission mode at the Mn K-edge (6.539 keV) and Ag K-edge (25.514 keV) utilizing ionization chambers and Si (1 1 1) double crystal monochromator. . The initial ion chamber was filled with 50/50% He/N_2 and 100% Ar gas mixtures for the Mn and Ag K-edge measurements, respectively, while the transmission ion chamber was filled with 85/15% N_2/Ar and 100% Ar, respectively. A Mn or Ag metal foil was used for initial beam energy calibration and were measured simultaneously with each sample to ensure proper alignment of multiple XAS scans. Two spectra were collected

for each sample at each element edge to improve the signal to noise ratio. Each XAS spectrum was aligned utilizing the common Mn or Ag metal reference, merged, deglitched, and normalized using Athena. The standard AUTOBK algorithm was employed to limit background contributions below Rbkg = 1.0 Å. The Mn K-edge spectra were fit using k, k^2 and k^3 k-weightings simultaneously with a k-range of 2.0–13.5 $Å^{-1}$ utilizing a Hanning window with dk = 1. An R-range of 1.0–4.3 Å was used for all Mn K-edge EXAFS fits. The Ag K-edge was similarly fit in k, k^2 and k^3 k-weightings, but a k-range of 2.0–10.0 $Å^{-1}$ was employed due to poor signal to noise ratio at high k. An R-range of 1.0–3.7 Å was used to fully encompass the 1^{st} and 2^{nd} shell peaks in each spectra. The Mn K-edge spectra were modeled using structural models based on the $I4/m$ $Ag_{1.8}Mn_8O_{16}$ crystal structure generated by FEFF6. Likewise, the Ag K-edge spectra were modeled using a mixture of $Ag_{1.8}Mn_8O_{16}$ and $Fm\bar{3}m$ Ag metal crystal structures. The determination of which phases to include in the model was dictated by the physical/statistical significant of the fitted parameters of the specific phase. If a phase resulted in statistically insignificant or physically impossible parameters, it was excluded from the overall model. To accurately track the relative amplitudes of each phase, the S_0^2 parameter, which accounts for intrinsic losses in the electron propagation and scattering process that governs XAS, was fit to either the Mn or Ag metal standard and applied to all experimental fits.

4.2.3 Electrochemistry

CR 2320 coin cell batteries were used to probe the electrochemical performance of silver hollandite samples with the same silver content and different crystallite sizes. Composite electrodes were prepared by mixing silver hollandite with conductive carbon and PVDF binder for a composition of 85% active material, 5% Super P conductive carbon black, 5% graphite, and 5% binder and coating onto an aluminum foil substrate. The coatings were dried under vacuum for 12 hours and, to ensure intimate contact of the electrode material with the aluminum current collector, pressed using a hydraulic press to afford a thin film with a thickness $\sim$2 μm. Electrodes were cut into circular discs, 0.5 inches or 1.27 cm in diameter,

with a single electrode containing an average of 2.7 mg active material. Cells were fabricated with lithium metal anodes and 1 M $LiPF_6$ in 30/70 (v/v) ethylene carbonate/dimethyl carbonate as the electrolyte. Galvanostatic cycling, over a 50 cycle range, was performed on a Maccor Series 4000 Battery Test System in a chamber maintained at 30°C. Cycling tests were conducted using a constant applied current of 41 mA/g between 2.0–3.8 V and held at 3.8 V for 2 h after each charge. A BioLogic VSP multichannel potentiostat was used to conduct the following experiments: AC impedance measurements (by employing a 10 mV sinus amplitude and a frequency range from either 100 kHz–10 mHz or 1 MHz–1 mHz), discharge of 2-electrode cells either at a constant current (9.1 mA/g) or by applying a pulse-type current (GITT, 40 mA/g) for 90 seconds, and cyclic voltammetry of 2-electrode cells over 8 consecutive cycles. AC impedance was measured subsequent to each rest period of a 10 segment discharge experiment where cells were subjected to an applied discharge current of 9.1 mA/g for 2 h and allowed to rest for 22h before collecting impedance until the cells reached 2.0 V. Galvanostatic intermittent titration technique (GITT) type testing was performed by applying an intermittent pulse-type discharge current (40 mA/g) for 90 seconds followed by a 2 h rest period at open circuit. Cyclic voltammetry was collected at room temperature between 2.0–3.8 V at a rate of 0.05 mV/sec for 8 cycles.

4.2.4 Acknowledgment of Collaboration

The research in Chapter IV was conducted in collaboration with Jianping Huang (Stony Brook University) and Dr. Altug Poyraz, Dr. Christopher Pelliccione, Dr. Yimei Zhu and Dr. Lijun Wu (Brookhaven National Laboratory). The galvanostatic cycling and CV data was collected by Jianping and he analyzed a portion of the AC impedance data. The XPS data was obtained by Dr. Poyraz while Dr. Pelliccione collected and analyzed the XAS data. TEM imaging studies were performed by Dr. Wu at BNL.

4.3 Results and Discussion

For the first time, Chapter IV describes $Ag_xMn_8O_{16}$ ($x = 1.4$) synthesized by an aqueous, low-temperature co-precipitation technique to afford silver hollandite with distinct crystallite sizes (10 and 15 nm) and equivalent silver content (x). Keeping the silver content (x) in $Ag_{1.4}Mn_8O_{16}$ constant allows for the deconvolution of electrochemical effects related to crystallite size versus those related to silver content and has not been reported until now.

4.3.1 Structural and Elemental Composition

Powder X-ray diffraction (XRD) in **Figure 4.1** indicates that $Ag_{1.4}Mn_6O_{18}$, with equivalent values of x, maintain similar crystalline structures that are consistent with an $Ag_{1.8}Mn_8O_{16}$ reference pattern[53] and contain no crystalline impurities.

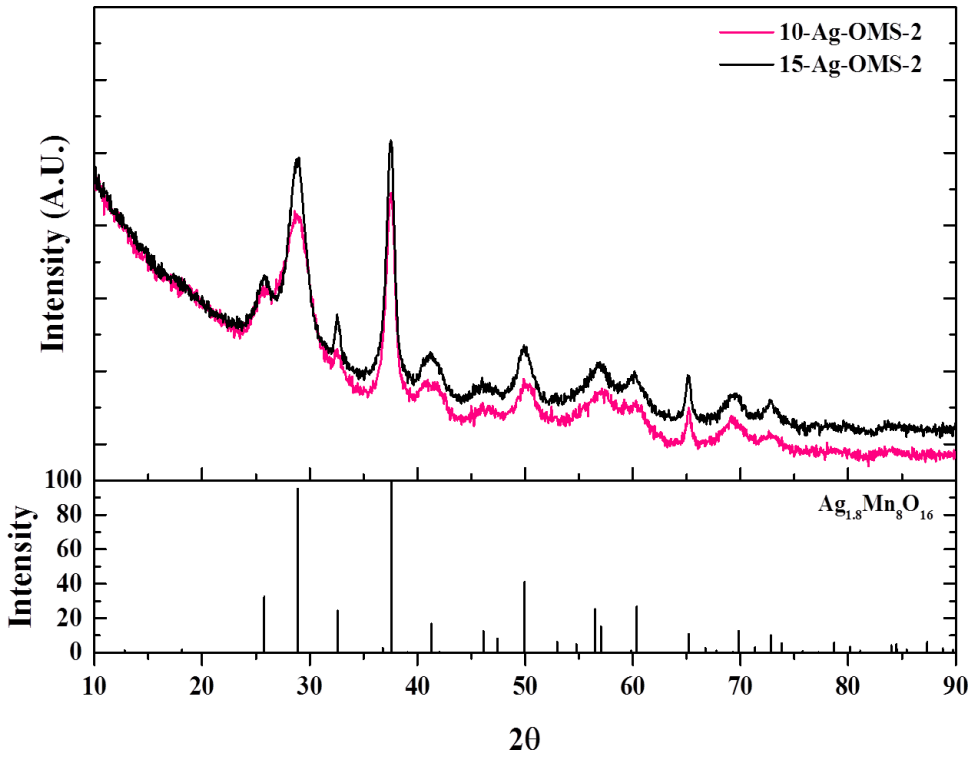

Figure 4.1. Powder X-ray diffraction (XRD) of 10-Ag-OMS-2 ($Ag_{1.38}Mn_8O_{16}$, pink) and 15-Ag-OMS-2 ($Ag_{1.35}Mn_8O_{16}$, black) with reference pattern $Ag_{1.8}Mn_8O_{16}$ (ICSD 60155)

Intensities of $Ag_{1.38}Mn_8O_{16}$ decrease compared to $Ag_{1.35}Mn_8O_{16}$, resulting in a broadening of peaks with decreased intensities in the diffraction pattern and crystallite sizes were

calculated to be 10 and 15 nm, respectively. For simplicity, the low crystallite sample will be denoted 10-Ag-OMS-2 while the high crystallite samples will appear as 15-Ag-OMS-2 in this chapter. The silver and manganese content of 10-Ag-OMS-2 and 15-Ag-OMS-2 samples were determined though inductively coupled plasma-optical emission spectroscopy (ICP-OES). Silver content of 15-Ag-OMS-2 and 10-Ag-OMS-2, as a function of crystallite size, is plotted in **Figure 4.2** and compared to a typical series of $Ag_xMn_6O_{18}$ prepared by the same technique.

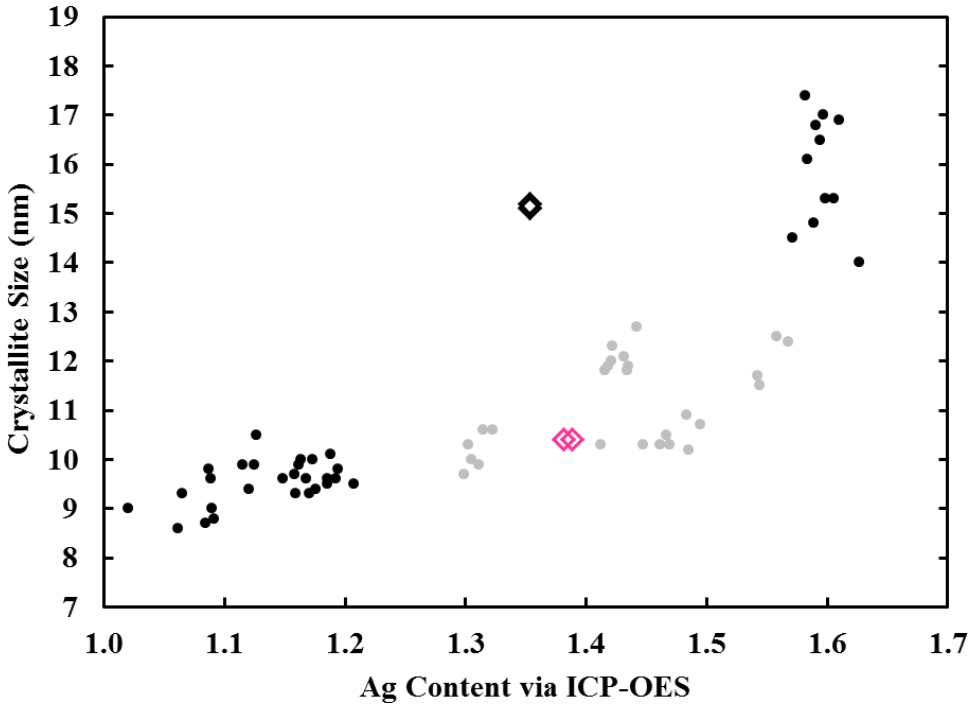

Figure 4.2. Silver content of 15-Ag-OMS-2 (black diamonds – high crystallite size, $Ag_{1.35}Mn_8O_{16}$) and 10-Ag-OMS-2 (pink diamonds – low crystallite size, $Ag_{1.38}Mn_8O_{16}$) determined via ICP-OES as a function of crystallite size compared to a typical series of $Ag_xMn_6O_{18}$ in which black circles correspond to high silver, large crystallite and low silver, small crystallite size samples while gray circles denote intermediate silver contents and crystallite sizes

Elemental analysis via ICP-OES confirms analogous silver contents (x) of 1.35 for 15-Ag-OMS-2 and 1.38 for 10-Ag-OMS-2 which is an intermediate silver content within a typical series of silver hollandite synthesized by co-precipitation (**Figure 4.2**). The crystallite size of 15-Ag-OMS-2 (15 nm) is most similar to the high silver, large crystallite material while the size of 10-Ag-OMS-2 (10 nm) resembles low silver, small crystallite size $Ag_xMn_6O_{18}$

investigated in Chapter III.[110] The surface area of same silver content, different crystallite size silver hollandite nanorods was measured by nitrogen adsorption using the BET method. The low crystallite size material, 10-Ag-OMS-2, exhibited a surface area of 107 m^2/g which is nearly two times the surface area of the higher crystallite size material, 15-Ag-OMS-2 (48 m^2/g).

4.3.2 Electron Imaging

Figures 4.3 a and **d** show transmission electron microscopy (TEM) images of $Ag_{1.4}Mn_8O_{16}$ and demonstrates that the degree of bundling of the smaller crystallite size (10-Ag-OMS-2) nanorods exceeds that of the larger size nanorods (15-Ag-OMS-2). The high degree of bundling facilitates more intimate connection of the 10-Ag-OMS-2 material and the enhanced interparticle contact can provide greater electrical contact, especially in terms of electrode fabrication, creating the opportunity for improved electrochemical performance. Selected area diffraction (**Figures 4.3 b**, **c**, **e**, and **f**) indicates a preferred orientation relationship among the 10-Ag-OMS-2 nanorods when they are bundled together. The ordered interface within the 10-Ag-OMS-2 material may play a positive role in the lateral *ab* diffusion of lithium ions between hollandite nanorods.

EELS analysis in **Figure 4.4**, with survery spectra shown in **Figure A6**, indicates that the composition of 10-Ag-OMS-2 and 15-Ag-OMS-2 nanorods in the connected area or nanorod interface is quite similar to that in the interior of the nanorods although the Mn valence is slightly lower at the interface. The EELS data implies that the interconnected or bundled 10-Ag-OMS-2 and 15-Ag-OMS-2 nanorods exhibit similar Ag concentration, Mn valence, and oxygen vacancies. However, examination of an isolated 10-Ag-OMS-2 nanorod (**Figure 4.3 d**) *versus* bundled 10-Ag-OMS-2 nanorods (**Figure 4.3 b**) demonstrate greater oxygen vacancies on the surface and a significantly lower Mn valence where the nanorods are exposed to the vacuum.

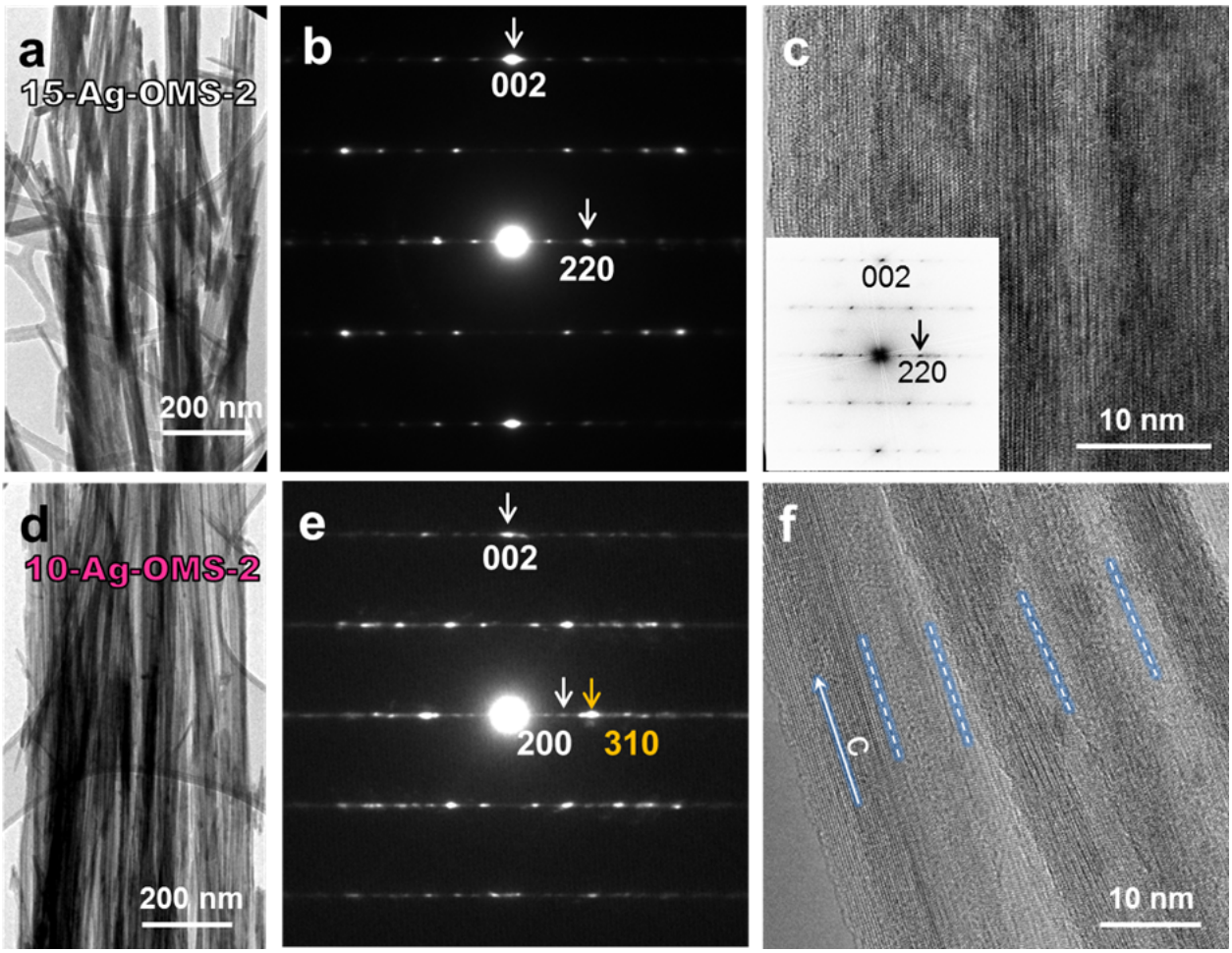

Figure 4.3. (a,d) TEM images, (b,e) electron diffraction patterns (EDPs) and (c,f) HRTEM images of (a-c) 15-Ag-OMS-2 and (d-f) 10-Ag-OMS-2

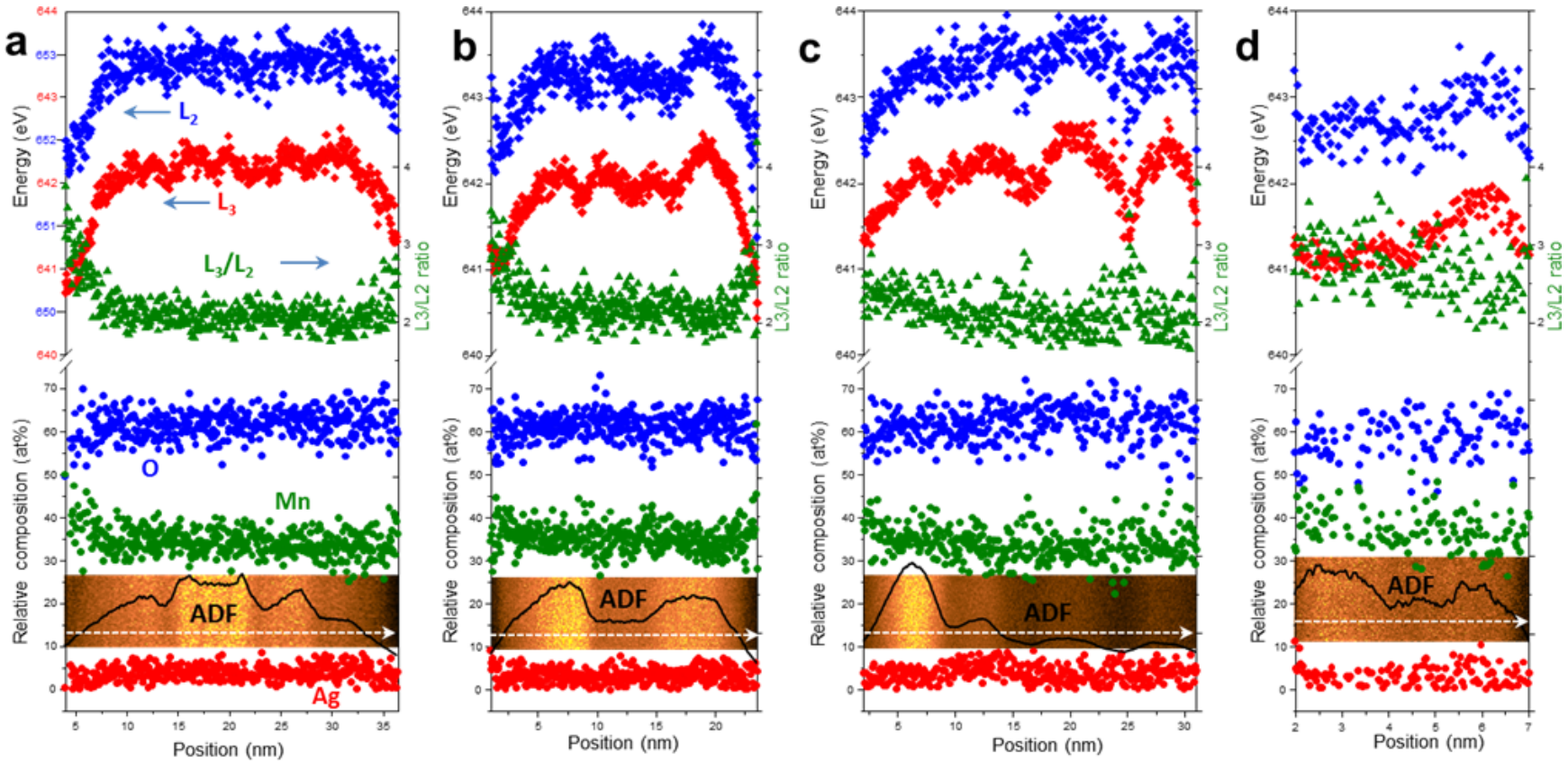

Figure 4.4. EELS analysis showing Ag (red circles), Mn (green circles), and O (blue circles) composition in $Ag_{1.4}Mn_8O_{16}$ nanorods: (a,c) 15-Ag-OMS-2 and (b,d) 10-Ag-OMS-2. The energy of Mn L_3 (red diamonds), Mn L_2 (blue diamonds), and their intensity ratio L_3/L_2 (green triangles) are also included. Partial STEM-HAADF survey images (the whole survey images are shown in **Figure A6**) and simultaneously acquired STEM-HAADF intensity signal (black line) during EELS acquisition is embedded at the bottom of each figure where the dashed white arrow indicates the scan line direction

4.3.3 Determination of Water and Oxygen Content

Thermogravimetric analysis (TGA) was used to monitor the thermal decomposition and water and oxygen content of 10-Ag-OMS-2 and 15-Ag-OMS-2 $Ag_{1.4}Mn_8O_{16}$ nanorods. The TGA experimental details were adapted from previous thermal investigation of hollandite-type structures.[55,110,134–136] Below 360°C, dehydration of absorbed surface water on hollandite nanorods and water within the tunneled MnO_6 motif is observed (**Figure 4.5**). An average water content of 0.8 and 1.1 H_2O per $Ag_xMn_6O_{18}$ formula unit ($Ag_xMn_6O_{18}{\cdot}nH_2O$) was calculated for 15-Ag-OMS-2 and 10-Ag-OMS-2, respectively.

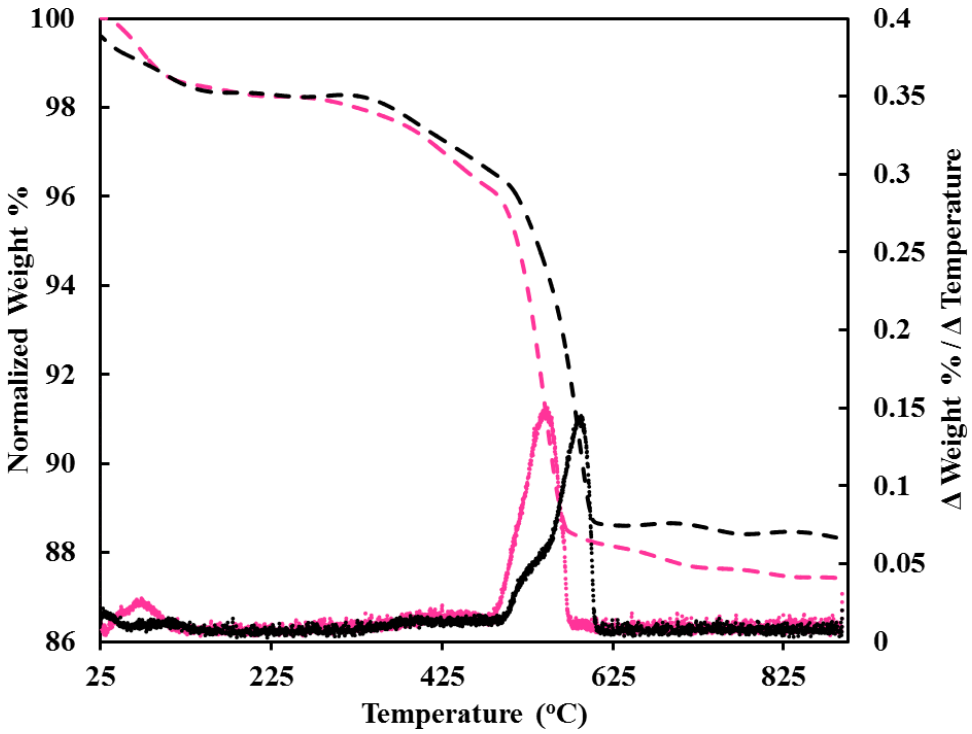

Figure 4.5. TGA and first derivative of weight as a function of temperature for $Ag_{1.35}Mn_8O_{16}$ (15-Ag-OMS-2, black) and $Ag_{1.38}Mn_8O_{16}$ (10-Ag-OMS-2, pink)

Under an atmosphere of nitrogen, the decomposition of $Ag_xMn_6O_{18}$ occurs between 360-750°C. The transition metal oxide undergoes a series of weight-loss events which begins with the collapse of the MnO_6 tunneled structure, subsequent formation of silver metal and

Mn_2O_3, and decomposition of Mn_2O_3 into Mn_3O_4 (**Equation 4.1**).[134,135]

$$\begin{aligned} Ag_xMn_8O_{16} \cdot nH_2O &\longrightarrow Ag_xMn_8O_{16} \\ \longrightarrow xAg + 4Mn_2O_3 + 2O_2 &\longrightarrow xAg + \frac{8}{3}Mn_3O_4 + \frac{4}{6}O_2 \end{aligned} \tag{4.1}$$

Small crystallite size 10-Ag-OMS-2 decomposes at lower temperatures compared to the high crystallite size 15-Ag-OMS-2, thus demonstrating that the nanocrystalline material with decreased crystallite size has a lower intrinsic thermal stability. XRD analysis of samples after high-temperature TGA confirms the exclusive presence of Mn_3O_4 and silver metal (Ag^0), consistent with decomposition process illustrated in **Equation 4.1**.[110] The significant weight loss event (10% of initial mass) during the decomposition of $Ag_{1.4}Mn_6O_{18}$ can be directly attributed to the evolution of O_2. The oxygen content of 10-Ag-OMS-2 and 15-Ag-OMS-2 can systematically assessed from the TGA weight-loss profile by using the first derivative, as a function of temperature, to precisely determine the region of oxygen loss for the calculation (**Figure 4.5**). 10-Ag-OMS-2 and 15-Ag-OMS-2 demonstrate oxygen contents of approximately 14.9 which indicates both the presence of oxygen vacancies compared to conventional silver hollandite, $Ag_{1.8}Mn_8O_{16}$, and that oxygen content depends on silver content of $Ag_xMn_6O_y$ (where x = silver content, y = oxygen content) rather than crystallite size.

4.3.4 Electronic Structure Analysis

Full XPS survey spectra (0–1300 eV) of $Ag_{1.4}Mn_8O_{16}$, 10-Ag-OMS-2 and 15-Ag-OMS-2, are shown in **Figure A7**. The XPS core-level Ag3d (360-385 eV), Mn2p (630-665 eV), Mn3s (75-100 eV), and O1s (520-545 eV) spectra of 10-Ag-OMS-2 and 15-Ag-OMS-2 are compared in **Figure 4.6**. The Ag3d core-level spectrum (**Figure 4.6 a**) illustrates $3d_{5/2}$ and $3d_{3/2}$ peaks at binding energy (BE) values of 367.9 and 373.8–373.9 eV for 10-Ag-OMS-2 and 15-Ag-OMS-2 materials. The $3d_{5/2}$ and $3d_{3/2}$ peaks are consistent with previous XPS analysis of silver hollandite nanofibers which demonstrate BEs of 367.8 and 373.8 eV and are representative of silver ions in the +1 oxidation state.[135] In the Mn2p region of the XPS

spectra (**Figure 4.6 b**), $2p_{3/2}$ and $2p_{1/2}$ peaks were observed at 642.6–642.7 and 654.1 eV, respectively, for 10 and 15 nm $Ag_{1.4}Mn_8O_{16}$ (**Table 4.1**). The Mn2*p* BEs also correspond to previously reported XPS data of silver hollandite (642.2 and 653.9 eV) and can be attributed to a mixture of Mn^{4+} and Mn^{3+} oxidation states.[135,140–142]

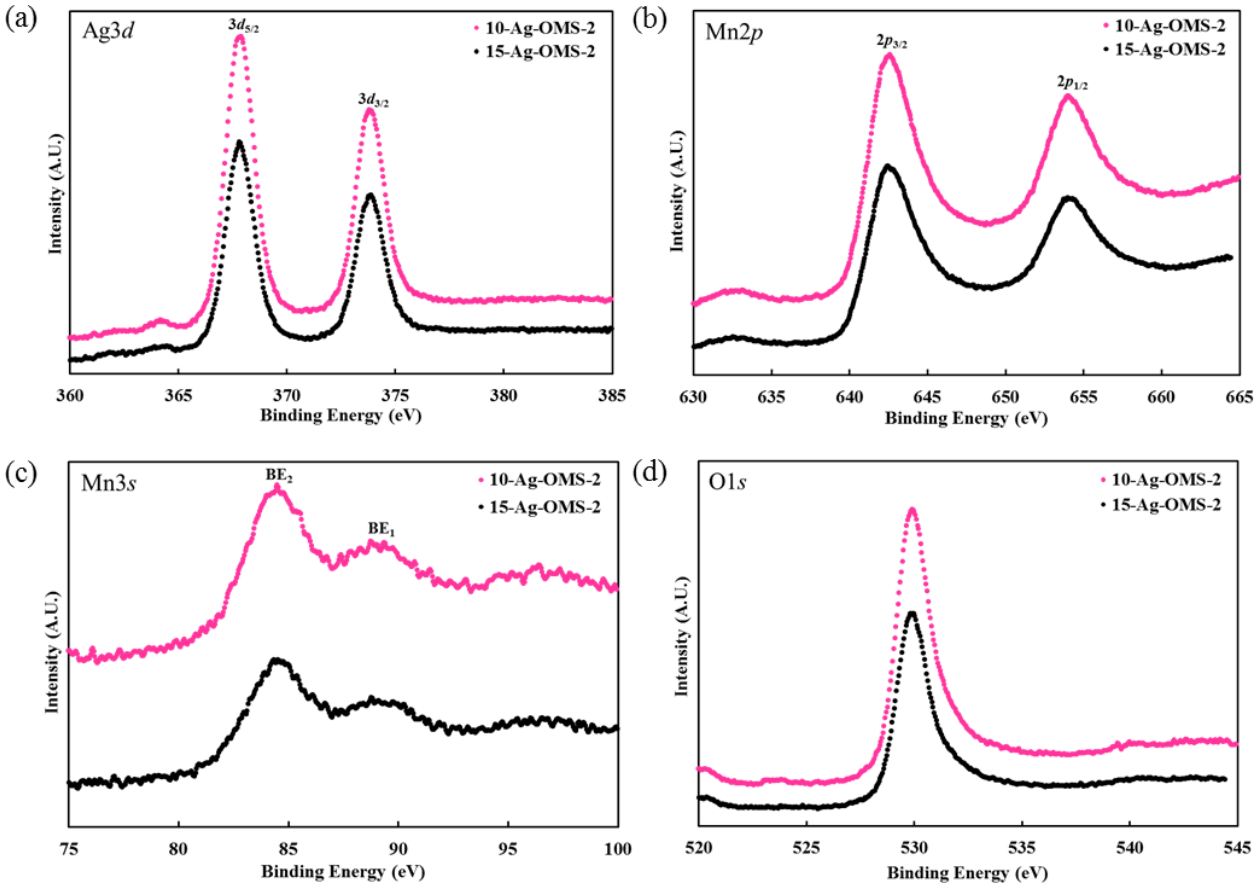

Figure 4.6. XPS (a) Ag3*d*, (b) Mn2*p*, (c) Mn3*s*, and (d) O1*s* core-level spectra for 10-Ag-OMS-2 and 15-Ag-OMS-2

To accurately identify the average oxidation state (AOS) of manganese of nanocrystalline silver hollandite nanorods, the Mn3*s* core-level region was analyzed and the degree of peak splitting was determined (**Figure 4.6 c**). Utilization of peak splitting values in the Mn3*s* XPS spectrum was introduced by Galakhov et al. as a method to establish the AOS of manganese.[143] The literature has demonstrated a linear correlation of the AOS of manganese with respect to the degree of peak splitting or energy difference (ΔE_{Mn3s}) between the main BE_2 peak and remaining BE_1 satellite peaks in the Mn3*s* region.[141–144] The expression for

linear correlation of AOS to Mn3s peak splitting is shown in **Equation 4.2**.[143–145]

$$Average\ Oxidation\ State\ (AOS) = 8.956 - 1.124(\Delta E_{Mn3s}) \tag{4.2}$$

Analysis of the Mn3s core-level region determines peak splitting values of 4.55 for 10 Ag-OMS-2 and 4.77 for 15-Ag-OMS-2 (**Table 4.1**). The AOS, as a result of the energy difference between Mn3s peaks, is calculated to be 3.83 and 3.78 for 10-Ag-OMS-2 and 15-Ag-OMS-2, respectively. XPS illustrates no significant difference between the average oxidation state of manganese in 10 and 15 nm $Ag_{1.4}Mn_8O_{16}$. The XPS results agree with those from TGA which provided equivalent oxygen contents for 10-Ag-OMS-2 and 15-Ag-OMS-2.

The last region of interest in the XPS spectra, the O1s region, is shown in **Figure 4.6 d** and can be deconvoluted into 3 separate peaks, each indicative of a different oxygen species. These oxygen species include oxygen bound to manganese (Mn-O-Mn), oxygen in the form of a surface hydroxyl attached to manganese (Mn-O-H), and oxygen as surface absorbed water (H-O-H).[140,141,146] The O1s regions of 10-Ag-OMS-2 and 15-Ag-OMS-2 were fit with 3 separate peaks (**Figure 4.7**) and the binding energies and relatively peak areas for 3 separate fitting regions (Mn-O-Mn, Mn-O-H, and H-O-H) are summarized in **Table 4.1**.

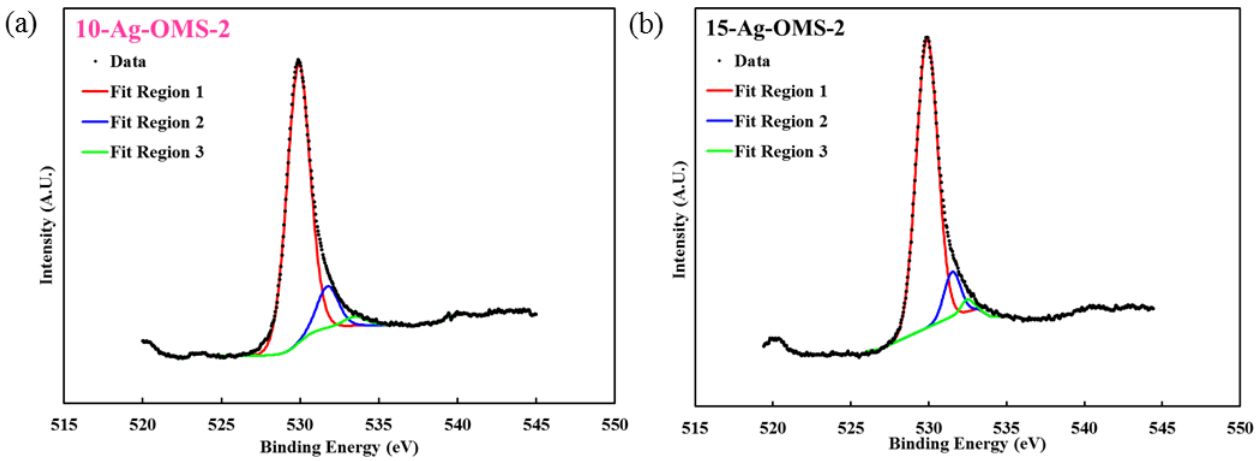

Figure 4.7. XPS O1s core-level spectra with three distinct fitting regions for (a) 10-Ag-OMS-2 and (b) 15-Ag-OMS-2

Table 4.1. Manganese and oxygen XPS data for 10-Ag-OMS-2 and 15-Ag-OMS-2

	Mn2p (eV)		**Mn3s (eV)**			**O1s (eV)**			
Sample	**$2p_{1/2}$**	**$2p_{3/2}$**	**BE_1**	**BE_2**	**ΔE[a]**	**State**	**BE (eV)**	**Area (%)**	**Average Oxidation State[b]**
10-Ag-OMS-2	642.6	654.1	89.051	84.502	4.55	Mn-O-Mn	529.90	85.5	3.83
						Mn-O-H	531.75	11.8	
						H-O-H	533.50	2.7	
15-Ag-OMS-2	642.7	654.1	89.179	84.579	4.60	Mn-O-Mn	529.89	87.6	3.78
						Mn-O-H	531.52	10.3	
						H-O-H	532.47	2.1	

[a] Δ E = BE_1 - BE_2

[b] Average oxidation state (AOS) = 8.956 - 1.126(ΔE_{Mn3s})

The relative peak areas illustrate that a majority of the oxygen in silver hollandite exists as lattice oxygen bound to manganese (85.5–87.9%), followed by surface adsorbed hydroxyls (10.3–11.8%) and water (2.1–2.7%). To that end, the quantity of Mn-O-Mn and Mn-O-H can be considered to be equivalent since the difference in the samples falls within the level of uncertainty for the fitting results. The dried $Ag_{1.4}Mn_8O_{16}$ materials were kept under a dry, inert atmosphere prior to measurements, however, the materials act as molecular sieves and absorb ambient water upon contact with the atmosphere and the difference in H-O-H (surface absorbed water) is not unexpected. As a whole, the water quantity remains low, suggesting that only a small amount of water was absorbed during sample preparation. In essence, XPS data illustrates that 10-Ag-OMS-2 and 15-Ag-OMS-2 display comparable manganese oxidation states and oxygen environments.

4.4 Electrochemical Evaluation

4.4.1 Cycling

The impact that crystallite size and nanorod bundling has on the electrochemical behavior of 10 and 15 nm $Ag_{1.4}Mn_8O_{16}$ was initially examined by galvanostatic cycling tests which were performed with a constant current of 41 mA/g between 2.0–3.8 V. Galvanostatic cycling of $Li/Ag_{1.4}Mn_8O_{16}$ electrochemical cells in **Figure 4.8**, over 50 cycles, reveals enhanced performance of the small crystallite size, high surface area material (10-Ag-OMS-2) over the large crystallite size material (15-Ag-OMS-2). During the first cycle, 10-Ag-OMS-2 delivers almost 15X higher discharge capacity than 15-Ag-OMS-2 (147 *vs.* 10.5 mAh/g). After 50 cycles, 10-Ag-OMS retains a capacity 7X greater than 15-Ag-OMS-2 (50 *vs.* 7 mAh/g). Discrepancies in the voltage profiles of high and low crystallite size silver hollandite, as a function of capacity, were also observed (**Figure 4.9**).

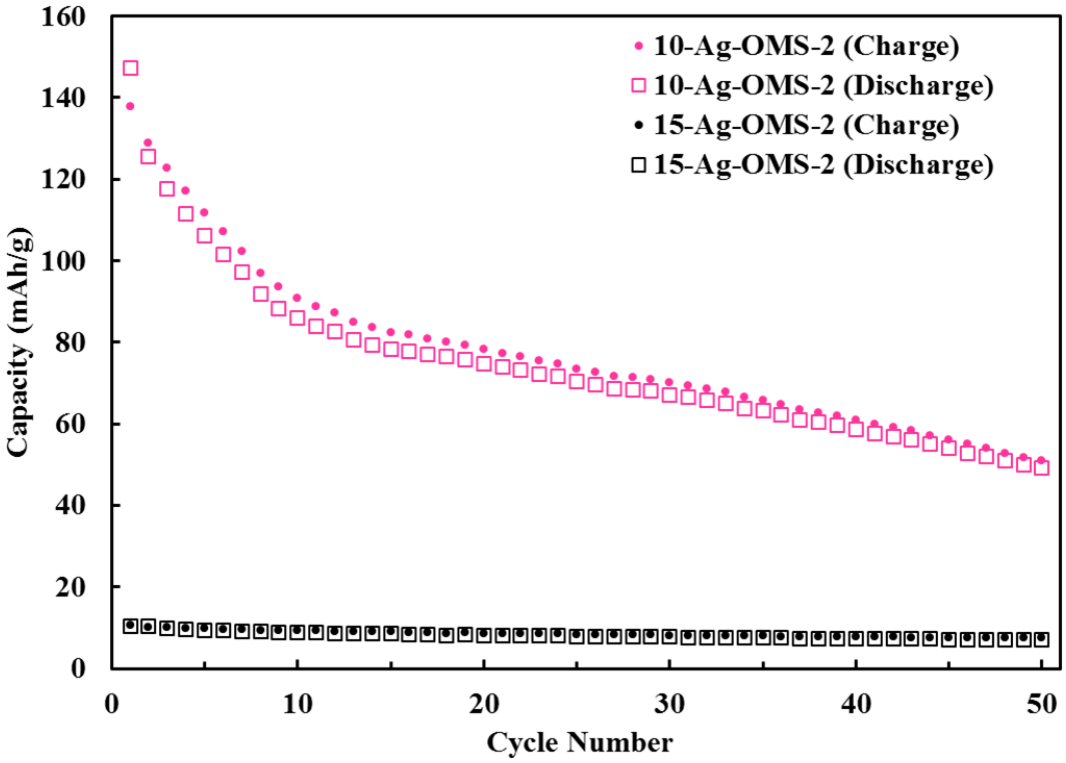

Figure 4.8. Galvanostatic cycling of $Li/Ag_{1.4}Mn_8O_{16}$ cells, 10-Ag-OMS-2 (pink) and 15-Ag-OMS-2 (black), with discharge (squares) and charge (circles) capacity plotted as a function of cycle number

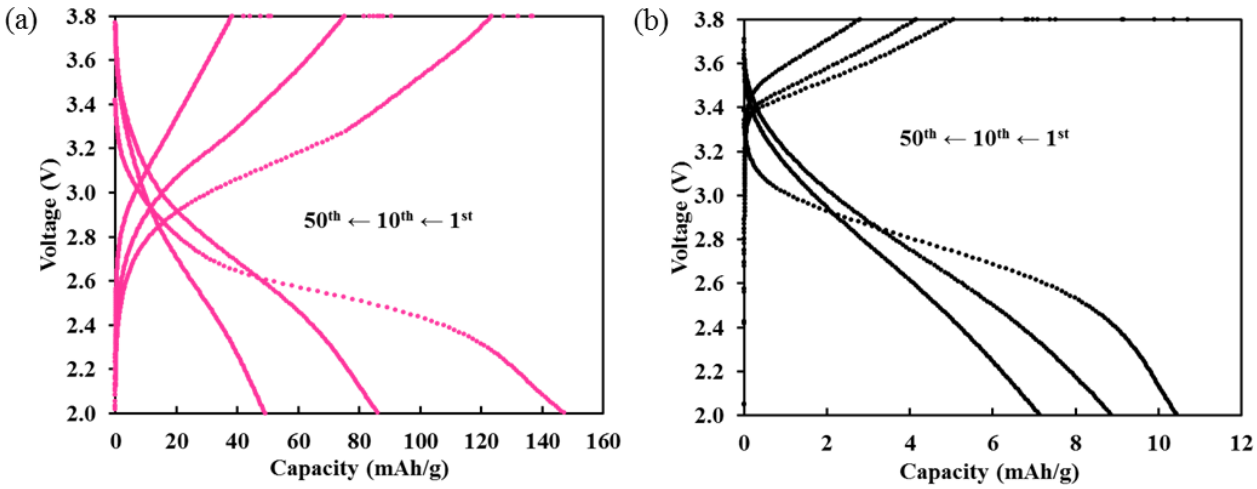

Figure 4.9. Voltage profiles as a function of capacity for cycles 1, 10, and 50: (a) 10-Ag-OMS-2 and (b) 15-Ag-OMS-2

During the first discharge, the onset of a voltage plateau is observed at approximately 3.0 V for 15-Ag-OMS-2 while the transition is occurs at a lower voltage of 2.7 V for 10-Ag-OMS-2. By cycle 10, however, the voltage plateau is not evident in either $Ag_{1.4}Mn_8O_{16}$ sample. As the silver hollandite materials are charged, a sharp increase in the voltage is observed for 15-Ag-OMS-2 whereas a more gradual increase in voltage is observed for 10-Ag-OMS-2. Increased polarization of the high crystallite size material, 15-Ag-OMS-2, during charge compared to low crystallite size silver hollandite, 10-Ag-OMS-2, is likely a contributing factor to the low capacity and decreased performance of the high crystallite size material.

To further explore the effect of both crystallite size and nanorod bundling on the electrochemical performance of $Ag_{1.4}Mn_8O_{16}$, 15-Ag-OMS-2 was subjected to wet grinding in a micronising mill. The intention of milling 15-Ag-OMS-2 was to decrease the crystallite size which was anticipated to provide more intimate contact of the nanorods and possibly lead to the bundling phenomenon observed with 10-Ag-OMS-2 nanorods. The XRD in **Figure A8** illustrates that the structure of the milled 15-Ag-OMS-2 material, labeled 15-M-Ag-OMS-2, remained intact and the calculated crystallite size did not change. Although the crystallite size, calculated from the (2 1 1) peak at ~37.5° which is a lattice plane in the *ab*-direction that bisects the hollandite tunnel, did not change, decreased intensities of peaks relating to the *c*-direction are observed in **Figure A8**. Peaks with decreased intensity that correspond to lattice planes which span the *c*-direction of the $Ag_{1.4}Mn_8O_{16}$ nanorods include the (2 2 0) reflection at 25.8°, (1 3 0)/(3 1 0) at 28.9°, and (2 4 0)/(4 2 0) at 41.4°. The diffraction data suggests that milling the 15-Ag-OMS-2 sample decreased the length of the nanorods, which is typically on the order of a few microns, but did not influence the overall width of the nanorods. Notably, the surface area of $Ag_{1.4}Mn_8O_{16}$ nanorods increased from 48 m^2/g (15-Ag-OMS-2) to 63 m^2/g (15-M-Ag-OMS-2, milled). Additionally, TGA illustrated no significant change after milling with similar thermal stabilities of dried 15-Ag-OMS-2 and 15 M-Ag-OMS-2 and oxygen contents of 14.9 and 15.0, respectively (**Figure A9**).

Electrochemical investigation of 15-M-Ag-OMS-2 by galvanostatic cycling shows that the capacity remains low, stabilizing at 3 mAh/g after 50 cycles (**Figure 4.10**). Further, the milled material displays a discharge profile which increases in the first 10 cycles and stabilizes while the discharge capacity non-milled 15-Ag-OMS-2 continually fades over 50 cycles.

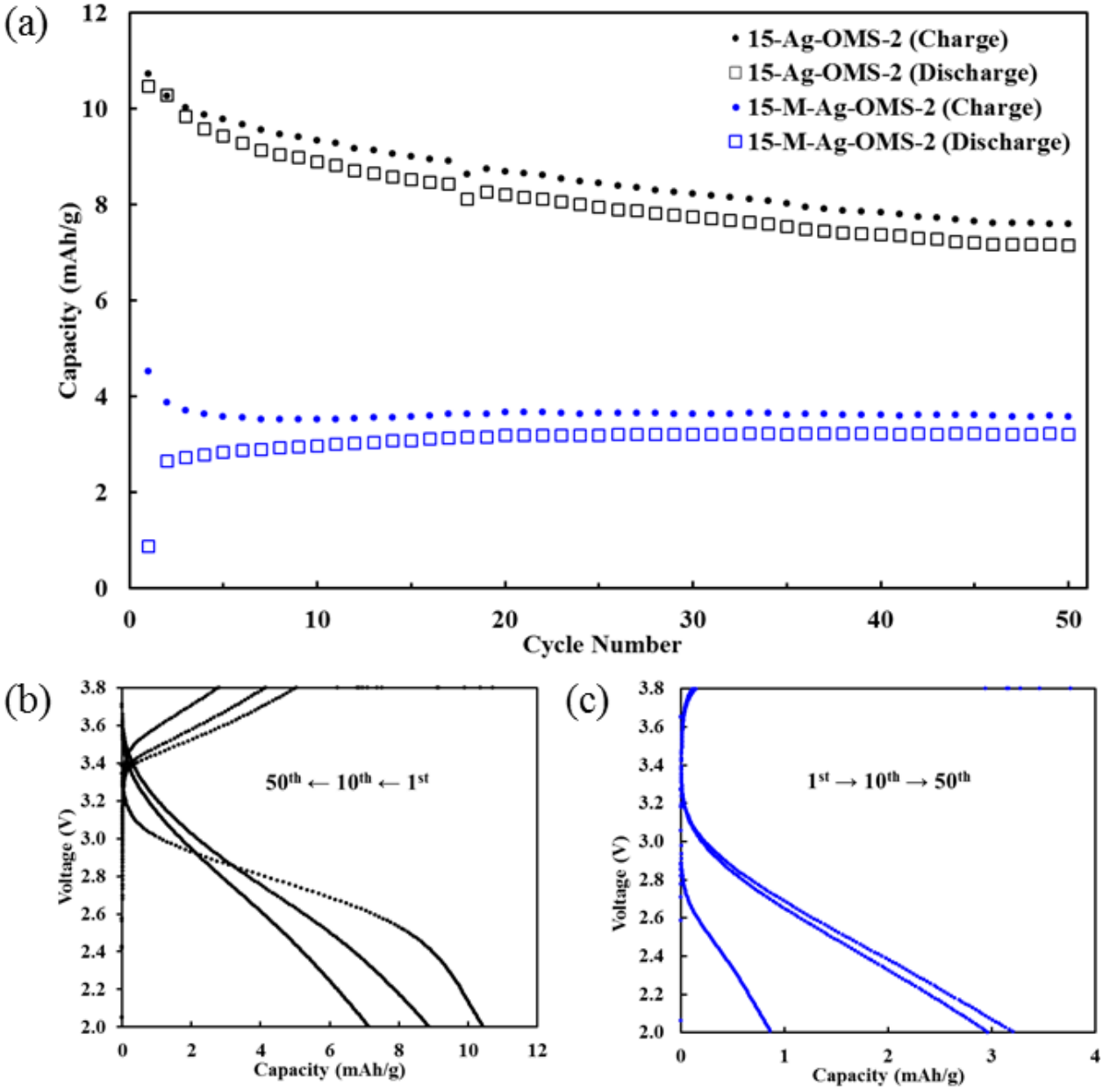

Figure 4.10. (a) Galvanostatic cycling data of Li/$Ag_{1.4}Mn_8O_{16}$ cells, 15-Ag-OMS-2 and 15-M-Ag-OMS-2, with discharge (squares) and charge (circles) capacity plotted as a function of cycle number. Voltage profiles as a function of capacity for cycles 1, 10, and 50: (b) 15-Ag-OMS-2 and (c) 15-M-Ag-OMS-2

Notably, the voltage profile of 15-M-Ag-OMS-2 does not display a voltage plateau and significant polarization is observed, especially during charge (**Figure 4.10 b** and **c**). This study suggests that the bundling and intimate interparticle contact of small crystallite size $Ag_{1.4}Mn_8O_{16}$ nanorods (10-Ag-OMS-2), rather than crystallite size alone, may play a predominate role in the electrochemistry.

In addition to galvanostatic cycling, cyclic voltammetry measurements display unique redox properties of 10-Ag-OMS-2 and 15-Ag-OMS-2 (**Figure 4.11**). Current densities of 10-Ag-OMS-2 are significantly larger than those of 15-Ag-OMS-2 and the capacities during the first reduction processes are calculated to be approximately 76 mAh/g and 13 mAh/g for 10-Ag-OMS-2 and 15-Ag-OMS-2, respectively. The capacity difference observed during cyclic voltammetry is consistent with the results of galvanostatic cycling tests.

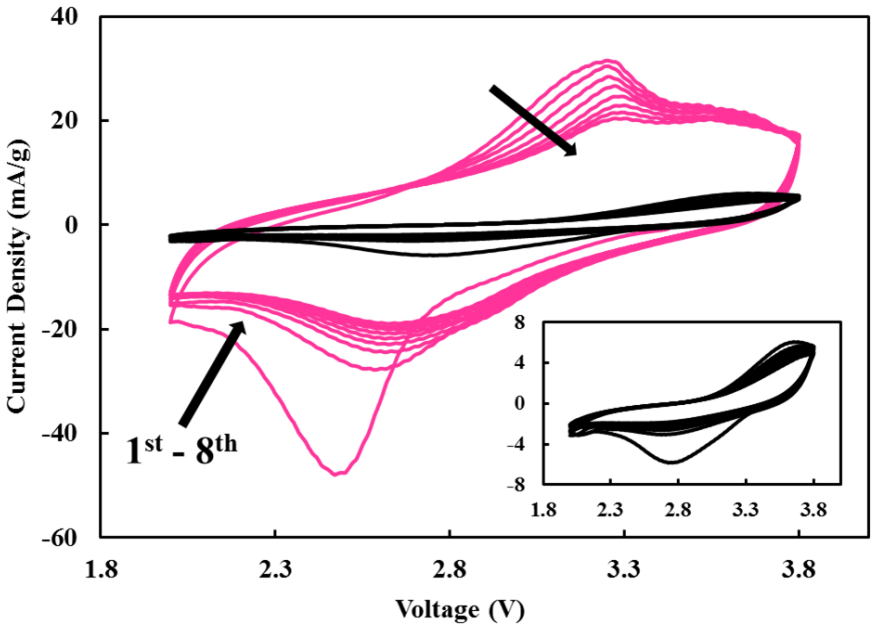

Figure 4.11. CV of 10-Ag-OMS-2 (pink) and 15-Ag-OMS-2 (black) at a rate of 0.5 mV/sec for 8 cycles with 15-Ag-OMS-2, inset

After the first cycle, decreasing current densities are observed in the CV of both 10-Ag-OMS-2 and 15-Ag-OMS-2. Cathodic and anodic peaks in the first cycle occur at 2.50 V and 3.22 V for 10-Ag-OMS-2, respectively, whereas 15-Ag-OMS-2 shows a higher cathodic peak position at 2.75 V and an anodic peak position at 3.70 V. Peak separation of 10-Ag-OMS-2

is 0.7 V, which is smaller than the 1.0 V peak separation of 15-Ag-OMS-2, indicating the increased polarization of large crystallite size material.

Increased electrochemical performance of nanostructure materials in highly bundled arrays, similar to 10-Ag-OMS-2 and 15-Ag-OMS-2, has been observed previously. Electrode materials for lithium batteries based on nanostructured CuO[147] and Mn_2OBO_3[148] display similar bundling behavior. In 2012, Wang et. al prepared CuO particles using a precipitation technique and CuO was observed to assemble into structures with bundle-like morphologies. When utilized as an anode in lithium based batteries, the bundle-like CuO electrode material exhibited increased stability, high capacity, and excellent rate performance. The CuO architecture was then "disassembled" via a grinding procedure and the electrode experienced lower capacities and increased capacity fade over 50 cycles suggesting that the enhanced electrochemical performance stems from the bundled assembly of CuO nanoparticles which allows for increased contact area.[147] Further, Li et. al prepared small and large Mn_2OBO_3 nanorod bundles via a hydrothermal reaction. Smaller Mn_2OBO_3 nanorods displayed lower resistance, higher capacity, and increased stability compared to larger Mn_2OBO_3 nanorod bundles due to increased surface area and shorter lengths for Li^+ diffusion.[148]

4.4.2 Impedance as a Function of Depth of Discharge

PEIS (potentiostatic electrochemical impedance spectroscopy) or AC impedance was performed on intact coin cells containing 10-Ag-OMS-2 or 15-Ag-OMS-2 cathodes. 10-Ag-OMS-2 and 15 Ag-OMS-2 demonstrate similar Nyquist plots before discharge (**Figure 4.12**) with markedly different semicircle diameters. An equivalent circuit model (**Figure 4.12**, inset) was utilized to fit the impedance data prior to discharge. The fitted charge transfer resistance of 10-Ag-OMS-2 was approximately 50 Ω while that of 15-Ag-OMS-2 was about 159 Ω, indicating a faster charge transfer process at the interface of the small crystallite size, higher surface area material and the electrolyte.

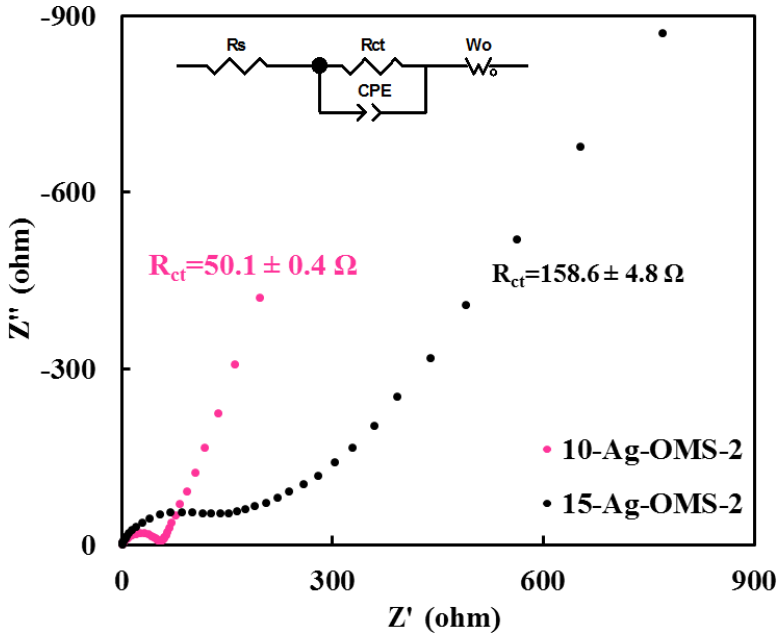

Figure 4.12. Nyquist plots of 10-Ag-OMS-2 (pink) and 15-Ag-OMS-2 (black) before discharge with the charge transfer resistance defined as R_{ct}. Equivalent circuit model used to fit the AC impedance data is inset

In an effort to investigate the evolution of AC impedance during discharge, cells containing 10-Ag-OMS-2 and 15-Ag-OMS-2 electrodes were discharged for 2 h at a rate of 9.1 mA/g and allowed to rest for 22 h before collecting impedance measurements at open circuit voltage (**Figure 4.13**). Upon discharge to 2.0 V, 10-Ag-OMS-2 delivered a capacity of 138 mAh/g, corresponding to 4.3 electron equivalents of lithium (Li^+) inserted per $Ag_{1.38}Mn_8O_{16}$ (**Figure 4.13 b**). In contrast, the capacity of 15-Ag-OMS-2 was only 44 mAh/g (1.4 electron equivalents) demonstrating poor lithiation properties (**Figure 4.13 d**). During discharge, the Nyquist plots of 10-Ag-OMS-2 maintained similar shape while diameter of the semicircles grew larger with increasing depths of discharge (**Figure 4.13 a**). AC impedance of 10-Ag-OMS-2 establishes that the charge transfer resistance gradually increases during discharge. After the 1st discharge pulse, the Nyquist plots of 15-Ag-OMS-2 display dramatic changes with the absence of a semicircle in the high frequency regions which implies changes in the electrochemical environment at the interface of the electrode and the electrolyte (**Figure 4.13 c**).

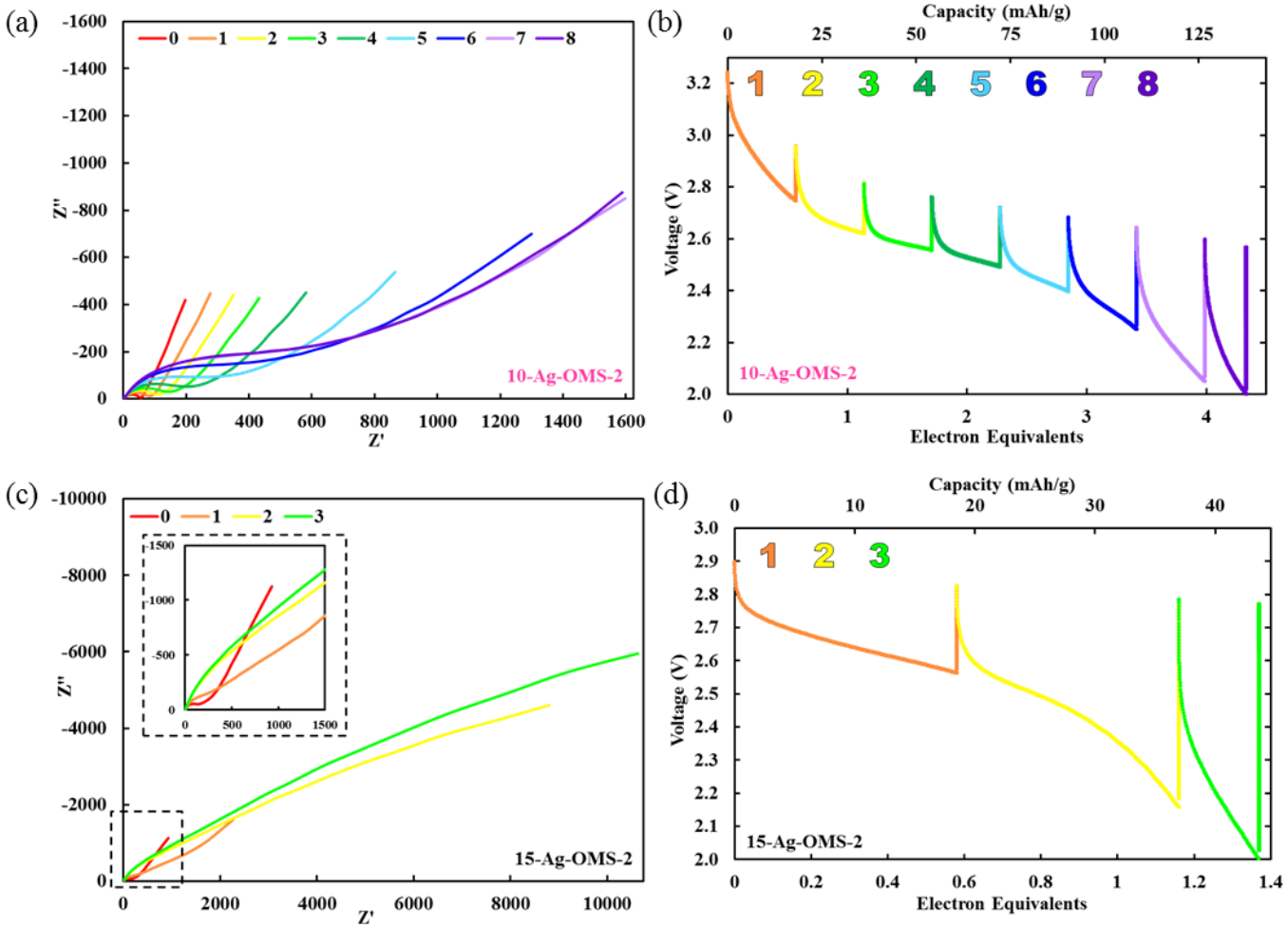

Figure 4.13. AC impedance as a function of discharge for $Li/Ag_{1.4}Mn_8O_{16}$ cells: (a) 10-Ag-OMS-2 and (c) 15-Ag-OMS-2. Pulsed-discharge profiles from GITT electrochemical testing of $Li/Ag_{1.4}Mn_8O_{16}$ cells over ≤ 8 discharge pulses: (b) 10-Ag-OMS-2 and (d) 15-Ag-OMS-2. In Nyquist plots (a,c), 0 corresponds to impedance before discharge while 1–8 indicate impedance after sequential discharge steps. In discharge profiles (b,d), 1–8 corresponds to sequential discharge steps

In addition, Warburg coefficients were calculated based on Z‘ = $\sigma\omega^{-1/2}$,[149] where Z‘ is the real part of the impedance, σ is the Warburg coefficient, and ω is the angular frequency, **Table 4.2**. Both 10 and 15 nm $Ag_{1.4}Mn_8O_{16}$ materials exhibited increasing Warburg coefficients during discharge, indicative of sluggish Li ion diffusion at high lithiation levels. Notably, 10-Ag-OMS-2 kept a comparatively low Warburg coefficient value of 230 $\Omega \cdot s^{-1/2}$ at 4.3 electron equivalents of lithiation, whereas the Warburg coefficient value of 15-Ag-OMS-2 increased approximately 12-fold from 196 to 2295 $\Omega s^{-1/2}$ after an insertion of 1.4 electron equivalents Li^+. These results suggest that the apparent differences in the electrochemical performance can primarily be attributed to Li^+ diffusion.

Table 4.2. Warburg coefficients of 10-Ag-OMS-2 and 15-Ag-OMS-2 during discharge

	Warburg Coefficients σ ($\Omega \cdot s^{-1}$)	
States of Discharge	**10-Ag-OMS-2**	**15-Ag-OMS-2**
Before Discharge	41	196
1st	55	393
2nd	64	1812
3rd	71	2295
4th	85	
5th	121	
6th	185	
7th	232	
8th	230	

4.4.3 Lithium Diffusion

To study Li^+ diffusion within 10-Ag-OMS-2 and 15-Ag-OMS-2, galvanostatic intermittent titration technique (GITT) was employed by applying a 40 mA/g discharge pulse for 90 seconds followed by a 2 h rest period at open circuit (**Figure 4.14**). When the cells were discharged to 2.0 V in the GITT tests, 10-Ag-OMS-2 achieved ~4.8 electron equivalents

transfer while 15-Ag-OMS-2 was only able to deliver 0.7 electron equivalent. The low capacity of the large crystallite size sample, 15-Ag-OMS-2, is consistent with the galvanostatic cycling and CV electrochemical measurements discussed earlier in Chapter IV.

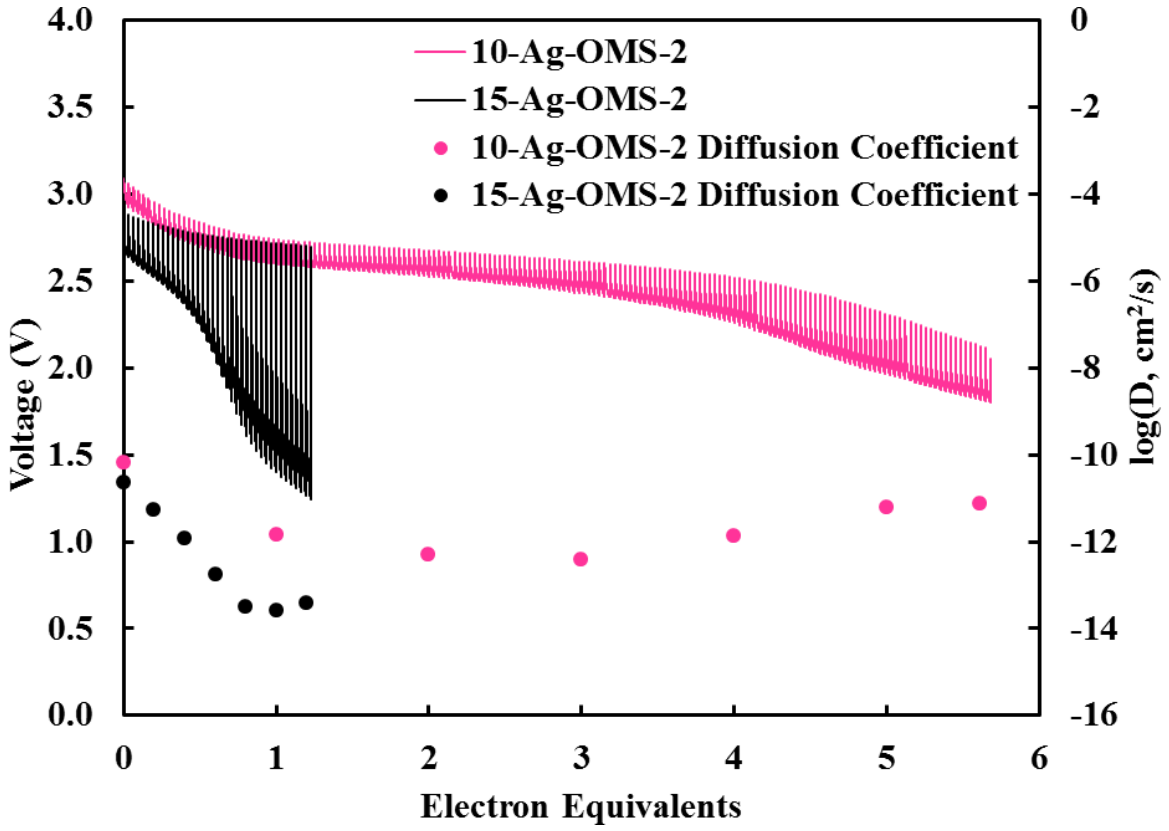

Figure 4.14. Pulsed-discharge profiles, as a function of electron equivalents, from GITT electrochemical testing of Li/$Ag_{1.4}Mn_8O_{16}$ cells containing 10-Ag-OMS-2 and 15-Ag-OMS-2

Lithium ion diffusion coefficients (D^{Li^+}) were calculated using the following equation:[150,151]

$$D_{Li^+} = \frac{4}{\pi}\left(\frac{iV_m}{ZFS}\frac{\frac{dE}{d\delta}}{\frac{dE}{d\sqrt{t}}}\right)^2 when\ t \ll \frac{L^2}{D_{Li^+}} \tag{4.3}$$

In **Equation 4.3**, L = finite diffusion length, i = applied current, V_m = molar volume of Ag-OMS-2, F = Faraday's constant, S = electrode surface area, $dE/d\delta$ = slope of the coulometric titration curve, and $dE/d\sqrt{t}$ = slope of voltage versus square root of time plot during constant current pulse. The 10 and 15 nm $Ag_{1.4}Mn_8O_{16}$ materials showed similar diffusion coefficients near 4 x 10^{-11} cm^2/s before discharge and a gradual decrease in the

diffusion coefficients as the depth of discharge increased. Nonetheless, the D_{Li^+} of 15-Ag-OMS-2 rapidly dropped to 2 x 10^{-14} cm^2/s after 1 electron equivalent of lithium ion insertion, indicating poor Li^+ diffusion in the large crystallite size material. In comparison, 10-Ag-OMS-2 displayed a small decrease of D_{Li^+} during discharge and maintained D_{Li^+} values ranging from 4 10^{-13} cm^2/s to 7 10^{-11} cm^2/s (below 5.6 electron equivalents). The inefficiency of Li^+ transport is likely a major reason leading to the low capacity of large crystallite size material. Furthermore, it has been reported that surface defects create additional diffusion pathways for Li ion,[110] thus the sluggish Li ion diffusion in 15-Ag-OMS-2 may result from the increased thickness and decreased bundling of the nanorods.

4.4.4 *Ex-Situ* Characterization of Electrochemically Cycled Electrodes

Ex-situ X-ray absorption spectroscopy (XAS) was performed on 10-Ag-OMS-2 and 15-Ag-OMS-2 electrodes to monitor structural differences at various states of lithiation in $Ag_{1.4}Mn_8O_{16}$ nanorods. **Figure 4.15** shows the k^2-weighted $|\chi(R)|$ (Fourier transform of $\chi(k)$) spectra of both the Mn and Ag K-edges of undischarged, discharged (2.0 V), and charged (3.8 V) electrodes. Visual inspection of the $|\chi(R)|$ spectra shows distinct differences between the local structural changes of 10-Ag-OMS-2 and 15-Ag-OMS-2. The small crystallite size material, 10-Ag-OMS-2, shows large changes in the Mn K-edge 2^{nd} shell peaks between $\sim$ 2 and 3.5 Å in **Figure 4.15** when discharged to 2.0 V (3 molar electron equivalents), suggesting large changes in the Mn–Mn coordination environment associated with Li^+ insertion. Large crystallite size $Ag_{1.4}Mn_8O_{16}$ (15-Ag-OMS-2), however, does not exhibit any structural changes upon lithiation or delithiation, suggesting only subtle structural variations from the undischarged crystal structure are occurring. A similar trend is observed in the Ag K-edge spectra, with 10-Ag-OMS-2 clearly undergoing significant structural changes during lithiation/delithiation, while the 15-Ag-OMS-2 shows nearly no structural fluctuations.

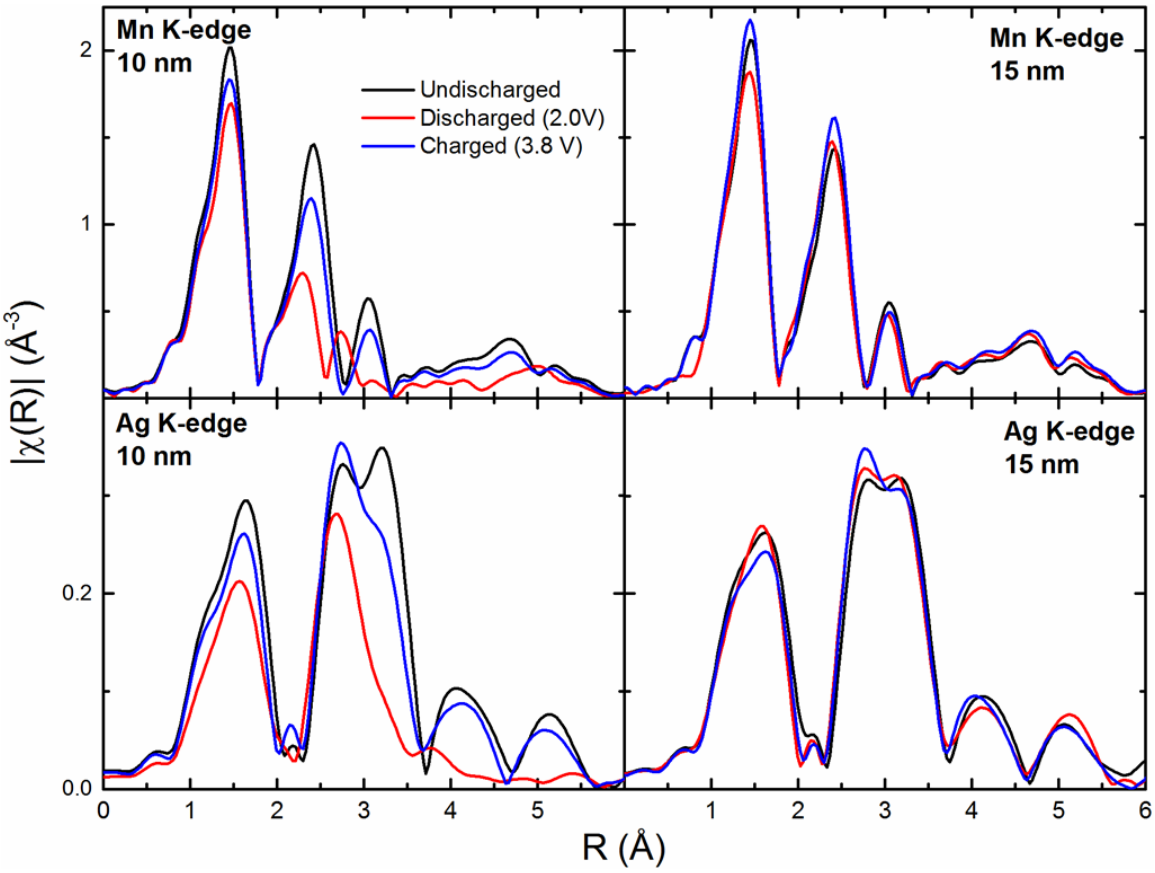

Figure 4.15. ***Ex-situ*** X-ray absorption spectroscopy (XAS) of 10-Ag-OMS-2 (left) and 15-Ag-OMS-2 (right) electrodes showing k^2-weighted $|\chi(R)|$ spectra from Mn (top) and Ag (bottom) K-edges. Electrochemical states include: undischarge (black), discharged to 2.0 V (red), and charged to 3.8 V (blue)

To obtain a more quantitative measure of the structural variations occurring in 10 and 15 nm $Ag_{1.4}Mn_8O_{16}$, both the Mn and Ag K-edge spectra were fit using theoretical structural models and the results are shown in **Figure 4.16**. As expected from the $|\chi(R)|$ in **Figure 4.15**, 10-Ag-OMS-2 shows significant interatomic distance expansion when lithiated to 3.8 V with Mn–$Mn_{\text{edge sharing}}$ octahedra expanding from 2.95 ± 0.02 Å in the undischarged state to 3.01 ± 0.06 Å upon lithiation. On the other hand, 15-Ag-OMS-2 shows no statistically significant changes in the Mn–$Mn_{\text{edge sharing}}$ octahedra distance which remains at 2.94 ± 0.04 Å when discharged to 2.0 V (∼0.25 electrons). A similar trend is observed in the Mn–$Mn_{\text{corner sharing}}$ octahedra, initially with an interatomic distance of 3.43 ± 0.02 Å and 10 Ag-OMS-2 expanding to 3.60 ± 0.04 Å at 2.0 V discharge while 15-Ag-OMS-2 remains at 3.44

$\pm$ 0.02 Å. When recharged to 3.8 V, 10-Ag-OMS-2 relaxes back to a similar crystal structure observed in the undischarged state, with the only statistically significant difference being the Mn–$Mn_{\text{edge sharing}}$ interatomic distance at 2.97 $\pm$ 0.02 Å, opposed to the undischarged value of 2.95 $\pm$ 0.02 Å. Recharged 15-Ag-OMS-2 remains in the undischarged crystal structure, as anticipated.

The Ag K-edge exhibits a similar trend as observed in the Mn K-edge. It is clear from **Figure 4.15** that there is not a substantial change in the Ag local atomic environment of 15-Ag-OMS-2, regardless of electrochemical state, while 10-Ag-OMS-2 exhibits significant changes. EXAFS modeling results (**Figure 4.16**) illustrate Ag metal (Ag^0) formation upon discharge to 2.0 V, indicating the Ag^+ atoms initially located at the $2a$ crystallographic site (i.e. within the tunnel) of the pristine crystal structure have migrated through the tunnel walls and have been reduced to metallic Ag^0 nanoparticles on the outside of the distorted hollandite structure. When recharged to 3.8 V, XAS confirms that Ag^0 formation in 10 nm $Ag_{1.4}Mn_8O_{16}$ is not reversible and 30 $\pm$ 12% of the Ag atoms within the undischarged hollandite structure have irreversibly been reduced to Ag^0.

XAS and EXAFS modeling has established the structural evolution of 10-Ag-OMS-2 during electrochemical cycling from $Ag_{1.4}Mn_8O_{16}$ to a distorted hollandite structure with Ag^0 metal nanoparticles whereas 15-Ag-OMS-2 does not demonstrate any significant structural change. The robust tunneled structure of 15-Ag-OMS-2 during cycling leaves fewer channels for Li ion transport within the nanorod, leading to inefficient Li ion diffusion within the electrode material and low delivered capacity. The structure of 10-Ag-OMS-2 is less stable upon lithiation causing the hollandite structure to distort and facilitating additional pathways for the transport of Li ions which, in turn, allows for greater access of the cathode material and higher realized capacities. Further, 10-Ag-OMS-2 exhibits the formation of metallic Ag^0 nanoparticles which contributes to the formation of a conductive percolation networking within the electrode and enhances the electrochemical behavior of the material compared to the more electrochemically inert 15-Ag-OMS-2 material.

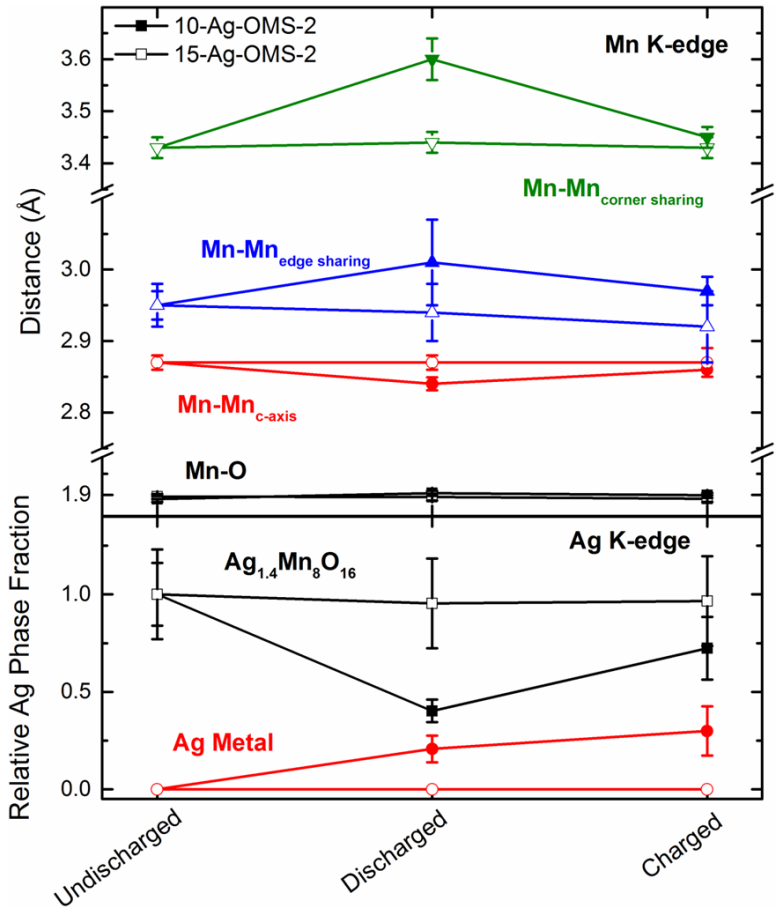

Figure 4.16. EXAFS modeling results of the (top) Mn–O/Mn–Mn near neighbor distances as determined from Mn K-edge spectra. Distinct Mn–O, Mn–Mn along the *c*-axis (red), edge sharing octahedra (blue), and corner sharing octahedra (green) distances are displayed for both the 10-Ag-OMS-2 (closed symbols) and 15-Ag-OMS-2 (open symbols) electrodes. Relative phase ratio of Ag species (bottom) as determined from the Ag K-edge EXAFS spectra

4.5 Conclusion

Silver hollandite, $Ag_xMn_6O_{18}$ ($x = 1.4$), with crystallite sizes of 10 and 15 nm has successfully been prepared via a co-precipitation reaction. Uniform silver content (x) in $Ag_xMn_6O_{18}$ allowed for the deconvolution of electrochemical effects related to crystallite size versus those related to silver content. The as-prepared materials were confirmed to be structurally analogous by XRD, HRTEM, XPS, and TGA. Small crystallite size $Ag_{1.4}Mn_8O_{16}$ (10-Ag-OMS-2) delivered a first cycle discharge capacity of 147 mAh/g while the large crystallite size material (15-Ag-OMS-2) delivered 10.5 mAh/g when discharge to 2.0 V. In addition, AC impedance

measurements of $Ag_{1.4}Mn_8O_{16}$ materials revealed increasing Warburg coefficients during discharge, indicative of sluggish Li^+ diffusion at high lithiation levels. Notably, 10-Ag-OMS-2 maintained a relatively low Warburg coefficient (230 $\Omega \cdot s^{-1/2}$) upon discharge to 4.3 electron equivalents, whereas the Warburg coefficient of 15-Ag-OMS-2 increased nearly 12-fold from the non-discharged state to 1.4 electron equivalents. Electrochemically cycled 10-Ag-OMS-2 and 15-Ag-OMS-2 cathodes were probed using *ex-situ* XAS to monitor structural changes of $Ag_{1.4}Mn_8O_{16}$ at various stages of lithiation. The low crystallite size material (10 Ag-OMS-2) proved to be structurally unstable during Li^+ intercalation leading to distortion of $Ag_{1.4}Mn_8O_{16}$ and formation of metallic Ag^0 nanoparticles while structural changes in 15-Ag-OMS-2 were not observed. Further, TEM imaging shows a high degree of bundling of 10-Ag-OMS-2 nanorods compared to 15-Ag-OMS-2. The superior electrochemical performance of 10-Ag-OMS-2 is likely due to a combination of electrical contact and structural distortion. On one hand, the small crystallite size $Ag_{1.4}Mn_8O_{16}$ increases surface area of silver hollandite nanorods causing the nanorods to bundle together which facilitates more intimate connection of the 10-Ag-OMS-2 material and enhances interparticle contact. On the other hand, structural distortion of 10-Ag-OMS-2 during lithiation and delithiation generates additional pathways for Li^+ diffusion and the reduction of Ag^+ to Ag^0 leads to the formation of a conductive percolation network within the cathode. A similar size-changing paradigm can be applied to other 1-D electrode materials to increase interparticle contact and induce specific electrochemical behavior.

CHAPTER V

ONE-POT PREPARATION OF $AgFeO_2$ AND A SERIES OF $AgFeO_2/\gamma$-Fe_2O_3 COMPOSITES WITH DISTINCT COMPOSITIONS AND CRYSTALLITE SIZES

5.1 Introduction

In 2012, an initial reflux-based synthesis demonstrated the feasibility of a low-temperature synthesis to produce pure, stoichiometric $AgFeO_2$ which was inherently nanocrystalline.[75] Few articles describe the synthesis of non-stoichiometric A^+:B^{3+} delafossites (ABO_2).[69,76,94,152] Of most relevance, is a manuscript by Krehula and Musiċ that describes the precipitation of $AgFeO_2$ with varying ratios of $[Ag^+]$:$[Fe^{3+}]$. A series of reactions utilizing aqueous solutions of silver nitrate ($AgNO_3$) and iron(III) nitrate ($Fe(NO_3)_3{\cdot}9H_2O$), in basic solutions of NaOH or TMAH (tetramethylammonium hydroxide), and carried out at 160°C in hydrothermal bombs were assessed.[76] A majority of the products were not pure-phase and the materials collected post-synthesis either included a mixture of the 2H and 3R crystalline polytypes of $AgFeO_2$ or some combination of α-FeOOH, Fe_2O_3, Ag^0, and Ag_2O impurities. Specific samples were studied by field emission scanning electron microscopy (FE-SEM) to estimate the particle size. Krehula and Musiċ found that 50:50 $[Ag^+]$:$[Fe^{3+}]$ reactions afforded $AgFeO_2$ nanoparticles in the range of 20–30 nm. Compared to equivalent phases of $AgFeO_2$ from lower $[Ag^+]$ reactions, the particle size was considerably reduced. The data implies that compositional control of silver delafossites does, in fact, effect crystallite size and emphasizes the need for an optimized method to achieve pure, single-phase ternary oxides.

One-pot synthetic approaches have been successfully used to achieve improved material function in energy storage applications.[153,154] Recently, precise manipulation of starting reagents afforded silver ferrite/maghemite composites (Ag_xFeO_y, where y = 2 - (1-x)/2 and Ag_xFeO_y = a composite of $x$$AgFeO_2$ + (1-x)/2 γ-Fe_2O_3) with Ag/Fe ratios (x) from 0.2–1.0 and crystallite sizes ranging between 10 and 18 nm for low and high Ag/Fe ratios, respec-

tively, via one-pot synthesis.[155,156] The silver ferrite/maghemite composites in the lowest silver regime ($x = 0.2$) demonstrated profound improvement with reversible capacities approximately 100% higher than stoichiometric $AgFeO_2$. While the significance of Ag_xFeO_y composition was noted, the role and importance of the one-pot synthesis method were not explored. Chapter V provides an in-depth examination of one-pot chemically synthesized nanocrystalline Ag_xFeO_y composite materials. A series of nanocrystalline Ag_xFeO_y composite materials is fully characterized through X-ray diffraction (XRD), Raman spectroscopy, transmission electron microscopy (TEM), X-ray photoelectron spectroscopy (XPS), X-ray absorption spectroscopy (XAS), and thermogravimetric analysis (TGA).

5.2 Experimental

5.2.1 General Methods and Materials

Silver ferrite was synthesized via a co-precipitation reaction modified from previously reported schemes.[74,75,78,108,155] Silver nitrate, iron(III) nitrate, and sodium hydroxide reagents were used as received from vendor. Water utilized during synthesis was deionized water filtered through a Thermo Scientific Barnstead Nanopure ultrapure water purification system. Aqueous solutions of silver nitrate, iron(III) nitrate, and sodium hydroxide dissolved in deionized water were combined, affording rapid formation of a dark red-brown precipitate in solution. The reaction mixture was heated under reflux. Solid silver ferrite was obtained by centrifugation, washed with H_2O, and reduced to dryness *in vacuo*. During the non-stoichiometric synthesis of Ag_xFeO_y composites ($x = 0.2$, 0.4, 0.6, 0.8), the mass of $Fe(NO_3)_3{\cdot}9H_2O$ was kept constant and $AgNO_3$ was altered to achieve the corresponding Ag/Fe ratio. Semi-crystalline maghemite (γ-Fe_2O_3) was prepared using a similar method and $Fe(NO_3)_3{\cdot}9H_2O$ as a reagent. Commercial nanopowder maghemite (20 nm, 99.5+% purity) from US Research Nanomaterials, Inc. was used a reference material for synthesized semi-crystalline maghemite.

5.2.2 Characterization

X-Ray powder diffraction (XRD) spectra of silver ferrite composites and thermal decomposition products were collected with Cu Kα radiation and Bragg-Brentano focusing geometry using a Rigaku SmartLab X-Ray diffractometer and a D/tex detector. The XRD spectra were measured in a 2θ range from 5° to 90°. Rigaku PDXL2 software with an ICDD PDF-2 database was used for search-match analysis. Silver ferrite crystallite sizes were approximated by applying the Scherrer equation to the (0 0 6) reflection at a 2θ value of approximately 28° in the XRD pattern. Quantitative elemental analysis of silver and iron, determined by inductively coupled plasma-optical emission spectroscopy (ICP-OES), was performed on a ThermoScientific iCap 6000 ICP spectrometer. Brunauer-Emmett-Teller (BET) surface area measurements were collected on a Quantachrome Nova 4200e using an 11-point BET method, nitrogen gas adsorbate, and 100 mg silver ferrite. Prior to BET measurements, silver ferrite samples were dried under vacuum at 60°C for 6 h to remove chemisorbed surface water. A Joel JSM-6010PLUS was used to collect scanning electron microscopy (SEM) images of silver ferrite composites in secondary electron imaging mode at a magnification of 10 kX or backscattered electron composition imaging mode at 5 kX. Energy dispersive X-ray spectroscopy (EDS) was employed during SEM to map and quantitatively asses elemental Ag, Fe, and O. Raman data were collected using a Horiba Scientific XploRA ONE Raman microscope equipped with a 532 nm laser. Silver ferrite samples were pressed into pellets with 5% graphite prior to measurement at room temperature. The laser beam was focused on the sample using a 50x microscope objective and a laser power of 10%. Spectra were collected in the range of 200-900 cm^{-1} and the acquisition time was set to 60 seconds with 15 scan accumulations. Simultaneous thermogravimetric analysis/differential scanning calorimetry (TGA/DSC) was run on a TA Instruments SDT Q600 and used to investigate the thermal stability and oxygen content of silver ferrite composites (Ag/Fe = 0.2, 0.4, 0.6, 0.8, 1.0). Samples weighing approximately 15 mg were placed in alumina thermogravimetric analysis pans and heated from room temperature to 1,000°C under an atmosphere of

nitrogen gas at a rate of 1°C/min.

Room temperature iron K-edge X-ray absorption spectra were gathered in transmission mode on beam line X-11A at Brookhaven National Laboratory's National Synchrotron Light Source (NSLS-I) facility. The electron storage ring was operating at 2.8 GeV with the stored current ranging between 200–300 mA. A Si (1 1 1) double crystal was used as a monochromator for the X-Ray energy, which was calibrated using a metallic Fe foil. XANES data were evaluated with Athena data analysis software. Metallic Fe foil reference data was simultaneously collected with all silver ferrite spectra. The silver ferrite data were calibrated and aligned with respect to the Fe foil and subsequently normalized to mitigate absorption differences between spectra and allows for quantitative analysis of pre-edge features. X-ray photoelectron spectroscopy (XPS) was performed on a RHK Technology UHV 7500 variable temperature UHV atomic force and scanning tunneling microscope as a complementary surface-sensitive technique to probe the elemental composition. The UHV chamber, under a base pressure of 2 x 10^{-10} Torr, was equipped with a non-monochromatized Al-Kα X-ray source (hν = 1486.6 eV) operating with a 30 mA current and an accelerating voltage of 10 kV. In addition, the UHV chamber utilized a SPECS Phoibos 100 MCD analyzer. Powder samples of silver ferrite and iron(III) oxide reference materials were adhered to a conductive copper tape and mounted onto a sample holder. Charging effects in XPS spectra were corrected by calibrating the binding energy of the adventitious C1s peak to 284.8 eV.

5.2.3 Acknowledgment of Collaboration

The research in Chapter V was conducted in collaboration with Dr. Altug Poyraz, Dr. David Bock, Dr. Kevin Kirshenbaum, Dr. Wei Zhang, and Dr. Feng Wang (Brookhaven National Laboratory). The XPS data was obtained by Dr. Poyraz, Dr. Bock, and Dr. Kirshenbaum. Dr. Kirshenbaum also assisted with the fitting of the Raman and XAS data while TEM imaging studies were performed by Dr. Zhang at BNL.

5.3 Results and Discussion

A one-pot, non-stoichiometric co-precipitation technique has been employed in Chapter V (**Equation 5.1**) to produce a series of Ag_xFeO_y composites ($0.2 \leq x \leq 0.8$), stoichiometric $AgFeO_2$, and semi-crystalline maghemite (γ-Fe_2O_3). Nanocrystalline maghemite was prepared using a similar one-pot co-precipitation synthesis using only $Fe(NO_3)_3$ as the starting reagent. Silver ferrite/maghemite composites that are silver ferrite deficient and contain increasing quantities of maghemite, Ag_xFeO_y ($0.2 \leq x \leq 1.0$, $y = 2$ ((1-x)/2)), are denoted by the formula in **Equation 5.2** for simplicity.

$$x\mathrm{AgNO_3} + \mathrm{Fe(NO_3)_3} \xrightarrow[\Delta\ \mathrm{H_2O}]{\mathrm{NaOH}} \mathrm{Ag}_x\mathrm{FeO}_y \left(y = 2 - \frac{1-x}{2}\right) \tag{5.1}$$

$$\mathrm{Ag}_x\mathrm{FeO}_y \ = \ x\mathrm{AgFeO_2} + \frac{1-x}{2}\ \gamma\text{-}\mathrm{Fe_2O_3} \tag{5.2}$$

5.3.1 Structure and Elemental Composition

Recently, the composite nature of Ag_xFeO_y was established as a mixture of crystalline silver ferrite, $AgFeO_2$, and amorphous maghemite, γ-Fe_2O_3, using X-ray absorption spectroscopy (XAS) and Raman spectroscopic analyses.[155] Powder X-ray diffraction (XRD) patterns of the as-synthesized silver ferrite/maghemite composites in **Figure 5.1** are consistent with a mixture of rhombohedral (3R-$AgFeO_2$) and hexagonal (2H-$AgFeO_2$) phases and demonstrate peak broadening as the Ag/Fe ratio decreases, which directly correlates to reduced crystallite size.

Notably, the diffraction patterns do not illustrate presence of metallic silver (Ag^0) or additional oxide impurity phases (e.g. Ag_2O, FeOOH) typically associated with the synthesis of delafossites.[74,77,90,103,105] Semi-crystalline maghemite was produced as a control material for both structural and electrochemical comparison to Ag_xFeO_y composites and stoichiometric $AgFeO_2$ and the XRD is shown in **Figure A10**. Maghemite exhibits two broad diffraction peaks near 2θ values of 35° and 62° which correspond to the most intense peaks of a

crystalline γ-Fe_2O_3 sample.

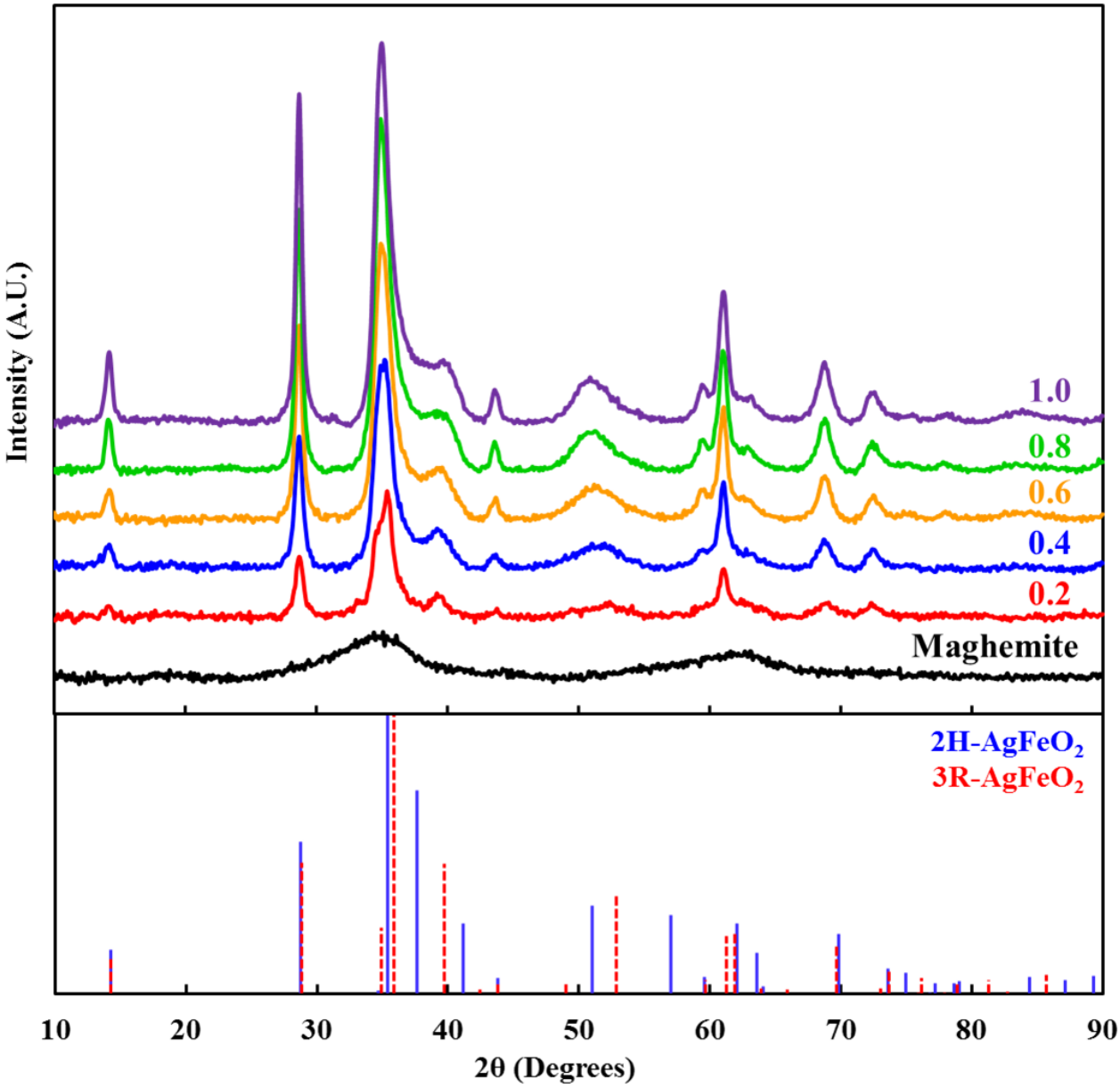

Figure 5.1. XRD of silver ferrite/maghemite composites (Ag_xFeO_y), stoichiometric $AgFeO_2$, and synthesized nanocrystalline maghemite (γ-Fe_2O_3) with corresponding 2H (01-070-1452) and 3R-$AgFeO_2$ (01-075-2147) reference patterns

The broad, often asymmetric peak at a maximum 2θ of ~50–52° in the diffraction pattern (**Figure 5.1**) is consistent with previous $AgGaO_2$,[72] $AgScO_2$,[90] and $AgFeO_2$[76] patterns and has been attributed to a mixture of rhombohedral (3R-$AgFeO_2$) and hexagonal (2H-$AgFeO_2$) phases. This peak in the XRD of Ag_xFeO_y composites is unique in the fact that it appears

to shift with a change in Ag/Fe composition (**Figure 5.2**) where Ag_xFeO_y (x <1) materials demonstrate a shift to higher values of 2θ.[155]

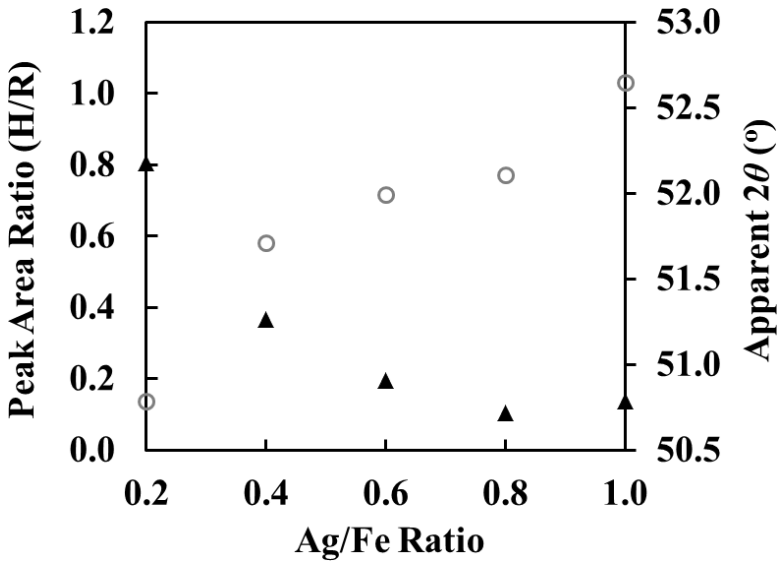

Figure 5.2. Apparent 2θ values (triangles) and peak area ratio of 3H/2R (circles) from linear combination fitting

Locking 2θ values to (0 1 8) and (1 0 5) peak positions of the 3R-$AgFeO_2$ (50°) and 2H-$AgFeO_2$ (52°) phases, respectively, allowed for linear combination fitting of the region. Using the fitting results, the ratios of the peak areas in the 50–52° 2θ range were determined and the relative compositions of 3R and 2H phases in Ag_xFeO_y composites ($0.2 \leq x \leq 1.0$) are shown in **Figure 5.2**. Linear combination fitting indicates that the low silver $Ag_{0.2}FeO_{1.6}$ composite is predominately comprised of the 3R-AgFeO2 phase, whereas the stoichiometric $AgFeO_2$ material contains nearly equivalent amounts of 3R and 2H phases.

The crystallite sizes of Ag_xFeO_y composites and $AgFeO_2$, calculated by applying the Scherrer equation to the (0 0 6) reflection at a 2θ value of approximately 28° in the XRD pattern, are shown in **Figure 5.3**. Crystallite size displays a linear trend with decreasing size as a function of low silver content or small Ag/Fe reaction ratio. Inductively coupled plasma optical emission spectroscopy (ICP-OES) was used to determine silver and iron content of silver ferrite/maghemite composites and the corresponding Ag/Fe ratios were verified to be analogous to the anticipated reaction ratio (**Figure 5.3**). These results indicate that the one-

pot aqueous co-precipitation method utilized in this chapter allows for precise manipulation of the silver ferrite and maghemite phase composition of Ag_xFeO_y composite materials.

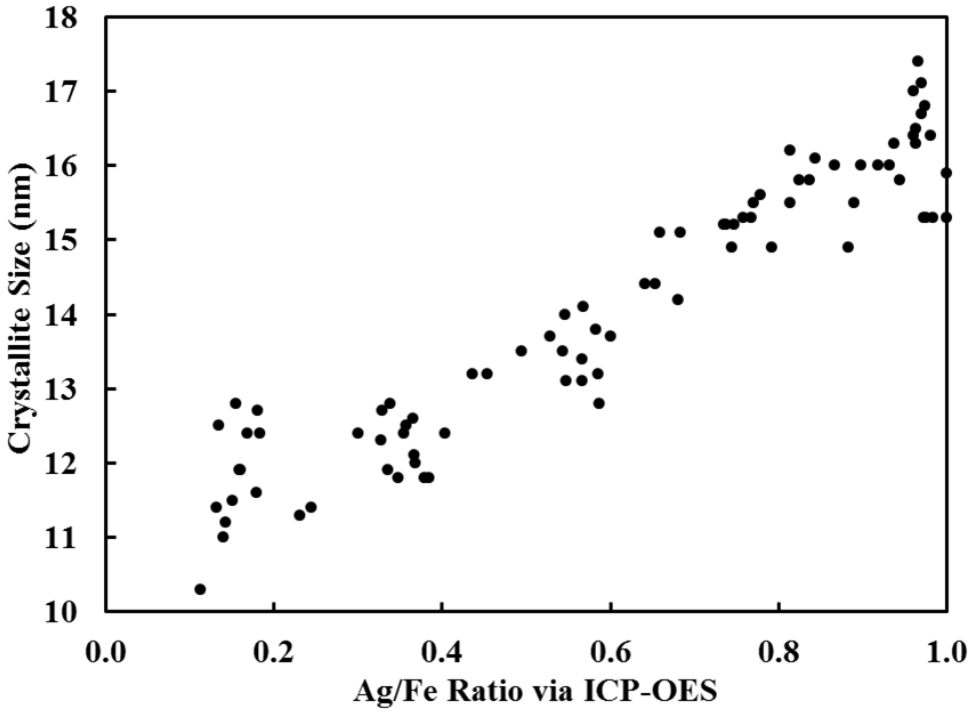

Figure 5.3. Crystallite size of Ag_xFeO_y composites ($0.2 \leq x \leq 0.8$) and $AgFeO_2$

5.3.2 Surface Area Analysis

The surface area of Ag_xFeO_y composites and $AgFeO_2$ was measured by adsorption of N_2 adsorption analysis using the Brunauer-Emmett-Teller (BET) method and the results are summarized in **Table 5.1**. Larger surface areas were measured for Ag_xFeO_y composites compared to $AgFeO_2$ which displays a surface area of 51 m^2/g. Between Ag/Fe ratios of 0.2 and 1.0 (i.e. a 6 nm difference in crystallite size), a 5-fold increase in BET surface area is demonstrated. The significant increase in surface area of Ag_xFeO_y composites, as a function of x, can be explained by the presence of larger quantities of amorphous maghemite, γ-Fe_2O_3, in the composite material. A surface area of 225 m^2/g was measured for nanocrystalline γ-Fe_2O_3 ($\sim$2 nm) which correlates well with the magnitude of surface area observed for Ag_xFeO_y composites primarily composed of maghemite.

Table 5.1. BET surface area analysis of silver ferrite composites ($0.2 \leq x \leq 0.8$), stoichiometric $AgFeO_2$, and maghemite (γ-Fe_2O_3)

Composite Material	**Surface Area (m^2/g)**
$\mathbf{Ag_{0.2}FeO_{1.6}}$	256
$\mathbf{Ag_{0.4}FeO_{1.7}}$	185
$\mathbf{Ag_{0.6}FeO_{1.8}}$	123
$\mathbf{Ag_{0.8}FeO_{1.9}}$	73
$\mathbf{AgFeO_2}$	51
$\boldsymbol{\gamma}$**-**$\mathbf{Fe_2O_3}$	225

5.3.3 Electron Imaging

Powders of pristine $Ag_{0.2}FeO_{1.6}$, $Ag_{0.6}FeO_{1.8}$, and $AgFeO_2$, directly post-synthesis, were examined using transmission electron microscopy (TEM) to elucidate composition and morphology. Annular dark-field (ADF) images (**Figure 5.4 A-C**) obtained via TEM indicate that particle sizes of $AgFeO_2$, $Ag_{0.6}FeO_{1.8}$, and $Ag_{0.2}FeO_{1.6}$ decrease with reduction of the Ag/Fe ratio (x) which agrees with crystallite size and elemental analysis data in **Figure 5.3**. Pure-phase $AgFeO_2$ was detected by selected area diffraction (**Figure 5.4 D-E**) in all composites and is consistent with XRD measurements.

High resolution TEM (HRTEM) imaging shows high crystallinity of 2H-$AgFeO_2$ nanoparticles in $Ag_{0.2}FeO_{1.6}$ composites with no evidence of an amorphous layer on the surface (**Figure 5.5**). In localized areas of the ADF images, however, porous, irregularly-shaped γ-Fe_2O_3 particles were identified and displayed poor crystallinity by electron diffraction.

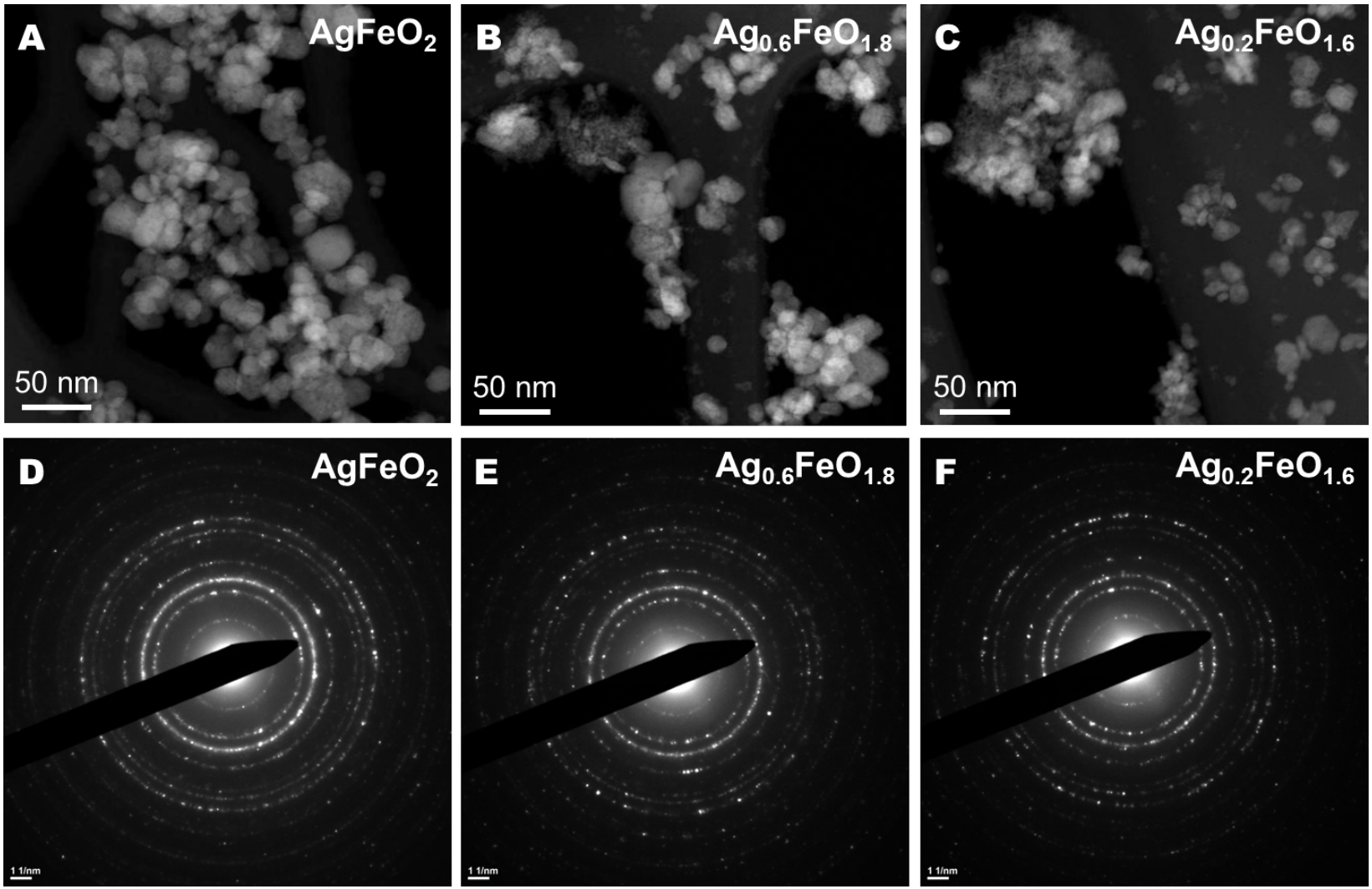

Figure 5.4. TEM microstructure and phase identification of Ag_xFeO_y nanoparticles by annular dark-field (ADF) imaging (top) and selected area electron diffraction patterns (bottom): (A,D) $AgFeO_2$, (B,E) $Ag_{0.6}FeO_{1.8}$, and (C,F) $Ag_{0.2}FeO_{1.6}$

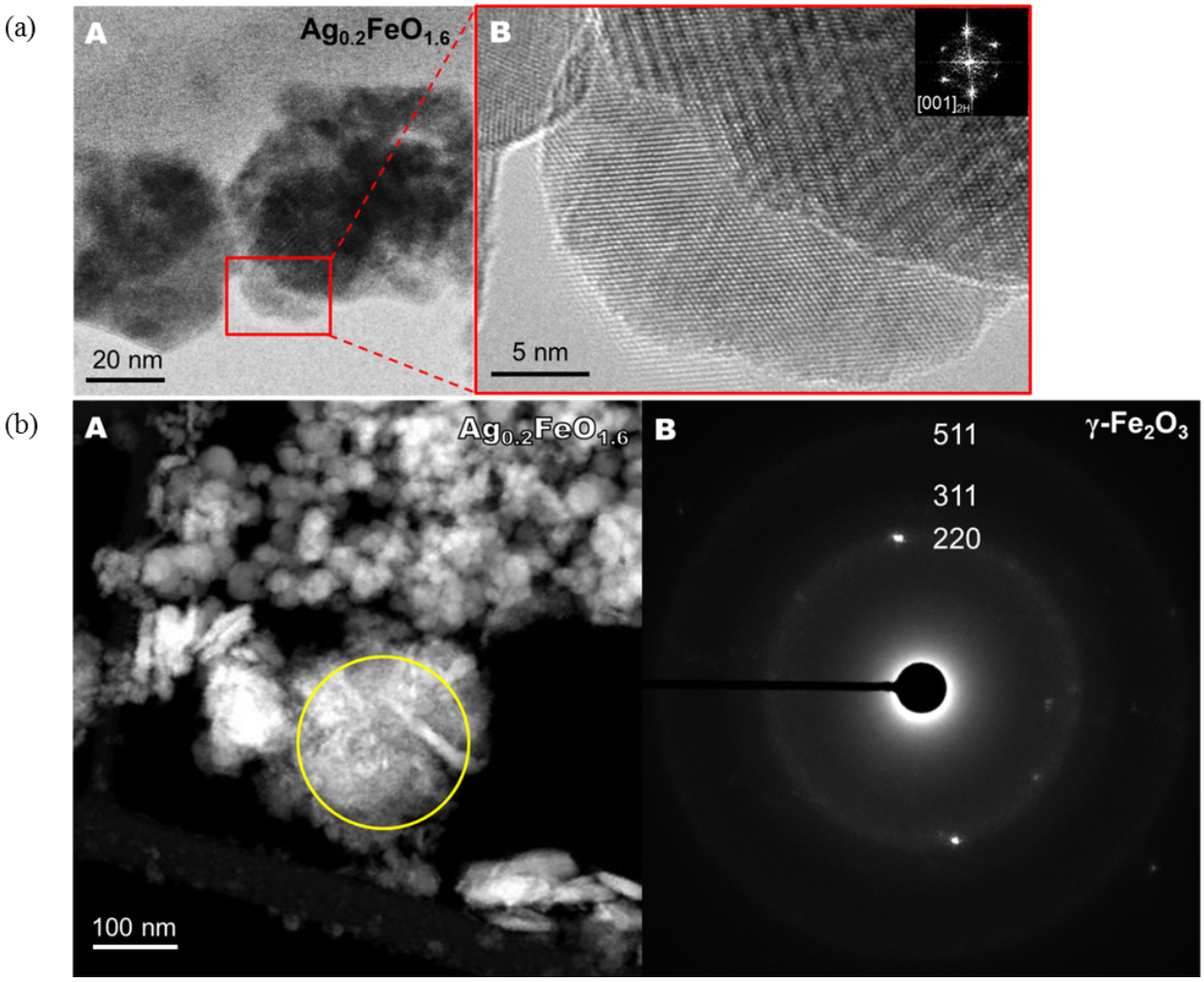

Figure 5.5. (a) Local structure of a $Ag_{0.2}FeO_{1.6}$ nanoparticle via a bright-field TEM image (**A**) and high-resolution TEM (HRTEM) image (**B**) recorded within the area marked by the red box. The Fast Fourier Transform (FFT) pattern, inset, produced from the HRTEM image indicates that the selected particle possesses the 2H-$AgFeO_2$ structure. (b) Identification of the γ-Fe_2O_3 phase in $Ag_{0.2}FeO_{1.6}$ from a localized ADF image (**A**) and the corresponding electron diffraction pattern (**B**) recorded from the area within the yellow circle. The diffuse diffraction rings, which are indexed to (2 2 0), (3 1 1), and (5 1 1) demonstrate the poor crystallinity of the γ-Fe_2O_3 phase

Electron energy loss spectroscopy (EELS) mapping of $Ag_{0.2}FeO_{1.6}$, a high iron content composite prepared by the one-pot co-precipitation method, illustrates relatively well-dispersed nanoparticles and uniform distribution of Ag and Fe with localized areas of high Fe concentration which is expected due to the high concentration of maghemite in the composite (**Figure 5.6**).

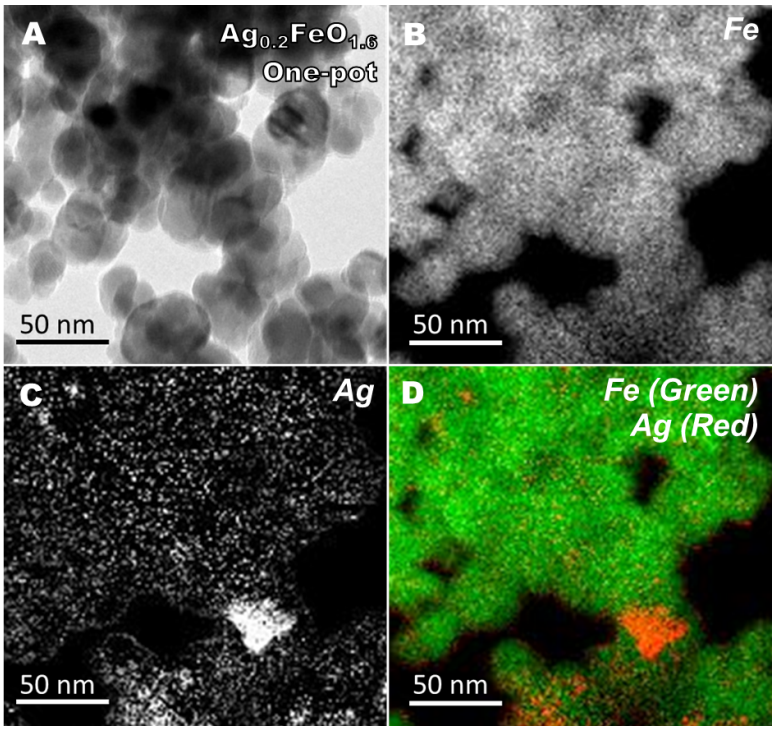

Figure 5.6. Transmission electron microscopy (TEM) of $Ag_{0.2}FeO_{1.6}$, a one-pot generated silver ferrite/maghemite composite. Distribution of Ag and Fe from TEM images (A) and the corresponding electron energy loss spectroscopy (EELS) maps of Fe (B) and Ag (C). (D) Superposition of Fe (green) and Ag (red) EELS maps

In addition, scanning electron microscopy (SEM) imaging reveals the agglomeration of small primary particles into larger granular particles (∼1-5 μm diameters) for $AgFeO_2$, γ-Fe_2O_3, $Ag_{0.2}FeO_{1.6}$, and the 0.2 Ag/Fe mechanical mixture (**Figure A11**, images **A** and **B**). Energy dispersive X-ray spectroscopy (EDS) mapping illustrates a rather homogeneous distribution of Ag and Fe ($AgFeO_2$, $Ag_{0.2}FeO_{1.6}$, and 0.2 mechanical mixture) and Fe and O (γ-Fe_2O_3) across particle aggregates with visibly decreased intensity of elemental Ag in low silver ferrite content materials (**Figure A11**, images **C** and **D**) which agrees with the

EELS data. Further, EDS mapping confirms that although the composites are composed of two phases (i.e. $AgFeO_2$ and γ-Fe_2O_3) there is no evidence of aggregation within the bulk material. Notably, Ag/Fe ratios calculated from the EDS spectra give values of 0.99 and 0.17 for $AgFeO_2$ and $Ag_{0.2}FeO_{1.6}$, respectively (**Figure A11**, image **E**). In combination with the results from XRD, TEM and SEM imaging confirm the composite nature of Ag_xFeO_y materials as a combination of crystalline $AgFeO_2$ and poorly crystalline γ-Fe_2O_3.

5.3.4 Vibrational and Absorption Spectroscopy

To further probe the localized structure of silver ferrite/maghemite composites, micro-Raman spectroscopy was utilized. Raman data of $AgFeO_2$ has been reported previously and E_g and A_{1g} peaks were measured at 345 and 638 cm^{-1}, respectively.[74,77,90,103,105] The stoichiometric $AgFeO_2$ material prepared via one-pot co-precipitation demonstrates peaks at 350 and 631 cm^{-1}, consistent with the E_g and A_{1g} literature values (**Figure 5.7**). As the Ag/Fe ratio decreases, Raman spectra continue to show intrinsic silver ferrite peaks while shoulders detected at 285, 374, and 707 cm^{-1} increase in intensity. The E_g and A_{1g} peaks in the vibrational Raman spectrum of the delafossite are attributed to fundamental bond distances, energies, and angles of the delafossite structure and do not change in position or relative intensity, suggesting that the silver ferrite structure remains intact even in the composite materials. The peaks at 285, 374, and 707 cm^{-1} appear among the low silver content samples (x <1.0) and are reminiscent of the Raman spectrum of iron oxide, maghemite (γ-Fe_2O_3).[157,158]

The distinct presence of maghemite in the Raman spectra allowed us to evaluate the total contribution of silver ferrite in various materials using γ-Fe_2O_3 and $AgFeO_2$ as references and applying classic least squares (CLS) fitting. Using the maghemite and $AgFeO_2$ spectra as references, CLS fitting was used to determine the contribution of the reference spectra to a mixed component spectrum. Intensity of the $AgFeO_2$ Raman spectral pattern decreased linearly as a function of decreasing Ag/Fe ratio, leading to a percent contribution of $AgFeO_2$ representative of the silver content in each sample (**Figure 5.8**).

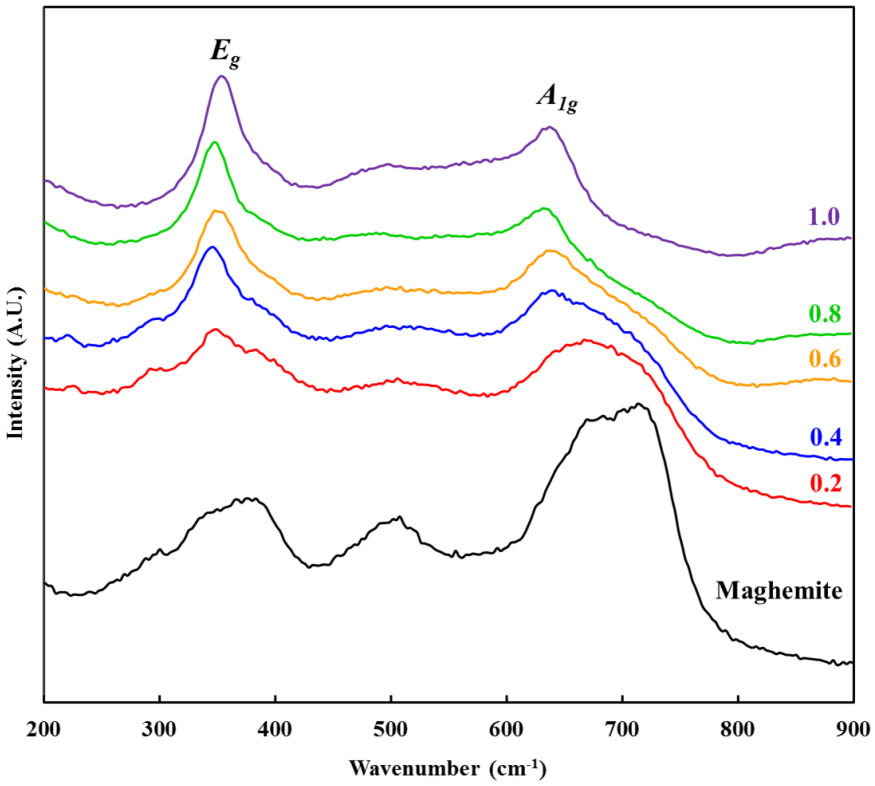

Figure 5.7. Raman spectroscopy of Ag_xFeO_y composites, $AgFeO_2$, and synthesized nanocrystallite maghemite (γ-Fe_2O_3)

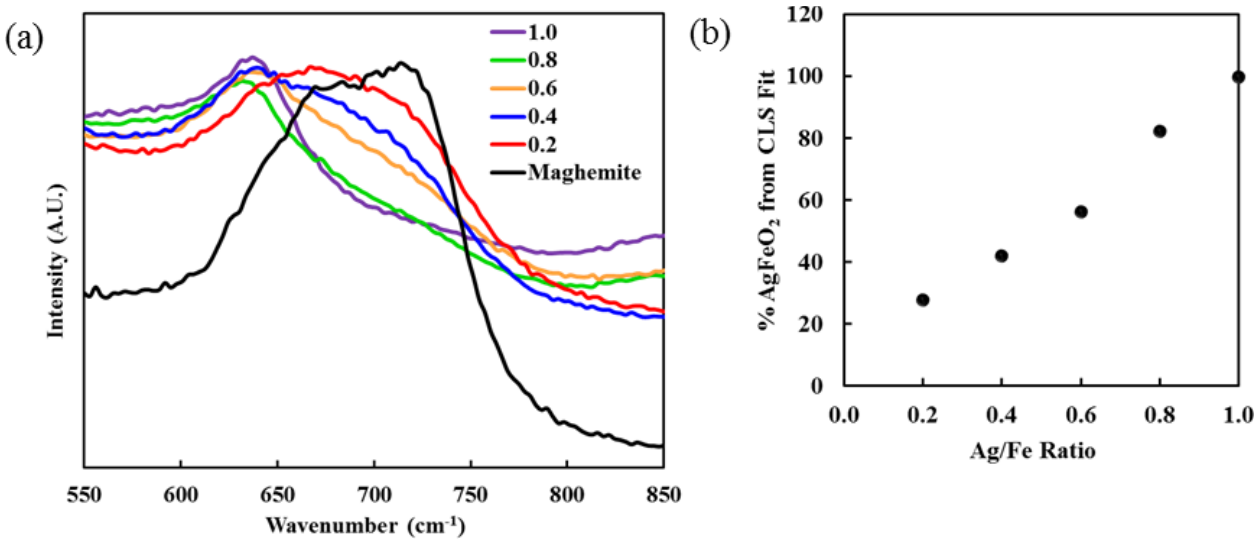

Figure 5.8. (a) Region (550-850 cm^{-1}) of Raman spectra used for classic least squares fitting (b) Percent of $AgFeO_2$ *versus* Ag/Fe ratio from fitting

Results from CLS fitting suggest that a combination of $AgFeO_2$ and γ-Fe_2O_3 are present rather than a solid solution of $AgFeO_2$ with Ag^+ vacancies. The discernible nature of maghemite in Raman spectra, though imperceptible by bulk XRD, is indicative of amorphous γ-Fe_2O_3. The data concerning a co-precipitation synthesis using only Fe^{3+} as the reagent, in addition to a previous article, indicate that it is possible to synthesize γ-Fe_2O_3 using an aqueous technique that employs $Fe(NO_3)_3$ and a weak base.[159] Therefore, it is reasonable to assume that non-crystalline maghemite (γ-Fe_2O_3) and nanocrystalline silver ferrite ($AgFeO_2$) are synthesized in parallel via the one-pot co-precipitation technique to afford composite materials of varying degrees.

The composite nature of Ag_xFeO_y composites (x <1.0) as an amalgamation of crystalline silver ferrite, $AgFeO_2$, and amorphous maghemite, γ-Fe_2O_3, was also verified by X-ray absorption (XAS) analysis. The sensitivity of XANES (X-ray absorption near edge structure) to oxidation state and coordination number provided a useful complement to characterization of the nanocrystalline silver ferrite composites by XRD and Raman. Iron K-edge and silver K-edge data were collected and compared to a variety of reference materials (metallic Fe, FeO, Fe_3O_4, and Fe_2O_3 for iron; metallic Ag and Ag_2O for silver). The Fe K-edges for the various silver ferrite samples were all nearly equivalent to the absorbance spectrum of Fe_2O_3 with an edge energy of approximately 7127 eV, establishing an iron oxidation state of +3 for all samples (**Figure 5.9**). Based on XAS data, the average iron oxidation state does not vary to any significant extent, since the Fe-edge energies range by <0.1 eV (between 7126.9 and 7127.4 eV) and no direct correlation between silver content (x) and Fe edge position is observed.

The normalized absorbance intensity of the iron pre-edge peak decreases linearly as the amount of silver in the delafossite samples increases (**Figure 5.10**). The decrease in intensity and change in appearance of the pre-edge peak from silver deficient composites to stoichiometric $AgFeO_2$ would generally be attributed to a slight change in either the oxidation state of iron, the coordination environment of iron, or a combination of the two. A

k^3-weighted $|\chi(R)|$ plot of EXAFS data shows no significant change up to 3.0 Å as a function of Ag content. The FeAg scattering path (3.0–3.5 Å) in the EXAFS (extended X-ray absorption fine structure) region of the XAS spectra, however, change as a function of silver concentration (**Figure 5.11**).

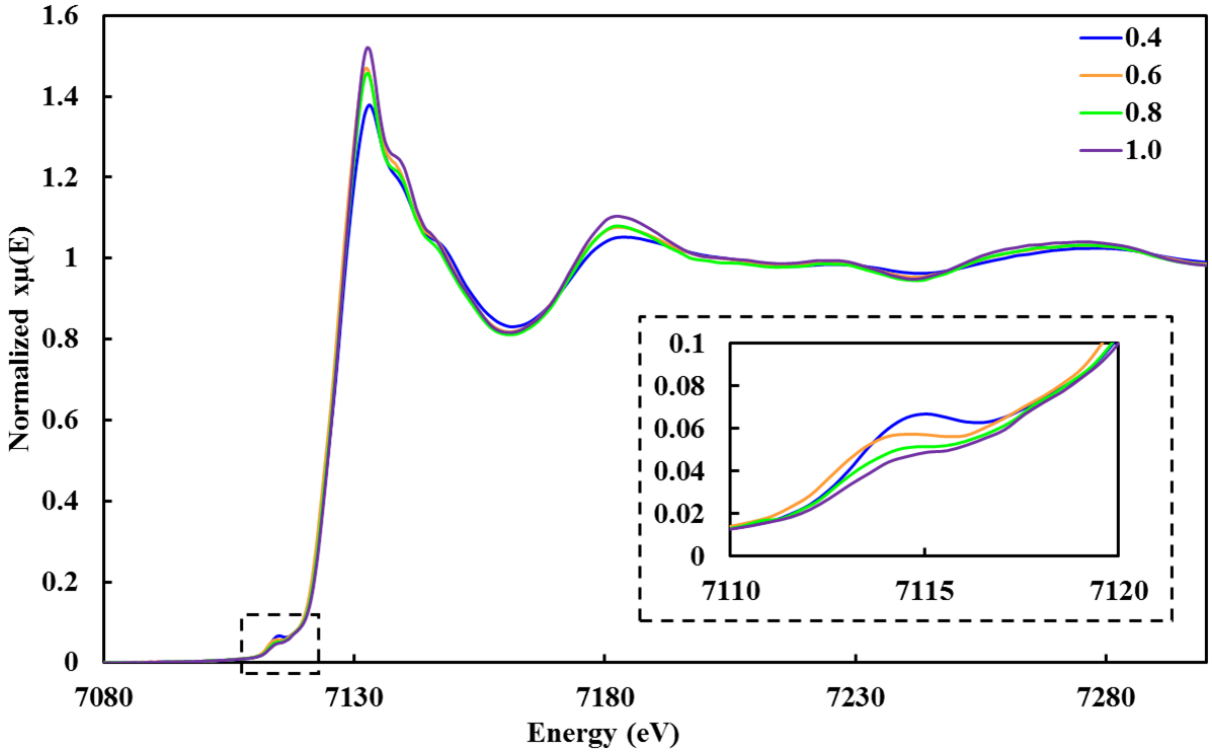

Figure 5.9. XANES Iron K-edge spectra of $AgFeO_2$ and Ag_xFeO_y composites ($x = 0.4$, 0.6, 0.8) with magnification of the pre-edge region inset

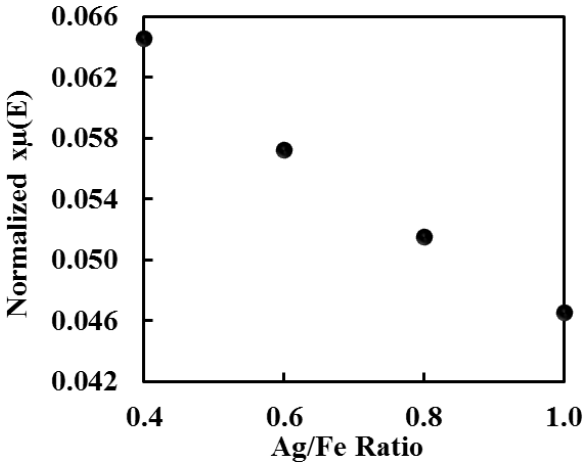

Figure 5.10. Intensity of Fe XANES pre-edge feature as a function of Ag/Fe ratio

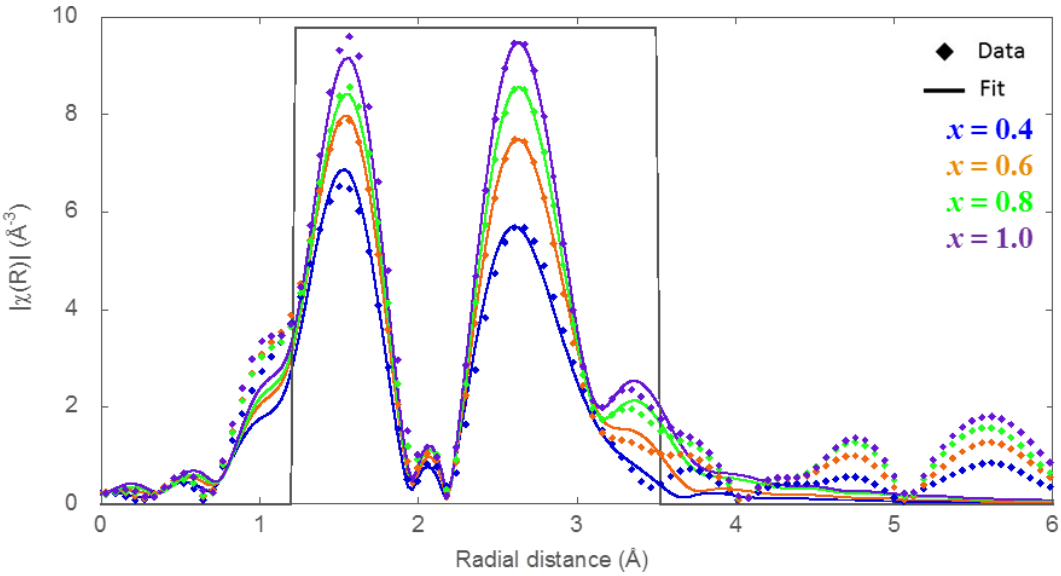

Figure 5.11. k^3-weighted $|\chi(R)|$ (diamonds) of $AgFeO_2$ and Ag_xFeO_y composites ($x = 0.4$, 0.6, 0.8) overlayed with EXAFS fitting results (line). The region used for fitting is denoted by the outlined box

It is evident that oxidation state of iron in Ag_xFeO_y composites not change after examination of the iron K-edge. Several iron-containing minerals demonstrate more intense pre-edge peaks for coordination numbers of 4 or 5 and lower pre-edge absorption for 6-coordinate iron in the 3+ oxidation state. $AgFeO_2$ is composed of layers of FeO_6 octahedra (**Figure 1.6**) and would be expected to have a pre-edge peak of relatively low intensity. While pre-edge features in octahedral transition metal complexes are ordinarily resultant of forbidden 1s $\rightarrow$ 3d electronic transitions, such transitions are allowed when the local symmetry is distorted, commonly observed in octahedral iron-containing compounds owing to facile 3d $\rightarrow$ 4p orbital mixing. Notably, the Raman data indicate the presence of a non-crystalline maghemite, γ-Fe_2O_3, phase which is a spinel structure comprised of both tetrahedral and octahedral Fe^{3+}. The tetrahedral Fe^{3+} in γ-Fe_2O_3 contributes to an increase in pre-edge intensity compared to exclusively octahedral Fe^{3+}. The pre-edge intensity of Ag_xFeO_y composites increases with smaller values of x and can be associated with greater amounts of maghemite as established by Raman analysis.

XANES data at the Ag K-edge were also collected for $AgFeO_2$ and Ag_xFeO_y composites.

Silver was determined to be in the +1 oxidation state where absorption spectra in the XANES region were indistinguishable for all Ag/Fe ratios. Thus, the XANES results indicate that the silver and iron oxidation states do not change as a function of crystallite size. In addition, iron experiences a difference in the pre-edge region which is consistent with the presence of maghemite in Ag_xFeO_y composites with decreased values of x.

5.3.5 Electronic Structure Analysis

Full XPS survey spectra (0-1300 eV), for the detection all existing elements, of representative high and low silver samples ($AgFeO_2$ and $Ag_{0.2}FeO_{1.6}$, respectively) and iron(III) oxide references are depicted in **Figure A12**. The XPS core-level Ag3d (360-385 eV), Fe2p (700-750 eV), and O1s (525-535 eV) spectra of Ag_xFeO_y composites (x = 0.2, 0.4, 0.6, 0.8), stoichiometric $AgFeO_2$, and commercial α-Fe_2O_3 and γ-Fe_2O_3 are compared in **Figures 5.12 a**, **b**, and **c**. A previous XPS study of stoichiometric $AgFeO_2$ reveals analogous core-level Ag3d and Fe2p spectra.[160] Peaks in the core-level spectra remain consistent across the series (**Figures 5.12 a**, **b**, textbfc), indicating no structural disparity between samples as expected from the uniform powder XRD patterns in **Figure 5.1**. To examine the silver to iron content of Ag_xFeO_y composites ($0.2 \leq x \leq 0.8$) and $AgFeO_2$, a ratio of the Ag3$d_{5/2}$ to Fe2$p_{3/2}$ peak areas was plotted (**Figure 5.12 d**). A positive linear trend was observed for peak area ratio as a function of increasing silver content.

XPS confirms the decreased quantity of silver in samples with x <1.0 and is complementary to the elemental analysis of Ag and Fe content obtained from ICP-OES. Further, core-level O1s spectra show a more intense tail toward the high binding energy side of the O1s peak of low silver content samples, indicative of chemisorbed water (i.e. increased concentration of absorbed hydroxyl groups).[161] Increased quantities of chemisorbed water in low silver, silver ferrite composites can directly be attributed to both increased surface area of small crystallites exposed to the ambient environment and maghemite content. Thermogravimetric analysis of silver ferrite samples, shown in **Figure 5.13 a**, quantitatively shows significantly larger amounts of absorbed water for samples with low silver contents.

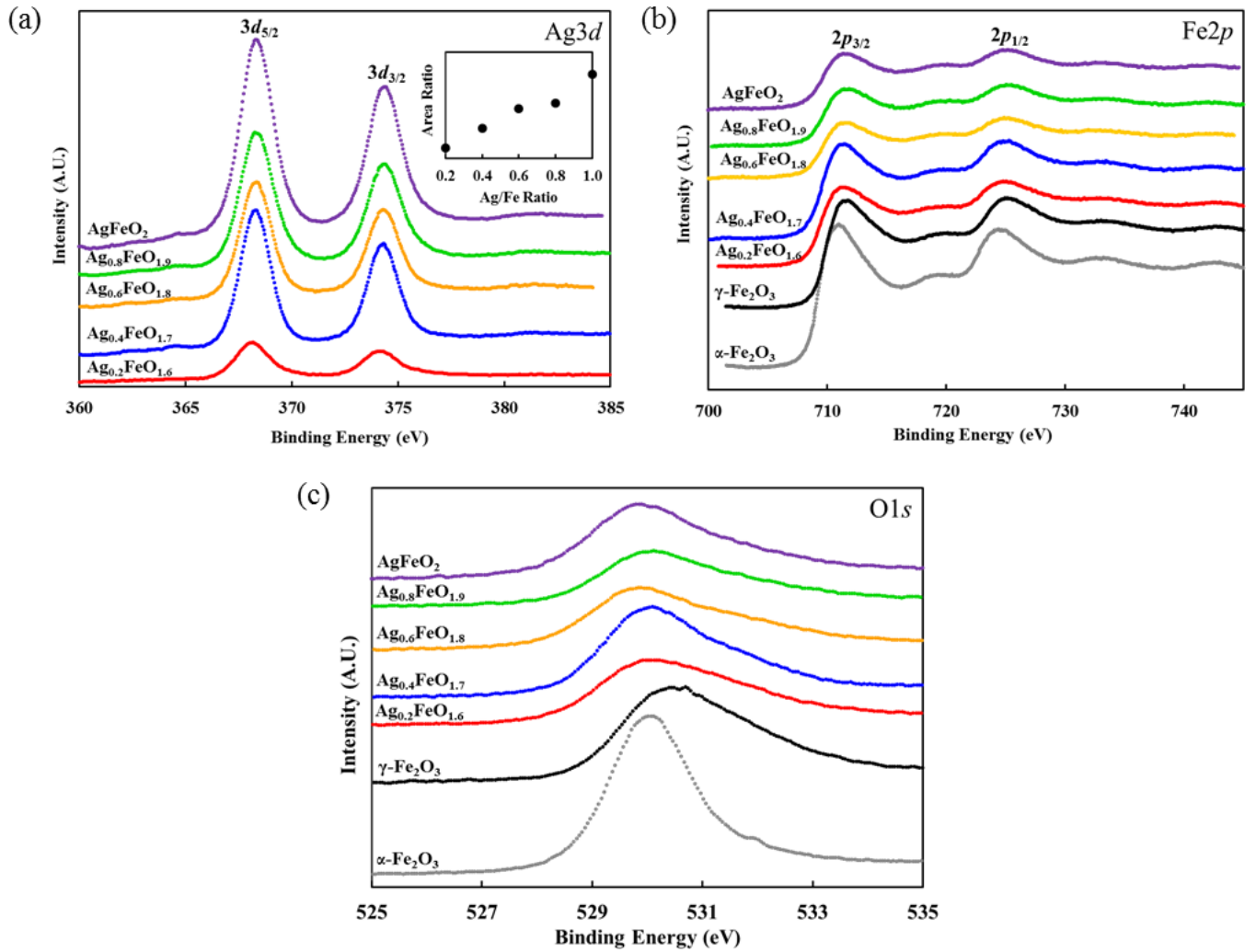

Figure 5.12. XPS (a) Ag3d, (b) Fe2p, and (c) O1s core-level spectra for silver ferrite samples with commercial α-Fe_2O_3 and γ-Fe_2O_3 as reference materials (d) ratio of Ag3$d_{5/2}$, Fe2$p_{3/2}$ peak areas as a function of silver content

5.3.6 Thermal Stability and Oxygen Content

In addition to structural and compositional aspects of silver ferrite, the thermal stability was investigated. Sheets et al. conducted a TGA experiment in 2008 that effectively quantified the oxygen content of ternary silver delafossite oxides.[98] Delafossite samples were placed in platinum thermogravimetric analysis pans and heated from 30°C–1000°C under an atmosphere of nitrogen gas. The decomposition of silver delafossites ($AgAlO_2$, $AgGaO_2$, $AgInO_2$, $AgScO_2$) in this study was observed between 600 and 800°C.

The reaction proposed to occur in the 600–800°C range is the decomposition of $AgMO_2$ (M = trivalent transition metal cation) into silver metal and the corresponding metal oxide, M_2O_3 (**Equation 5.3**). XRD of the TGA samples, after decomposition, confirmed the presence of both silver metal and M_2O_3. The following equation was used to determine the oxygen content parameter (δ) by using the percent weight loss of each sample:[98]

$$4\ Ag_{1+x}M^{3+}{}_{1+y}O_{1+\delta} \xrightarrow{\Delta} 4(1+x)\ Ag_{(metal)} + 2(1+y)\ M_2^{3+}O_3 + (1+2\delta-6y)\ O_2 \quad (5.3)$$

The aforementioned TGA experiment conducted by Sheets and coworkers is an ideal method to measure the oxygen content of stoichiometric $AgFeO_2$ and Ag_xFeO_y composites. The proposed silver ferrite formulas anticipate that there should be a difference in oxygen content within the series. Previous literature reports the decomposition of $AgFeO_2$ at 700°C which is similar to the decomposition temperature of the silver delafossites studied by Sheets et al.[78,82]

Thermogravimetric analysis (TGA) was conducted to measure the oxygen content and monitor the thermal decomposition of distinct silver ferrite composites (Ag_xFeO_y, x = 0.2, 0.4, 0.6, 0.8; $y = 2$ ((1-x)/2)) compared to $AgFeO_2$. The reaction that occurs during decomposition of silver ferrite composites, adapted from Sheet's previous work, is the conversion of $AgFeO_2$ to silver metal, solid α-Fe_2O_3, and O_2 gas (**Equation 5.4**). The percent weight loss during decomposition corresponds to the evolution of O_2 which can be used to precisely

calculate the oxygen content of $AgFeO_2$ and Ag_xFeO_y composites.

$$4\ Ag_xFeO_y \xrightarrow{\Delta} 4x\ Ag_{(metal)} + 2\ \alpha\text{-}Fe_2O_3 + x\ O_2 \left(0.2 \leq x \leq 1.0, y = 2 - \frac{1-x}{2}\right) \quad (5.4)$$

In the TGA decomposition profile, desolvation of water molecules from the surface and within the silver ferrites layered framework is initially observed from room temperature to approximately 300°C for all materials (**Figure 5.13**). Notably, absorbed water (10–12 weight %) incorporated in Ag_xFeO_y composites with small crystallite sizes and low silver content ($x = 0.2$, 0.4) considerably exceeds that of high silver content materials (4–6%), see **Figure 5.13 a**.

Ultimately, the increase in water is influenced by the presence of amorphous maghemite (γ-Fe_2O_3) which comprises a large majority of the composition of Ag_xFeO_y composites in the low silver regime and displays >20% absorbed water by weight in the same temperature range (**Figure 5.13 a**). The TGA profile of semi-crystalline γ-Fe_2O_3 agrees with previous thermal analysis of maghemite nanoparticles in the literature where γ-Fe_2O_3 exhibits dehydration of the structure and decomposition to α-Fe_2O_3.[162] Therefore, increased evolution of water in Ag_xFeO_y composites (x <0.4) can be directly attributed to the presence of poorly crystalline maghemite which allows for a larger quantity of the composite's surface area to be exposed to the ambient environment.

TGA was also used to monitor the decomposition temperature of silver ferrite composites, which was observed between 480 and 640°C, as a function of x or Ag/Fe ratio (**Figure 5.13 b**). The decomposition temperatures of Ag_xFeO_y composites ($x = 0.2$, 0.4, 0.6, 0.8; $y = 2 - ((1-x)/2)$) and $AgFeO_2$ are lower than those previously measured for silver delafossites (600–800°C).[98] It can be seen that decreased thermal stability is particularly significant for those materials with low values of x and small crystallite size and is likely due to a combination of the nanocrystalline nature of the composite material and increased quantities of amorphous maghemite. In this region, the weight loss during decomposition of $AgFeO_2$ and Ag_xFeO_y

composites corresponds to the evolution of O_2 which can be used to precisely calculate the oxygen content of diverse silver ferrite samples. Maghemite (γ-Fe_2O_3), while a major component of non-stoichiometric Ag_xFeO_y composites, does not affect the decomposition profile in the region of interest.

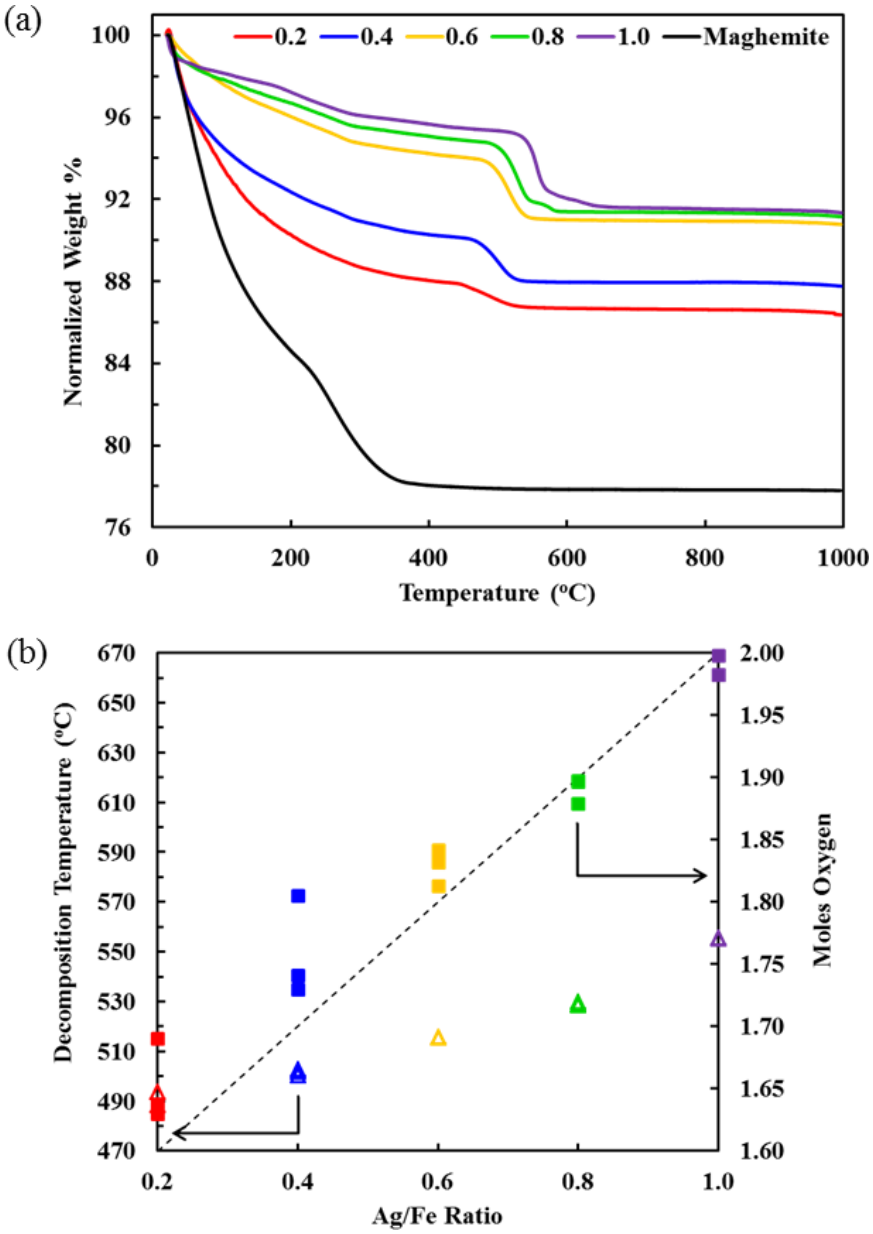

Figure 5.13. (a) Percent weight loss via thermogravimetric analysis (TGA) and (b) decomposition temperature (triangles), oxygen content (squares), and anticipated oxygen content (dashed line) of Ag_xFeO_y ($0.2 \leq x \leq 0.8$), $AgFeO_2$, and γ-Fe_2O_3

Post-analysis of TGA samples via XRD confirms the exclusive presence of silver metal (Ag^0) and hematite (α-Fe_2O_3) and the absence of $AgFeO_2$ (**Figure A13**) which was predicted per the decomposition reaction in **Equation 5.4**. A difference in oxygen content is expected as x in Ag_xFeO_y changes due to silver remaining in the +1 oxidation state and iron in the +3 oxidation state. The oxidation states of silver and iron in Ag_xFeO_y ($0.2 \leq x \leq 0.8$) and $AgFeO_2$ were determined through X-ray absorption spectroscopy as previously reported.[155] Knowing the starting material, end-products, and weight loss during breakdown of the silver ferrite structure, calculations can be performed to determine the precise amount of oxygen lost during the process and the overall oxygen content of the starting material. The calculated oxygen content (dashed line in **Figure 5.13 b**) corresponds well with the calculated experimental oxygen content of various silver ferrite materials and portrays a linear trend that decreases as x decreases. Silver ferrite containing materials can be denoted by Ag_xFeO_y ($0.2 \leq x \leq 1.0$) in which the amount of oxygen (y) in the chemical formula depends on x (**Equation 5.4**).

5.4 Conclusion

The one-pot, aqueous co-precipitation reaction proves to be an acceptable method for preparing Ag_xFeO_y composites, composed of $AgFeO_2$ and γ-Fe_2O_3, with reliable control of chemical composition and crystallite size. The composite nature of Ag_xFeO_y composites was established using several characterization techniques, including X-ray diffraction (XRD), Raman spectroscopy, X-ray photoelectron spectroscopy (XPS), thermogravimetric analysis (TGA), and X-ray absorption spectroscopy (XAS). Notably, electron imaging by TEM and SEM provided a local examination of the nanocrystalline structure of Ag_xFeO_y composites prepared by a one-pot co-precipitation technique and confirmed the presence of both $AgFeO_2$ and a poorly crystalline γ-Fe_2O_3 phase in intimate contact. The physical properties, surface area and thermal stability, of Ag_xFeO_y composites and $AgFeO_2$ were investigated and illustrated a significant dependence on maghemite, γ-Fe_2O_3, concentration. The synthetic approach demonstrated in Chapter V provides a new paradigm for composite synthesis,

which may be applicable toward new materials with energy storage applications.

CHAPTER VI

ELECTROCHEMICAL PERFORMANCE OF $AgFeO_2$ AND A SERIES OF ONE-POT $AgFeO_2/\gamma$-Fe_2O_3 COMPOSITES

6.1 Introduction

The delafossite mineral group consists of layered metal oxides with the general chemical formula ABO_2 (typically, A = 1+ metal cation, B = 3+ metal cation) and includes possible candidates for lithium-based secondary batteries owing to their layered crystalline motif which facilitates 2-D transport of ions within the structure. A limited number of reports in the literature describe the use of ABO_2 delafossite-type oxides in batteries, especially those based on lithium. Studies of $AgNiO_2$ in alkaline and zinc batteries,[86,87] $CuFeO_2$ as an anode in lithium-ion batteries,[89] or $AgCuO_2$, $AgCu_{0.5}Mn_{0.5}O_2$, and $CuFeO_2$ as cathodes in lithium-type batteries[85,88] have been reported. Further, delafossite-type cathodes that incorporate silver cations (A = Ag^+) into the layered structural motif are of special interest, due to the possibility for *in-situ* generation of an electrically conductive percolation network of Ag^0 metallic nanoparticles during lithiation of $AgFeO_2$. This paradigm was first established with silver vanadium oxide ($Ag_2V_4O_{11}$),[163] then later extended to silver vanadium phosphorous oxide ($Ag_2VO_2PO_4$)[67,106,107,164] and recently to silver ferrite ($AgFeO_2$)[75] by the Takeuchi group.

The impact that composition and crystallite size have on electrochemical behavior of transition metal oxide cathodes, such as magnetite (Fe_3O_4) and silver hollandite ($Ag_xMn_8O_{16}$)), has been reported by the Takeuchi group in the past.[63,64,109,165,166] Control of chemical and physical properties of transition metal oxides provides fundamental insight into electrochemical behavior. Smaller crystallite sizes of Fe_3O_4 and $Ag_xMn_8O_{16}$ result in higher surface area to volume ratios, thus decreasing the path length associated with ion transfer and allowing for the electrode material to facilitate the transfer of ions via faster rate kinetics. As the crystallite sizes of Fe_3O_4 and $Ag_xMn_8O_{16}$ decrease, the cathode material can achieve higher

discharge capacities and display enhanced rate performance.

Preliminary studies of nanostructured silver ferrite cathode materials demonstrated that $AgFeO_2$, 31 nm, is electrochemically active.[54,75] When used as a cathode material in lithium-based batteries, $AgFeO_2$ displayed consistent discharge capacities in excess of 50 mAh/g for 50 cycles. Examination of the discharged $AgFeO_2$ cathode via XRD and SEM reveals the presence of Ag^0 on the surface, a metallic species which has the ability to enhance conductivity by initiating the formation a percolation network of conductive nanoparticles. Such data indicates the potential of using $AgFeO_2$ as a rechargeable cathode material.

In Chapter VI, the electrochemistry of one-pot prepared Ag_xFeO_y composites *versus* semi-crystalline γ-Fe_2O_3 are compared using galvanostatic cycling, AC impedance, GITT testing, and cyclic voltammetry. Electrochemically cycled cathodes are then probed by a variety of *ex-situ* characterization techniques including XRD, X-ray absorption spectroscopy (XAS), and scanning electron microscopy (SEM) to provide insight into the discharge process of Ag_xFeO_y composites and $AgFeO_2$. The results demonstrate profound differences between Ag_xFeO_y composites, $AgFeO_2$, and γ-Fe2O3 as cathode materials in a lithium-based battery application.

6.2 Experimental

6.2.1 Characterization

X-ray absorption spectroscopy (XAS) measurements were acquired at the iron K-edge (7.112 keV) at sector 12-BM at the Advanced Photon Source at Argonne National Laboratory, Argonne, IL. Positive electrodes were removed from electrochemical cells at specific states of discharge, sealed between polyimide tape, and stored under inert atmosphere until XAS measurements were collected. Samples were mounted perpendicular to the incident X-ray beam and measured in transmission mode with 100% He and N_2 filling the incident and transmission ion chambers, respectively. A reference Fe metal foil was used for initial X-ray beam energy calibration and was measured simultaneously with silver ferrite electrodes

to facilitate proper alignment of multiple scans and allow for accurate comparison of X-ray absorption near-edge structure (XANES) shifts from which oxidation state as a function of discharge state was observed. A JEOL JSM-6010PLUS electron microscope was used to collect SEM images of silver ferrite/maghemite composites in secondary electron (SE) imaging mode or back-scattered electron (BSE) composition imaging mode. EDS was employed during SEM to map and quantitatively assess elemental Ag, Fe, and O composition.

6.2.2 Electrochemistry

CR 2320 coin cell batteries were used to probe the electrochemical performance of stoichiometric silver ferrite and silver ferrite composites varying crystallite sizes and compositions. Composite electrodes were prepared by mixing silver ferrite with conductive carbon and PVDF binder for a composition of 85% active material, 5% Super P conductive carbon black, 5% graphite, and 5% binder and coating onto an aluminum foil substrate. The coatings were dried under vacuum for 12 hours and, to ensure intimate contact of the electrode material with the aluminum current collector, pressed using a hydraulic press to afford a thin film with a thickness $\sim$2 μm. Electrodes were cut into circular discs, 0.5 inches or 1.27 cm in diameter, with a single electrode containing an average of 3.5 mg active material. An electrolyte solution of 1 M $LiPF_6$ in 30/70 (*v/v*) ethylene carbonate/dimethyl carbonate was used for galvanostatic cycling and galvanostatic intermittent titration technique (GITT) tests. Galvanostatic cycling, over a 50 cycle range, and GITT testing was performed on a Maccor Series 4000 Battery Test System in a chamber maintained at 30°C. Galvanostatic cycling tests were conducted using a two electrode assembly with lithium metal anode and an applied current of 0.15 mA/cm^2 between 1.5–3.5 V. GITT testing was employed with intermittent discharge (0.006 mA/cm^2) followed by open circuit rest. A 1 M $LiBF_4$ in 50/50 (*v/v*) ethylene carbonate/dimethyl carbonate electrolyte was used for cyclic voltammetry. Cyclic voltammetry data was collected using a three-electrode assembly containing lithium metal reference and auxiliary electrodes at room temperature. A rate of 0.05 mV/s was applied to the three-electrode cells for three consecutive cycles between voltage limits of 3.5

and 1.2 V.

6.2.3 Acknowledgment of Collaboration

The research in Chapter VI was conducted in collaboration with Dr. Christopher Pelliccione (Stony Brook University) who collected and analyzed the XAS data.

6.3 Electrochemical Evaluation

6.3.1 Cyclic Voltammetry

To investigate the redox properties of Ag_xFeO_y composites, $AgFeO_2$, and synthesized γ-Fe_2O_3, cyclic voltammetry data (1.2–3.5 V) was collected at a scan rate of 0.05 mV/sec using a three-electrode assembly containing lithium metal reference and auxiliary electrodes at room temperature. An irreversible peak near 1.7 V is observed in the first cathodic scan of Ag_xFeO_y composites and $AgFeO_2$ (**Figure 6.1**). The intensity of this peak decreases linearly as x decreases in Ag_xFeO_y (**Figure 6.1**, inset) and can be directly correlated to the irreversible reduction of $Ag^+ \rightarrow Ag^0$ and reduction of Fe^{3+} where stronger peaks are associated with higher capacities. The irreversible reduction of $Ag^+ \rightarrow Ag^0$ at 1.7 V has recently been observed in a lithium battery containing an $Ag_2C_8H_4O_4$ electrode with strong evidence of Ag^0 via diffraction after discharge.[167] There is also a noticeable shift in the potential of this peak as a function of x in Ag_xFeO_y which can be explained with two arguments. First, the peak is situated at 1.75, 1.69, and 1.65 V for $AgFeO_2$, $Ag_{0.8}FeO_{1.9}$, and $Ag_{0.6}FeO_{1.8}$ composite materials, respectively, and the shift to lower potential of low silver content materials ($x = 0.6$ and 0.8) can be rationalized as an increase in the γ-Fe_2O_3 component which leaves less Ag^+ to be reduced. Second, $Ag_{0.4}FeO_{1.7}$ and $Ag_{0.2}FeO_{1.6}$ display less polarization, shifting to 1.73 and 1.74 V, respectively, due to the decreased crystallite size which is less stable. The shift of Ag_xFeO_y composites with low silver content (x) can be rationalized as decreased stability of the small crystallite size material which leads to lower polarization upon reduction.

The first anodic peak appears around 1.9 V for high silver Ag_xFeO_y composites ($x = 0.8$,

1.0) suggesting oxidation of $Fe^{2+} \rightarrow Fe^{3+}$ which has been observed previously in α-Fe_2O_3 and γ-Fe_2O_3 electrodes for lithium batteries.[168–170] In addition, an irreversible anodic peak is present low silver Ag_xFeO_y composites ($x = 0.2$, 0.4) at approximately 3.2 V. Irreversible cathodic and anodic peaks at 1.7 and 1.9 V, respectively, dissipate by cycle 2 while the irreversible anodic peak at 3.2 V is still partially visible in $Ag_{0.2}FeO_{1.6}$ during cycle 3 (**Figure A14**).

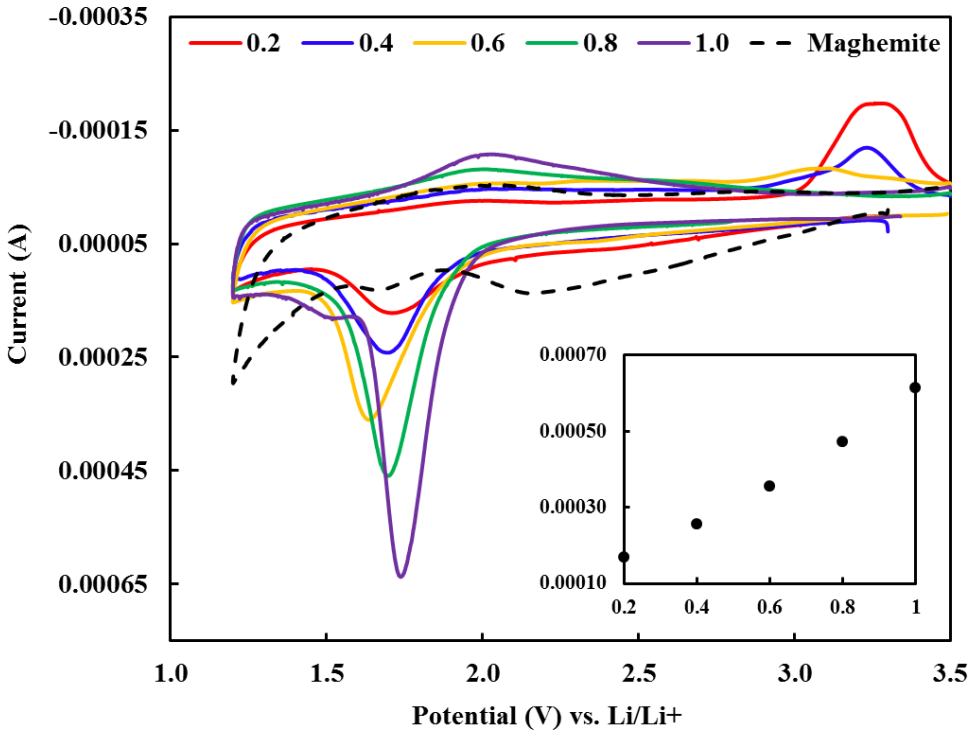

Figure 6.1. Cyclic voltammetry (CV) of $Li/AgFeO_2$, Li/Ag_xFeO_y ($x = 0.2$, 0.4, 0.6, 0.8), and Li/γ-Fe_2O_3 electrochemical cells with a scan rate of 0.05 mV/s. The intensity of 1.7 V anodic peak is inset

After the first cycle, successive scans reveal reversible peaks at lower current values which are consistent with the reversibility of Ag_xFeO_y composites and $AgFeO_2$. For comparison, cyclic voltammetry of nanocrystalline, synthesized γ-Fe_2O_3 was collected (**Figure 6.1**). In relation to Ag_xFeO_y composites, γ-Fe_2O_3 exhibits a unique cycle 1 profile with irreversible cathodic peaks at 1.7 and 2.2 V. A separate small cathodic peak appears near 1.5 V in cycle 2 during the redox of γ-Fe_2O_3. By cycle 3, the scan demonstrates decrease current values and a reversible pattern similar to Ag_xFeO_y composites (**Figure A14**). While a major component

of Ag_xFeO_y composites with low values of x, the contribution of maghemite to the redox behavior is not significant and the cyclic voltammogram of Ag_xFeO_y materials more closely resemble that of $AgFeO_2$.

6.3.2 Galvanostatic Cycling

To probe the contribution that Ag/Fe and maghemite content have on electrochemistry, galvanostatic cycling of Li/$AgFeO_2$, Li/Ag_xFeO_y, and Li/γ-Fe_2O_3 cells was conducted. The delivered capacities during cycling of Ag_xFeO_y composites, $AgFeO_2$, and synthesized γ-Fe_2O_3 electrodes are relatively stable from cycles 3 to 50, illustrating reversibility of the redox mechanism (**Figure 6.2**).

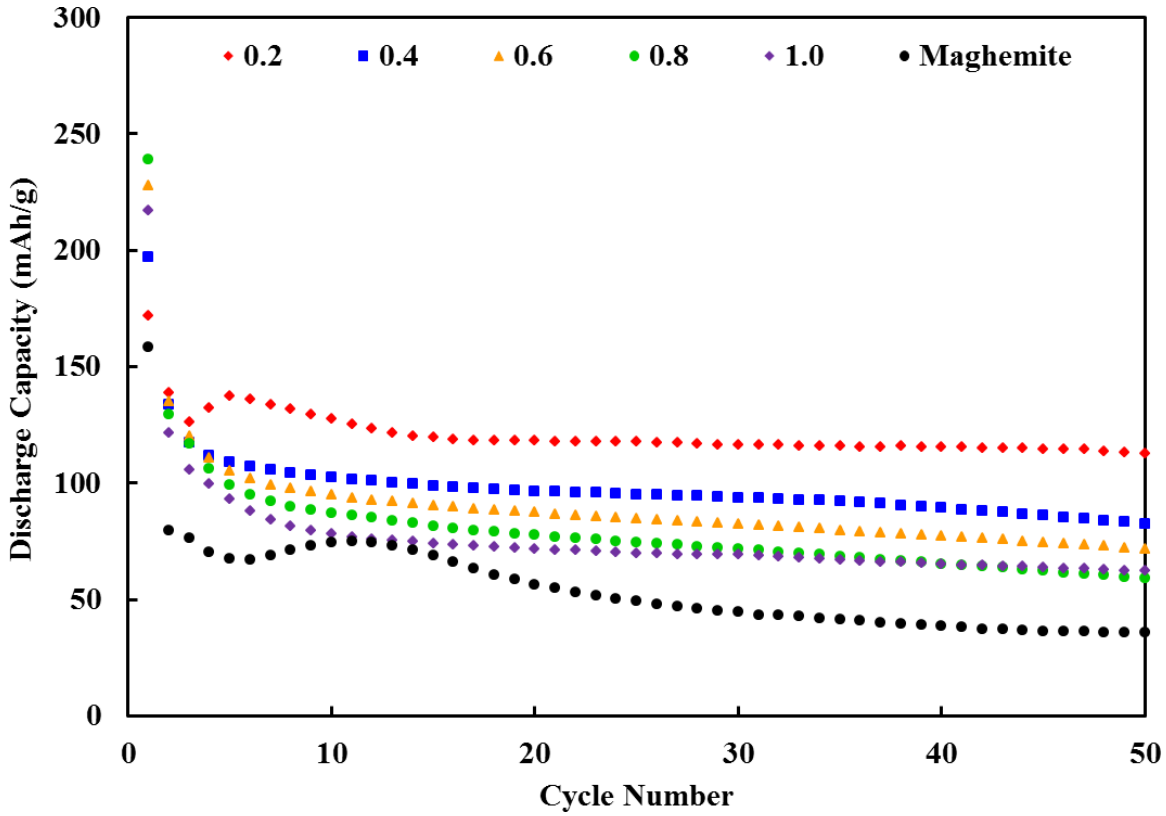

Figure 6.2. Galvanostatic cycling of Li/$AgFeO_2$, Li/Ag_xFeO_y (x = 0.2, 0.4, 0.6, 0.8), and Li/γ-Fe_2O_3 electrochemical cells with discharge capacity plotted over 50 cycles

Notably, there is a significant decrease in the discharge capacity between cycles 1 and 2 in **Figure 6.2** where the change in capacity is directly proportional to the Ag^+ content

of Ag_xFeO_y when considered with respect to electron equivalents. The change in discharge capacity between cycles 1 and 2 has been rationalized as the reduction of $Ag^+ \rightarrow Ag^0$ and is confirmed by the linear trend in a plot of electron count as a function of silver content (**Figure 6.3**).[155,156] Ag_xFeO_y composites with greater values of x show more substantial capacity change between cycle 1 and cycle 2 and these results imply that once formed, a portion of the silver metal is no longer electrochemically active.

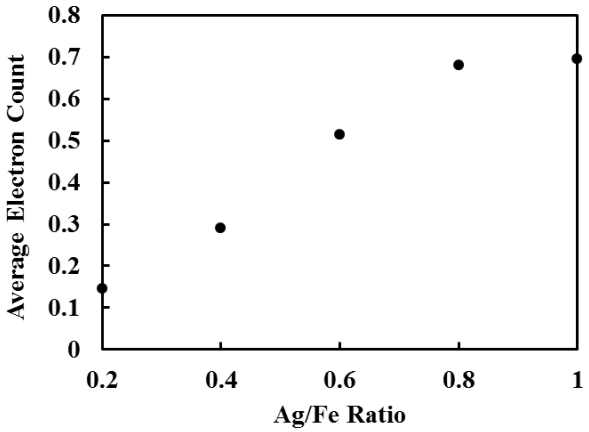

Figure 6.3. Difference in electron equivalents discharged between cycles 1 and 2 as a function of silver content for $AgFeO_2$ and Ag_xFeO_y composites (x = 0.2, 0.4, 0.6, 0.8)

A voltage plateau in the discharge region of cycle 1 (**Figure 6.4**) is observed near 1.8 V for $AgFeO_2$ and slightly increases for Ag_xFeO_y composites, the potential is consistent with the CV data which demonstrates Ag^+ reduction in the same region. The discharge voltage plateau disappears by cycle 2 which is expected due to the irreversible reduction of Ag^+ to Ag^0. Comparison of the cycle 1, 2, and 50 discharge profiles in **Figure 6.4** for Ag_xFeO_y composites and $AgFeO_2$ shows substantial change in efficiency among silver ferrite composites and stoichiometric $AgFeO_2$. Voltages profiles of Ag_xFeO_y composites (x = 0.2, 0.4, 0.6, 0.8) and $AgFeO_2$ are also included in **Figure A15** where they include charge curves and are separated by cycle. During cycle 1, the composite with the lowest silver ferrite content ($Ag_{0.2}FeO_{1.6}$) delivers only 72% of the discharge capacity of highest performing composite, $Ag_{0.8}FeO_{1.9}$ (239 mA/g). All materials exhibit relatively similar electrochemistry after reaching the end of cycle 2. However, the opposite trend is seen by cycle 50 when

$Ag_{0.2}FeO_{1.6}$ consistently delivers approximately 2X the discharge capacity (113 mAh/g) of the lowest performing cathode material, $Ag_{0.8}FeO_{1.9}$.

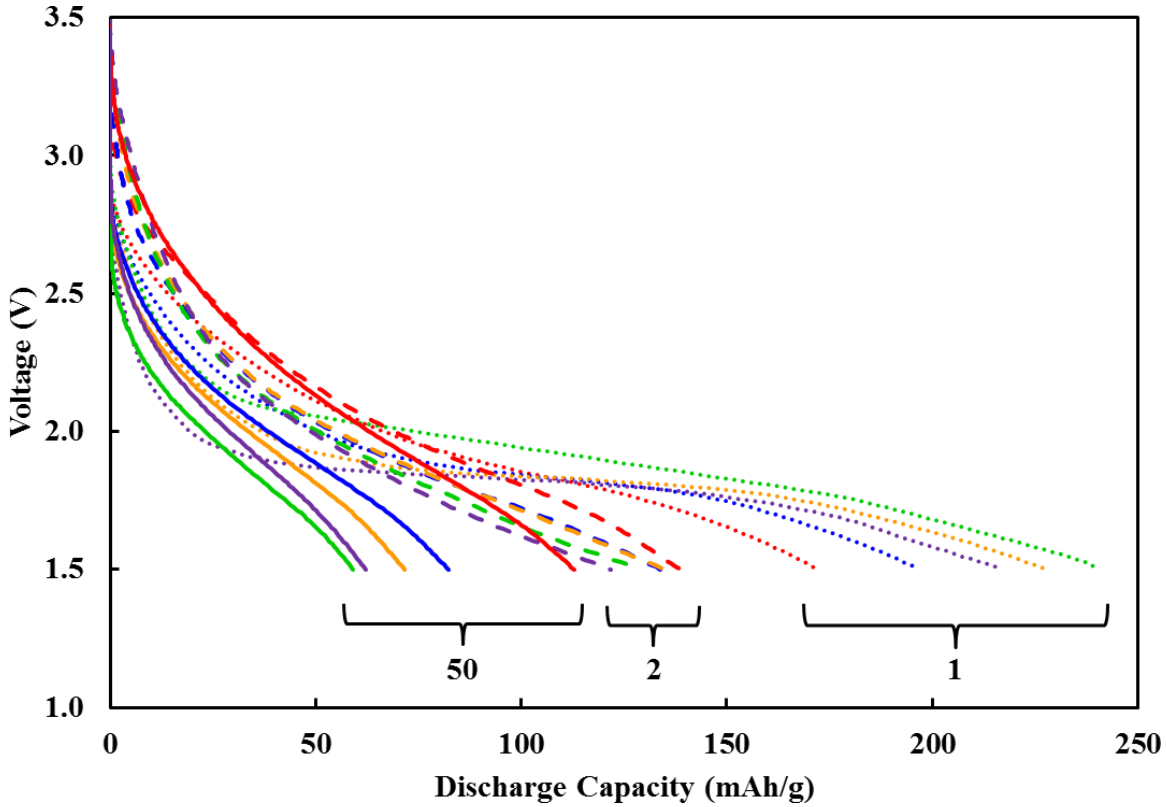

Figure 6.4. Capacity plotted as a function of voltage for $Li/AgFeO_2$ and Li/Ag_xFeO_y ($x =$ 0.2, 0.4, 0.6, 0.8) cells during galvanostatic cycling at cycles 1, 2, and 50

The stable cycle life and increased capacity of $Ag_{0.2}FeO_{1.6}$ compared to high silver ferrite content Ag_xFeO_y composites and $AgFeO_2$ is associated with the overall composition, decreased crystallite size, and increased surface area of the composite material. High surface area and inherent nanocrystallinity generate a decrease in the path length associated with ion transport within the cathode material which effectively lowers the kinetic ion transfer rate associated with discharge/charge processes. It is also evident from **Figure 6.2** that $Ag_{0.2}FeO_{1.6}$ displays distinct cycling profiles, especially within the initial 15 cycles, compared to Ag_xFeO_y composites with increasing x and $AgFeO_2$. A noticeable increase in capacity is observed between cycles 3–5 which begins to decrease and subsequently reach equilibrium, thus resulting in a peak-shaped curve near the beginning of the profiles. The shape of the

voltage profile of $Ag_{0.2}FeO_{1.6}$ (i.e. a composite comprised of γ-Fe_2O_3 and $AgFeO_2$ in which the silver/iron ratio is 0.2/1.0) is reminiscent of synthesized, semi-crystalline γ-Fe_2O_3 which demonstrates a similar peak with an onset 3 cycles later and slightly longer duration. Although maghemite contributes to the composites electrochemical behavior to some extent, the presence of $AgFeO_2$ significantly enhances the discharge capacity of $Ag_{0.2}FeO_{1.6}$ (113 mAh/g) by over 200% compared to semi-crystalline γ-Fe_2O_3 (36 mAh/g) over 50 cycles. The performance of the $Ag_{0.2}FeO_{1.6}$ composite with low silver content also demonstrates significant improvement over stoichiometric $AgFeO_2$ with an 82% increase in capacity (113 mAh/g) during discharge. These data indicate the advantage of fabricating an electrode using a composite of two different materials with unique properties rather than using a single material.

6.3.3 AC Impedance

Electrochemical impedance spectroscopy (EIS) was used to study the electrochemical processes at the electrode surface and within the bulk electrode to gain mechanistic insight into the electrochemistry of Ag_xFeO_y composites and $AgFeO_2$. Impedance measurements were initially collected for non-discharged electrochemical cells containing electrodes with representative Ag_xFeO_y materials ($x = 0.2$, 0.6, and 1.0), then collected again after the cells were discharged to 1 molar electron equivalent (partial discharge) and 2 electron equivalents (full discharge). Nyquist plots at various depths of discharge are illustrated in **Figure 6.5** for $AgFeO_2$, $Ag_{0.6}FeO_{1.8}$, and $Ag_{0.2}FeO_{1.6}$, respectively. The impedance data was fit to the equivalent circuit models in **Figure 6.4 a** where non-discharged and discharged cells were fit with separate circuits and the corresponding resistance values from fitting are summarized in **Table 6.1**. The equivalent circuits contain R, CPE, and Wo elements which correspond to resistance, double layer capacitance, and Warburg impedance, respectively, where discharged cells are modeled to a Randles circuit while non-discharged cells are modeled to a simplified version of the Randles circuit consisting of elements based on a series of RC Voigt-type analogs.

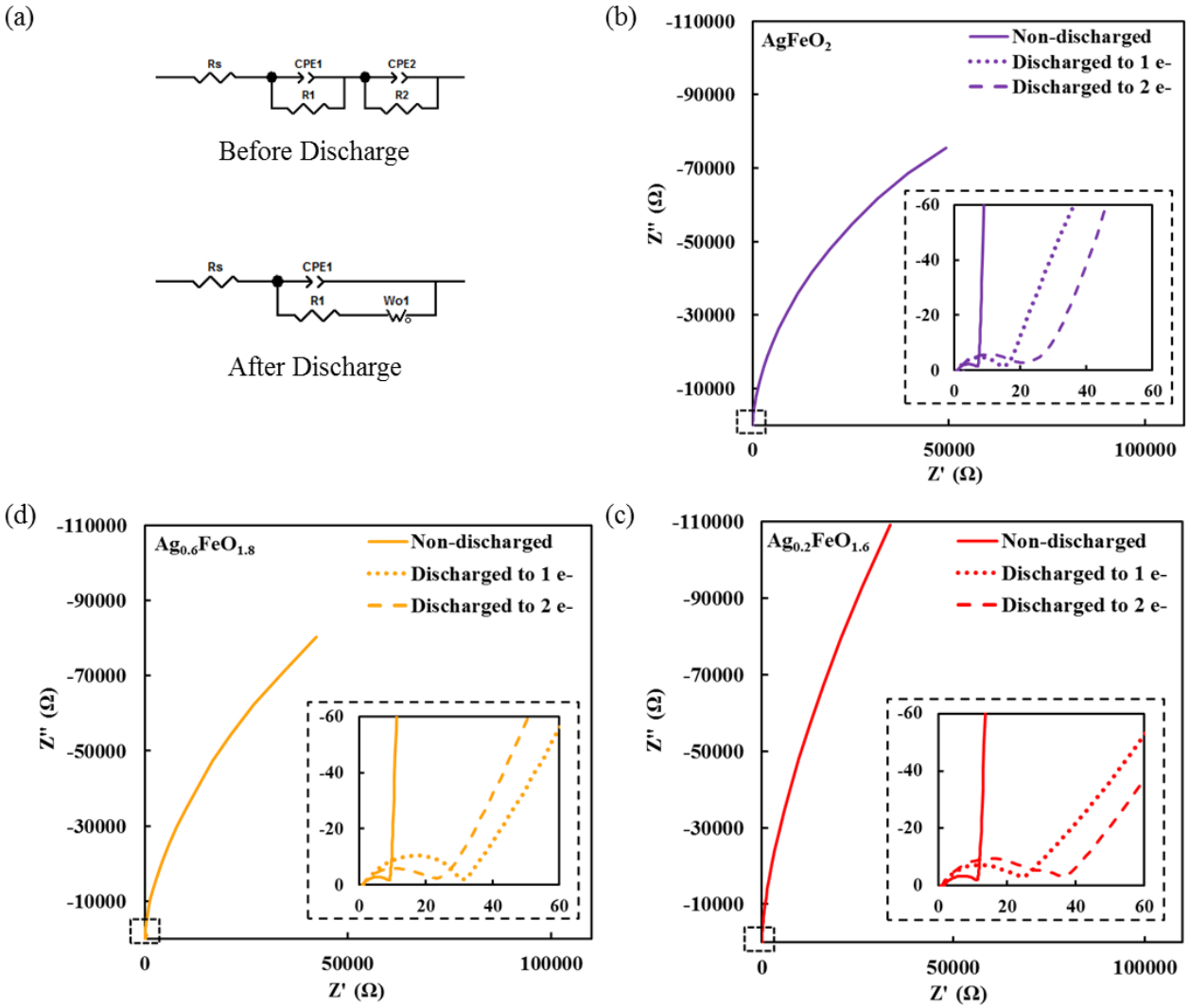

Figure 6.5. (a) Equivalent circuits used to fit AC impedance. Nyquist plots of representative materials: (b) $AgFeO_2$, (c) $Ag_{0.6}FeO_{1.8}$, and (d) $Ag_{0.2}FeO_{1.6}$

The Nyquist plots of non-discharged cells (**Figure 6.5 b-d**) exhibit a small semi-circle on the order of 6-10 Ω (R_1), indicating fast charge-transfer at the electrode interface and a tail that is sufficiently large and does not mimic typical Warburg-like diffusion. The magnitude of the impedance response (R_2) in the low frequency regime of non-discharged cells containing Ag_xFeO_y and $AgFeO_2$ electrodes is attributed to the transport of Li^+ within the electrode. This region was modeled using R_2 due to the curved shape of the Nyquist plots which could not be fit using a Warburg element. Significant resistance is observed in the low frequency region of non-discharged electrodes and suggests that the electrochemical

system is controlled by kinetics in the bulk electrode rather than diffusion.

Upon discharge or reduction of the electrochemical cells, a dramatic decrease in the low frequency region of the Nyquist plot is observed for Ag_xFeO_y (x = 0.2, 0.6) composites and $AgFeO_2$ electrodes. As anticipated, the ohmic resistance (R_s), commonly associated with resistance due to the electrolyte, remains consistent among all cells both before and after discharge. The charge-transfer resistance at the electrode/electrolyte interface (R_1) increases by over a factor of two across the series, after reduction, to approximately 12-30 Ω and is likely due to the formation of a resistive SEI layer on the surface of the electrode. It is important to note that the charge transfer resistance value (R_1) remains small demonstrating an inherent fast rate of charge-transfer at the electrode surface which is, in part, influenced by the presence of conductive carbon in the composite cathode.

Table 6.1. EIS fitting results of resistance in Ag_xFeO_y/Li cells at various depths of discharge

Discharge Depth (electron equiv.)		**0**	**1**	**2**
$AgFeO_2$	**R_s (Ω)**	1.08 ± 0.01	1.17 ± 0.008	1.25 ± 0.008
	R_1 (Ω)	6.33 ± 0.02	12.57 ± 0.06	17.76 ± 0.06
	R_2 (Ω)	100800 ± 3400		
$Ag_{0.6}FeO_{1.8}$	**R_s (Ω)**	1.08 ± 0.008	1.41 ± 0.02	1.17 ± 0.01
	R_1 (Ω)	8.34 ± 0.03	29.18 ± 0.13	18.95 ± 0.13
	R_2 (Ω)	104790 ± 5847		
$Ag_{0.2}FeO_{1.6}$	**R_s (Ω)**	1.74 ± 0.01	1.20 ± 0.01	1.08 ± 0.02
	R_1 (Ω)	10.10 ± 0.04	19.37 ± 0.19	28.36 ± 0.29
	R_2 (Ω)	180000 ± 13900		

The evolution of the low-frequency tail in discharged materials to emphasize Warburg diffusion of lithium ions, rather than kinetics, is a direct result of the increased conductivity of the cathode material. For this reason, the impedance response of discharged electrodes was modeled using a Warburg element (Wo) which represents the diffusion of Li^+ ions within the

bulk electrode. As established in a prior report, reduction of Ag^+ to metallic Ag^0 nanoparticles is observed in Ag_xFeO_y composites and $AgFeO_2$ upon discharge. The resistivity of the entire Ag_xFeO_y system decreases by nearly 6,000-fold upon discharge to 2 electron equivalents (**Table 6.1**). A similar phenomenon has been observed in a silver vanadium phosphorous oxide ($Ag_2VP_2O_8$) cathode material where the formation of Ag^0 during discharge significantly decreased the impedance of the cell from ~1 MΩ before discharge to ~500 Ω after discharge to 0.5 electron equivalents.

6.3.4 Galvanostatic Intermittent Titration Technique (GITT)

Galvanostatic intermittent titration technique (GITT) tests were carried out on two-electrode cells containing lithium metal anodes to examine the electrochemical kinetics of Ag_xFeO_y composites and $AgFeO_2$. Significant difference in polarization was discovered in Ag_xFeO_y and $AgFeO_2$ electrodes upon reduction. $Ag_{0.2}FeO_{1.6}$ illustrated higher operating voltages and decreased polarization during discharge to ~ 150 mA/g (**Figure 6.6**).

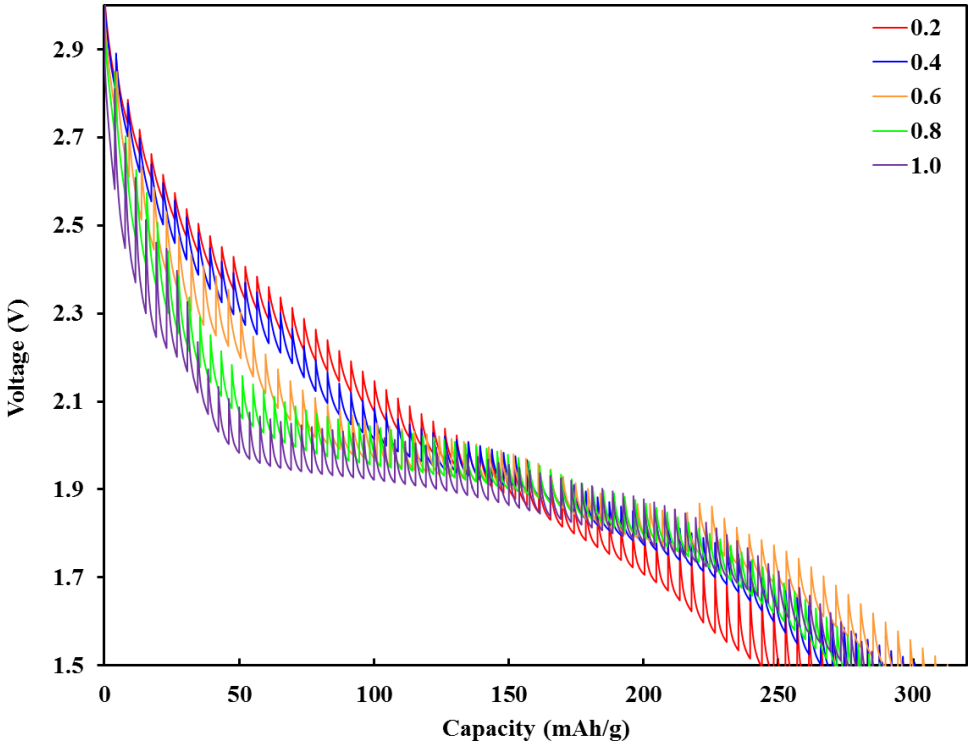

Figure 6.6. Capacity as a function of voltage for $AgFeO_2$/Li and Ag_xFeO_y/Li cells during GITT testing

Ag_xFeO_y composites with lower values of x demonstrate a sloped voltage profile throughout the discharge, whereas, $AgFeO_2$ shows a steep voltage change to 2.0 V followed by a broad plateau (**Figure 6.6**). The length of the 2.0 V plateau decreases with both crystallite size and silver content (x). GITT and cycling results are consistent with reduction of silver ion (Ag^+) to silver metal (Ag^0) and reduction of Fe^{3+} to Fe^{2+} during discharge. The reduction of Ag^+ to Ag^0, a displacement reaction, would be expected to result in higher polarization which is observed for high silver content materials as larger voltage drops at the beginning of discharge. It should be noted that Ag_xFeO_y composites with lower values of x demonstrate higher surface area, as seen with the BET measurements in **Table 5.1**, which is also a contributing factor to the decreased polarization.

6.3.5 *Ex-Situ* Analysis of Cathodes as a Function of Discharge/Charge

XRD of Ag_xFeO_y cathodes ($x = 0.2, 0.6, 1.0$), under inert atmosphere to prevent oxidation of reduced species, reveals the absence of crystalline material after a full discharge (**Figure 6.7**). The most intense reflections of crystalline $AgFeO_2$ in the composite cathode are visible near 2θ values of 30° and 60° in non-discharged coatings; however, these peaks are not distinguishable by XRD after the sample has been fully discharged to 2 electron equivalents. Scanning electron microscopy (SEM) analysis of an $AgFeO_2$ cathode upon discharge using BSE imaging displays localized areas of light contrast (high Z element, Ag) within the electrode (**Figure 6.8 a**). Point energy dispersive spectroscopy (EDS) was used for elemental analysis of a specified region (yellow circle) in the BSE image at a magnification of x3,000. The region was found to contain significant amounts of silver (Ag/Fe = 15.79), indicating that Ag^0 nanoparticles displaced upon reduction accumulate in localized areas of the electrode. In particular, the metallic Ag^0 nanoparticles formed upon reduction are so nanocrystalline that they cannot be detected by XRD; therefore, a more sensitive means of detection is critical.

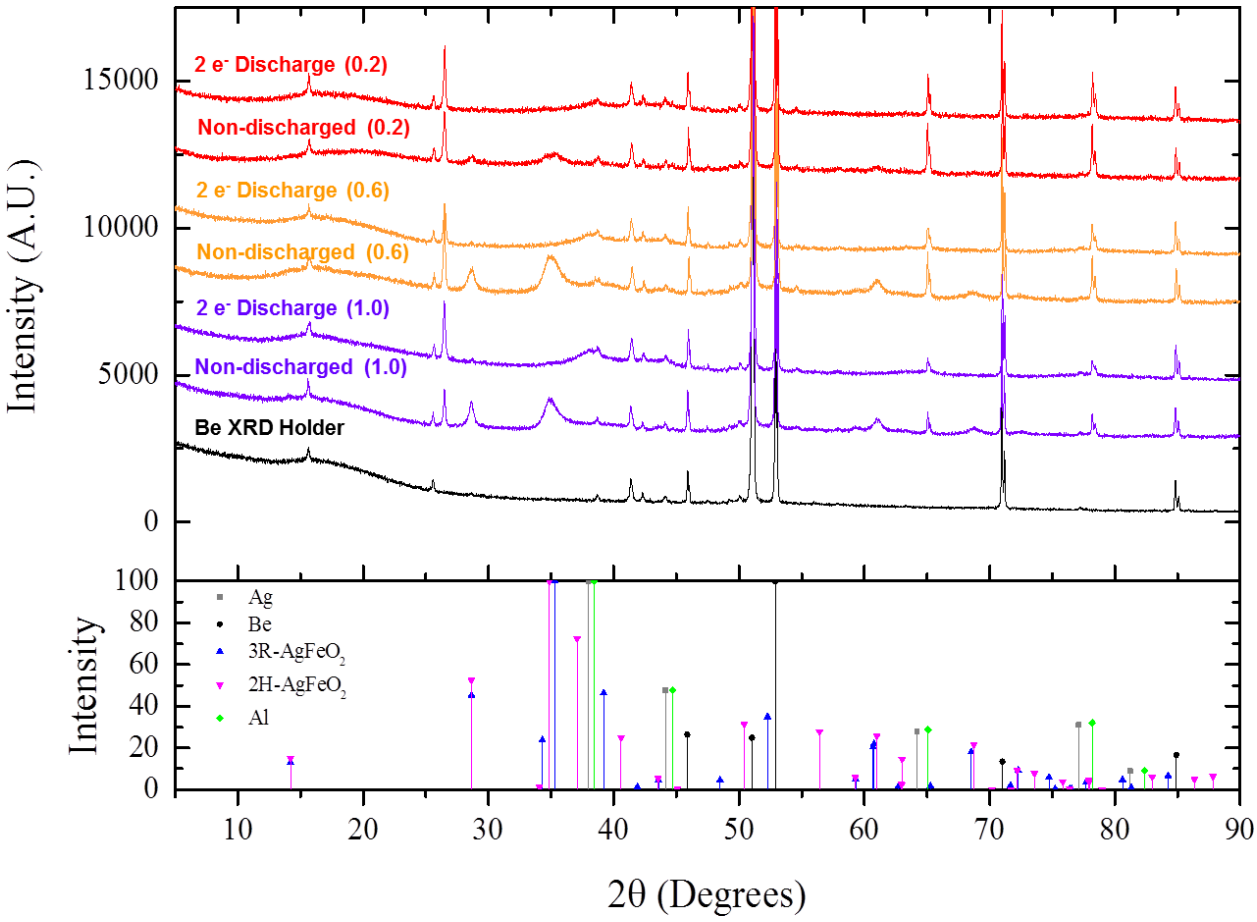

Figure 6.7. *Ex-situ* XRD of Ag_xFeOy composites (x = 0.2, 0.6) and $AgFeO_2$ before and after discharge to 2 electron equivalents in a 2-electrode electrochemical cell containing a lithium anode. XRD were collected in a sample holder equipped with a beryllium window to ensure an inert atmosphere. Coatings contain conductive carbon and binder coated onto an aluminum foil current collector. Reference patterns include Ag metal (ICSD 64706), beryllium (ICSD 1425), 3R-$AgFeO_2$ (PDF 01-075-2147), 2H-$AgFeO_2$ (ICSD 01-070-1452), and aluminum (ICSD 43423)

In an effort to further probe the redox mechanism of Ag_xFeO_y composites and $AgFeO_2$, *ex-situ* X-ray absorption spectroscopy (XAS) was conducted on cathodes which were recovered from electrochemical cells at various states of discharge and charge. XAS is a useful method to study the electrochemical processes displayed by Ag_xFeO_y composites since the materials are nanocrystalline in nature, especially after electrochemical testing. The sensitivity of XAS, particularly in the X-ray absorption near-edge structure (XANES) region, to localized structure allows for valuable insight into the oxidation state and coordination number of

the nanocrystalline material participating in the electrochemical reactions. XANES spectra of $AgFeO_2$ and $Ag_{0.2}FeO_{1.6}$ cathodes, as a function of discharge/charge depth, are shown in **Figure 6.8 b** and demonstrate a Fe K-edge energy dependence on the extent to which electrochemical cells were discharged or charged. The Fe K-edge position (defined as the maximum of the 1st derivative of xμ(E)) of $AgFeO_2$ and $Ag_{0.2}FeO_{1.6}$ in the non discharged state is ∼7127 eV, suggesting the Fe atoms in both composites exist in equivalent oxidation states. As $AgFeO_2$ is discharged, the edge position in **Figure 6.8 b** shifts to lower energies. Cathodes at partial (1 electron equivalent) and full (2 electron equivalents) discharge states exhibit edge energies of approximately 7125 eV, 2 eV lower than the non-discharged state. Upon complete charge, $AgFeO_2$ does not return to the edge position of the non-discharged state, consistent with irreversibility of the local structure when lithium is intercalated and de-intercalated during the first cycle. Evidence of the irreversible redox nature of $AgFeO_2$ was observed in galvanostatic cycling (**Figure 6.2**) where increase fade was observed compared to composite materials with lower silver ferrite contents. Compared to $AgFeO_2$, $Ag_{0.2}FeO_{1.6}$ shifts to significantly lower edge energy when partially and fully discharged, reaching ∼7123 eV. In addition to the reduced edge position, a small feature emerges near 7112 eV, similar to the edge feature of metallic Fe metal, which suggests a contribution of a Fe^0-like state after discharge. At a state of full charge, the XANES of $Ag_{0.2}FeO_{1.6}$ shifts back to the original edge position of about 7127 eV, indicating the highly reversible nature of the $Ag_{0.2}FeO_{1.6}$ which was observed during galvanostatic cycling.

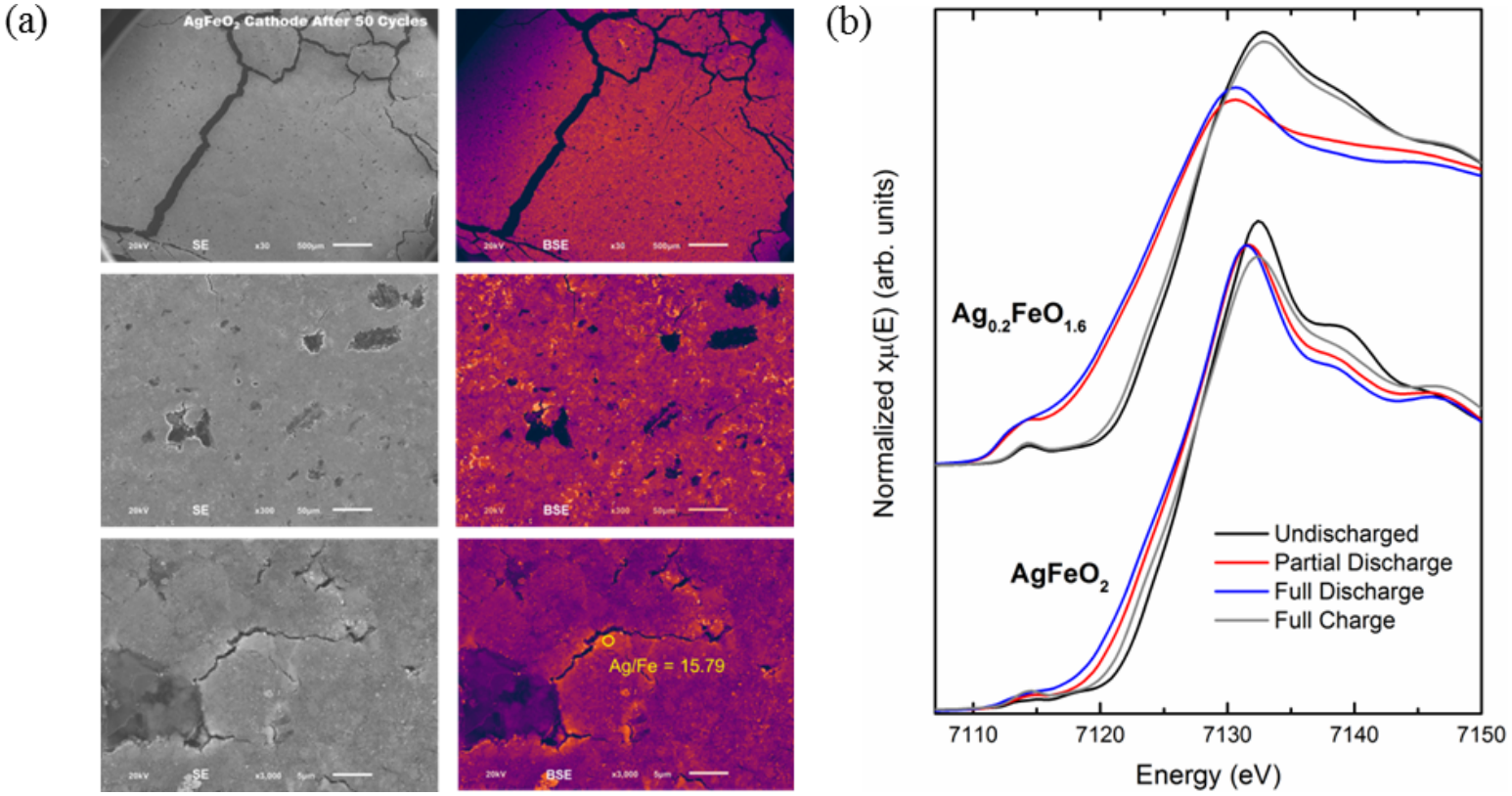

Figure 6.8. (a) *Ex-situ* scanning electron microscopy (SEM) images of an $AgFeO_2$ cathode, in the charged state, after 50 cycles. Secondary electron (SE) image (left) and back-scattered electron (BSE) images (right) were collected at magnifications of x30 (top), x300 (middle), and x3,000 (bottom). The colored BSE images illustrate high Z elements (Ag) in orange while lower Z elements (Fe, O, C) are colored pink or purple. Point energy dispersive spectroscopy (EDS) analysis was conducted on the light-orange region (yellow circle) of the x3,000 BSE image (bottom right) and indicates a high Ag content in that region of the charge $AgFeO_2$ cathode. (b) *Ex-situ* absorption spectroscopy (XAS) at the Fe K-edge of $AgFeO_2$ and $Ag_{0.2}FeO_{1.6}$

6.4 Conclusion

The viability of composites containing varying quantities of silver ferrite ($AgFeO_2$) and maghemite (γ-Fe_2O_3) as a cathode material in a lithium-based battery application has been examined. The composite nature of the low silver Ag_xFeO_y composites as a combination of crystalline silver ferrite ($AgFeO_2$) and non-crystalline maghemite (γ-Fe_2O_3) was established by Raman spectroscopic and X-ray absorption analyses in Chapter V. Electrochemical evaluation of silver ferrite composites was investigated using galvanostatic cycling, galvanostatic intermittent titration technique (GITT) type testing, AC impedance, and cyclic voltammetry. Results demonstrated that the presence of $AgFeO_2$ generated a significant enhancement in the performance of Ag_xFeO_y composites in comparison to the low capacity, poor reversibility of nanocrystalline γ-Fe_2O_3 material. Decreased crystallite size of Ag_xFeO_y composites ($x \leq 0.6$) effectively increases the surface area of the material in the cathode which allows for a greater amount of active material to be exposed to electrolyte as additional sites available for redox reactions and decreases the path length associated with ion transport within a cathode material. In pure $AgFeO_2$, Ag_xFeO_y composites, reduction of Ag^+ to metallic Ag^0 nanoparticles is observed and contributes to a ~6,000-fold decrease in impedance. Notably, $Ag_{0.2}FeO_{1.6}$ displays capacities 2X higher than stoichiometric $AgFeO_2$ and over 3X greater than nanocrystalline γ-Fe_2O_3. The results in Chapter VI demonstrate that the one-pot strategy to prepare composite materials yields increased delivered capacity. Further, we anticipate that the non-stoichiometric, low temperature, eco-friendly, one-pot co precipitation technique employed to synthesize the composite materials may translate well to industrial scales.

CHAPTER VII

ELECTROCHEMICAL CONSEQUENCES OF MECHANICALLY MIXING $AgFeO_2$ AND γ-Fe_2O_3 NANOPOWDERS *VERSUS* PREPARING $Ag_{0.2}FeO_{1.6}$ COMPOSITES ONE-POT

7.1 Introduction

A series of silver ferrite/maghemite composite materials (Ag_xFeO_y, where Ag_xFeO_y = composites of $x$$AgFeO_2$ + [(1-x)/2] γ-Fe_2O_3 and y=2-(1-x)/2) was prepared via a non-stoichiometric, one-pot co-precipitation strategy in Chapter V.[155,156] X-ray diffraction (XRD) confirmed the presence of silver ferrite, $AgFeO_2$, while the presence of maghemite, γ-Fe_2O_3, was identified through Raman spectroscopy and transmission electron microscopy (TEM). Battery-relevant electrochemistry of Ag_xFeO_y composites was measured using cyclic voltammetry, galvanostatic cycling, GITT testing, and AC impedance. Ag_xFeO_y composites with the lowest silver content (x) and smallest crystallite size, $Ag_{0.2}FeO_{1.6}$, exhibit excellent cyclability and deliver twice the discharge capacity (113 mAh/g) of $AgFeO_2$ with no maghemite component after 50 cycles.

The impact of a one-pot composite preparation on electrochemistry was determined by mechanically mixing nanocrystalline $AgFeO_2$ and γ-Fe_2O_3 powders to afford a material with an overall composition of $Ag_{0.2}FeO_{1.6}$. In Chapter VII, electrochemically cycled cathodes containing either one-pot composites or mechanical mixtures are probed by a variety of *ex-situ* characterization techniques including XRD, X-ray absorption spectroscopy (XAS), and scanning electron microscopy (SEM) to provide insight into the discharge process of one-pot Ag_xFeO_y composites versus stoichiometrically similar mechanical mixtures. The results demonstrate the profound differences between one-pot composites and mechanical mixtures as cathode materials in a lithium-based battery application.

7.2 Experimental

7.2.1 General Methods and Materials

A mechanically mixed sample was prepared by combining dry γ-Fe_2O_3 and $AgFeO_2$ powders in a SPEX mixer/mill.

7.2.2 Characterization

X-Ray powder diffraction (XRD) spectra of silver ferrite composites were collected with Cu Kα radiation and Bragg-Brentano focusing geometry using a Rigaku SmartLab X-Ray diffractometer and a D/tex detector. The XRD spectra were measured in a 2θ range from 5° to 90°. Rigaku PDXL2 software with an ICDD PDF-2 database was used for search-match analysis. Silver ferrite crystallite sizes were approximated by applying the Scherrer equation to the (0 0 6) reflection at a 2θ value of approximately 28° in the XRD pattern. Raman data were collected using a Horiba Scientific XploRA ONE Raman microscope equipped with a 532 nm laser. Silver ferrite samples were pressed into pellets with 5% graphite prior to measurement at room temperature. The laser beam was focused on the sample using a 50x microscope objective and a laser power of 10%. Spectra were collected in the range of 200–900 cm^{-1} and the acquisition time was set to 60 seconds with 15 scan accumulations.

7.2.3 Electrochemistry

CR 2320 coin cell batteries were used to probe the electrochemical performance of stoichiometric silver ferrite and silver ferrite composites varying crystallite sizes and compositions. Composite electrodes were prepared by mixing silver ferrite with conductive carbon and PVDF binder for a composition of 85% active material, 5% Super P conductive carbon black, 5% graphite, and 5% binder and coating onto an aluminum foil substrate. The coatings were dried under vacuum for 12 hours and, to ensure intimate contact of the electrode material with the aluminum current collector, pressed using a hydraulic press to afford a thin film with a thickness $\sim$2 μm. Electrodes were cut into circular discs, 0.5 inches or 1.27 cm in diameter, with a single electrode containing an average of 3.5 mg active material. An

electrolyte solution of 1 M $LiPF_6$ in 30/70 (*v/v*) ethylene carbonate/dimethyl carbonate was used for electrochemical testing. Galvanostatic cycling, over 50 cycles, was performed on a Maccor Series 4000 Battery Test System in a chamber maintained at 30°C. Galvanostatic cycling tests were conducted using a two electrode assembly with lithium metal anode and an applied current of 0.15 mA/cm^2 between 1.5–3.5 V.

7.2.4 Acknowledgment of Collaboration

The research in Chapter VII was conducted in collaboration with Zhou Lin (Stony Brook University) and Dr. Wei Zhang and Dr. Feng Wang (Brookhaven National Laboratory). Zhou performed the mechanical mixing of silver ferrite and maghemite materials and collected a portion of the galvanostatic cycling data while Dr. Zhang performed TEM analysis of the material.

7.3 Results and Discussion

7.3.1 XRD

A one-pot co-precipitation synthesis was used to prepare $Ag_{0.2}FeO_{1.6}$ composite material, $AgFeO_2$, and maghemite (γ-Fe_2O_3). Characterization of Ag_xFeO_y composites, $AgFeO_2$, and γ-Fe_2O_3 via XRD, BET, electron imaging, Raman spectroscopy, XAS, XPS, and TGA was summarized Chapter V and the electrochemical performance was investigated in Chapter VI. Ag_xFeO_y composites in the lowest silver regime ($x = 0.2$) demonstrated profound improvement in reversibility with capacities approximately 100% higher than stoichiometric $AgFeO_2$. In an effort to mimic $Ag_{0.2}FeO_{1.6}$ composite materials, a mechanical mixture of $AgFeO_2$ and semi-crystalline γ-Fe_2O_3 nanopowders were prepared to afford an overall composition of $Ag_{0.2}FeO_{1.6}$. Powder X-ray diffraction (XRD) of the $Ag_{0.2}FeO_{1.6}$ mechanical mixture is compared to one-pot $Ag_{0.2}FeO_{1.6}$ composite material, $AgFeO_2$, and maghemite (γ-Fe_2O_3) in **Figure 7.1**. The XRD pattern demonstrate by the $Ag_{0.2}FeO_{1.6}$ mechanical mixture is equivalent to $AgFeO_2$ with reflections of decreased intensity and no visible γ-Fe_2O_3 peaks.

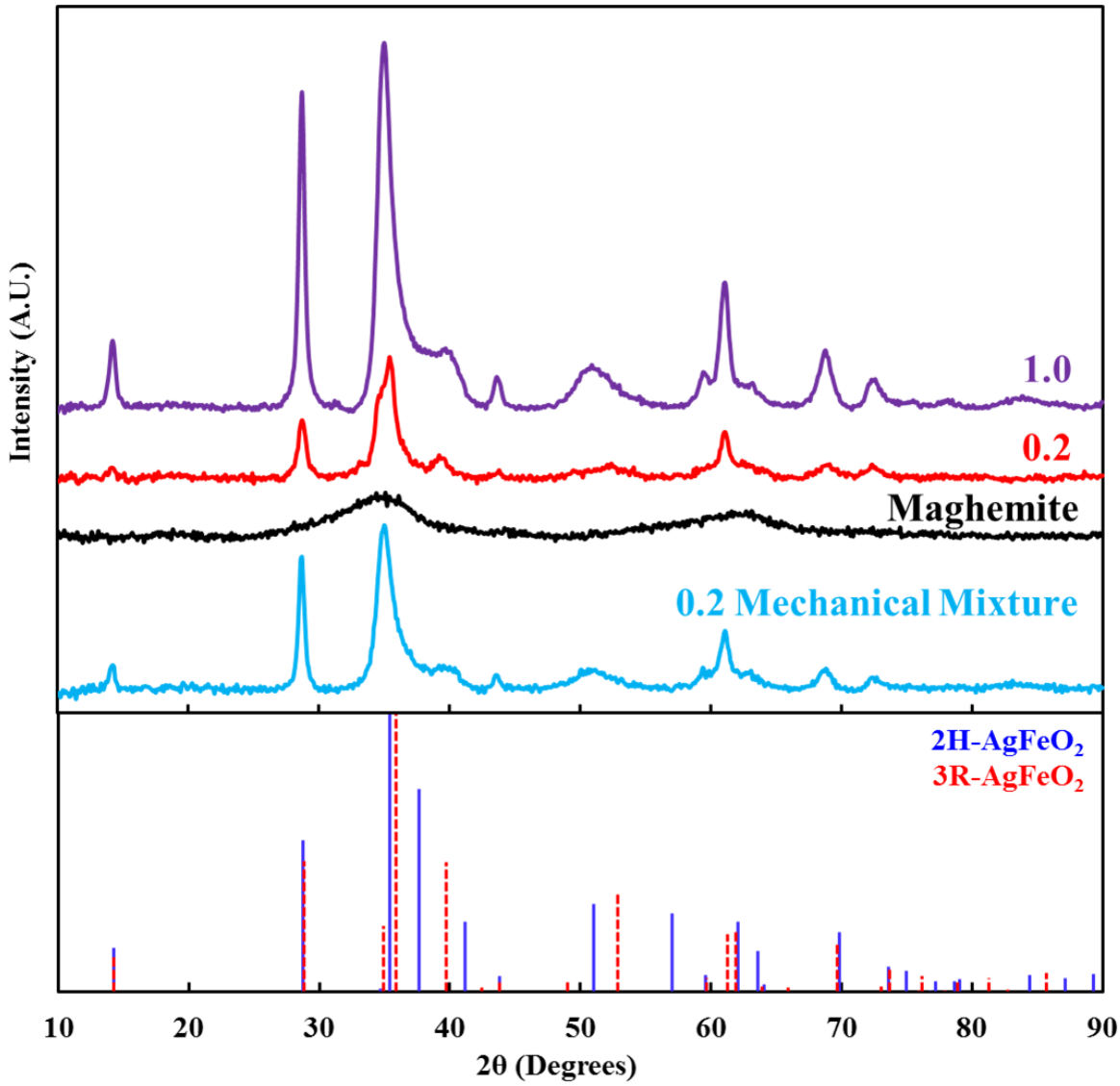

Figure 7.1. Powder X-ray diffraction (XRD) of $Ag_{0.2}FeO_{1.6}$, $AgFeO_2$, maghemite (γ-Fe_2O_3), and a 0.2 mechanical mixture with corresponding 2H-$AgFeO_2$ (PDF 01-070-1452) and 3R-$AgFeO_2$ (PDF 01-075-2147) reference patterns

7.3.2 Raman Spectroscopy

To determine the contribution of semi-crystalline γ-Fe_2O_3 in the $Ag_{0.2}FeO_{1.6}$ mechanical mixture, micro-Raman spectroscopy was utilized (**Figure 7.2**). The Raman spectrum of the $Ag_{0.2}FeO_{1.6}$ mechanical mixture is analogous to the spectrum of the one-pot prepared $Ag_{0.2}FeO_{1.6}$ composite, suggesting that the mechanical mixture of $AgFeO_2$ and semi-crystalline γ-Fe_2O_3 nanopowders is viable to use as a comparison for electrochemical studies.

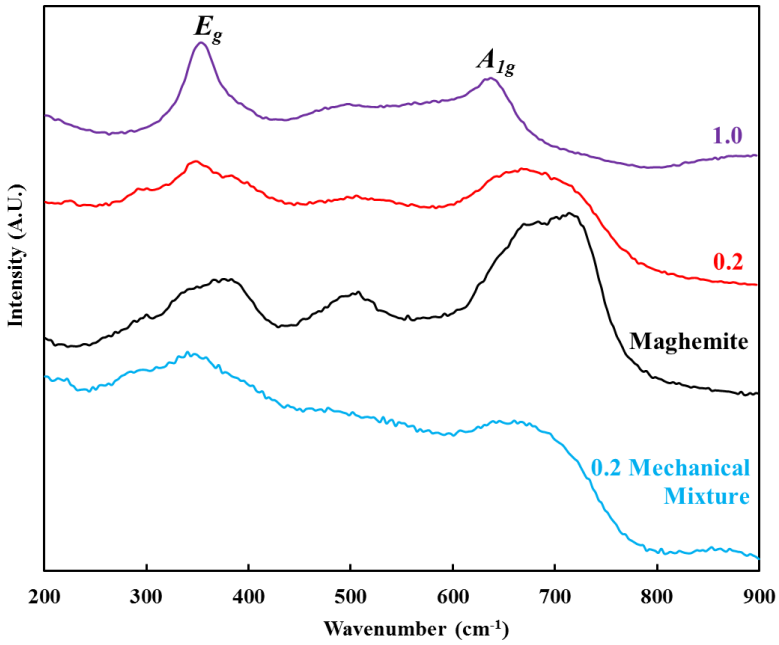

Figure 7.2. Raman spectroscopy of $Ag_{0.2}FeO_{1.6}$, $AgFeO_2$, maghemite (γ-Fe_2O_3), and a 0.2 mechanical mixture

7.3.3 TEM

Transmission electron microscopy (TEM) images of the one-pot $Ag_{0.2}FeO_{1.6}$ composite and the $Ag_{0.2}FeO_{1.6}$ mechanical mixture are depicted in **Figure 7.3**. Images **A** in **Figures 7.3 a** and **b** illustrate more significant aggregation of particles in the $Ag_{0.2}FeO_{1.6}$ mechanical mixture while the one-pot $Ag_{0.2}FeO_{1.6}$ composite is comprised of more uniformly distributed spherical nanoparticles. The EELS maps in image **D** indicate more isolated silver ferrite ($AgFeO_2$) and maghemite (γ-Fe_2O_3) regions for the mechanically mixed $Ag_{0.2}FeO_{1.6}$ material relative to the one-pot prepared $Ag_{0.2}FeO_{1.6}$ composite. Although the composite and mechanically mixed $Ag_{0.2}FeO_{1.6}$ materials contain the same ratio of $AgFeO_2$/γ-Fe_2O_3, the material generated one-pot affords reduced aggregation of nanoparticles which increases the contact among the $AgFeO_2$ and γ-Fe_2O_3 materials as well as the active material surface area directly available for electrochemical reaction. In addition, scanning electron microscopy (SEM) reveals agglomeration of small primary particles into larger granular particles (~1–5 μm diameters) for both the one-pot $Ag_{0.2}FeO_{1.6}$ and the 0.2 mechanical mixture along with

relatively homogeneous distribution of Ag and Fe via EDS mapping (**Figure A11**).

Previously, a multi-scale mathematical model was developed to account for mass transport in the agglomerate and crystal length-scales and used to analyze experimental discharge and voltage recovery data for iron oxide (magnetite, Fe_3O_4) electrodes. The model indicated that inclusion of a representative agglomerate distribution with a small fraction of large agglomerates could impact the values of the fitted diffusion coefficients by a factor of $\sim$2.[171] Thus, the distribution of the active materials within the electrode can significantly impact the electrochemical behavior of the system, resulting in the observed difference in functional capacity. Additionally, the reduction of the $Ag^+ \rightarrow Ag^0$ upon electrochemical discharge is expected to more effectively connect iron oxide particles in one-pot prepared highly dispersed Ag_xFeO_y composites with a conductive silver network, coming closer to the goal of electrochemically wiring each particle.[172,173]

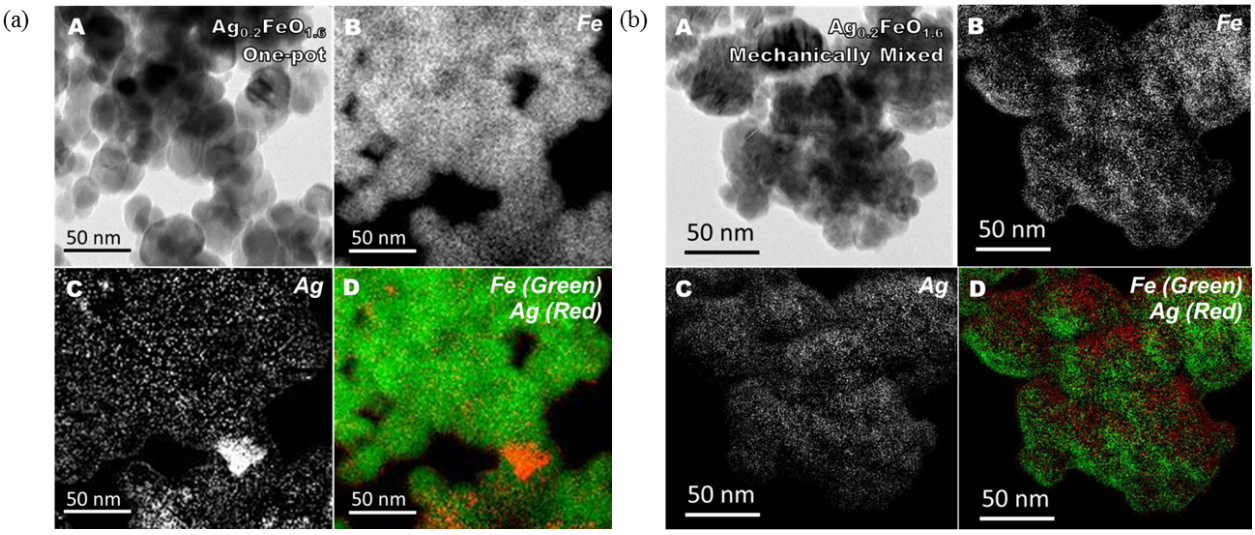

Figure 7.3. Transmission electron microscopy (TEM) of $Ag_{0.2}FeO_{1.6}$: (a) one-pot composite and (b) mechanically mixed composite. Distribution of Ag and Fe from TEM images (**A**) and the corresponding electron energy loss spectroscopy (EELS) maps of Fe (**B**) and Ag (**C**). (**D**) Superposition of Fe (green) and Ag (red) EELS maps

7.3.4 Electrochemical Evaluation

To determine significance of one-pot preparation on electrochemical performance of Ag_xFeO_y composites, silver ferrite ($AgFeO_2$) and maghemite (γ-Fe_2O_3) nanopowders were mechani-

cally mixed as a means of comparison. The low silver composite, $Ag_{0.2}FeO_{1.6}$, with the highest capacity was targeted for the mechanical mixing study and the results are shown in **Figure 7.4**. After 30 cycles, the $Ag_{0.2}FeO_{1.6}$ composite prepared one pot delivered a capacity (104 mAh/g) over 160% greater than that of the mechanically mixed $x = 0.2$ sample (40 mAh/g). The mechanical mixture also performed worse than $AgFeO_2$, delivering an energy density approximately 42% lower. In comparison, all of the Ag_xFeO_y composites ($0.2 \leq x \leq 0.8$) in Chapter VI met or exceeded the energy density of $AgFeO_2$ over 50 cycles (**Figure 6.2**).

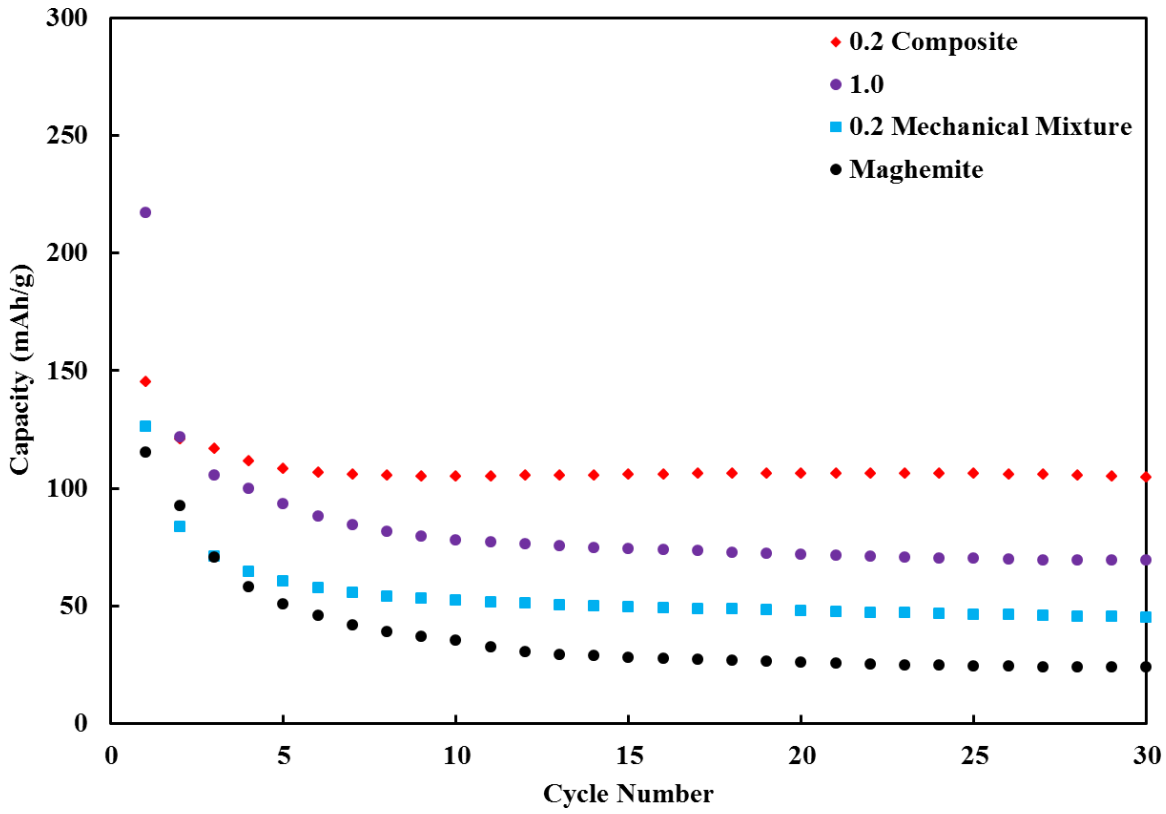

Figure 7.4. Galvanostatic cycling of Li/$Ag_{0.2}FeO_{1.6}$ electrochemical in which cathode materials are prepared either as a one-pot composite or mechanical mixture. Li/$AgFeO_2$ and γ-Fe_2O_3 cells are used as references over 30 cycles

Discharge curves of the $Ag_{0.2}FeO_{1.6}$ composite prepared one-pot and the $Ag_{0.2}FeO_{1.6}$ mechanical mixture during cycles 1 and 2 are shown in **Figure 7.5**. The one-pot $Ag_{0.2}FeO_{1.6}$ composite demonstrates a voltage plateau near 2.15 V on the first discharge while the voltage

plateau for the mechanical mixture is observed at 1.85 V. The increase in polarization of the $Ag_{0.2}FeO_{1.6}$ mechanical mixture is likely a result of decreased electrochemical contact within the cathode material due to aggregation of the $AgFeO_2$ and γ-Fe2O3 nanopowders. On the second discharge, the voltage drops at a faster rate in the cell containing the mechanical mixture suggesting increased resistance within the electrochemical system. These data indicate the advantage of preparing an Ag_xFeO_y composite one pot rather than mechanically mixing $AgFeO_2$ and γ-Fe_2O_3.

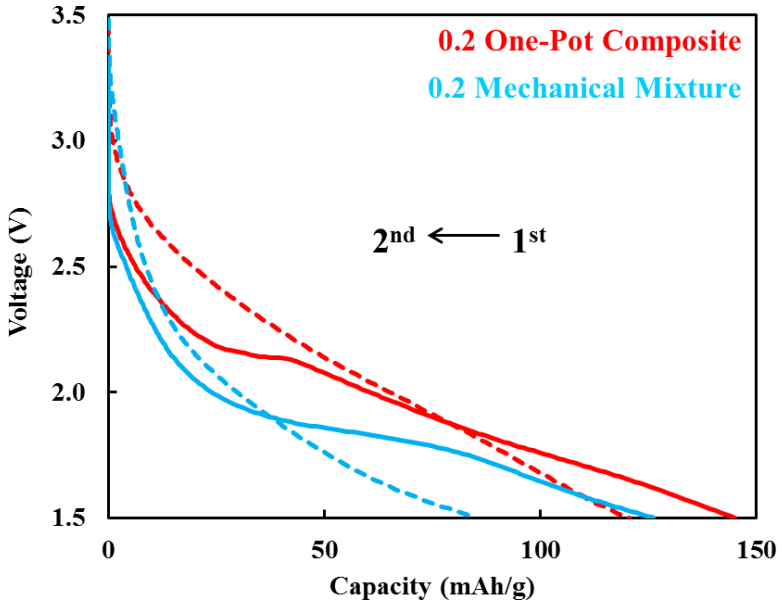

Figure 7.5. Capacity plotted as a function of voltage for Li/$AgFeO_2$ and Li/$Ag_{0.2}FeO_{1.6}$ cells during galvanostatic cycling at cycles 1 and 2

7.4 Conclusion

To determine the impact of a one-pot composite preparation on electrochemistry, nanocrystalline $AgFeO_2$ and γ-Fe_2O_3 powders were mechanically mixed to afford a $Ag_{0.2}FeO_{1.6}$ mixture. TEM imaging provided a local examination of the nanocrystalline structure of the Ag_xFeO_y composites and established the presence of both $AgFeO_2$ and a semi-crystalline γ-Fe_2O_3 phase in intimate contact. Following 30 cycles, the one-pot $Ag_{0.2}FeO_{1.6}$ composite delivers an capacity (104 mAh/g) profoundly higher than the $Ag_{0.2}FeO_{1.6}$ mechanical mixture (40 mAh/g). Mechanical mixing of $AgFeO_2$ and γ-Fe_2O_3 powders to mimic a one-pot

$Ag_{0.2}FeO_{1.6}$ composite yields lower delivered capacity and energy density where the results demonstrate the advantages of the directly prepared composite with more intimate particle connectivity. The results demonstrate that this one-pot strategy to prepare composite materials yields increased delivered energy. The notable electrochemistry of one-pot Ag_xFeO_y composites may involve reduced $AgFeO_2$ and γ-Fe_2O_3 aggregate sizes and a concomitant increase in $AgFeO_2/\gamma$-Fe_2O_3 crystallite contact not achievable through mechanical mixing. The approach may result in unexpected electrochemistry when compared to that of the individual components and can be extended to other electroactive materials.

CHAPTER VIII

ANALYSIS OF ELECTROCHEMICALLY CYCLED SILVER FERRITE/MAGHEMITE COMPOSITES VIA *IN-SITU* AND *EX-SITU* TECHNIQUES: INSIGHTS INTO THE LITHIATION/DELITHIATION MECHANISM

8.1 Introduction

The electrochemical performance of Ag_xFeO_y composites, $AgFeO_2$, and γ-Fe_2O_3 has been shown in Chapters VI and VII, however, the lithiation mechanism is not well understood. In Chapter VI, $Ag_{0.2}FeO_{1.6}$ displayed enhanced cycling efficiency and 100% higher capacity than $AgFeO_2$ over 50 cycles. *Ex-situ* XRD (**Figure 6.7**) of $Ag_{0.2}FeO_{1.6}$ and $AgFeO_2$ after discharge portrayed the conversion of the active material to a highly nanocrystalline component which could not be detected by diffraction. X-ray absorption spectroscopy (XAS) is a effective technique for the characterization of highly nanocrystalline, disordered cathode materials since it does not require long-range structural order. In addition, X-Ray absorption near-edge structure (XANES) reflects the oxidation state and coordination environment of the absorbing atom while extended X-ray absorption fine structure (EXAFS) provides quantitative information concerning short-range order structural parameters, such as interatomic distance and number of nearest neighbors to the absorbing atom. In the battery field, XAS is a common technique employed to elucidate the evolution of the oxidation state of transition metal oxides and determine failure mechanisms during electrochemical cycling.[174–178] The utilization of advanced *in-situ* and *ex-situ* techniques to probe electrochemically discharged and charged cathodes is highlighted in Chapter VIII as a means to provide insight into the lithiation/delithiation mechanism of an $Ag_{0.2}FeO_{1.6}$ composite and $AgFeO_2$. *In-situ* XRD is used as a complement to *ex-situ* XAS where the structural changes of $Ag_{0.2}FeO_{1.6}$ and $AgFeO_2$ cathodes are measured as a function of voltage.

8.2 Experimental

8.2.1 Characterization

In-situ **XRD** *In-situ* XRD measurements were conducted using a novel vacuum-sealed plastic pouch electrochemical cell in a Rigaku Miniflex diffractometer utilizing a D/tex 1D Si strip detector to facilitate fast and high quality spectra acquisition. A specially designed sample holder was used to ensure proper mounting of pouch cells and maximize data quality in the Bragg-Brentano XRD geometry. Both $AgFeO_2$ and $Ag_{0.2}FeO_{1.6}$ electrodes were discharged at 43 mA/g rate using a Bio-Logic multichannel potentiostat/galvanostat. XRD spectra were continuously collected during the discharge in a 2θ region of 25–85° with a step size of 0.03° and a scan rate of 3°/min after an initial XRD spectra was collected at open circuit voltage (OCV). All measurements were conducted in a low humidity dry room. After data acquisition, the XRD scans were correlated to the electrochemistry of the cell by comparing time-stamps of the electrochemical data and XRD scans respectively.

Ex-situ **XAS** $AgFeO_2$ and $Ag_{0.2}FeO_{1.6}$ electrodes for XAS analysis were prepared by electrochemically discharging and/or charging within a standard coin-type cell to specified depths of discharge/charge. Once the cell had reached the predetermined discharge/charge state, the cell was removed from electrochemical testing and the electrode was dried and sealed between Kapton tape and stored within an inert atmosphere until XAS data was collected to limit any oxidation from air exposure. XAS measurements of the Fe K-edge (7.112 keV) were acquired at Sector 12-BM at the Advanced Photon Source at Argonne National Laboratory, IL and the Ag K-edge (25.514 keV) spectra were collected at X8C beamline of the National Synchrotron Light Source I at Brookhaven National Laboratory, NY. Both Fe and Ag K-edge measurements were collected in transmission geometry with the incident and transmitted X-ray flux monitored with ionization chambers. For both Fe and Ag K-edge measurements, a Fe and Ag metal reference foil was utilized respectively for proper initial beam energy calibration and were measured simultaneously with each sample spectrum to

ensure proper alignment of multiple scans during data normalization and analysis.

The extended X-ray absorption fine structure (EXAFS) spectra were aligned, merged and normalized using Athena.[111,179] The background was removed below 1.0 Å using the standard AUTOBK algorithm. Both the Fe and Ag K-edge measurements were fit in Artemis with theoretical models generated from known crystal structures of rhombohedral $AgFeO_2$,[180] inverse-spinel γ-Fe_2O_3,[181] Fe metal[182] and Ag metal[115] using FEFF6.[111–113] All spectra were fit using a k range of 2–11 $Å^{-1}$ using a Hanning Fourier transform window with dk = 2 and fit simultaneously using k, k^2 and k^3 weighting. An R-range was used to fully encompass the first and second coordination shells, typically between 1–3.2 Å or 1–3.6 Å. Initially, a S_0^2 value of ~ 0.85 was determined from fitting Fe and Ag metal standards, and this term was utilized in all fits to account for intrinsic losses in the electron propagation and scattering process caused by core-hole effects.[183] The undischarged spectra of $AgFeO_2$ was fit using the rhombohedral $AgFeO_2$ crystal structure for both the Ag and Fe K-edge measurements. The $Ag_{0.2}FeO_{1.6}$ data was modeled using a combination of the $AgFeO_2$ structure combined with γ-Fe_2O_3. The discharged and subsequent charged electrochemical states were modeled using a combination of metallic (Ag or Fe) or the original $AgFeO_2$ structure. The data and subsequent fitting results dictated which phases that were included or excluded from each model. If a specific phase resulted in a small relative amplitude (near 0 with estimated standard deviations) or fitting variables were unrealistic and/or statistically insignificant, it was excluded from further models at that electrochemical state.

8.2.2 Electrochemistry

CR 2320 coin cell batteries were used to probe the electrochemical performance of stoichiometric silver ferrite and silver ferrite composites varying crystallite sizes and compositions. Composite electrodes were prepared by mixing silver ferrite with conductive carbon and PVDF binder for a composition of 55% active material, 30% carbon black, and 15% binder and coating onto a copper foil substrate. The coatings were dried under vacuum for 12 hours and, to ensure intimate contact of the electrode material with the copper current

collector, pressed using a hydraulic press to afford a thin film with a thickness ~2 μm. Electrodes were cut into circular discs, 0.5 inches or 1.27 cm in diameter, with a single electrode containing an average of 2 mg active material. An electrolyte solution of 1 M $LiPF_6$ in 30/70 (*v/v*) ethylene carbonate/dimethyl carbonate was used for electrochemical testing. Galvanostatic cycling, over 50 cycles, was performed on a Maccor Series 4000 Battery Test System in a chamber maintained at 30°C. Galvanostatic cycling tests were conducted using a two electrode assembly with lithium metal anode and a current density of 43 mA/g between 3.0–0.6 V or 3.0–0.1 V.

8.2.3 Acknowledgment of Collaboration

The research in Chapter VIII was conducted in collaboration with Dr. David Bock and Dr. Christopher Pellicione (Brookhaven National Laboratory). Dr. Bock and Dr. Pelliccione collected the *in-situ* XRD data. Dr. Pelliccione collected the XAS and analyzed both the XRD and XAS data.

8.3 Results and Discussion

8.3.1 *In-situ* XRD

To monitor the structural evolution of $AgFeO_2$ and $Ag_{0.2}FeO_{1.6}$ electrodes as a function of discharge *in-situ* X-ray diffraction (XRD) was collected. This method is preferred over the *ex situ* XRD shown in Chapter VI (**Figure 6.7**) because the novel vacuum-sealed plastic electrochemical pouch cell allows for *in operando* data collection and eliminates the possibility of oxidizing reduced species after cell disassembly or electrode transfer. *In-situ* XRD measurements of $AgFeO_2$ and $Ag_{0.2}FeO_{1.6}$ are shown in **Figures 8.1 and 8.2**, respectively. Intense diffraction peaks located at ~36°, 52°, and 65° correlate to the (1 1 0), (2 0 0) and (2 1 1) Li metal Bragg reflections, respectively.[124] Peaks at ~35°, 61° and 68° are from the (1 0 1), (1 0 10) and (2 -1 6) lattice planes of the nominal $AgFeO_2$ crystal structure.[180] All other small, unchanging diffraction peaks are related to other components of the *in-situ* pouch cell.

The $AgFeO_2$ electrode undergoes subtle crystalline changes during lithium insertion. As the material is discharged, minor amorphization is observed by the end of the long discharge plateau at ~2.8 V as indicated by a reduction in diffraction peak intensity and overall broadening of the peaks corresponding to $AgFeO_2$. This trend continues until the end of the discharge at 1.0 V. The *in situ* XRD data suggests that the initial $AgFeO_2$ material has experienced a minor transformation, but the overall crystal structure is still intact.

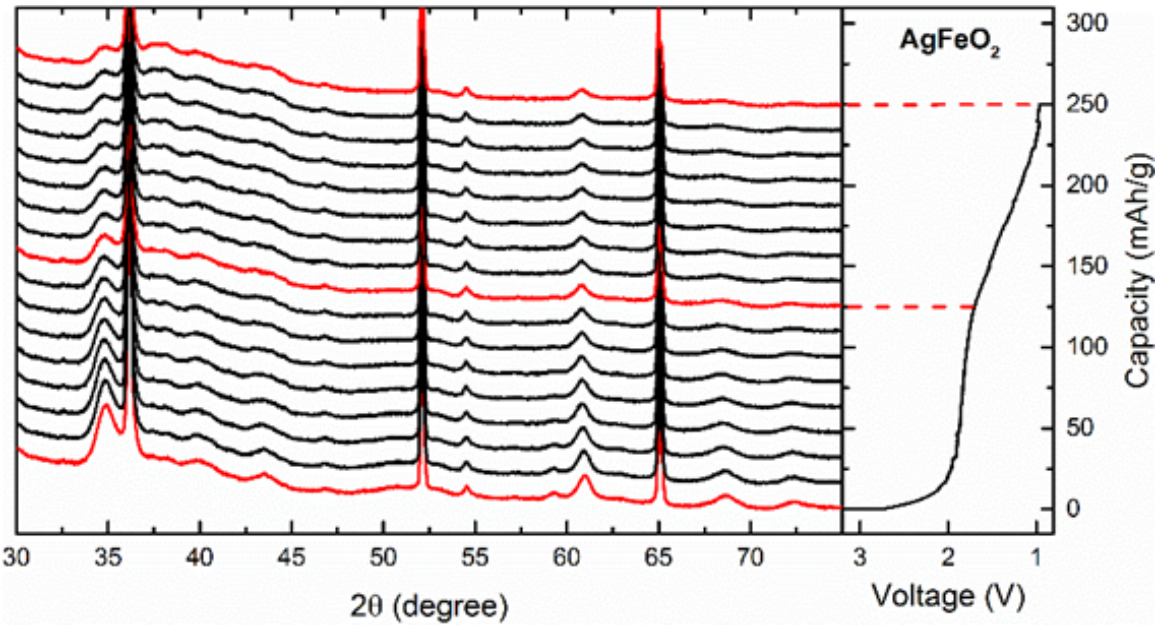

Figure 8.1. *In-situ* XRD of $AgFeO_2$ electrodes. Red lines indicate approximate depths of discharge of *ex-situ* XAS samples

The structural evolution of the $Ag_{0.2}FeO_{1.6}$ electrode is more difficult to definitively asses via *in situ* XRD measurements due to the small crystallite size (~10 nm), however, differences with respect to the $AgFeO_2$ electrode are obvious. Specifically, as lithium is intercalated into the layered structure, the broad and low intensity Bragg reflections related the initial structure disappear rapidly, by ~250 mAh/g (or ~1.4 V). As the diffraction peaks disappear, no new peaks are discernible suggesting that the $Ag_{0.2}FeO_{1.6}$ composite has become highly amorphous/nanocrystalline during phase conversion and cannot be detected with traditional laboratory XRD measurements. Continued discharge of the $Ag_{0.2}FeO_{1.6}$ electrode shows no change in the XRD pattern, indicating the phases formed during discharge continue to be

primarily amorphous/nanocrystalline.

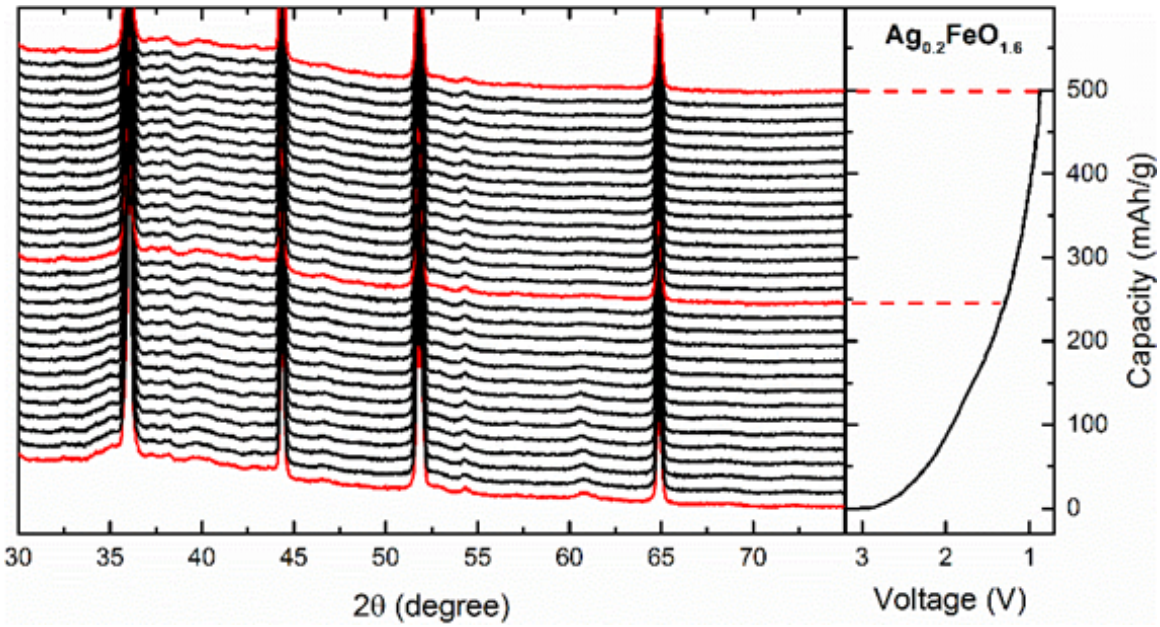

Figure 8.2. *In-situ* XRD of $Ag_{0.2}FeO_{1.6}$ electrodes. Red lines indicate approximate depths of discharge of *ex-situ* XAS samples

8.3.2 *Ex-Situ* XAS

X-ray absorption near edge structure (XANES) spectra of representative $AgFeO_2$, γ-Fe_2O_3, and $Ag_{0.2}FeO_{1.6}$ materials are illustrates in **Figure A16**. Linear combination fitting of the $Ag_{0.2}FeO_{1.6}$ composite was performed, using $AgFeO_2$ and amorphous γ-Fe_2O_3 as standards, to elucidate the composite nature of the one-pot prepared material and provide quantitative details (**Figure 8.3**). The fit determines that the $Ag_{0.2}FeO_{1.6}$ composite is composed of 79 $\pm$ 0.6% γ-Fe_2O_3 and 21 $\pm$ 0.6% $AgFeO_2$ which was expected per **Equation 5.2**.

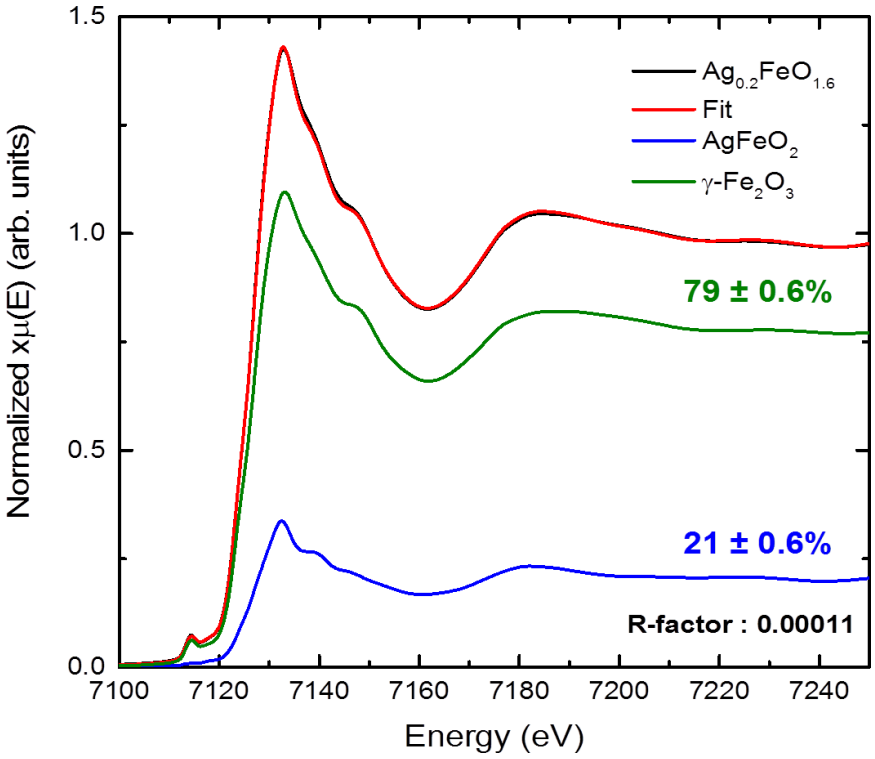

Figure 8.3. Linear combination fittng of pristine $Ag_{0.2}FeO_{1.6}$ using $AgFeO_2$ and γ-Fe_2O_3 as standards

To investigate the redox processes that occurring during discharge and charge, $Ag_{0.2}FeO_{1.6}$ and $AgFeO_2$ electrodes were removed from coin cells at specific depths of discharge or charge and XAS data was collected with particular focus on the EXAFS region. With regard to EXAFS, k^2-weighted $|\chi(R)|$ (Fourier transform of $\chi(k)$) of $AgFeO_2$ (Ag and Fe K-edge) and $Ag_{0.2}FeO_{1.6}$ (Fe K-edge) are shown in **Figure 8.4**. The depths of discharge targeted for the EXAFS study were partial discharge (~1 molar electron equivalent), full or 1st discharge (~2 electron equivalents), and full or 1st charge to 3.5 V.

The Ag K-edge of the $AgFeO_2$ electrode in **Figure 8.4** displays a sudden shift from the undischarged $AgFeO_2$ crystal structure to what qualitatively appears to be Ag metal (in comparison with Ag metal reference foil shown). This suggests that during the initial discharge of $AgFeO_2$, Ag atoms within the original structure migrate to the surface when lithium is inserted, and form metallic Ag^0 nanoparticles. The Ag^0 particles do not appear to change significantly as a function of electrochemical state due to the similar $|\chi(R)|$ of the

partially and fully discharged electrochemical states of $AgFeO_2$.

The Fe K-edge of the $AgFeO_2$ electrode material also suggests that Ag atoms are removed from the structure, as the small defined double-peak at ∼3.2 Å in **Figure 8.4** dissipates and is due to Ag atom contributions. It should be noted that the distance of ∼3.2 Å is uncorrected for phase shifts associated with the electron scattering process and are ∼0.4 Å shorter than the actual interatomic distances determined through theoretical modeling. When $AgFeO_2$ is partially discharged, the double-peak clearly disappears aligning well with the formation of Ag metal observed from the Ag K-edge. However, as the $AgFeO_2$ is continually lithiated, the original Fe-O/Fe-Fe framework of the initial crystal structure appears to remain intact as the 1st shell peak at ∼1.4 Å (Fe-O contribution) and the 2nd shell peak at ∼2.5 Å (Fe-Fe contribution) do not significantly change. This data is in agreement with the *in-situ* XRD measurements of $AgFeO_2$ where a slight broadening of the initial $AgFeO_2$ Bragg reflections and reduction in peak intensity is observed. Notably, these $AgFeO_2$ reflections are still present when the electrode is fully discharged to 1.0 V.

The Fe K-edge of the $Ag_{0.2}FeO_{1.6}$ electrode undergoes considerably different structural changes during the first discharge. As the material is partially discharged, the distinct 2nd shell peak between 2.5 and 3.0 Å, which includes contributions from both Fe-O and Fe-Fe, converts to a broad feature that encompasses the entire range between 2.0 and 3.0 Å. This peak becomes significantly broader upon the full discharge of the $Ag_{0.2}FeO_{1.6}$ cathode material. During charge or de-intercalation, it appears as if the initial structure is restored owing to the observation a similar, distinct 2nd shell peak relative to the undischarged $Ag_{0.2}FeO_{1.6}$ Fe K-edge spectrum.

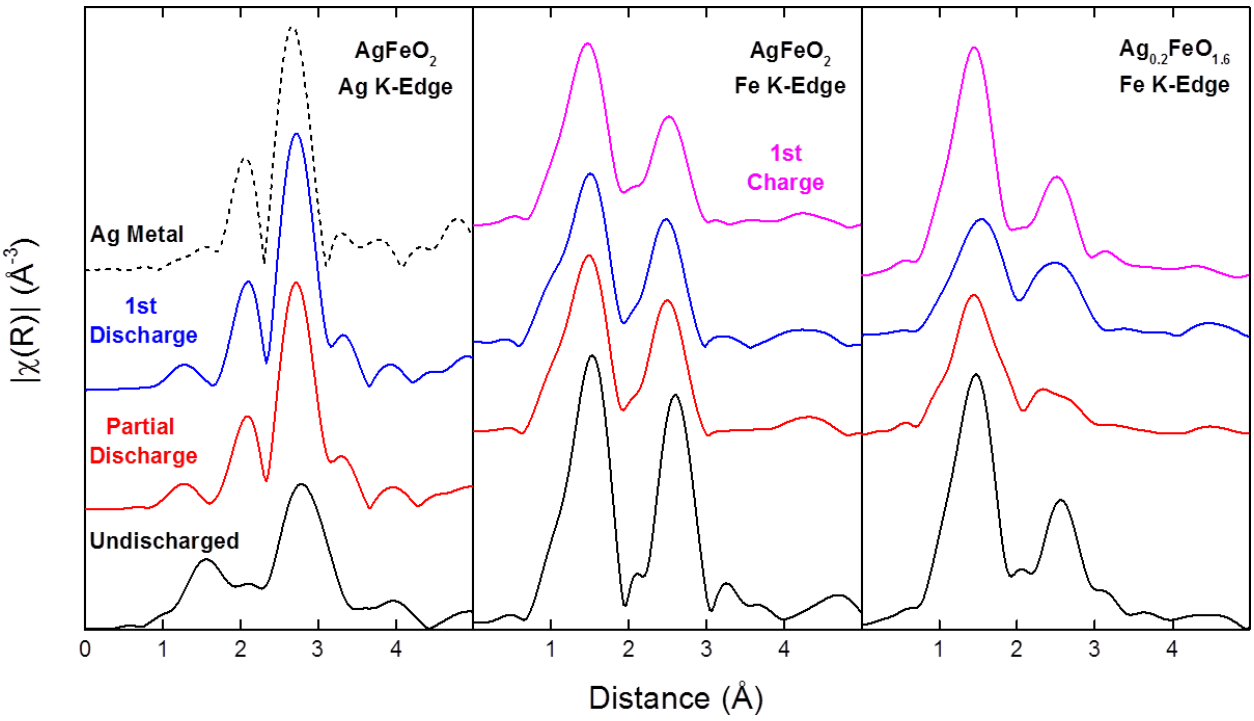

Figure 8.4. k^2-weighted | χ(R) | of $AgFeO_2$ (Ag and Fe K-edge) and $Ag^{0.2}FeO_{1.6}$ (Fe K-edge) in undischarged (black line), partially discharged (red line), 1st discharge (blue line), and 1st charge (pink line) electrochemical states. An Ag metal reference foil is also shown (dashed black line) for comparison

To quantify structural changes at the atomic-level, $AgFeO_2$ and $Ag_{0.2}FeO_{1.6}$ EXAFS spectra were modeled using a mixture of $AgFeO_2$, γ-Fe_2O_3, and Fe metal crystal structures. The EXAFS fitting results, which include the interatomic distance and number of neighboring atoms, from the Fe K-edge spectra are shown in **Figure 8.5**. The modeling results for $AgFeO_2$ align with the *in-situ* XRD data and the observations of the $|\chi(R)|$ spectra. No significant change in the Fe-O or Fe-Fe interatomic distances of $AgFeO_2$ are observed, with the exception of the contraction in the long range Fe-O contribution from 3.64 ± 0.01 Å to 2.95 ± 0.03 Å. The migration of Ag atoms out of the $AgFeO_2$ crystal structure were clearly observed in **Figure 8.4** as the partially discharged spectrum resulted in zero Fe-Ag neighboring atoms which may be the cause of Fe-O contraction within the discharged $AgFeO_2$ structure. Once the contraction of the long range Fe-O contributions has occur in the partially discharged $AgFeO_2$ state, no statistically significant changes in interatomic distances in

the fully discharged or charged states are observed. Additionally, the number of neighboring atoms of the closest Fe-O and Fe-Fe contributions decreases from the initial value of 4.8 ± 0.2 atoms to 3.5 ± 0.3 atoms when fully discharged. The reduction in observed neighboring atoms in discharge $AgFeO_2$ is likely due to either a decrease in particle size, leading to an increase in the ratio of surface terminated atoms to bulk atoms,[127,128,184] or amorphization of the crystal phase as the number of neighboring atoms and the Debye-Waller factor, which accounts for thermal and structural disorder, are highly correlated (as high as 90% in these fitting models). This is in agreement with the *in-situ* XRD measurements as a broadening of the crystalline peaks is observed with continued lithiation and are indicative of reduced crystallite size or amorphization of the crystal structure.

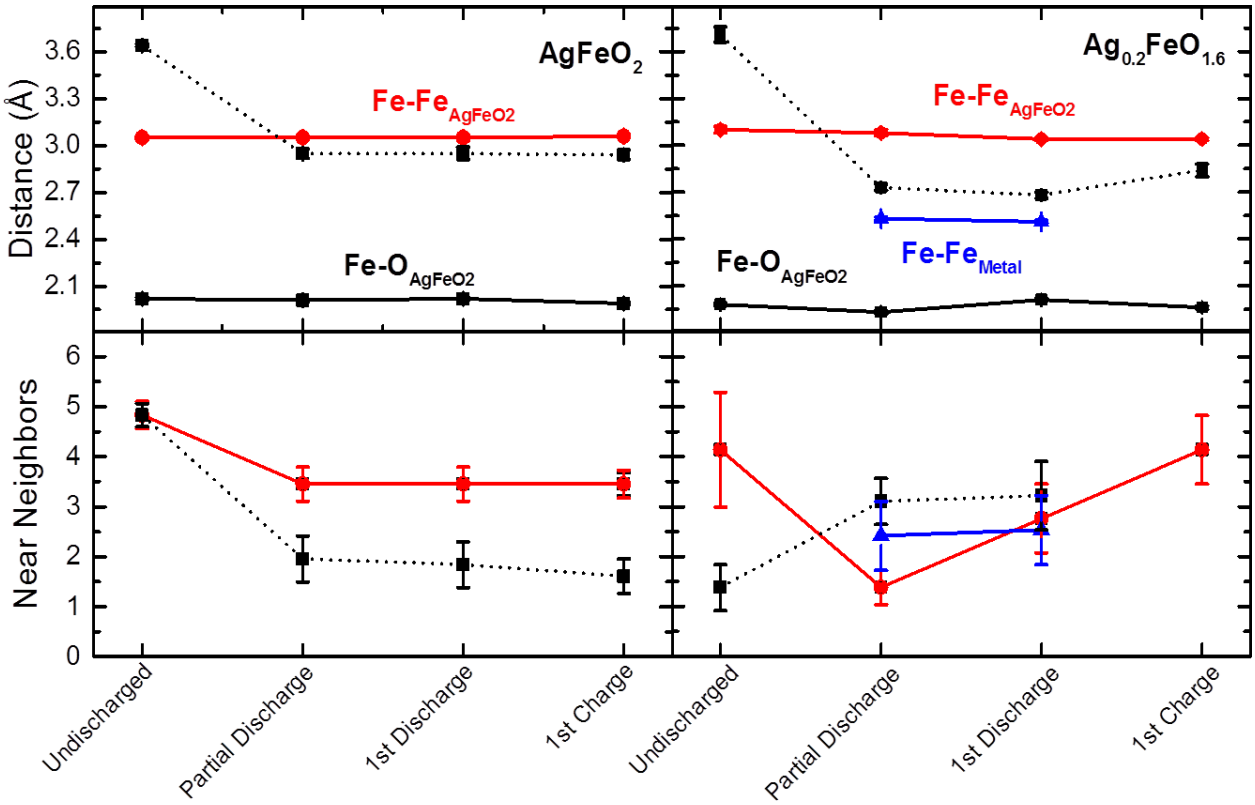

Figure 8.5. EXAFS modeling results of interatomic distance (top) and number of near neighbors (bottom) for $AgFeO_2$ and $Ag_{0.2}FeO_{1.6}$ (right), Fe-O (black lines) and Fe-Fe (red and blue lines) contributions

The Ag K-edge modeling results of the $AgFeO_2$ electrode confirm the formation of metallic

Ag^0 upon discharge. In particular, the reduced number of neighboring Ag-Ag atoms from the expected value of 12, based on the standard fcc crystal structure and assuming a spherical particle morphology, to 8.4 ± 1.0 neighboring atoms allows for the estimation of particle size, on the order of several nanometers in diameter. The particle size can be estimated due to surface termination effects which artificially reduce the average number of neighboring atoms.[128]

EXAFS analysis of $Ag_{0.2}FeO_{1.6}$ in **Figure 8.5** is more complex due to the presence of two phases in the pristine material, namely $AgFeO_2$ and γ-Fe_2O_3. These two phases have distinct Fe-Fe distances of which permits the direct observation of each phase (specifically, Fe-Fe_{AgFeO_2} is 3.10 ± 0.02 Å while Fe-$Fe_{\gamma\text{-}Fe_2O_3}$ distances are 2.97 ± 0.05 Å and 3.48 ± 0.05 Å). As the $Ag_{0.2}FeO_{1.6}$ was partially discharged, the distinction between $AgFeO_2$ and γ-Fe_2O_3 could no longer be resolved, therefore, a general iron oxide model based on a FeO crystal structure[114] was adopted. The FeO model includes a Fe-O contribution, fit to an interatomic distance of 1.98 ± 0.01 Å, and an Fe-Fe contribution, interatomic distance of 2.73 ± 0.02 Å. In addition, an Fe metal contribution was observed in the partially discharged state $Ag_{0.2}FeO_{1.6}$ which is unique compared to $AgFeO_2$. The Fe metal phase was also resolved due to the distinct interatomic distance, fit to 2.53 ± 0.01 Å. The observation of Fe metal in discharged $Ag_{0.2}FeO_{1.6}$ is accompanied by a decrease in the amplitude of the generic iron oxide phase. When $Ag_{0.2}FeO_{1.6}$ is fully discharged, there are no statistically significant changes in either the observed interatomic distances or number of neighboring atoms, thus suggesting that similar atomic structures are present. When charged to 3.5 V, $Ag_{0.2}FeO_{1.6}$ returns to a crystalline state that is similar the state that was observed in the undischarged spectrum, with the exception of the γ-Fe_2O_3. From the EXAFS modeling of $Ag_{0.2}FeO_{1.6}$, it appears that the structure reforms to a FeO-like state with a single Fe-O and Fe-Fe contribution in the structure. This structure is similar to that of $AgFeO_2$, which contains a single Fe-O and Fe-Fe contribution in the first two coordination shells, therefore, it is uncertain from this analysis whether the material returns to the original layered $AgFeO_2$

structure, or reverts to an FeO-like fcc arrangement.

8.3.3 Redox Mechanism

The XAS results suggest slightly different redox mechanisms for $AgFeO_2$ and $Ag_{0.2}FeO_{1.6}$ cathode materials during the discharge process and after charging to 3.5 V. EXAFS modeling illustrates that both $AgFeO_2$ and $Ag_{0.2}FeO_{1.6}$ experience migration of Ag^+ ions out of the crystal structure, also known as a reduction-displacement reaction. As mentioned previously, the reduction-displacement of $Ag^+ \rightarrow Ag^0$, within transition metal oxide cathode materials, is a paradigm was first established with silver vanadium oxide ($Ag_2V_4O_{11}$),[163] then later extended to silver vanadium phosphorous oxide ($Ag_2VO_2PO_4$)[67,106,107,164] and recently to silver ferrite ($AgFeO_2$).[75] In combination with the CV and galvanostatic cycling results in Chapter VI, Ag^+ reduction Ag^0must occur in parallel with the reduction of Fe^{3+}.

On the first discharge of $AgFeO_2$, it is likely that Fe^{3+} only partially reduces to Fe^{2+} since the $AgFeO_2$ *in-situ* XRD pattern showed a decrease in the crystallinity of $AgFeO_2$ and no evidence of a new iron oxide phase. However, the crystal structure of $Ag_{0.2}FeO_{1.6}$ rapidly amorphizes during discharge, reducing to FeO and eventually to metallic Fe^0. The decreased stability of the $Ag_{0.2}FeO_{1.6}$ material upon discharge can be attributed to the small crystallite size, leading to decreased stability upon Li^+ intercalation, and large non-crystalline γ-Fe_2O_3 component which provides a substantial amount of surface area with active sites available for reduction. Although, metallic Fe^0 is observed in discharged $Ag_{0.2}FeO_{1.6}$ electrodes, the capacity corresponds to 2 electron discharge process at the maximum (1 electron for Ag^+ reduction and the remaining capacity due to Fe^{3+} reduction). The EXAFS modeling shows that discharged $Ag_{0.2}FeO_{1.6}$ contains a generalized FeO-like iron oxide phase, which may include $AgFeO_2$, and small contribution from metallic Fe^0. It can be rationalized that the contribution of metallic Fe^0 is a small component that results from the structural instability of the large amorphous γ-Fe_2O_3 phase upon reduction, during which a small portion of γ-Fe_2O_3 is reduced to metallic Fe^0. Since this contribution is not significant, an increase in delivered capacity would not be anticipated.

Upon charge, the oxidation of $AgFeO_2$ and $Ag_{0.2}FeO_{1.6}$ electrodes is reversible with both materials returning to a state similar to undischarged material via EXAFS modeling and the stability during cycling. EXAFS modeling shows that the structure of $AgFeO_2$ and $Ag_{0.2}FeO_{1.6}$ upon charge is similar to that of $AgFeO_2$, which contains a single Fe-O and Fe-Fe contribution in the first two coordination shells, therefore, it is uncertain from this analysis whether the material returns to the original layered $AgFeO_2$ structure, or reverts to an rock salt FeO-like structure.

Taking into consideration electrochemical data and results obtained from advanced *in-situ* and *ex-situ* characterization techniques, a generalized redox mechanism is proposed in **Equation 8.1** for the $AgFeO_2$ component where the reduction-displacement reaction of Ag^+ is followed by the reversible reduction and oxidation of iron, $Fe^{3+} \leftrightarrow Fe^2$. A second generalized redox mechanism is proposed in **Equation 8.2** for the γ-Fe_2O_3 component where Li^+ is intercalated into the structure to afford a rock salt $LiFe_2O_3$ structure, as observed in other γ-Fe_2O_3 electrodes cycled above 1.0 V.[185–187] In Ag_xFeO_y composites, **Equations 8.1** and **8.2** are expected to occur in parallel where the full reduction of $Ag^+ \rightarrow Ag^0$ is observed followed by the reduction of Fe^{3+} in $AgFeO_2$ and γ-Fe_2O_3.

$$\begin{aligned} AgFeO_2 \ + \ x\,Li^+ \ + \ x\,e^- \ &\rightleftharpoons \ Li_xAg_{1-x}FeO_2 \ + \ (1-x)\,Ag^0 \text{ where } x \ \leq \ 1 \\ LiFeO_2 \ + \ Ag^0 \ + \ y\,Li^+ \ + \ y\,e^- \ &\rightleftharpoons \ Li_{1+y}O \ + y\,FeO \ + \ Ag^0 \text{ where } y \ \leq \ 1 \end{aligned} \tag{8.1}$$

$$\gamma{-}Fe_2O_3 \ + \ z\,Li^+ \ z\,e^- \ \rightleftharpoons \ Li_zFe_2O_3 \text{ where } z \ + \ y \ \leq \ 1 \tag{8.2}$$

8.4 Electrochemical Evaluation at Lower Discharge Voltages

Iron oxide electrode materials, especially those based on Fe_2O_3, are typically discharged to low voltages in the range of 0.01–3.0 V.[168–170] In Chapters VI and VII, $AgFeO_2$ and Ag_xFeO_y composites were cycled much higher, between 1.5–3.5 V. Cycling $AgFeO_2$ and Ag_xFeO_y composites to lower voltages will allow access to redox couples that are typically observed below 1.5 V, such as the reduction of Fe^{2+} to Fe metal, thus increasing the gravimetric

capacity of the cathode material. **Figures 8.6** and **8.7** show $AgFeO_2$ and $Ag_{0.2}FeO_{1.6}$ discharged to 0.6 and 0.1 V, respectively. During the first cycle, $AgFeO_2$ and $Ag_{0.2}FeO_{1.6}$ electrodes demonstrate plateaus near 1.8 V ($Ag^+ \rightarrow Ag^0$) and 1.0 V. The plateau at 1.0 V, in **Figures 8.7**, shows a gradual sloping region when discharged further to 0.1 V. The beginning of this plateau can be related to the reduction of $Fe^{3+} \rightarrow Fe^{2+}$ while the reduction of $Fe^{2+} \rightarrow$ occurs later during the 1.0 V plateau and within the sloping region following it.

Notably, the delivered capacities of $AgFeO_2$ and $Ag_{0.2}FeO_{1.6}$ in **Figures 8.6** and **8.7**, during the first and subsequent cycles, are significantly higher than the capacities that were observed in Chapters VI and VII. First cycle discharge capacities display values as high as ~2000 mAh/g when discharged to 0.1 V, thus exceeding the theoretical capacity of fully discharged $AgFeO_2$ at 548 mAh/g (4 electrons) and γ-Fe_2O_3 at 1007 mAh/g (6 electrons). The excess capacity delivered by $AgFeO_2$ and $Ag_{0.2}FeO_{1.6}$ electrochemical cells is related to the decomposition of the electrolyte and the formation of the SEI and Li_2O on the surface of the pristine electrode at the electrolyte interface, a process that coincides with the irreversible capacity loss in the first few cycles.[36,37,42,118–120] The plateau near 1.0 V is observed in cycles 1–50 when $AgFeO_2$ and $Ag_{0.2}FeO_{1.6}$ are discharged to 0.1 V, however, the discharge profiles to 0.6 V do not show a plateau at 1.0 V by cycle 50 suggesting differences in the stability of the materials over multiple cycles.

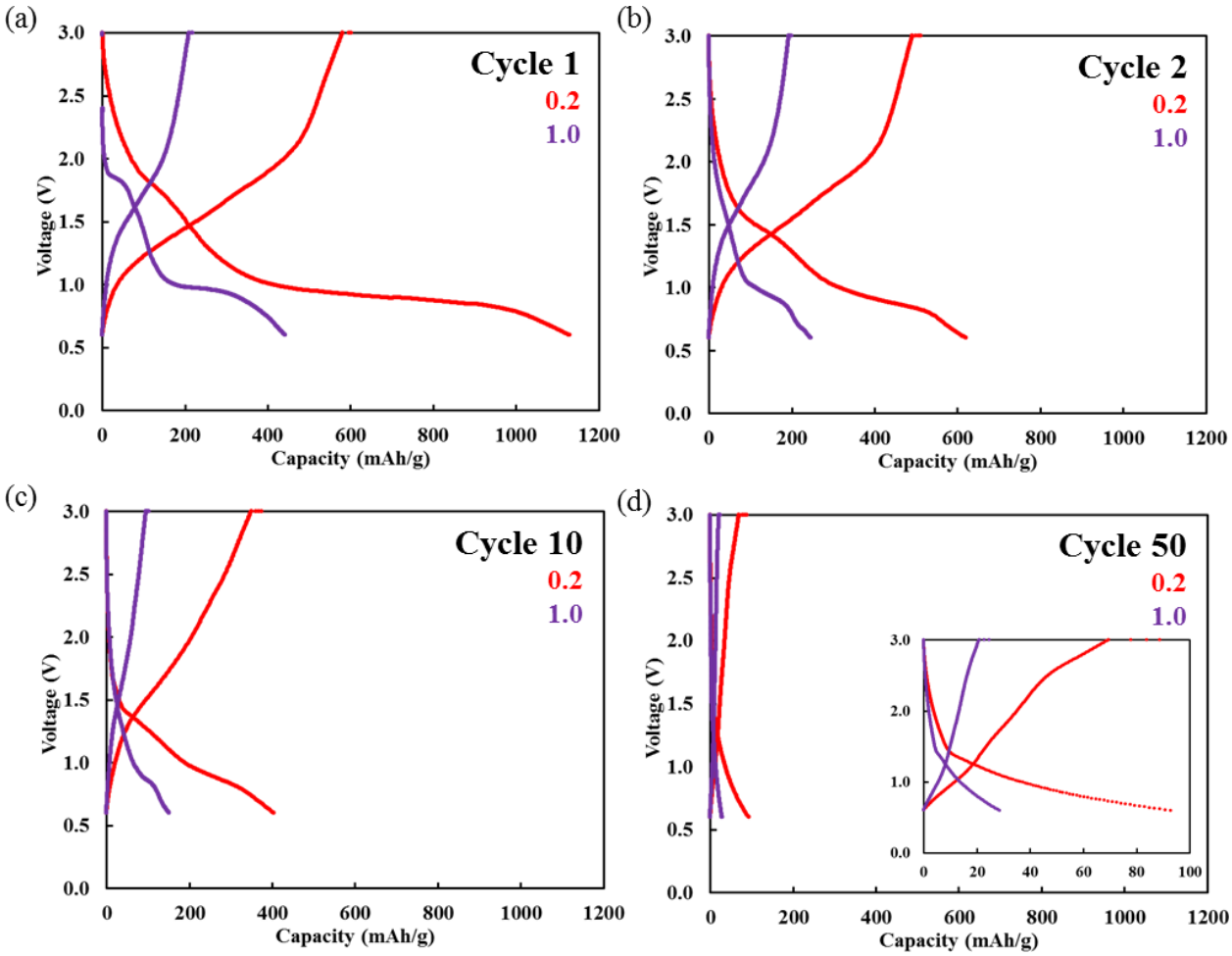

Figure 8.6. Voltage profiles for Li/$AgFeO_2$ and Li/$Ag_{0.2}FeO_{1.6}$ electrochemical cells discharged to 0.6 V at: (a) cycle 1, (b) cycle 2, (c) cycle 10, and (d) cycle 50

Significant differences in the reversibility of the redox mechanism of $AgFeO_2$ and $Ag_{0.2}FeO_{1.6}$ electrodes discharged to 0.6 and 0.1 V are observed in **Figures 8.8** and **8.9**. Overall, $AgFeO_2$ shows poor cycle life compared to $Ag_{0.2}FeO_{1.6}$ when discharge to low voltage. This different is more obvious when the electrodes are discharged to 0.1 V where $AgFeO_2$ delivers a capacity of 383 mAh/g after 50 cycles while $Ag_{0.2}FeO_{1.6}$ delivers a capacity of 61 mAh/g. The increased electrochemical performance of $Ag_{0.2}FeO_{1.6}$ may be a result of the small crystallite size and large amorphous γ-Fe_2O_3 component of the material which facilitates more reversible reduction of oxidation of iron oxide.

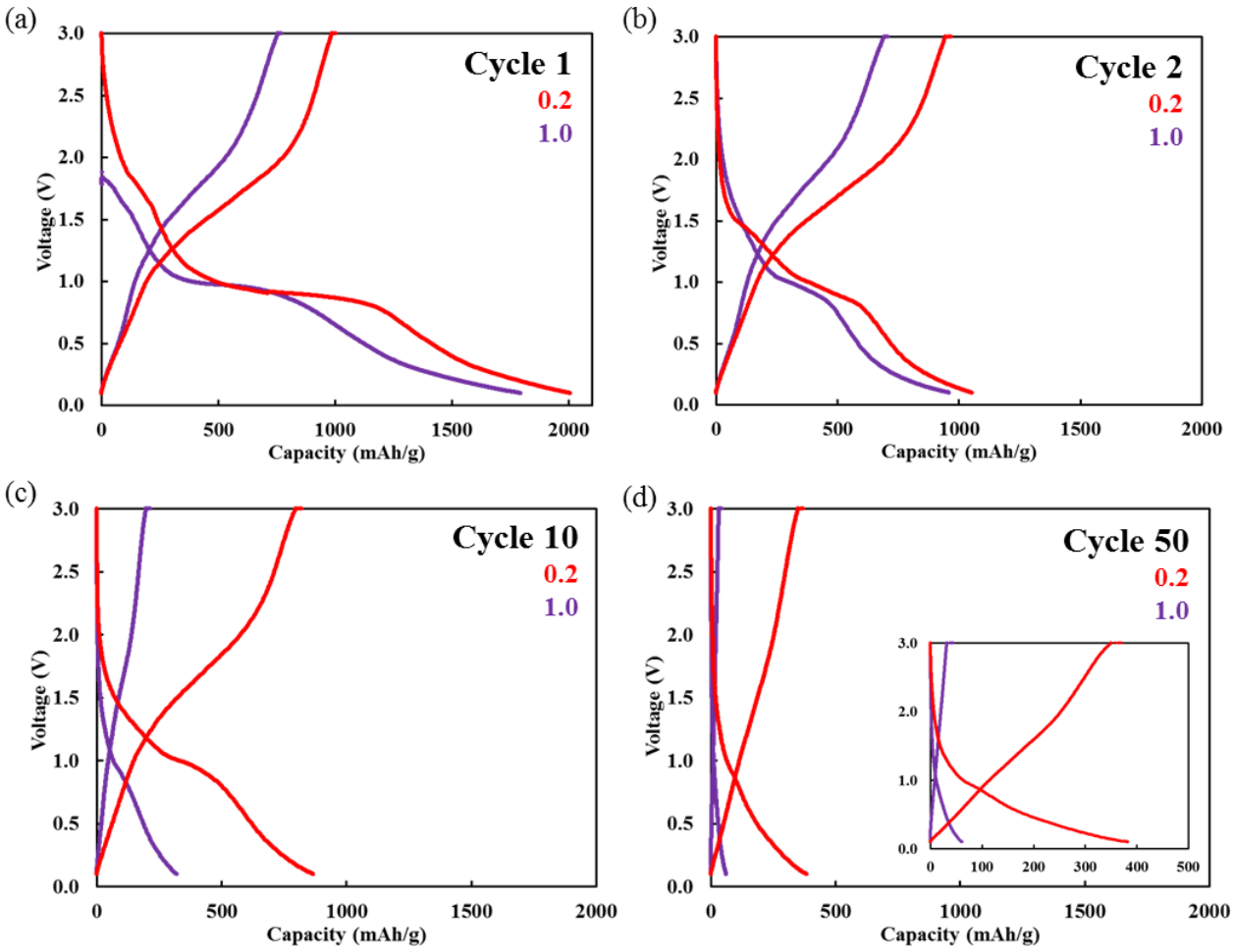

Figure 8.7. Voltage profiles for $Li/AgFeO_2$ and $Li/Ag_{0.2}FeO_{1.6}$ electrochemical cells discharged to 0.1 V at: (a) cycle 1, (b) cycle 2, (c) cycle 10, and (d) cycle 50

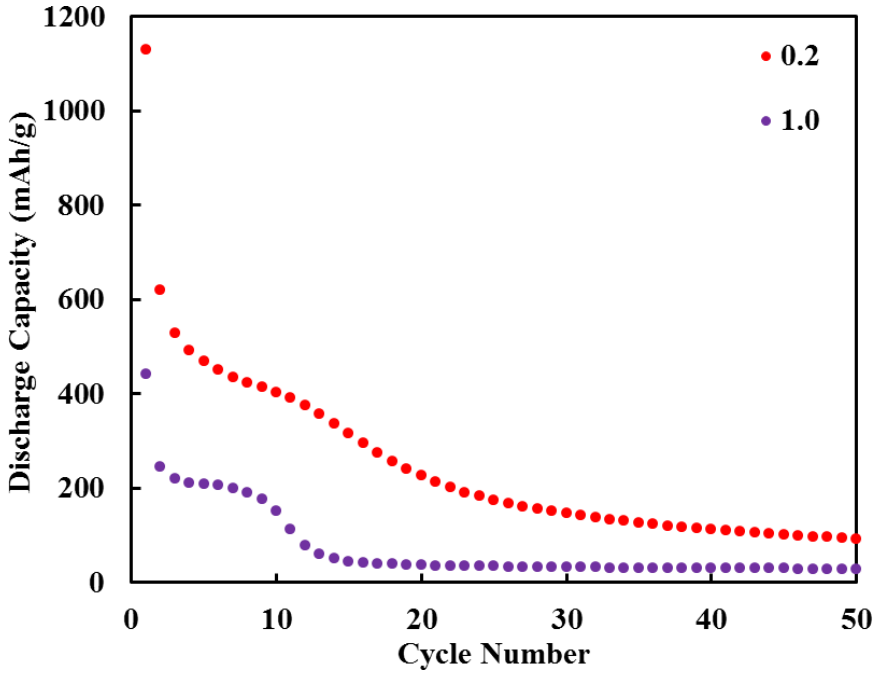

Figure 8.8. Discharge capacity, over 50 cycles, for Li/$AgFeO_2$ and Li/$Ag_{0.2}FeO_{1.6}$ electrochemical cells discharged to 0.6 V

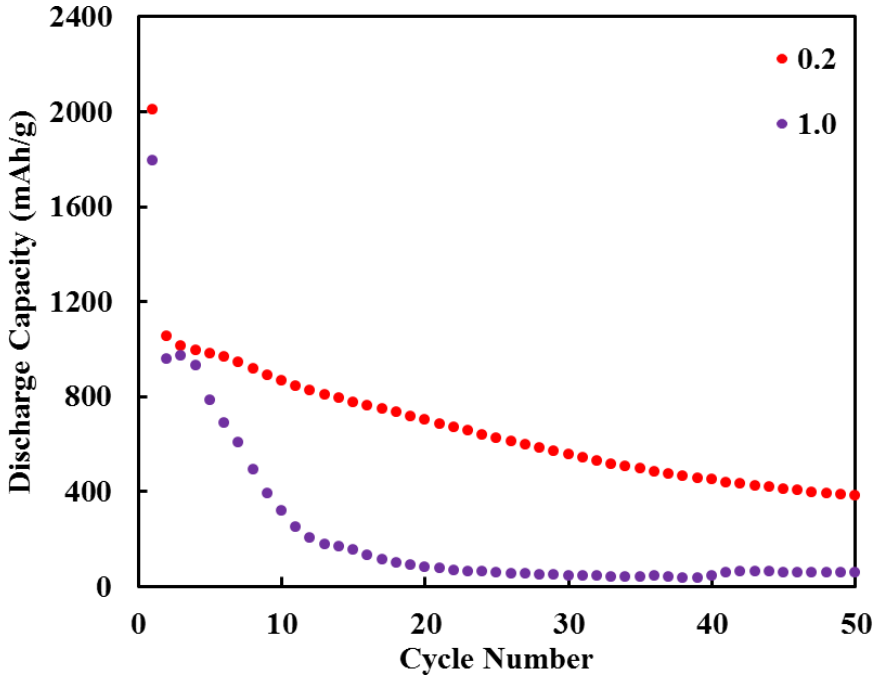

Figure 8.9. Discharge capacity, over 50 cycles, for Li/$AgFeO_2$ and Li/$Ag_{0.2}FeO_{1.6}$ electrochemical cells discharged to 0.1 V

The redox mechanism of $AgFeO_2$ and $Ag_{0.2}FeO_{1.6}$ can be modified, as in **Equation 8.3**, to include the reduction of Fe^{2+} to metallic Fe^0.

$$\begin{aligned}
AgFeO_2 \;+\; x\,Li^+ \;+\; x\,e^- \;&\rightleftharpoons\; Li_xAg_{1-x}FeO_2 \;+\; (1-x)\,Ag^0 \text{ where } x \;\leq\; 1 \\
LiFeO_2 \;+\; Ag^0 \;+\; y\,Li^+ \;+\; y\,e^- \;&\rightleftharpoons\; Li_{1+y}O \;+ y\,FeO \;+\; Ag^0 \text{ where } y \;\leq\; 1 \\
FeO \;+\; 2\,Li^+ \;+\; 2\,e^- \;&\rightleftharpoons\; Li_2O \;+\; 2\,Fe^0 \\
\gamma{-}Fe_2O_3 \;+\; z\,Li^+\,z\,e^- \;&\rightleftharpoons\; Li_zFe_2O_3 \text{ where } z \;+\; y \;\leq\; 1 \\
LiFe_2O_3 \;+\; 5\,Li^+ \;+\; 5\,e^- \;&\rightleftharpoons\; 3\,Li_2O \;+\; 2\,Fe^0
\end{aligned} \tag{8.3}$$

8.5 Conclusion

Advanced *in-situ* and *ex-situ* techniques were utilized in Chapter VIII to investigate electrochemically discharged and charged cathodes and provided meaningful insight into the lithiation/delithiation mechanism of an $Ag_{0.2}FeO_{1.6}$ composite and $AgFeO_2$. *In-situ* XRD monitored the structural evolution of $AgFeO_2$ and $Ag_{0.2}FeO_{1.6}$, as a function of depth of discharge, and demonstrated significantly different mechanisms. The crystal structure of $AgFeO_2$ remained intact after discharge to 1.0 V while the diffraction pattern of $Ag_{0.2}FeO_{1.6}$ indicated complete amorphization of the crystalline material. $AgFeO_2$ and $Ag_{0.2}FeO_{1.6}$ electrodes were partially discharged, fully discharged, and fully charged and the structural changes were interrogated using *ex-situ* XAS. EXAFS modeling confirmed the phases present at each electrochemical state, thus allowing for a redox mechanism to be proposed which includes to reduction of $Ag^+ \rightarrow Ag^0$ and $Fe^{3+} \rightarrow Fe^{2+}$. $AgFeO_2$ is proposed to cycle between a lithiated $AgFeO_2$ phase ($LiFeO_2$) and the rock salt FeO phase while the substantial amorphous γ-Fe_2O_3 component of Ag_xFeO_y composites is expected to cycle between γ-Fe_2O_3 and a rock salt $LiFe_2O_3$ phase when discharge to 1.5 V. Discharge of $AgFeO_2$ and $Ag_{0.2}FeO_{1.6}$ electrodes to lower voltages, 0.6 or 0.1 V,allows for the $Fe^{2+} \rightarrow Fe^0$ redox couples to be accessed near 1.0 V, thus resulting in high gravimetric capacities. Chapter VIII illustrates the promise of an electrode comprised of an amorphous γ-Fe_2O_3 phase and crystalline $AgFeO_2$

which provides unique electrochemistry and enhanced performance.

CHAPTER IX

CONTROLLING $AgFeO_2$ CRYSTALLITE SIZE TO AFFECT ELECTROCHEMISTRY

9.1 Introduction

A majority of delafossite syntheses incorporate some type of base (e.g. NaOH, KOH) in their reaction schemes. While base is commonplace in these synthetic reactions, the effects that base concentration has on the size of the delafossite product have not been investigated. As Sheets et al. states, the primary role of the NaOH mineralizer in the synthesis of delafossite-type oxides is to increase the solubility of the metal complexes by increasing the hydroxide concentration.[90] Conversely, the role of base has been studied in reactions that afford iron oxide nanoparticles known as magnetite, Fe_3O_4.[188,189] It was discovered that the crystallite size of Fe_3O_4 nanoparticles decreased with increasing pH.

Such a phenomenon can be explained by the theory of nucleation and subsequent growth processes of colloids proposed by LaMer et al. in 1950.[190] During this process, nucleation is initiated upon the introduction of reagents or precursors into solution. When the precursor concentration is increased rapidly to the critical level of saturation, referred to as supersaturation, a large quantity of clusters are formed. The formation of clusters in solution causes a decrease in the precursor concentration and affords the seeds or nucleation sites required for crystalline nano-sized particles to grow. These nanoparticles grow by means of an Ostwald ripening mechanism.[191–193] The faster a nucleation event occurs, the smaller the nanoparticle size will be. Bases, like NaOH, are found to increase the rates of delafossite reactions due to the fact that they increase solubility of metal oxide and their corresponding hydroxides.[90] As a consequence, higher concentrations of base will lead to faster nucleation events and smaller metal oxide nanoparticles (**Figure 9.1**).

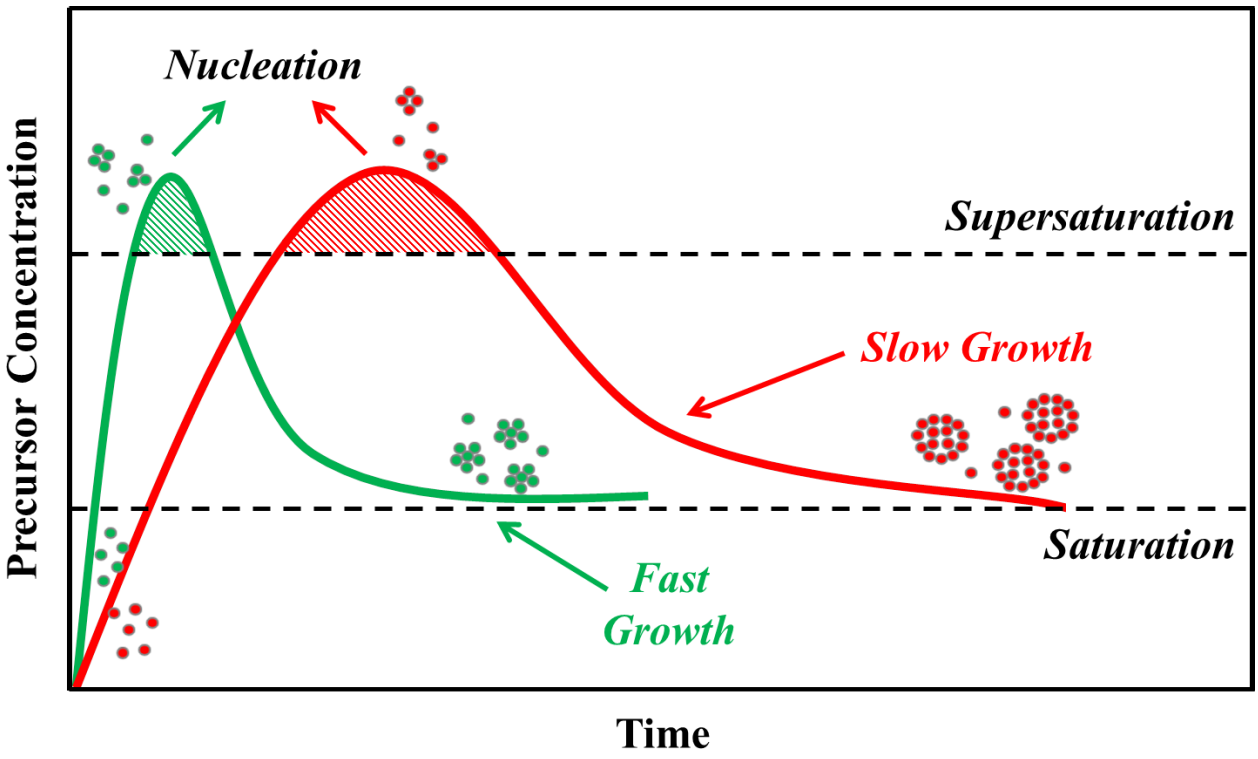

Figure 9.1. LaMer nucleation with fast and slow rates

In contrast to changing the stoichiometry of reagents, a separate method to control crystallite size is to use constraining materials. Constraining materials encompass structures like dendrimers, amphoteric surfactants (micelles), carbon matrices, and metal-oleates.[194,195] Although constraining materials are a means of precisely controlling particle size and shape, separation from the end product is not always trivial. The advantage of the technique described herein is that narrow size distribution of $AgFeO_2$ crystallites can be achieved via direct synthesis without the need for constraining materials.

9.2 Experimental

9.2.1 General Methods and Materials

Silver ferrite was synthesized via a co-precipitation reaction modified from previously reported schemes.[74,78] Silver nitrate, iron(III) nitrate, and sodium hydroxide reagents were used as received from the vendors. Water utilized during synthesis was deionized water filtered through a Thermo Scientific Barnstead Nanopure ultrapure water purification system.

9.2.2 Characterization

Silver ferrite samples were characterized by X-Ray diffraction (XRD), inductively coupled plasma-optical emission spectroscopy (ICP-OES), simultaneous thermogravimetric analysis/differential scanning calorimetry (TGA/DSC), and Brunauer-Emmett-Teller (BET) surface area analysis. XRD spectra were collected with Cu Kα radiation and Bragg-Brentano focusing geometry using a Rigaku MiniFlex or a SmartLab X-Ray diffractometer and a D/tex detector. XRD spectra were measured in a 2θ range from 5° to 90° and crystallite sizes were calculated by applying the Scherrer equation to the (0 0 6) reflection near a value 2θ of 28° in the diffraction pattern. TGA/DSC samples of $AgFeO_2$ were heated to 580°C at a rate of 5°C/min under an atmosphere of nitrogen gas using a SDT Q600 from TA Instruments. Quantitative elemental analysis for the elemental analysis of silver and iron concentration in silver ferrite samples was completed on a ThermoScientific iCap 6000 ICP spectrometer. Surface area measurements were collected on a Quantachrome Nova 4200e using an 11-point BET method.

9.2.3 Synthesis of $AgFeO_2$

Aqueous solutions of sodium hydroxide, silver nitrate, and iron nitrate were combined. A dark red-brown precipitate formed immediately. After reflux, the solid $AgFeO_2$ was obtained by centrifugation, washed with DI H_2O, and reduced to dryness in vacuo.

9.3 Results and Discussion

9.3.1 Structural and Elemental Composition

The low-temperature, low-pressure co-precipitation method reported above affords pure silver ferrite and proves to be highly reproducible with yields of the delafossite exceeding 90%. The X-ray diffraction (XRD) pattern of $AgFeO_2$ in **Figure 9.2** illustrates pure silver ferrite and does not demonstrate presence of metallic silver (Ag^0) or additional oxide impurity phases (e.g. Ag_2O, FeOOH) typically observed during delafossite synthesis.[74,77,90,103,105] The peaks in the XRD pattern are broad due to the nanocrystalline nature of silver ferrite and

the average crystallite size of $AgFeO_2$, prepared in Chapter V, was calculated to be 17 nm using the Scherrer equation.

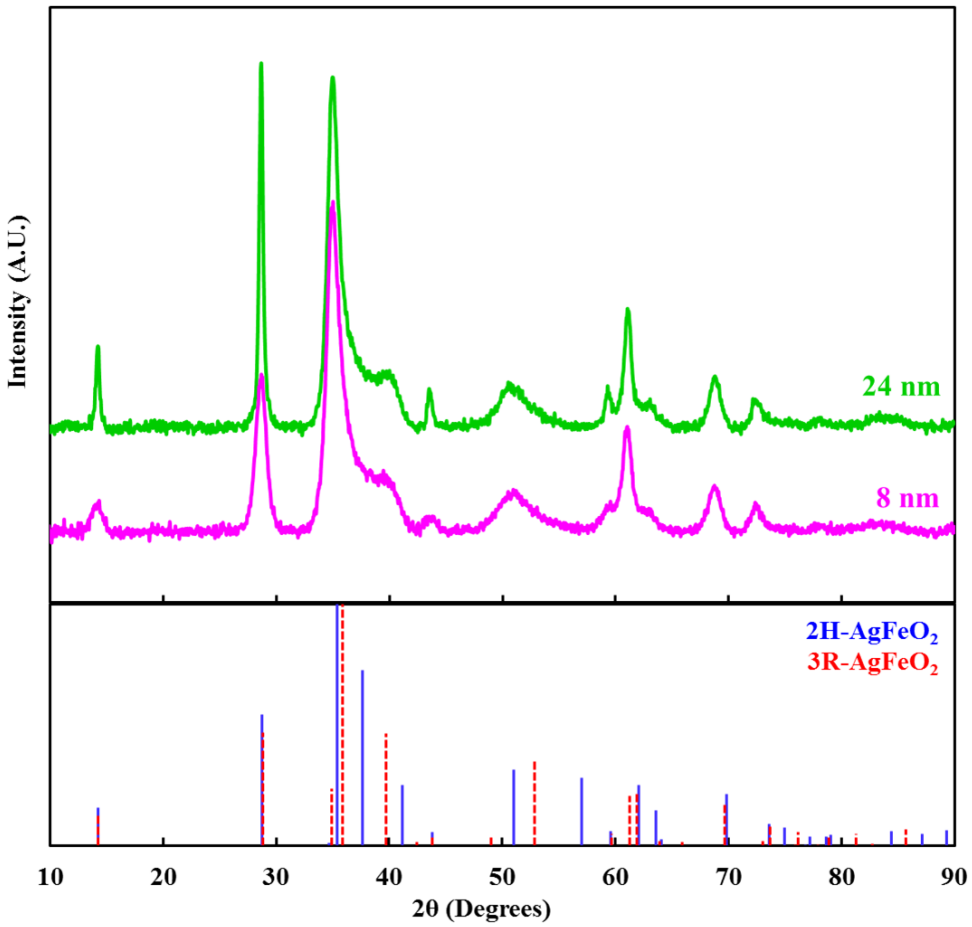

Figure 9.2. $AgFeO_2$ with 3R-$AgFeO_2$ reference pattern (ICSD 31919)

Once it was verified that $AgFeO_2$ could be obtained reproducibly and free of impurity phases via co-precipitation, the concentration of base, sodium hydroxide, or overall concentration of the reaction was altered in an effort to effect the crystallite size of silver ferrite. Silver ferrite was initially synthesized with typical reaction parameters, including the necessary amount of base for the reaction to remain neutral upon completion (i.e. 4 equivalents of sodium hydroxide, NaOH). Small crystallite size–8 nm–silver ferrite was obtained by increasing the concentration of NaOH used and increasing the concentration of the reaction. The powder XRD patterns of small and large $AgFeO_2$ are shown in **Figure 9.2** with $AgFeO_2$ obtained from the typical reaction parameters employed in Chapter V. The crystallite size of

$AgFeO_2$ is calculated from the diffraction pattern using the Scherrer equation. The relative 2θ positions of the $AgFeO_2$ peaks did not shift and no new peaks were apparent, therefore, it can be rationalized that the structure of the bulk material has not been affected.

Inductively coupled plasma-optical emission spectroscopy (ICP-OES) was used to quantify the silver and iron content of $AgFeO_2$ materials (**Table 9.1**). The corresponding Ag/Fe ratios were calculated to be 1.0 ± 0.05 for all silver ferrite samples. In combination with the diffraction results, it is apparent that $AgFeO_2$ materials with different crystallite sizes maintain equivalent compositions and morphology.

Table 9.1. ICP-OES of $AgFeO_2$ samples with different crystallite sizes

Crystallite Size (nm)	**Ag/Fe Ratio via ICP-OES**
8 nm	0.95
17 nm	0.97
24 nm	1.02

9.3.2 Thermal Stability

Thermogravimetric analysis (TGA) was employed to measure the decomposition of $AgFeO_2$ as a function of temperature (**Figure 9.3**). The weight loss before 300°C in 8 and 24 nm $AgFeO_2$ accounts for ∼10% and 4% of the total sample weight, respectively, and is due to the dehydration of physisorbed and interlayer water in the structure. The 8 nm sample displays greater mass lost to water, likely a result of the larger surface area of the small crystallite available to accommodate water molecules. The significant weight loss event near 550^0C is the decomposition of $AgFeO_2$ to Ag metal and hematite (α-Fe_2O_3), as described in Chapter V.

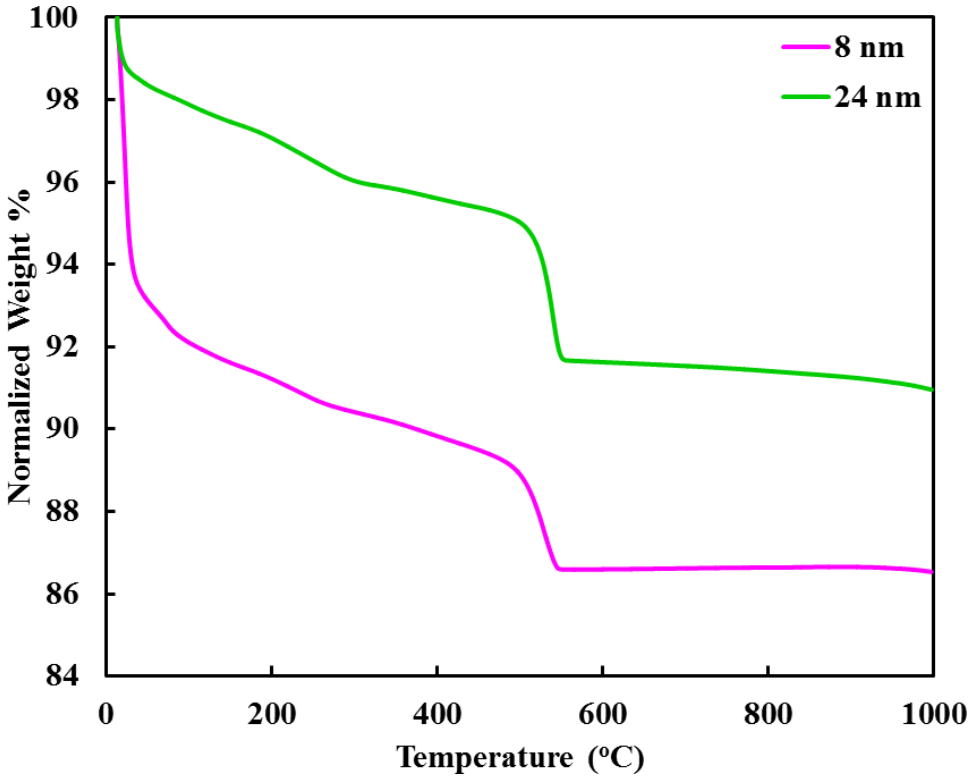

Figure 9.3. Simultaneous TGA/DSC of $AgFeO_2$

9.3.3 Surface Area Analysis

The final method of characterization used to elucidate the physical properties of silver ferrite nanoparticles was multi-point Brunauer-Emmett-Teller (BET) surface area analysis. The adsorption of nitrogen (N_2) gas molecules on the surface of $AgFeO_2$ crystallites was used to measure the surface area of the solid material and the results are summarized in **Table 9.2**. Large $AgFeO_2$ (24 nm) has a lower average surface area, 23 m^2/g, relative to small $AgFeO_2$ with a surface area of 85 m^2/g. As anticipated, when compared to 17 nm $AgFeO_2$ obtained in Chapter V, the BET surface area follows a distinct trend in which small crystallite size materials display higher surface areas.

Table 9.2. BET surface area analysis of $AgFeO_2$ samples with different crystallite sizes

Crystallite Size (nm)	Surface Area (m^2/g
8 nm	85
17 nm	51
24 nm	23

9.3.4 Electrochemical Evaluation

Galvanostatic cycling of 8 and 24 nm $AgFeO_2$ was conducted and **Figure 9.4** shows the evolution of the discharge capacity of $AgFeO_2$ electrodes over 50 cycles while the voltage profiles are illustrated in **Figure 9.5**. First cycle discharge capacities of small and large $AgFeO_2$ (**Figure 9.4**) are extremely efficient and come close to the theoretical capacity of $AgFeO_2$, 274 mAh/g.

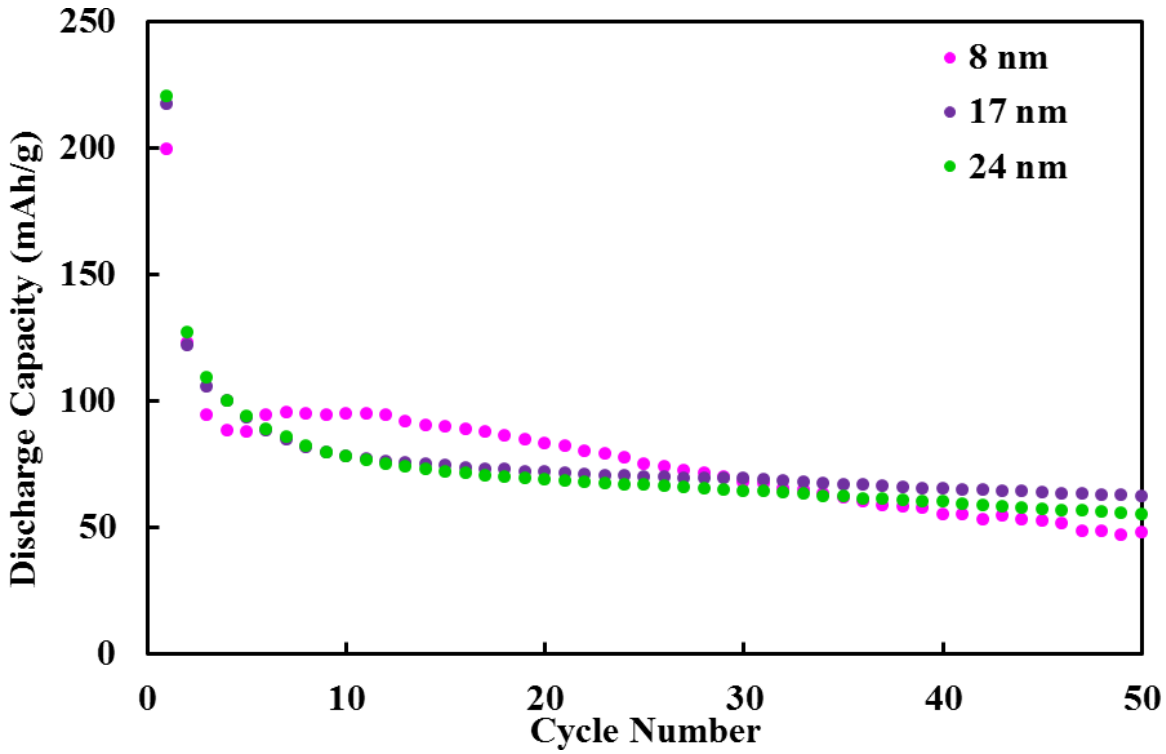

Figure 9.4. Galvanostatic cycling of Li/$AgFeO_2$ electrochemical cells with discharge capacity plotted as a function of cycle number for 8, 17, and 24 nm materials

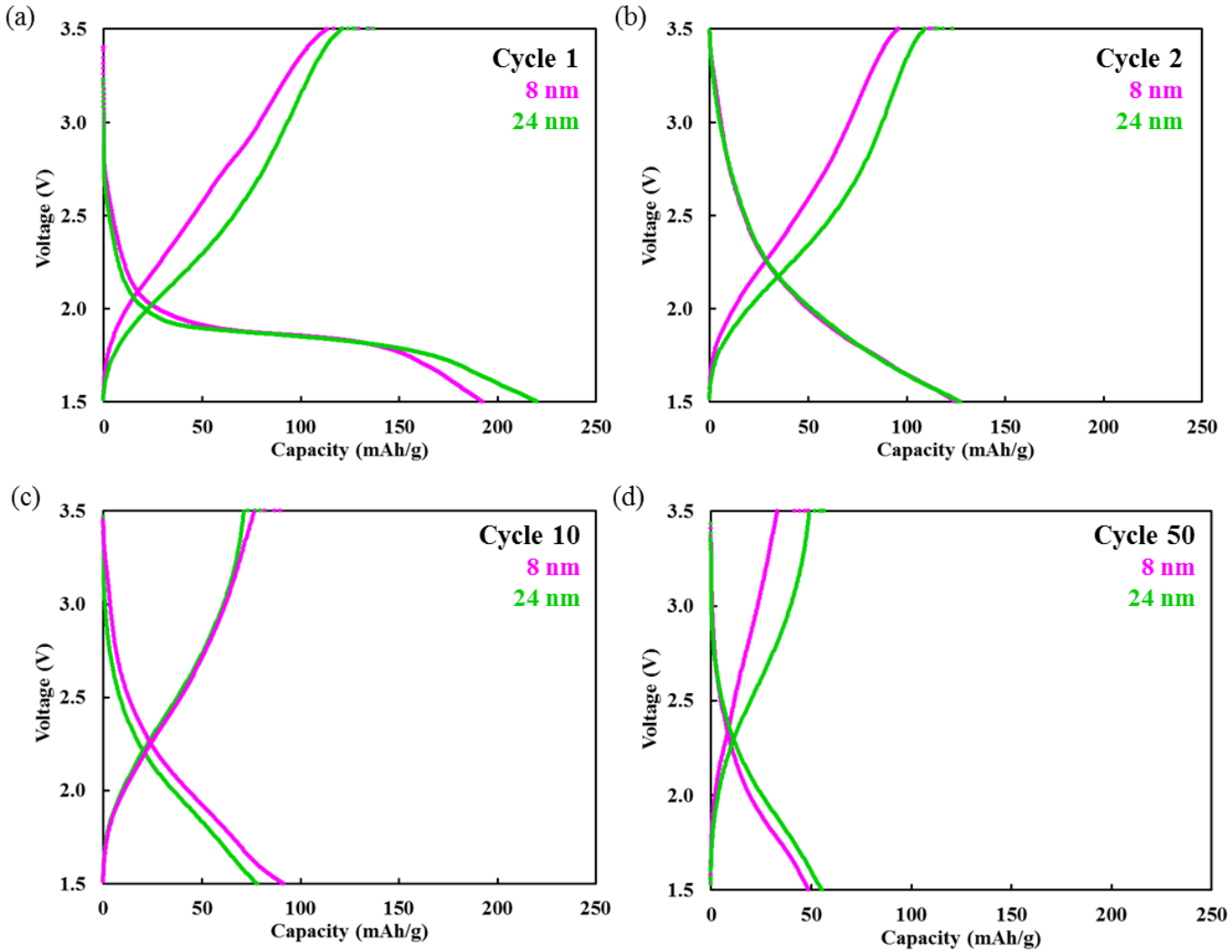

Figure 9.5. Capacity plotted as a function of voltage for Li/$AgFeO_2$ cells during galvanostatic cycling at cycles: (a) 1, (b) 2, (c) 10, and (d) 50

Unfortunately, significant capacity is lost by cycle 2 which has previously been rationalized as the irreversible reduction of Ag^{+} to metallic Ag^{0}.[155] The continuous cycling of 24 nm Li/$AgFeO_2$ electrochemical cells demonstrates profound stability over 50 cycles, generating a similar discharge capacity profile to the 17 nm $AgFeO_2$ discussed in Chapter VI and illustrated in **Figure 6.2**. A distinct cycling profile is produce by 8 nm $AgFeO_2$ where the discharge capacity is up to 25% greater than 17 and 24 nm cells in the first 30 cycles, then fades to a similar capacity by the end of cycle 50.

Investigation of the voltage profiles of 8 and 24 nm $AgFeO_2$ in **Figure 9.5** reveals similar redox mechanism. In cycle 1 (**Figure 9.5 a**), a voltage plateau is observed near 1.9 V and can be attributed to the simultaneous reduction of Ag§+ to Ag^{0} and Fe^{3+} to Fe^{2+}. The voltage profiles in the following cycles–2, 10, and 50–are similar for 8 and 24 nm $AgFeO_2$ and do not show voltage plateaus.

9.4 Conclusion

The method reported herein affords a single composition of $AgFeO_2$ with crystallite sizes on the nanoscale. Distinct crystallite sizes of silver ferrite, 8 and 24 nm, were obtained by varying both base and reaction concentrations. Electrochemical cells containing 8 nm $AgFeO_2$ electrode show promising electrochemical performance with up to 25% higher capacities than 17 and 24 nm $AgFeO_2$ in the first 30 cycles.

CHAPTER X

SUMMARY

A 0-D spinel-based anode material, $MgFe_2O_4$, was prepared using a combination of co-precipitation and hydrothermal reactions with a subsequent, relatively low-temperature calcination step in Chapter II and the influence of particle size and morphology on electrochemical behavior was established using *ex situ* X-ray absorption spectroscopy (XAS) and transmission electron microscopy (TEM) imaging. EELS (electron energy loss spectroscopy) mapping of the discharged materials illustrate subtle differences between the reduction processes where small particles are transformed to MgO and metallic Fe^0 while large 200-300 nm particles are mainly composed of $MgFe_2O_4$ which was also confirmed by EXAFS modeling. Notably, TEM imaging of discharged magnesium ferrite powder electrodes provide the first evidence of MgO after the reduction of magnesium ferrite

1-D silver hollandite, $Ag_xMn_8O_{16}$, nanorods were investigated in Chapters III and IV as viable cathode materials for lithium-based battery applications. In Chapter III, a 7-fold increase in capacity for low silver, small crystallite size material ($Ag_{1.2}Mn_8O_{16}$, L-Ag-OMS-2) compared to high silver, large crystallite size ($Ag_{1.6}Mn_8O_{16}$, H-Ag-OMS-2) was observed with delivered first cycle capacities of 160 and 23 mAh/g, respectively. The dramatic difference in capacity was rationalized as oxygen vacancies due to MnO_6 octahedral distortion, detected by electron energy loss spectroscopy (EELS), which facilitate Li^+ diffusion in the *ab* plane of silver hollandite nanorods demonstrating that surface defects, through such vacancies, play a significant role in electrochemical performance. $Ag_{1.4}Mn_6O_{18}$, with crystallite sizes of 10 and 15 nm was successfully prepared via a co-precipitation in Chapter IV. Uniform silver content ($x = 1.4$) in $Ag_xMn_8O_{16}$ allowed for the deconvolution of electrochemical effects related to crystallite size versus those related to silver content which had not been possible previously. TEM imaging shows a high degree of bundling of 10-Ag-OMS-2 nanorods compared to 15-Ag-OMS-2 and the 10-Ag-OMS-2 delivered a first cycle discharge capacity of 147 mAh/g while

the large crystallite size material (15-Ag-OMS-2) delivered 10.5 mAh/g upon discharge to 2.0 V. The small crystallite size material (10 Ag-OMS-2) proved to be structurally unstable during Li^+ intercalation via EXAFS modeling, leading to distortion of $Ag_{1.4}Mn_8O_{16}$ and formation of metallic Ag^0 nanoparticles while structural changes in 15-Ag-OMS-2 were not observed. On one hand, the small crystallite size $Ag_{1.4}Mn_8O_{16}$ increases surface area of silver hollandite nanorods causing the nanorods to bundle together which facilitates more intimate connection of the 10-Ag-OMS-2 material and enhances interparticle contact. On the other hand, structural distortion of 10-Ag-OMS-2 during lithiation and delithiation generates additional pathways for Li^+ diffusion and the reduction of Ag^+ to Ag^0 leads to the formation of a conductive percolation network within the cathode.

Cathode materials based on a 2-D layered $AgFeO_2$ materials were examined in Chapters V, VI, VII, VIII, and IX. A one-pot, non-stoichiometric co-precipitation reaction proved to be an acceptable method for preparing Ag_xFeO_y composites, composed of $AgFeO_2$ and γ-Fe_2O_3, with reliable control of chemical composition and crystallite size. The composite nature of Ag_xFeO_y composites was established using several characterization techniques, including X-ray diffraction (XRD), Raman spectroscopy, X-ray photoelectron spectroscopy (XPS), thermogravimetric analysis (TGA), and X-ray absorption spectroscopy (XAS) in Chapter V. Electron imaging by TEM and SEM provided a local examination of the nanocrystalline structure of Ag_xFeO_y composites prepared by a one-pot co-precipitation technique and confirmed the presence of both $AgFeO_2$ and a poorly crystalline γ-Fe_2O_3 phase in intimate contact. Electrochemical evaluation of Ag_xFeO_y composites was investigated in Chapter VI using galvanostatic cycling, galvanostatic intermittent titration technique (GITT) type testing, AC impedance, and cyclic voltammetry. In $AgFeO_2$ and Ag_xFeO_y electrodes, reduction of Ag^+ to metallic Ag^0 nanoparticles is observed and contributes to a $\sim$6,000-fold decrease in impedance. Further, $Ag_{0.2}FeO_{1.6}$ displays capacities 2X higher than stoichiometric $AgFeO_2$ and over 3X greater than nanocrystalline γ-Fe_2O_3. In Chapter VII, nanocrystalline $AgFeO_2$ and γ-Fe_2O_3 powders were mechanically mixed to afford a $Ag_{0.2}FeO_{1.6}$ mixture to study the

impact of a one-pot composite preparation on electrochemistry. TEM imaging showed more significant aggregation of particles in the $Ag_{0.2}FeO_{1.6}$ mechanical mixture while the one-pot $Ag_{0.2}FeO_{1.6}$ composite is comprised of more uniformly distributed spherical nanoparticles. Following 30 cycles, the one-pot $Ag_{0.2}FeO_{1.6}$ composite delivers an capacity (104 mAh/g) profoundly higher than the $Ag_{0.2}FeO_{1.6}$ mechanical mixture (40 mAh/g). Mechanical mixing of $AgFeO_2$ and γ-Fe_2O_3 powders to mimic a one-pot $Ag_{0.2}FeO_{1.6}$ composite yields lower delivered capacity where the results demonstrate the advantages of the directly prepared composite with more intimate particle connectivity not achievable through mechanical mixing. Advanced *in-situ* and *ex-situ* techniques were utilized in Chapter VIII to investigate electrochemically discharged and charged cathodes and provided meaningful insight into the lithiation/delithiation mechanism of an $Ag_{0.2}FeO_{1.6}$ composite and $AgFeO_2$. EXAFS modeling confirmed the phases present at each electrochemical state, thus allowing for a redox mechanism to be proposed which includes to reduction of $Ag^+ \rightarrow Ag^0$ and $Fe^{3+} \rightarrow Fe^{2+}$. $AgFeO_2$ is proposed to cycle between a lithiated $AgFeO_2$ phase ($LiFeO_2$) and the rock salt FeO phase while the substantial amorphous γ-Fe_2O_3 component of Ag_xFeO_y composites is expected to cycle between γ-Fe_2O_3 and a rock salt $LiFe_2O_3$ phase when discharge to 1.5 V. *In-situ* XRD was used as a complement to *ex-situ* XAS where the structural changes of $Ag_{0.2}FeO_{1.6}$ and $AgFeO_2$ cathodes are measured as a function of voltage. Discharge of $AgFeO_2$ and $Ag_{0.2}FeO_{1.6}$ electrodes to lower voltages, 0.6 or 0.1 V,allows for the $Fe^{2+} \rightarrow Fe^0$ redox couples to be accessed near 1.0 V, thus resulting in high gravimetric capacities. Finally, small (8 nm) and large (24 nm) $AgFeO_2$ were prepared by a one-pot co-precipitation reaction in Chapter VIII. Electrochemical cells containing 8 nm $AgFeO_2$ electrode show promising electrochemical performance with up to 25% higher capacities than 17 nm ("normal" size) and 24 nm (large) $AgFeO_2$ in the first 30 cycles.

The data presented in this dissertation provides considerable insight into the behavior of 0-D ($MgFe_2O_4$), 1-D ($Ag_xMn_8O_{16}$, and 2-D ($AgFeO_2$) cathode materials for lithium battery applications. The non-stoichiometric, co-precipitation and hydrothermal methods utilized

to prepared transition oxide materials with distinct chemical and physical properties are low-temperature, eco friendly, and economically feasible and may translate well to industrial scales. The particle morphology, presence of surface defects, and interrod or interparticle contact of $MgFe_2O_4$, $Ag_xMn_8O_{16}$, and Ag_xFeOy electrode materials played critical roles in electrochemical performance. Advanced *in-situ* and *ex-situ* techniques provided the necessary sensitivity to characterize discharge nanostructured transition metal oxides and establish valid redox mechanisms.

REFERENCES

[1] Nagaura, T.; Tozawa, K. *Prog. Batteries and Solar Cells* **1990**, *9*, 209–217.

[2] Makimura, Y.; Ohzuku, T. *J. Power Sources* **2003**, *119*, 156–160.

[3] Du Pasquier, A.; Plitz, I.; Menocal, S.; Amatucci, G. *J. Power Sources* **2003**, *115*, 171–178.

[4] Kang, S. H.; Kim, J.; Stoll, M. E.; Abraham, D.; Sun, Y. K.; Amine, K. *J. Power Sources* **2002**, *112*, 41–48.

[5] Ohzuku, T.; Makimura, Y. *Chem. Lett.* **2001**, *30*, 642–643.

[6] Padhi, A. K.; Nanjundaswamy, K. S.; Goodenough, J. B. *J. Electrochem. Soc.* **1997**, *144*, 1188–1194.

[7] Ferg, E.; Gummow, R. J.; Dekock, A.; Thackeray, M. M. *J. Electrochem. Soc.* **1994**, *141*, L147–L150.

[8] Tarascon, J. M.; Wang, E.; Shokoohi, F. K.; Mckinnon, W. R.; Colson, S. *J. Electrochem. Soc.* **1991**, *138*, 2859–2864.

[9] Thackeray, M. M.; David, W. I. F.; Bruce, P. G.; Goodenough, J. B. *Mater. Res. Bull.* **1983**, *18*, 461–472.

[10] Thackeray, M. M.; Johnson, P. J.; Depicciotto, L. A.; Bruce, P. G.; Goodenough, J. B. *Mater. Res. Bull.* **1984**, *19*, 179–187.

[11] Ohzuku, T.; Kitagawa, M.; Hirai, T. *J. Electrochem. Soc.* **1990**, *137*, 769–775.

[12] Thackeray, M. M.; de Kock, A.; Rossouw, M. H.; Liles, D.; Bittihn, R.; Hoge, D. *J. Electrochem. Soc.* **1992**, *139*, 363–366.

[13] Manthiram, A.; Chemelewski, K.; Lee, E. S. *Energy Environ. Sci.* **2014**, *7*, 1339–1350.

[14] Yamada, A.; Chung, S. C. *J. Electrochem. Soc.* **2001**, *148*.

[15] Yamada, A.; Kudo, Y.; Liu, K. Y. *J. Electrochem. Soc.* **2001**, *148*, A747–A754.

[16] Yabuuchi, N.; Ohzuku, T. *J. Power Sources* **2003**, *119*, 171–174.

[17] Dahn, J. R.; Fuller, E. W.; Obrovac, M.; Vonsacken, U. *Solid State Ionics* **1994**, *69*, 265–270.

[18] Albrecht, S.; Kumpers, J.; Kruft, M.; Malcus, S.; Vogler, C.; Wahl, M.; Wohlfahrt-Mehrens, M. *J. Power Sources* **2003**, *119*, 178–183.

[19] Chen, C. H.; Liu, J.; Stoll, M. E.; Henriksen, G.; Vissers, D. R.; Amine, K. *J. Power Sources* **2004**, *128*, 278–285.

[20] Kostecki, R.; Lei, J. L.; McLarnon, F.; Shim, J.; Striebel, K. *J. Electrochem. Soc.* **2006**, *153*, A669–A672.

[21] Akimoto, J.; Takahashi, Y.; Gotoh, Y.; Mizuta, S. *J. Cryst. Growth* **2001**, *229*, 405–408.

[22] Kim, J. K.; Cheruvally, G.; Ahn, J. H.; Hwang, G. C.; Choi, J. B. *J. Phys. Chem. Solids* **2008**, *69*, 2371–2377.

[23] Laubach, S.; Laubach, S.; Schmidt, P. C.; Ensling, D.; Schmid, S.; Jaegermann, W.; Thissen, A.; Nikolowski, K.; Ehrenberg, H. *Phys. Chem. Chem. Phys.* **2009**, *11*, 3278–3289.

[24] Liu, C. F.; Neale, Z. G.; Cao, G. Z. *Mater. Today* **2016**, *19*, 109–123.

[25] Linden, D.; Reddy, T. *Handbook of Batteries*; McGraw-Hill handbooks; McGraw-Hill Education, 2001.

[26] Goodenough, J. B.; Park, K. S. *J. Am. Chem. Soc.* **2013**, *135*, 1167–1176.

[27] Etacheri, V.; Marom, R.; Elazari, R.; Salitra, G.; Aurbach, D. *Energy Environ. Sci.* **2011**, *4*, 3243–3262.

[28] Nitta, N.; Wu, F. X.; Lee, J. T.; Yushin, G. *Mater. Today* **2015**, *18*, 252–264.

[29] Whittingham, M. S. *Dalton Trans.* **2008**, 5424–5431.

[30] Bruce, P. G.; Scrosati, B.; Tarascon, J. M. *Angew. Chem. Int. Ed.* **2008**, *47*, 2930–2946.

[31] Guo, Y. G.; Hu, J. S.; Wan, L. J. *Adv. Mater.* **2008**, *20*, 4384–4384.

[32] Wang, Y.; Cao, G. Z. *Adv. Mater.* **2008**, *20*, 2251–2269.

[33] Lee, K. T.; Cho, J. *Nano Today* **2011**, *6*, 28–41.

[34] Kim, M. G.; Cho, J. *Adv. Funct. Mater.* **2009**, *19*, 1497–1514.

[35] Sivakumar, N.; Gnanakan, S. R. P.; Karthikeyan, K.; Amaresh, S.; Yoon, W. S.; Park, G. J.; Lee, Y. S. *J. Alloys Compd.* **2011**, *509*, 7038–7041.

[36] Gong, C.; Bai, Y. J.; Qi, Y. X.; Lun, N.; Feng, J. *Electrochim. Acta* **2013**, *90*, 119–127.

[37] Pan, Y.; Zhang, Y.; Wei, X. P.; Yuan, C. L.; Yin, J. L.; Cao, D. X.; Wang, G. L. *Electrochim. Acta* **2013**, *109*, 89–94.

[38] Yin, Y. H.; Zhang, B.; Zhang, X. T.; Xu, J. J.; Yang, S. T. *J. Sol-Gel Sci. Technol.* **2013**, *66*, 540–543.

[39] Liu, H. W.; Liu, H. F. *J. Electron. Mater.* **2014**, *43*, 2553–2558.

[40] Rai, A. K.; Thi, T. V.; Gim, J.; Kim, J. *Mater. Charact.* **2014**, *95*, 259–265.

[41] Permien, S.; Indris, S.; Scheuermann, M.; Schurman, U.; Mereacre, V.; Powell, A. K.; Kienle, L.; Bensch, W. *J. Mater. Chem. A* **2015**, *3*, 1549–1561.

[42] Qiao, H.; Luo, L.; Chen, K.; Fei, Y. Q.; Cui, R. R.; Wei, Q. F. *Electrochim. Acta* **2015**, *160*, 43–49.

[43] Yin, Y.; Huo, N.; Liu, W.; Shi, Z.; Wang, Q.; Ding, Y.; Zhang, J.; Yang, S. *Scripta Mater.* **2016**, *110*, 92–95.

[44] Antao, S. M.; Hassan, I.; Crichton, W. A.; Parise, J. B. *Am. Mineral.* **2005**, *90*, 1500–1505.

[45] Antao, S. M.; Hassan, I.; Parise, J. B. *Am. Mineral.* **2005**, *90*, 219–228.

[46] Verma, S.; Joy, P. A.; Khollam, Y. B.; Potdar, H. S.; Deshpande, S. B. *Mater. Lett.* **2004**, *58*, 1092–1095.

[47] Chandradass, J.; Jadhav, A. H.; Kim, H. *Appl. Surf. Sci.* **2012**, *258*, 3315–3320.

[48] Chandradass, J.; Jadhav, A. H.; Kim, K. H.; Kim, H. *J. Alloys Compd.* **2012**, *517*, 164–169.

[49] Sasaki, T.; Ohara, S.; Naka, T.; Vejpravova, J.; Sechovsky, V.; Umetsu, M.; Takami, S.; Jeyadevan, B.; Adschiri, T. *J. Supercrit. Fluids* **2010**, *53*, 92–94.

[50] Ilhan, S.; Izotova, S. G.; Komlev, A. A. *Ceram. Int.* **2015**, *41*, 577–585.

[51] Nonkumwong, J.; Ananta, S.; Jantaratana, P.; Phumying, S.; Maensiri, S.; Srisombat, L. *J. Magn. Magn. Mater.* **2015**, *381*, 226–234.

[52] Loganathan, A.; Kumar, K. *Appl. Nanosci.* **2015**, *6*, 629–639.

[53] Chang, F. M.; Jansen, M. *Angew. Chem. Int. Ed. Eng.* **1984**, *23*, 906–907.

[54] Vicat, J.; Fanchon, E.; Strobel, P.; Qui, D. T. *Acta Crystallogr. Sec. B: Struct. Sci.* **1986**, *B42*, 162–167.

[55] Feng, Q.; Kanoh, H.; Miyai, Y.; Ooi, K. *Chem. Mater.* **1995**, *7*, 148–153.

[56] Bish, D. L.; Post, J. E. *Am. Mineral.* **1989**, *74*, 177–186.

[57] Chen, X.; Shen, Y. F.; Suib, S. L.; O'Young, C. L. *Chem. Mater.* **2002**, *14*, 940–948.

[58] Ozawa, T.; Suzuki, I.; Sato, H. *J. Phys. Soc. Jpn.* **2006**, *75*, 014802.

[59] Chen, J.; Li, J.; Li, H.; Huang, X.; Shen, W. *Microporous and Mesoporous Mater.* **2008**, *116*, 586–592.

[60] Li, L. Y.; King, D. L. *Chem. Mater.* **2005**, *17*, 4335–4343.

[61] Chen, J.; Juan, L.; Liu, Q.; Huang, X.; Shen, W. *Chin. J. Catal.* **2007**, *28*, 1034–1036.

[62] Zhu, S.; Marschilok, A. C.; Lee, C. Y.; Takeuchi, E. S.; Takeuchi, K. J. *Electrochem. Solid-State Lett.* **2010**, *13*, A98–A100.

[63] Takeuchi, K. J.; Yau, S. Z.; Menard, M. C.; Marschilok, A. C.; Takeuchi, E. S. *ACS Appl. Mater. Interfaces* **2012**, *4*, 5547–5554.

[64] Takeuchi, K. J.; Yau, S. Z.; Subramanian, A.; Marschilok, A. C.; Takeuchi, E. S. *J. Electrochem. Soc.* **2013**, *160*, A3090–A3094.

[65] Chen, J.; Tang, X.; Liu, J.; Zhan, E.; Li, J.; Huang, X.; Shen, W. *Chem. Mater.* **2007**, *19*, 4292–4299.

[66] Sun, Y. M.; Hu, X. L.; Zhang, W. X.; Yuan, L. X.; Huang, Y. H. *J. Nanopart. Res.* **2011**, *13*, 3139–3148.

[67] Takeuchi, E. S.; Marschilok, A. C.; Tanzil, K.; Kozarsky, E. S.; Zhu, S.; Takeuchi, K. J. *Chem. Mater.* **2009**, *21*, 4934–4939.

[68] Zhang, G. Q.; Hendrickson, M.; Plichta, E. J.; Au, M.; Zheng, J. P. *J. Electrochem. Soc.* **2012**, *159*, A310–A314.

[69] Shin, Y. J.; Kwak, J. H.; Yoon, S. *Bull. Korean Chem. Soc.* **1997**, *18*, 775–778.

[70] Tanaka, M.; Hasegawa, M.; Higuchi, T.; Tsukamoto, T.; Tezuka, Y.; Shin, S.; Takei, H. *Physica B* **1998**, *245*, 157–163.

[71] Berthelot, R.; Pollet, M.; Doumerc, J. P.; Delmas, C. *Inorg. Chem.* **2011**, *50*, 4529–4536.

[72] Ouyang, S.; Chen, D.; Wang, D.; Li, Z.; Ye, J.; Zou, Z. *Cryst. Growth Des.* **2010**, *10*, 2921–2927.

[73] Kumar, S.; Marinel, S.; Miclau, M.; Martin, C. *Mater. Lett.* **2012**, *70*, 40–43.

[74] Nagarajan, R.; Tomar, N. *J. Solid State Chem.* **2009**, *182*, 1283–1290.

[75] Farley, K. E.; Marschilok, A. C.; Takeuchi, E. S.; Takeuchi, K. J. *Electrochem. Solid-State Lett.* **2012**, *15*, A23–A27.

[76] Krehula, S.; Musiċ, S. *Journal of Molecular Structure* **2013**, *1044*, 221–230.

[77] Shahriari, D. Y.; Erdman, N.; Haug, U. T. M.; Zarzyczny, M. C.; Marks, L. D.; Poeppelmeier, K. R. *J. Phys. Chem. Solids* **2003**, *64*, 1437–1441.

[78] Murthy, Y. L. N.; Rao, T. K.; Viswanath, I. V. K.; Singh, R. *J. Magn. Magn. Mater.* **2010**, *322*, 2071–2074.

[79] Krause, A.; Pilawski, K. *Z. Anorg. Allg. Chem.* **1931**, *197*, 301–306.

[80] Krause, A.; Lewandowski, A. *Z. Anorg. Allg. Chem.* **1972**, *389*, 71–74.

[81] Ishiguro, T.; Kitawaza, A.; Mitzutani, N.; Kato, M. *J. Solid State Chem.* **1981**, *40*, 170–174.

[82] Shannon, R. D.; Rogers, D. B.; Prewitt, C. T. *Inorg. Chem.* **1971**, *10*, 723–727.

[83] Krause, A.; Ciokowna, M. *Z. Anorg. Allg. Chem.* **1932**, *204*, 20–28.

[84] Croft, W. J.; Tombs, N. C.; England, R. E. *Acta Crystallogr.* **1964**, *17*, 313.

[85] Sauvage, F.; Muoz-Rojas, D.; Poeppelmeier, K. R.; Casa-Pastor, N. *J. Solid State Chem.* **2009**, *182*, 374–380.

[86] Nagaura, T. *Prog. Batteries Solar Cells* **1982**, *4*, 105–107.

[87] Kleshchuk, V. K.; Raikhel'son, L. B.; Bekreneva, L. A.; Garmash, L. A.; Mikhailova, K. A. *Z. Prikl. Khim.* **1991**, *64*, 326–330.

[88] Sukeshini, A. M.; Kobayashi, H.; Tabuchi, M.; Kageyama, H. *Solid State Ionics* **2000**, *128*, 33–41.

[89] Lu, L.; Wang, J. Z.; Zhu, X. B.; Gao, X. W.; Liu, H. K. *J. Power Sources* **2011**, *196*, 7025–7029.

[90] Sheets, W. C.; Mugnier, E.; Barnabe, A.; Marks, T. J.; Poeppelmeier, K. R. *Chem. Mater.* **2006**, *18*, 7–20.

[91] Marquardt, M. A.; Ashmore, N. A.; Cann, D. P. *Thin Solid Films* **2006**, *496*, 146–156.

[92] Ramesha, K.; Prakash, A. S.; Sathiya, M.; Madra, G.; Shukla, A. K. *Materials Science and Engineering B* **2011**, *176*, 141–146.

[93] Hosogi, Y.; Kato, H.; Kudo, A. *J. Mater. Chem.* **2008**, *18*, 647–653.

[94] Park, M. H.; Shin, Y. J. *Solid State Ionics* **2004**, *167*, 331–334.

[95] Choi, W. J.; Park, M. H.; Shin, Y. J. *J. Korean Chem. Soc.* **2005**, *49*, 623–627.

[96] Kang, J. S.; Lee, S. S.; Lee, H. J.; Kim, G.; Kim, D. H.; Song, H. K.; Shin, Y. J.; Jung, M. C.; Shin, H. J.; Lee, J. E.; Min, B. I. *IEEE Trans. Magn.* **2009**, *45*, 2580–2583.

[97] Ataoui, K. E.; Doumerc, J. P.; Ammar, A.; Grenier, J. C.; Dordor, P.; Pouchard, M. *C. R. Chim.* **2004**, *7*, 29–34.

[98] Sheets, W. C.; Stampler, E. S.; Bertoni, M. I.; Sasaki, M.; Marks, T. J.; Mason, T. O.; Poeppelmeier, K. R. *Inorg. Chem.* **2008**, *47*, 2696–2705.

[99] Krause, A.; Buczkowski, W. *Z. Anorg. Allg. Chem.* **1931**, *200*, 144–152.

[100] Krause, A.; Czapska, Z.; Stock, J. *Z. Anorg. Allg. Chem.* **1932**, *204*, 385–394.

[101] Krause, A.; Lewandowski, A. *Z. Anorg. Allg. Chem.* **1932**, *206*, 328–336.

[102] Hahn, H.; Lorent, C. d. *Z. Anorg. Allg. Chem.* **1955**, *279*, 281–288.

[103] Winchainchai, A.; Dordor, P.; Doumerc, J. P.; Marquestaut, E.; Pouchard, M.; Hagenmuller, P. *J. Solid State Chem.* **1988**, *74*, 126–131.

[104] Otabe, T.; Ueda, K.; Kudoh, A.; Hosono, H.; Kawazoe, H. *Appl. Phys. Lett.* **1998**, *72*, 1036–1038.

[105] Clayton, J. E.; Cann, D. P.; Ashmore, N. *Thin Solid Films* **2002**, *411*, 140–146.

[106] Marschilok, A. C.; Kozarsky, E. S.; Tanzil, K.; Zhu, S.; Takeuchi, K. J.; Takeuchi, E. S. *J. Power Sources* **2010**, *195*, 6839–6846.

[107] Kim, Y. J.; Marschilok, A. C.; Takeuchi, K. J.; Takeuchi, E. S. *J. Power Sources* **2011**, *196*, 6781–6787.

[108] Yau, S. Z.; Farley, K. E.; Marschilok, A. C.; Takeuchi, E. S.; Takeuchi, K. J. *ECS Trans.* **2012**, *41*, 21–28.

[109] Zhu, S.; Marschilok, A. C.; Takeuchi, E. S.; Takeuchi, K. J. *Electrochem. Solid-State Lett.* **2009**, *12*, A91–A94.

[110] Wu, L.; Xu, F.; Zhu, Y.; Brady, A. B.; Huang, J.; Durham, J. L.; Dooryhee, E.; Marschilok, A. C.; Takeuchi, E. S.; Takeuchi, K. J. *ACS Nano* **2015**, *9*, 8430–8439.

[111] Ravel, B.; Newville, M. *J. Synchrotron Radiat.* **2005**, *12*, 537–541.

[112] de Leon, J. M.; Rehr, J. J.; Zabinsky, S. I.; Albers, R. C. *Phys. Rev. B* **1991**, *44*, 4146–4156.

[113] Rehr, J. J.; de Lleon, J. M.; Zabinsky, S. I.; Albers, R. C. *J. Am. Chem. Soc.* **1991**, *113*, 5135–5140.

[114] Jette, E. R.; Foote, F. *J. Chem. Phys.* **1933**, *1*, 29–36.

[115] Owen, E. A.; Yates, E. L. *Philos. Mag.* **1933**, *15*, 472–488.

[116] Langford, J. I.; Wilson, A. J. C. *J. Appl. Crystallogr.* **1978**, *11*, 102–113.

[117] Patterson, A. L. *Phys. Rev.* **1939**, *56*, 978–982.

[118] Hu, Y. Y.; Liu, Z. G.; Nam, K. W.; Borkiewicz, O. J.; Cheng, J.; Hua, X.; Dunstan, M. T.; Yu, X. Q.; Wiaderek, K. M.; Du, L. S.; Chapman, K. W.; Chupas, P. J.; Yang, X. Q.; Grey, C. P. *Nature Mater.* **2013**, *12*, 1130–1136.

[119] Ponrouch, A.; Taberna, P. L.; Simon, P.; Palacin, M. R. *Electrochim. Acta* **2012**, *61*, 13–18.

[120] Laruelle, S.; Grugeon, S.; Poizot, P.; Dolle, M.; Dupont, L.; Tarascon, J. M. *J. Electrochem. Soc.* **2002**, *149*, A627–A634.

[121] Borghols, W. J. H.; Wagemaker, M.; Lafont, U.; Kelder, E. M.; Mulder, F. M. *J. Am. Chem. Soc.* **2009**, *131*, 17786–17792.

[122] Meethong, N.; Huang, H. Y. S.; Speakman, S. A.; Carter, W. C.; Chiang, Y. M. *Adv. Funct. Mater.* **2007**, *17*, 1115–1123.

[123] Wagemaker, M.; Mulder, F. M.; Van der Ven, A. *Adv. Mater.* **2009**, *21*, 2703–2709.

[124] Nadler, M. R.; Kempter, C. P. *Anal. Chem.* **1959**, *31*, 2109–2109.

[125] Bock, D. C.; Pelliccione, C. J.; Zhang, W.; Wang, J.; Knehr, K. W.; Wang, J.; Wang, F.; West, A. C.; Marschilok, A. C.; Takeuchi, K. J.; Takeuchi, E. S. *ACS Appl. Mater. Interfaces* **2016**, *8*, 11418–11430.

[126] Zhang, W.; Bock, D. C.; Pelliccione, C. J.; Li, Y.; Wu, L.; Zhu, Y.; Marschilok, A. C.; Takeuchi, E. S.; Takeuchi, K. J.; Wang, F. *Adv. Energy Mater.* **2016**, *6*, 1502471.

[127] Calvin, S.; Luo, S. X.; Caragianis-Broadbridge, C.; McGuinness, J. K.; Anderson, E.; Lehman, A.; Wee, K. H.; Morrison, S. A.; Kurihara, L. K. *Appl. Phys. Lett.* **2005**, *87*.

[128] Calvin, S.; Miller, M. M.; Goswami, R.; Cheng, S. F.; Mulvaney, S. P.; Whitman, L. J.; Harris, V. G. *J. Appl. Phys.* **2003**, *94*, 778–783.

[129] Frenkel, A. I.; Hills, C. W.; Nuzzo, R. G. *J. Phys. Chem. B* **2001**, *105*, 12689–12703.

[130] Ching, S.; Suib, S. L. *Comments Inorg. Chem.* **1997**, *19*, 263–282.

[131] Hammersley, A. P.; Svensson, S. O.; Hanfland, M.; Fitch, A. N.; Hausermann, D. *High Press. Res.* **1996**, *14*, 235–248.

[132] Toby, B. H.; Von Dreele, R. B. *J. Appl. Crystallogr.* **2013**, *46*, 544–549.

[133] Gao, T.; Norby, P. *Eur. J. Inorg. Chem.* **2013**, *2013*, 4948–4957.

[134] Tanaka, Y.; Tsuji, M.; Tamaura, Y. *Phys. Chem. Chem. Phys.* **2000**, *2*, 1473–1479.

[135] Chen, J.; Tang, X.; Liu, J.; Zhan, E.; Li, J.; Huang, X.; Shen, W. *Chem. Mater.* **2007**, *19*, 4292–4299.

[136] Huang, H.; Meng, Y.; Labonte, A.; Dobley, A.; Suib, S. L. *J. Phys. Chem. C* **2013**, *117*, 25352–25359.

[137] Tang, X.; Chen, J.; Li, Y.; Li, Y.; Xu, Y.; Shen, W. *Chem. Eng. J.* **2006**, *118*, 119–125.

[138] Ye, Q.; Zhao, J.; Huo, F.; Wang, J.; Cheng, S.; Kang, T.; Dai, H. *Catal. Today* **2011**, *175*, 603–609.

[139] Ozacar, M.; Poyraz, A. S.; Genuino, H. C.; Kuo, C. H.; Meng, Y.; Suib, S. L. *Appl. Catal. A* **2013**, *462-463*, 64–74.

[140] Yan, W. B.; Ayvazian, T.; Kim, J.; Liu, Y.; Donavan, K. C.; Xing, W. D.; Yang, Y. G.; Hemminger, J. C.; Penner, R. M. *ACS Nano* **2011**, *5*, 8275–8287.

[141] Chigane, M.; Ishikawa, M. *J. Electrochem. Soc.* **2000**, *147*, 2246–2251.

[142] Toupin, M.; Brousse, T.; Belanger, D. *Chem. Mater.* **2004**, *16*, 3184–3190.

[143] Galakhov, V. R.; Demeter, M.; Bartkowski, S.; Neumann, M.; Ovechkina, N. A.; Kurmaev, E. Z.; Logachevskaya, N. I.; Mukovskii, Y. M.; Mitchell, J.; Ederer, D. L. *Phys. Rev. B* **2002**, *65*.

[144] Santos, V. P.; Soares, O. S. G. P.; Bakker, J. J. W.; Pereira, M. F. R.; Orfao, J. J. M.; Gascon, J.; Kapteijn, F.; Figueiredo, J. L. *J. Catal.* **2012**, *293*, 165–174.

[145] Toupin, M.; Brousse, T.; Belanger, D. *Chem. Mater.* **2002**, *14*, 3946–3952.

[146] Ozacar, M.; Poyraz, A. S.; Genuino, H. C.; Kuo, C. H.; Meng, Y. T.; Suib, S. L. *Appl. Catal. A* **2013**, *462*, 64–74.

[147] Wang, L. L.; Cheng, W.; Gong, H. X.; Wang, C. H.; Wang, D.; Tang, K. B.; Qian, Y. T. *J. Mater. Chem.* **2012**, *22*, 11297–11302.

[148] Li, A. H.; Xu, L. Q.; Li, S. L.; He, Y. Y.; Zhang, R. R.; Zhai, Y. J. *Nano Res.* **2015**, *8*, 554–565.

[149] Ho, C.; Raistrick, I. D.; Huggins, R. A. *J. Electrochem. Soc.* **1980**, *127*, 343–350.

[150] Weppner, W.; Huggins, R. A. *J. Electrochem. Soc.* **1977**, *124*, 1569–1578.

[151] Wen, C. J.; Boukamp, B. A.; Huggins, R. A.; Weppner, W. *J. Electrochem. Soc.* **1979**, *126*, 2258–2266.

[152] Chen, M.; Zheng, X. M. *Indian J. Chem., Sec. A* **2001**, *40A*, 298–302.

[153] Devaraju, M. K.; Truong, Q. D.; Honma, I. *Appl. Mater. Today* **2015**, *1*, 95–99.

[154] Giardi, R.; Porro, S.; Topuria, T.; Thompson, L.; Pirri, C. F.; Kim, H.-C. *Appl. Mater. Today* **2015**, *1*, 27–32.

[155] Durham, J. L.; Kirshenbaum, K.; Takeuchi, E. S.; Marschilok, A. C.; Takeuchi, K. J. *Chem. Commun.* **2015**, *51*, 5120–5123.

[156] Durham, J. L.; Kirshenbaum, K.; Takeuchi, E. S.; Marschilok, A. C.; Takeuchi, K. J. *MRS Adv.* **2016**, *1*, 389–394.

[157] Dar, M. I.; Shivashankar, S. A. *RSC Adv.* **2014**, *4*, 4105–4113.

[158] Chaudhari, N. S.; Warule, S. S.; Muduli, S.; Kale, B. B.; Jouen, S.; Lefez, B.; Hannoyer, B.; Ogale, S. B. *Dalton Trans.* **2011**, *40*, 8003–8011.

[159] Maiti, D.; Manju, U.; Velaga, S.; Devi, P. S. *Cryst. Growth Des.* **2013**, *13*, 3637–3644.

[160] Kang, J.-S.; Kwak, J. H.; Shin, Y. J.; Han, S. W.; Kim, K. H.; Min, B. I. *Phys. Rev. B* **2000**, *61*, 10682–10687.

[161] Allen, G. C.; Curtis, M. T.; Hooper, A. J.; Tucker, P. M. *J. Chem. Soc., Dalton Trans.* **1974**, *14*, 1525–1530.

[162] Azadmanjiri, J.; Simon, G. P.; Suzuki, K.; Selomulya, C.; Cashion, J. D. *J. Mater. Chem.* **2012**, *22*, 617–625.

[163] Takeuchi, K. J.; Marschilok, A. C.; Davis, S. M.; Leising, R. A.; Takeuchi, E. S. *Coord. Chem. Rev.* **2001**, *219221*, 283–310.

[164] Durham, J. L.; Poyraz, A. S.; Takeuchi, E. S.; Marschilok, A. C.; Takeuchi, K. J. *Acc. Chem. Res.* **2016**, *49*, 1864–1872.

[165] Zhu, S.; Marschilok, A. C.; Takeuchi, E. S.; Yee, G. T.; Wang, G.; Takeuchi, K. J. *J. Electrochem. Soc.* **2010**, *157*, A1158–A1163.

[166] Menard, M. C.; Marschilok, A. C.; Takeuchi, K. J.; Takeuchi, E. S. *Electrochim. Acta* **2013**, *94*, 320–326.

[167] Xue, J.; Fan, C.; Deng, Q.; Zhao, M.; Wang, L.; Zhou, A.; Li, J. *Electrochim. Acta* **2016**, *219*, 418–424.

[168] Maiti, D.; Aravindan, V.; Madhavi, S.; Devi, P. S. *J. Power Sources* **2015**, *276*, 291–298.

[169] Wu, Y. Z.; Zhu, P. B.; Reddy, M. V.; Chowdari, B. V. R.; Ramakrishna, S. *ACS Appl. Mater. Interfaces* **2014**, *6*, 1951–1958.

[170] Han, Y.; Wang, Y. J.; Li, L.; Wang, Y. P.; Jiao, L. F.; Yuan, H. T.; Liu, S. X. *Electrochim. Acta* **2011**, *56*, 3175–3181.

[171] Knehr, K. W.; Brady, N. W.; Cama, C. A.; Bock, D. C.; Lin, Z.; Lininger, C. N.; Marschilok, A. C.; Takeuchi, K. J.; Takeuchi, E. S.; West, A. C. *J. Electrochem. Soc.* **2015**, *162*, A2817–A2826.

[172] Dudney, N. J.; Li, J. C. *Science* **2015**, *347*, 131–132.

[173] Kirshenbaum, K.; Bock, D. C.; Lee, C. Y.; Zhong, Z.; Takeuchi, K. J.; Marschilok, A. C.; Takeuchi, E. S. *Science* **2015**, *347*, 149–154.

[174] Chae, B. M.; Oh, E. S.; Lee, Y. K. *J. Power Sources* **2015**, *274*, 748–754.

[175] Kodama, R.; Terada, Y.; Nakai, I.; Komaba, S.; Kumagai, N. *J. Electrochem. Soc.* **2006**, *153*, A583–A588.

[176] Kobayashi, S.; Kottegoda, I. R. M.; Uchimoto, Y.; Wakihara, M. *J. Mater. Chem.* **2004**, *14*, 1843–1848.

[177] Kim, T.; Song, B. H.; Lunt, A. J. G.; Cibin, G.; Dent, A. J.; Lu, L.; Korsunsky, A. M. *Chem. Mater.* **2016**, *28*, 4191–4203.

[178] Ouvrard, G.; Zerrouki, M.; Soudan, P.; Lestriez, B.; Masquelier, C.; Morcrette, M.; Hamelet, S.; Belin, S.; Flank, A. M.; Baudelet, F. *J. Power Sources* **2013**, *229*, 16–21.

[179] Newville, M. *J. Synchrotron Radiat.* **2001**, *8*, 322–324.

[180] Shannon, R. D.; Rogers, D. B.; Prewitt, C. T. *Inorg. Chem.* **1971**, *10*, 719–723.

[181] Pecharroman, C.; Gonzalezcarreno, T.; Iglesias, J. E. *Phys. Chem. Mineral.* **1995**, *22*, 21–29.

[182] Basinski, Z. S.; Humerothery, W.; Sutton, A. L. *Proc. R. Soc. London, Ser. A* **1955**, *229*, 459–467.

[183] Rehr, J. J.; Albers, R. C. *Rev. Mod. Phys.* **2000**, *72*, 621–654.

[184] Beale, A. M.; Weckhuysen, B. M. *Phys. Chem. Chem. Phys.* **2010**, *12*, 5562–5574.

[185] Koo, B.; Xiong, H.; Slater, M. D.; Prakapenka, V. B.; Baasubramanian, M.; Podsiadlo, P.; Johnson, C. S.; Rajh, T.; Shevchenko, E. V. *Nano Lett.* **2012**, *12*, 2429–2435.

[186] Manuel, J.; Kim, J. K.; Ahn, J. H.; Cheruvally, G.; Chauhan, G. S.; Choi, J. W.; Kim, K. W. *J. Power Sources* **2008**, *184*, 527–531.

[187] Kanzaki, S.; Yamada, A.; Kanno, R. *J. Power Sources* **2007**, *165*, 403–407.

[188] Vayssires, L.; Chanac, C.; Tronc, E.; Jolivet, J. P. *J. Colloid Interface Sci.* **1998**, *205*, 205–212.

[189] Darminto,; Cholishoh, M. N.; Perdana, F. A.; Baqiya, M. A.; Mashuri,; Cahyono, Y.; Triwikantoro, *AIP Conf. Proc.* **2011**, *1415*, 234–237.

[190] LaMer, V. K.; Dinegar, R. H. *J. Am. Chem. Soc.* **1950**, *72*, 4847–4854.

[191] Grtz, H. *Scripta Mater.* **1997**, *37*, 9–16.

[192] Smet, Y. D.; Deriemaeker, L.; Finsy, R. *Langmuir* **1997**, *13*, 6884–6888.

[193] Murray, C. B.; Kagan, C. R.; Bawendi, M. G. *Annu. Rev. Mater. Sci.* **2000**, *30*, 545–610.

[194] Zhang, S.; Lee, J.; Sun, S. *Open Surf. Sci. J.* **2012**, *4*, 26–34.

[195] Laurent, S.; Forge, D.; Port, M.; Roch, A.; Robic, C.; Elst, L. V.; Muller, R. N. *Chem. Rev.* **2008**, *108*, 2064–2110.

APPENDIX

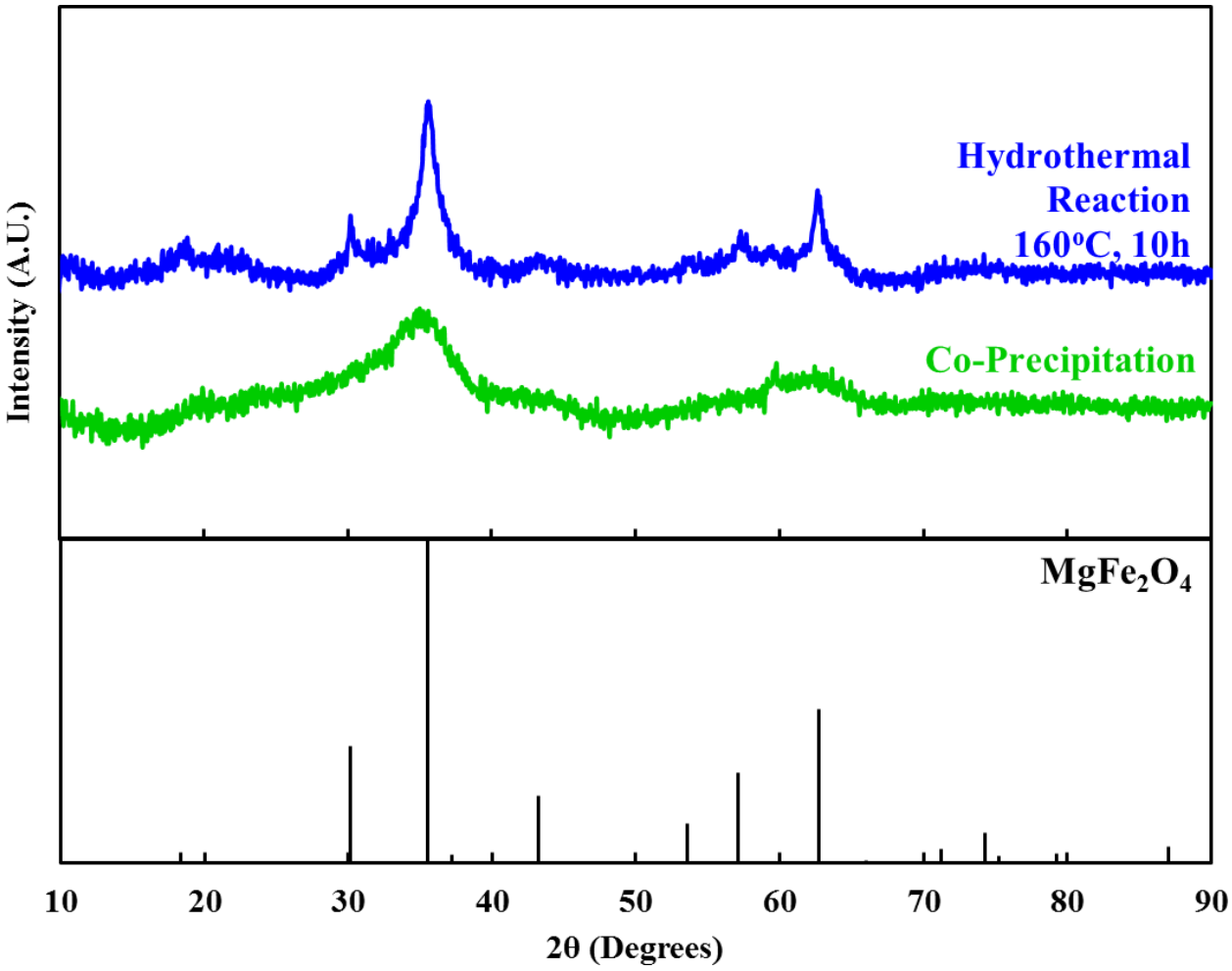

Figure A1. X-ray diffraction (XRD) of $MgFe_2O_4$ after co-precipitation (green) and hydrothermal (blue) reactions

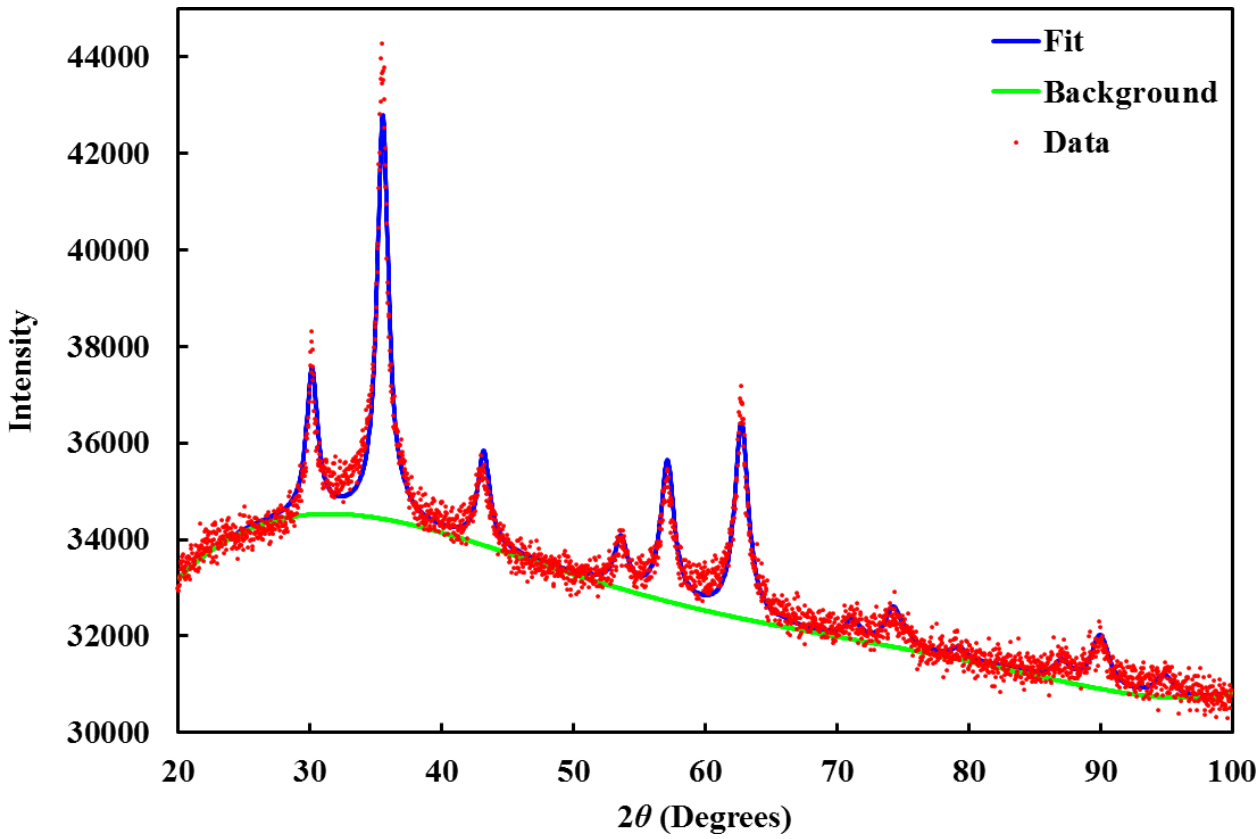

Figure A2. Rietveld refinement of 10 nm $MgFe_2O_4$

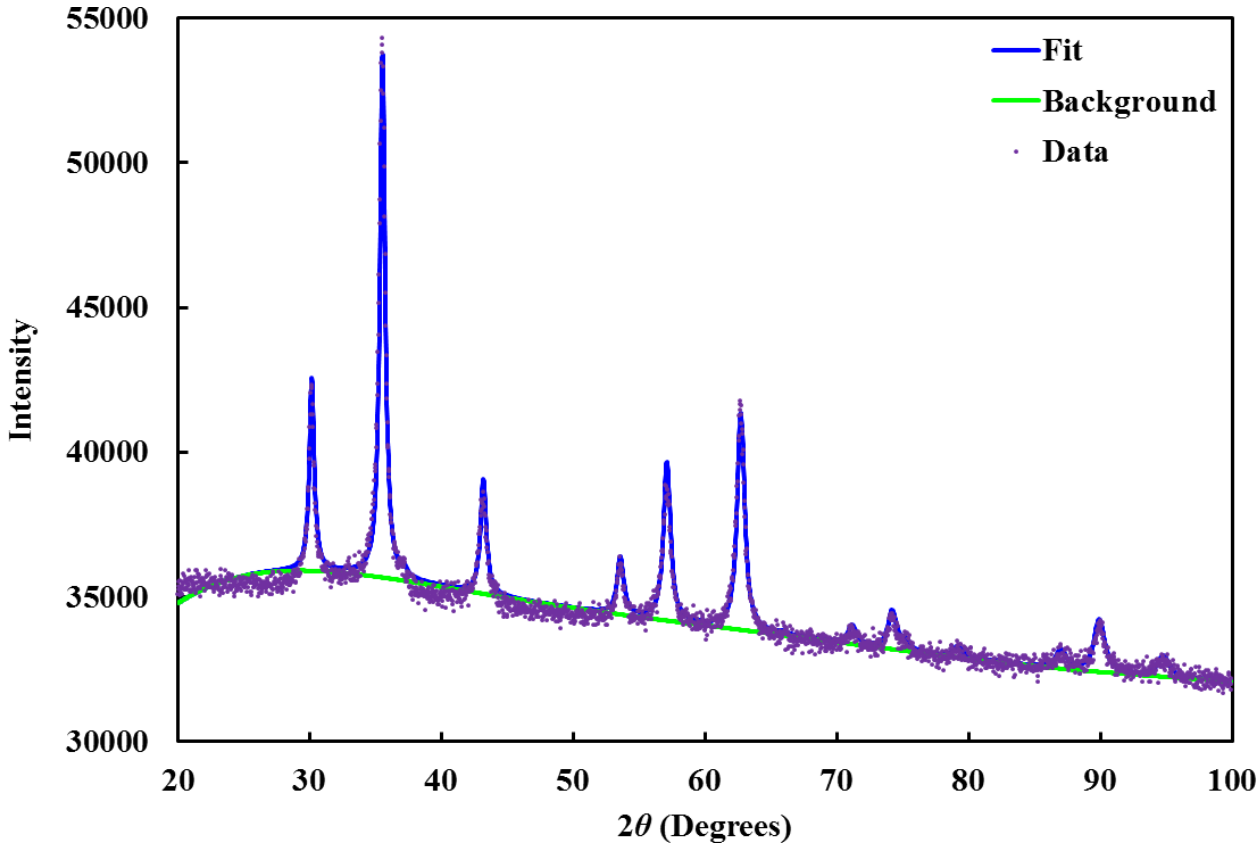

Figure A3. Rietveld refinement of 19 nm $MgFe_2O_4$

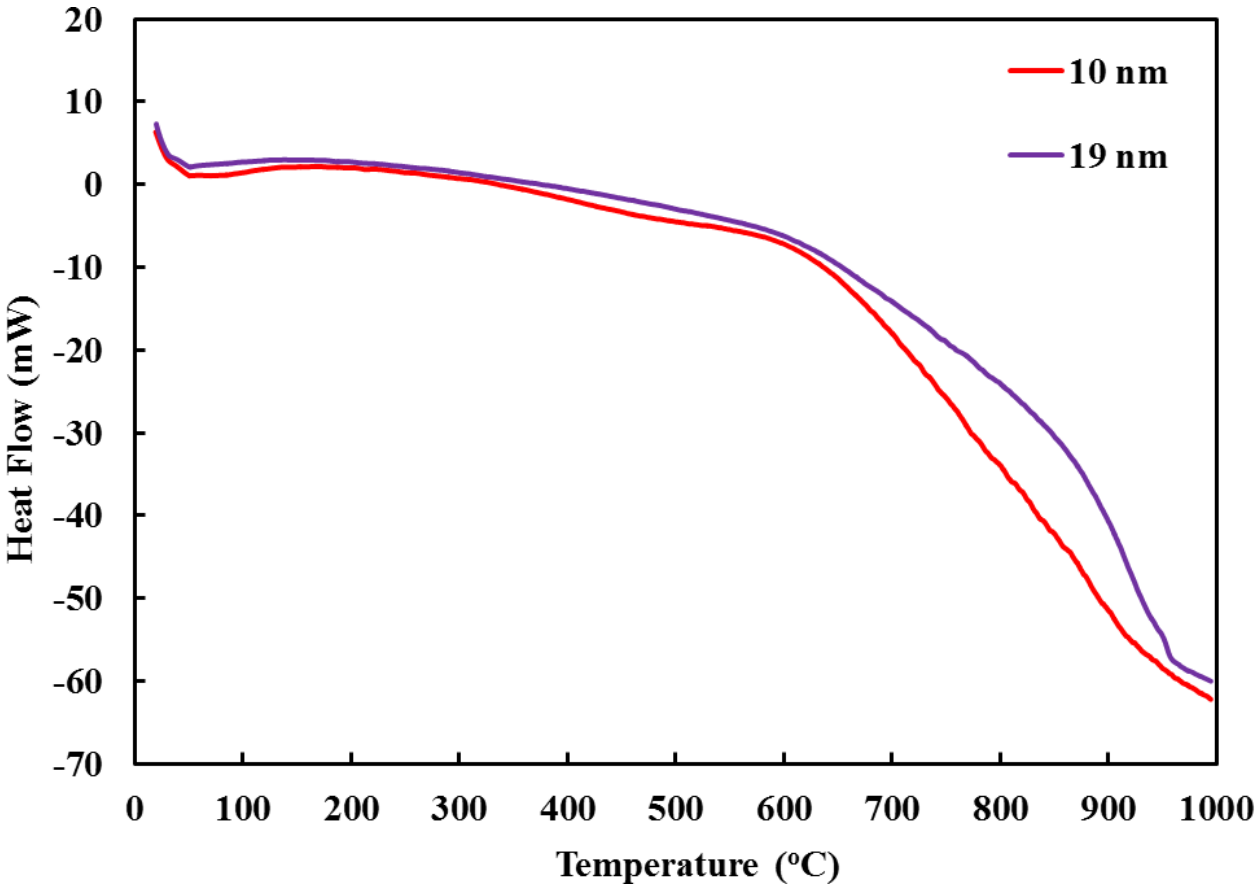

Figure A4. Differntial scanning calorimetry (DSC) curve of 10 and 19 nm $MgFe_2O_4$ to 1000°C

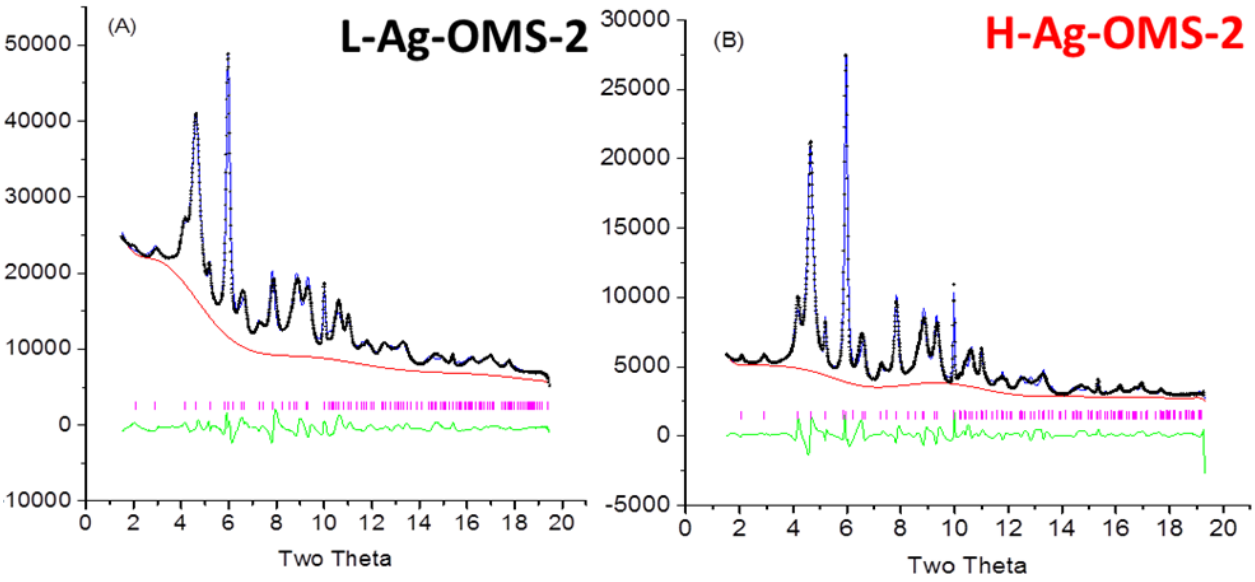

Figure A5. Synchrotron diffraction data and Rietveld refinement of (a) $Ag_{1.22}Mn_8O_{16}$ (L-Ag-OMS-2) and (b) $Ag_{1.66}Mn_8O_{16}$ (H-Ag-OMS-2)

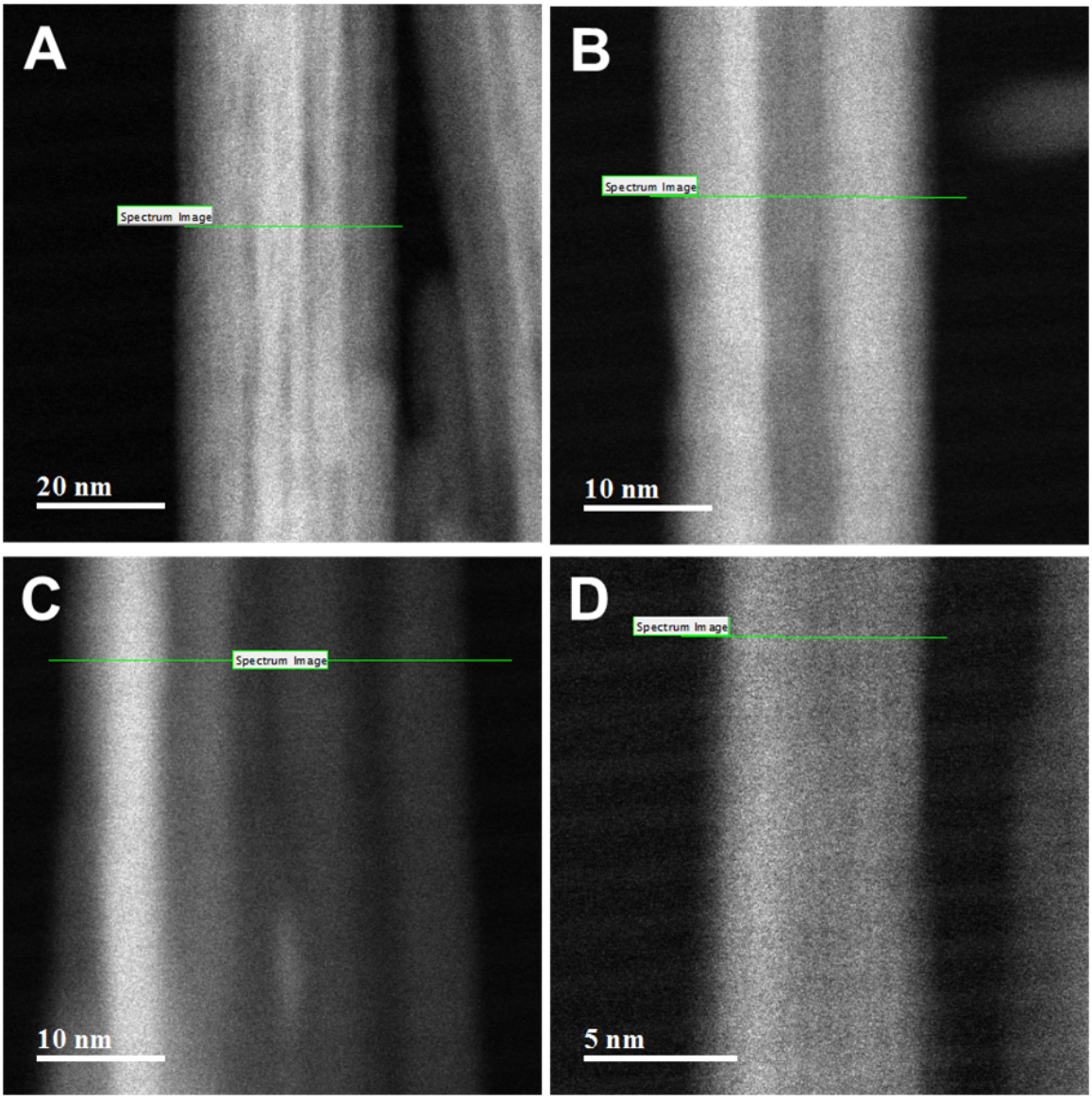

Figure A6. Survey of STEM-HAADF images for EELS of (A,C) 15-Ag-OMS-2 and (B,D) 10-Ag-OMS-2. The horizontal green line corresponds to the location where the EELS spectra were collected. Survey images A-D correspond directly to the EELS spectra (a-d) in **Figure 4.4**.

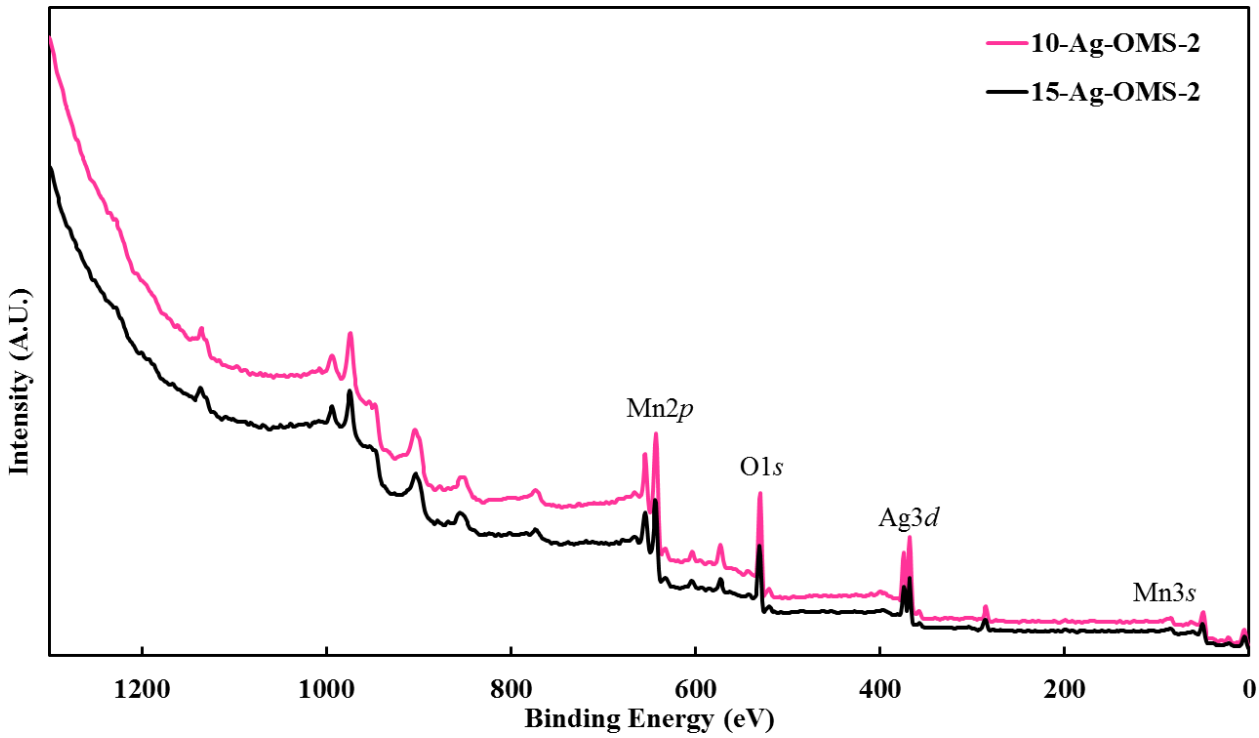

Figure A7. XPS survey spectra (0-1300 eV) for 10-Ag-OMS-2 and 15-Ag-OMS-2 with Mn2p, O1s, Ag3d, and Mn3s core-level regions denoted

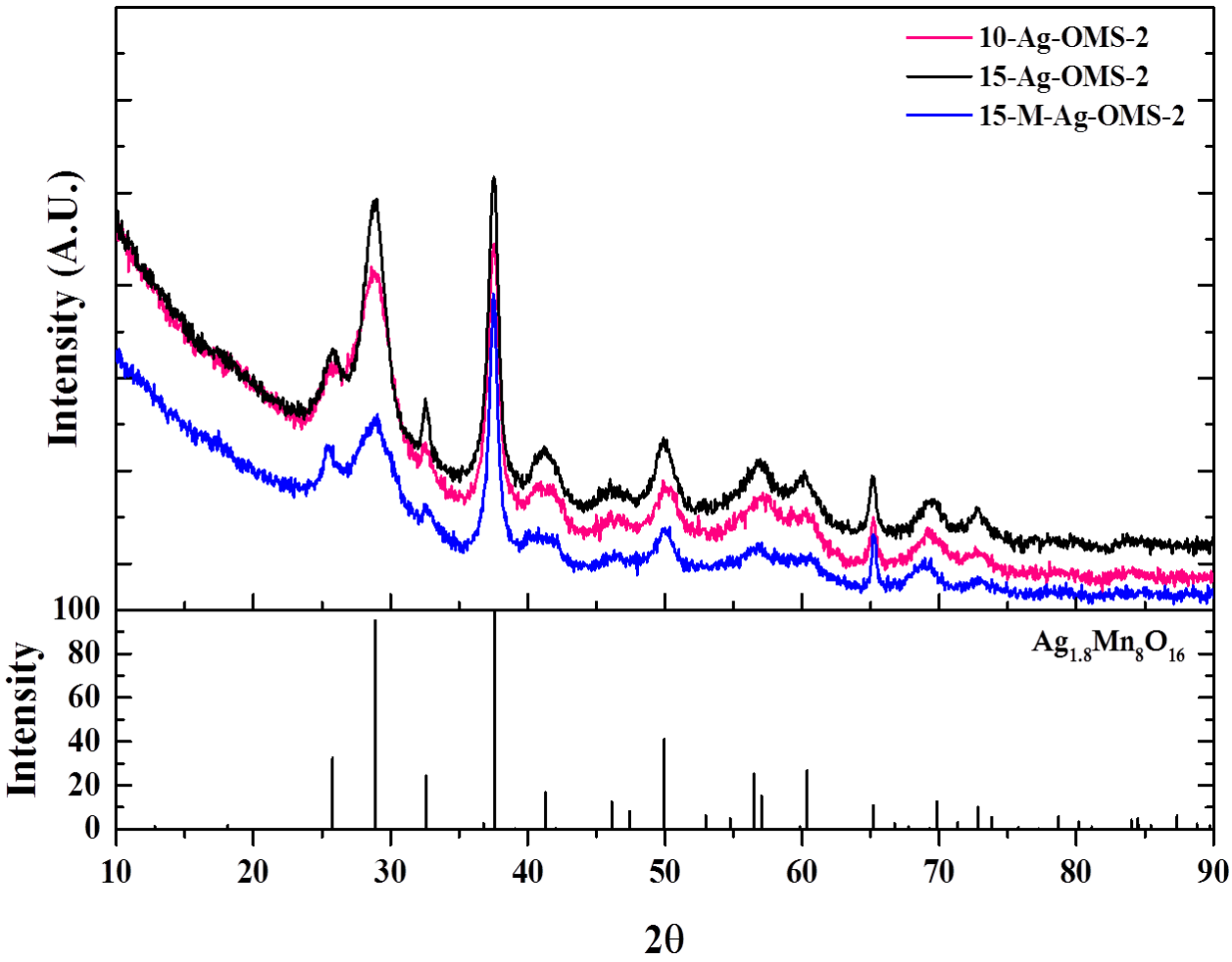

Figure A8. Powder X-ray diffraction (XRD) of 10-Ag-OMS-2 (pink), 15-Ag-OMS-2 (black), and 15-M-Ag-OMS-2 (milled, blue) with reference pattern $Ag_{1.8}Mn_8O_{16}$ (ICSD 60155)

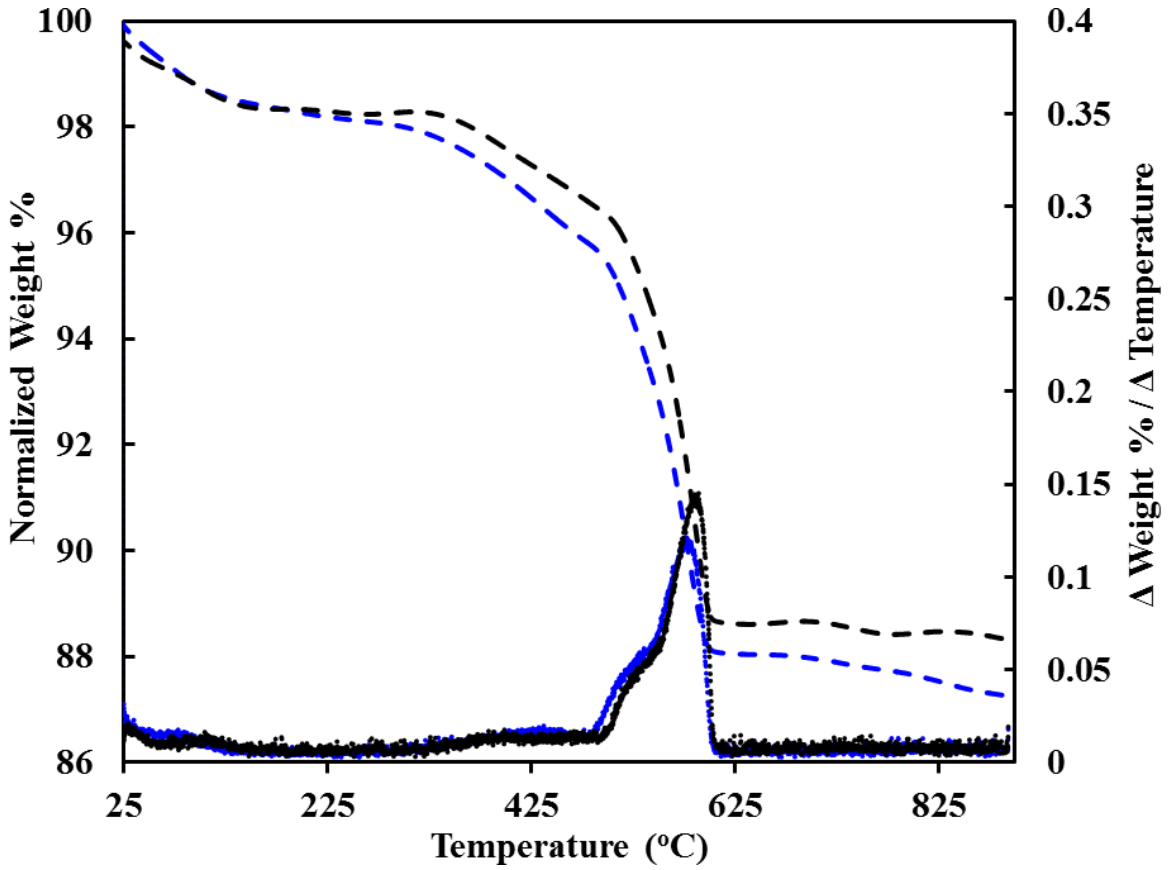

Figure A9. TGA and first derivative of weight as a function of temperature for 15-Ag-OMS-2 (black) and 15-M-Ag-OMS-2 (blue, milled)

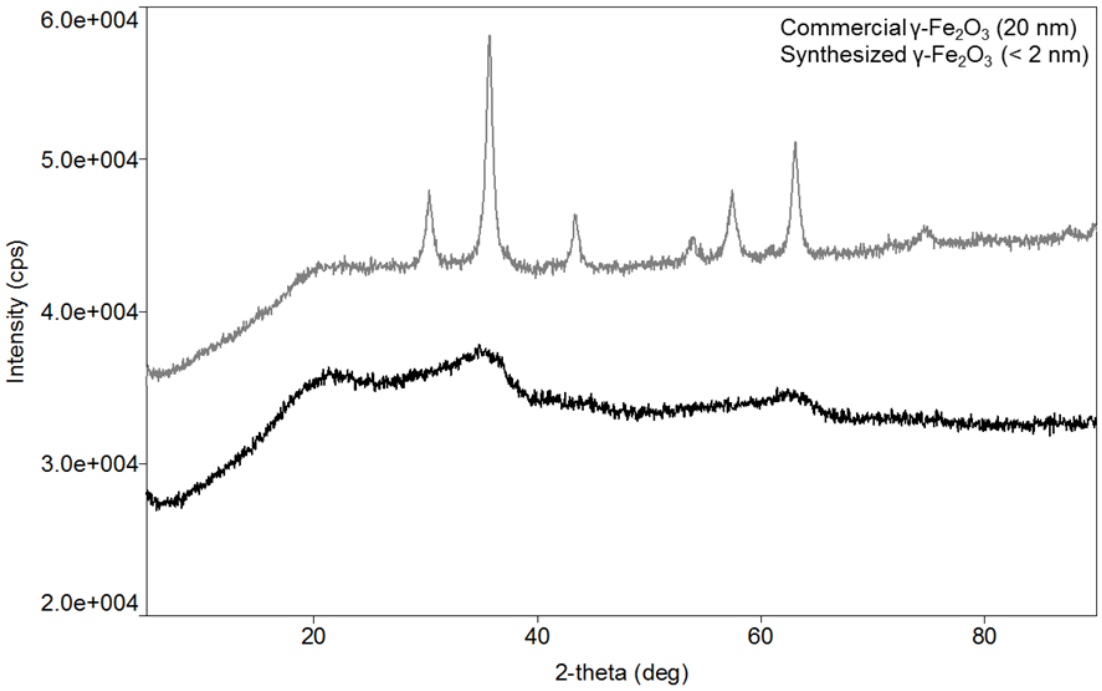

Figure A10. Powder X-ray diffraction of semi-crystalline maghemite (γ-Fe_2O_3, <2 nm) and commercial γ-Fe_2O_3 (20 nm) as reference materials

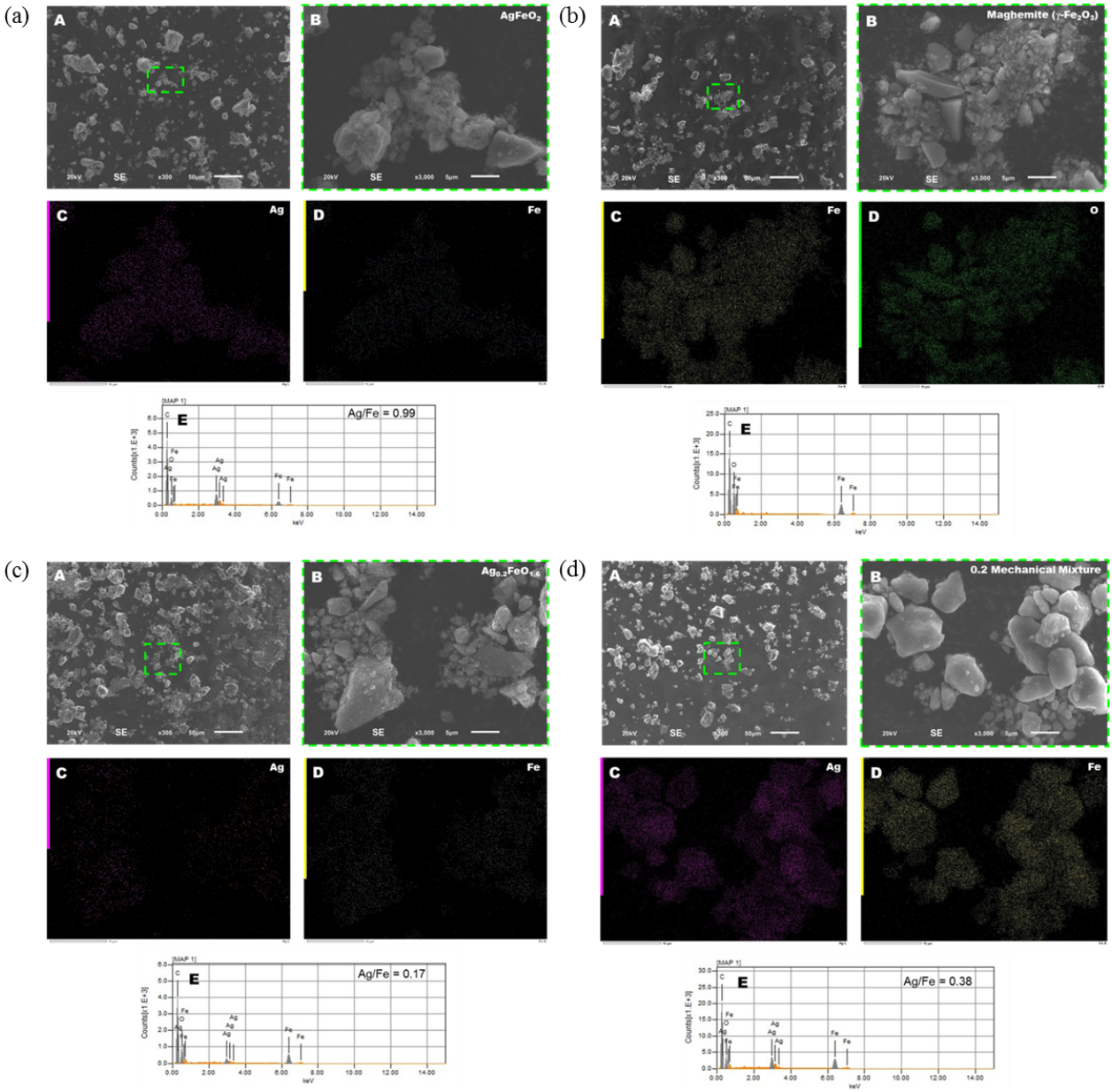

Figure A11. SEM imaging and EDS analysis of (a) $AgFeO_2$, (b) γ-Fe_2O_3, (c) $Ag_{0.2}FeO_{1.6}$, and (d) 0.2 Ag/Fe mechanical mixture. (A,B) SE images at x300 and x3,000 (green box), respectively. (C,D) EDS mapping of Ag and Fe for Ag_xFeO_y composites and Fe and O for γ-Fe_2O_3. (E) EDS spectrum from EDS analysis (C,D) with quantitative Ag/Fe ratio

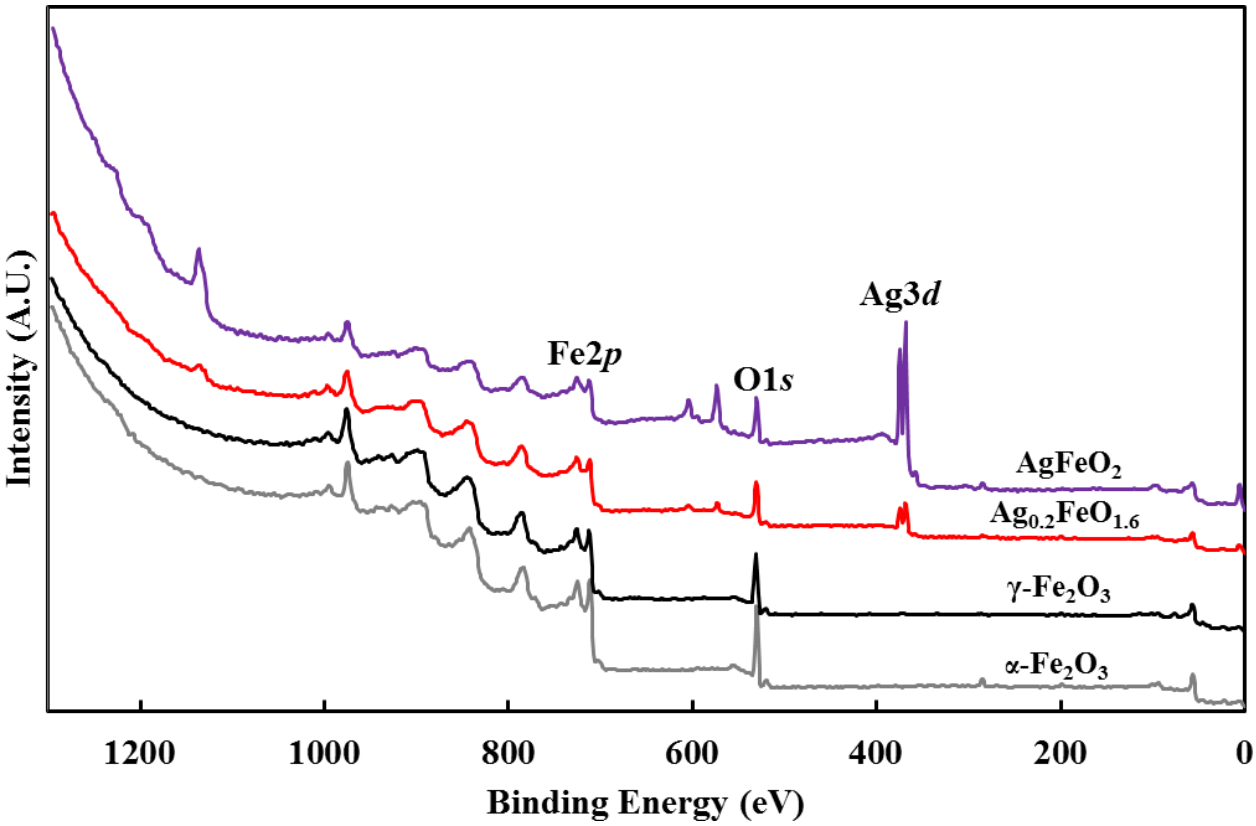

Figure A12. XPS survery spectra (0-1300 eV) for $Ag_{0.2}FeO_{1.6}$ and $AgFeO_2$ with commercial α-Fe_2O_3 and γ-Fe_2O_3 as reference materials and Ag3*d*, Fe2*p*, and O1*s* core-level regions denoted

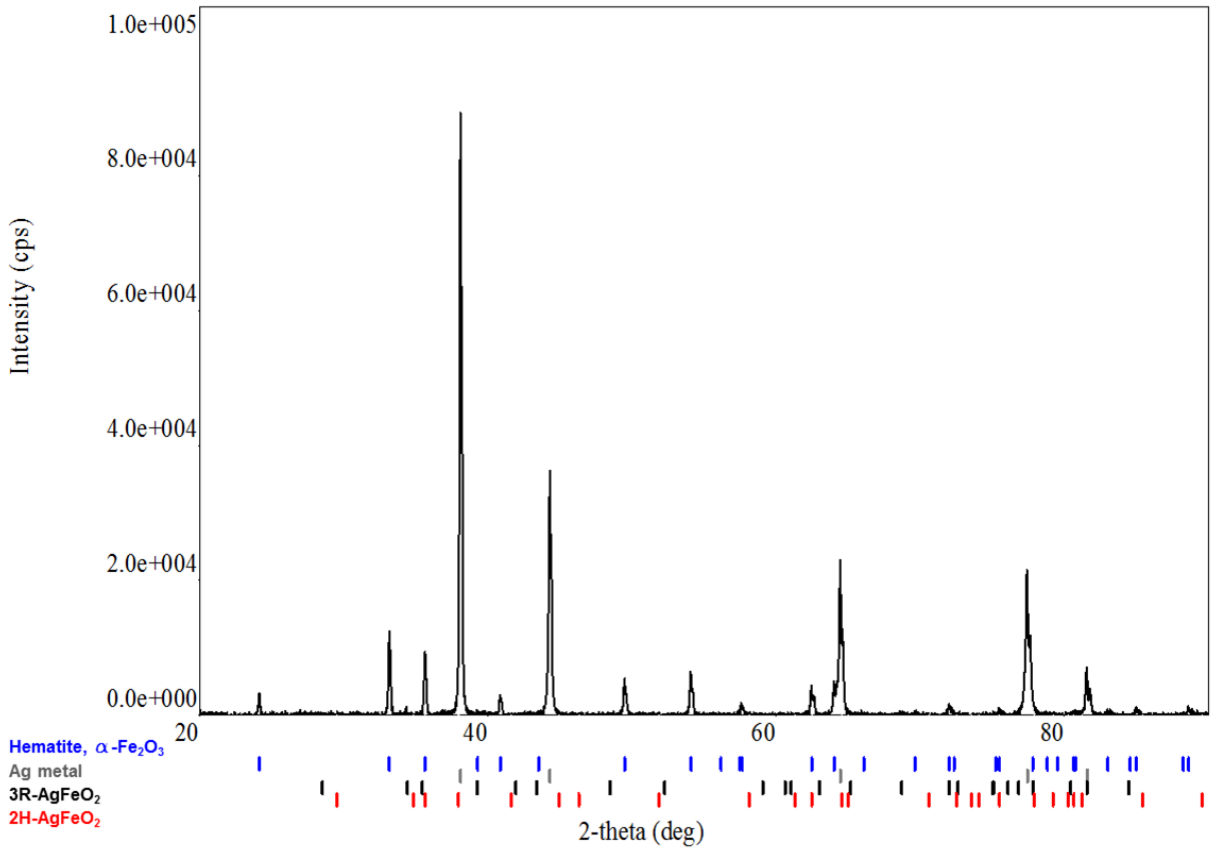

Figure A13. XRD representative of stoichiometric $AgFeO_2$ and Ag_xFeO_y composites after TGA showing the presence of Ag metal and hematite (α-Fe_2O_3) with reference patterns for hematite (ICSD 64599), Ag metal (ICSD 64706), 3R-$AgFeO_2$ (PDF 01-075-2147), and 2H-$AgFeO_2$ (PDF 01-070-1452) polytypes

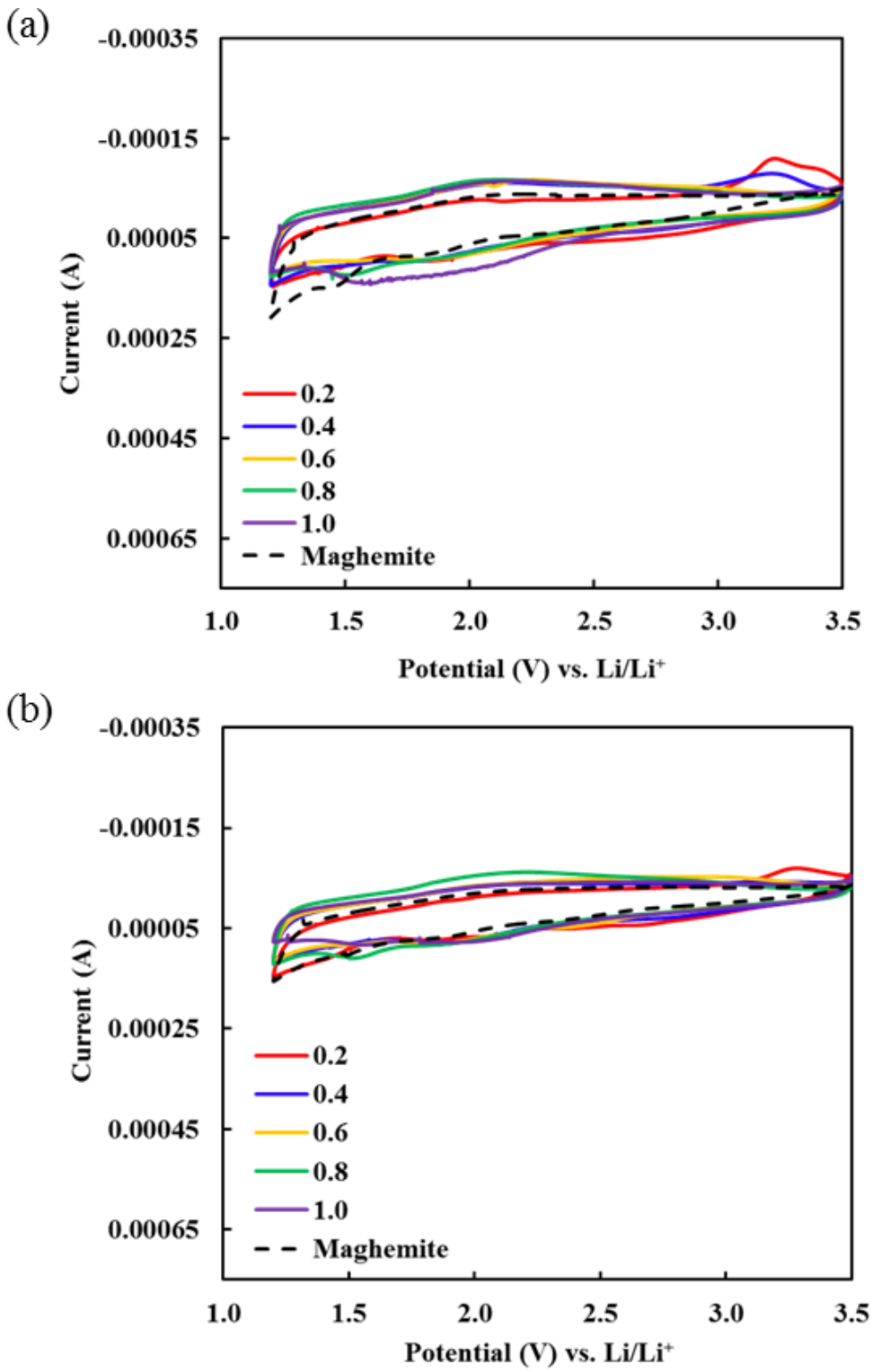

Figure A14. Cyclic voltammetry (CV) of Li/$AgFeO_2$, Li/Ag_xFeO_y, and Li/γ-Fe_2O_3 electrochemical cells with a scan rate of 0.05 mV/s: (a) cycle 2 and (b) cycle 3

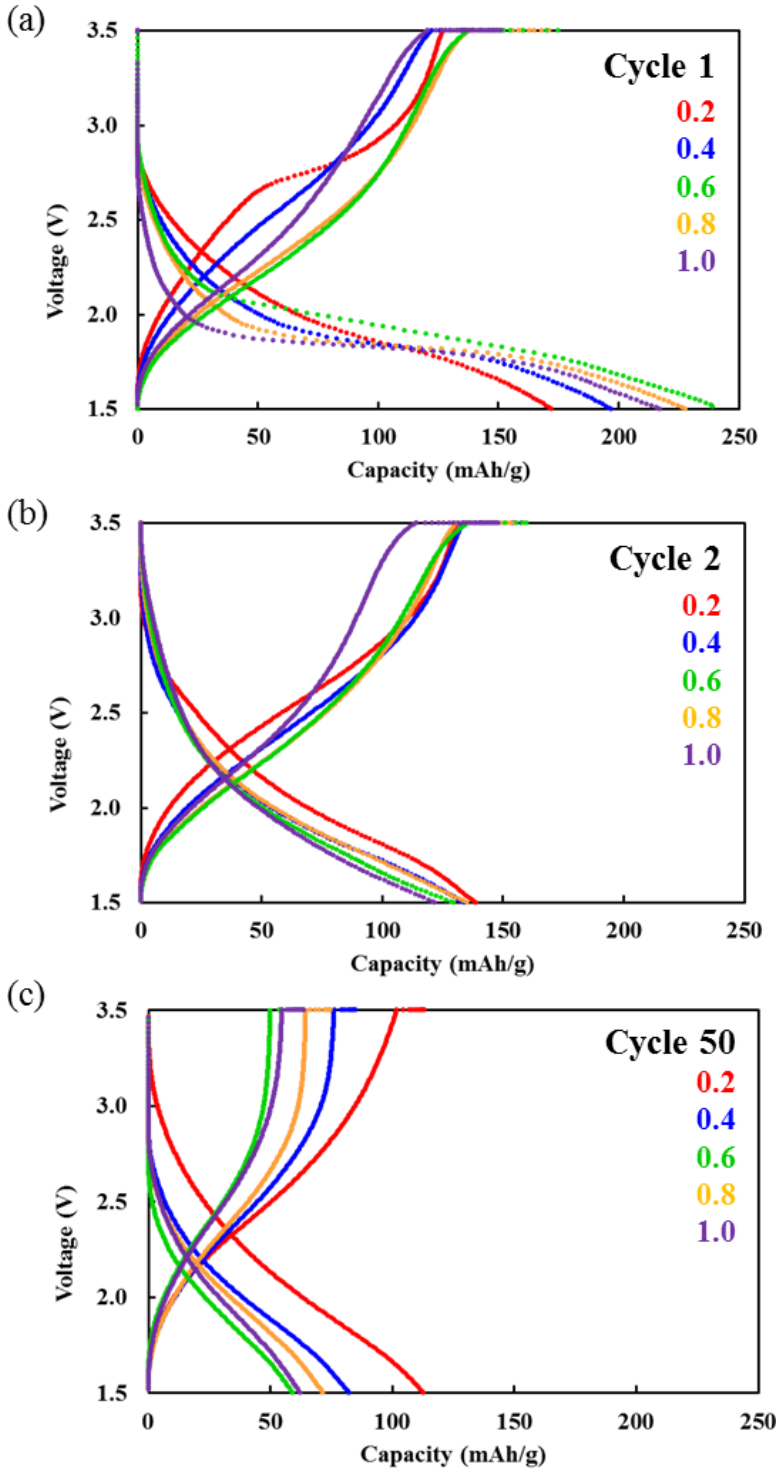

Figure A15. Voltage profiles of $Li/AgFeO_2$ and Li/Ag_xFeO_y ($x = 0.2, 0.4, 0.6, 0.8$) electrochemical cells: (a) cycle 1, (b) cycle 2, and (c) cycle 50

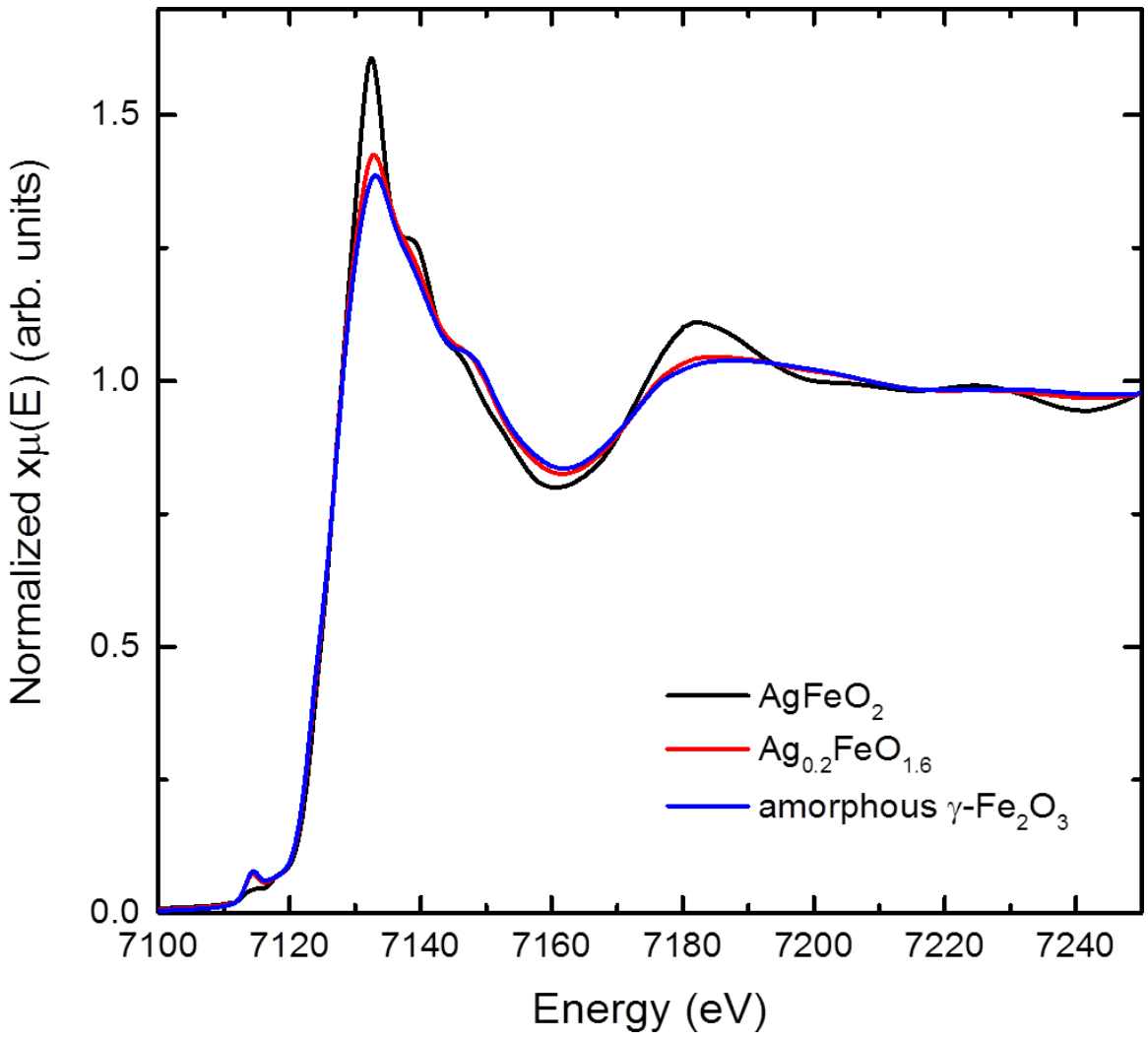

Figure A16. XANES spectra of pristine $AgFeO_2$, $Ag_{0.2}FeO_{1.6}$, and γ-Fe_2O_3